

Clumped isotope geochemistry of British Middle and Upper Jurassic sedimentary archives

Richmal B. Paxton

100102700



A thesis submitted for the degree of
Doctor of Philosophy
School of Environmental Sciences
University of East Anglia
2022

This copy of the thesis has been supplied on condition that anyone who consults it is understood to recognise that its copyright rests with the author and that use of any information derived therefrom must be in accordance with current UK Copyright Law. In addition, any quotation or extract must include full attribution.

Abstract:

Clumped isotope (Δ_{47}) data from British Middle and Upper Jurassic diagenetic and biogenic (skeletal) carbonates is presented. Δ_{47} provides an assumption-free measure of carbonate formation temperature, which, when used in paleotemperature equations, allow derivation of the precipitating fluid $\delta^{18}\text{O}$.

The earliest microspar cements, from the bodies of early diagenetic, mudstone-hosted, septarian concretions (British Middle and Upper Jurassic), formed at temperatures between $9 \pm 5^\circ\text{C}$ and $18 \pm 5^\circ\text{C}$, from pore fluids with $\delta^{18}\text{O}$ between $0.2 \pm 1.1\text{‰}$ and $-2.2 \pm 1.1\text{‰}$ VSMOW. The results confirm syndepositional concretion growth from marine pore fluids. Concretion body cements are proposed as robust archives of benthic palaeotemperatures.

Metre-scale, sandstone-hosted calcite concretions from the Bathonian Valtos Sandstone Formation (Great Estuarine Group) initiated at temperatures of $45 \pm 6^\circ\text{C}$ from isotopically depleted, meteoric pore waters ($-12.4 \pm 1.1\text{‰}$ VSMOW); the fluid compositions unequivocally identify cementation as an early Paleocene event. Temperatures rise in the outer part of the concretions to $73 \pm 8^\circ\text{C}$, and $\delta^{18}\text{O}_{\text{FLUID}}$ compositions become enriched ($2.1 \pm 1.1\text{‰}$ VSMOW). This heating records interaction between meteoric-water and hot lavas formed during the earliest Hebridean Igneous Event. The high temperature signal is found in Valtos Sandstone Formation concretions basin-wide, implying that the porous sandstone was a conduit for hot water in the early Paleocene.

Δ_{47} values in 'pristine' aragonite shells (*Praemytilus strathairdensis*) from the lagoonal, Lealt Shale Formation (Great Estuarine Group), give a range of temperatures (23-58 °C), mostly too high to represent growth environment. Values above 35 °C are interpreted to have undergone partial solid-state resetting of Δ_{47} under burial temperatures $>50^\circ\text{C}$ but $<100^\circ\text{C}$. The lowest temperatures (20-30 °C) and lagoon water $\delta^{18}\text{O}_{\text{FLUID}}$ compositions (0‰ to -2‰ VSMOW) are plausible palaeoenvironmental values. Wider reassessment of preservation criteria for Δ_{47} studies of biogenic aragonite is recommended.

Access Condition and Agreement

Each deposit in UEA Digital Repository is protected by copyright and other intellectual property rights, and duplication or sale of all or part of any of the Data Collections is not permitted, except that material may be duplicated by you for your research use or for educational purposes in electronic or print form. You must obtain permission from the copyright holder, usually the author, for any other use. Exceptions only apply where a deposit may be explicitly provided under a stated licence, such as a Creative Commons licence or Open Government licence.

Electronic or print copies may not be offered, whether for sale or otherwise to anyone, unless explicitly stated under a Creative Commons or Open Government license. Unauthorised reproduction, editing or reformatting for resale purposes is explicitly prohibited (except where approved by the copyright holder themselves) and UEA reserves the right to take immediate 'take down' action on behalf of the copyright and/or rights holder if this Access condition of the UEA Digital Repository is breached. Any material in this database has been supplied on the understanding that it is copyright material and that no quotation from the material may be published without proper acknowledgement.

Contents

Abstract:.....	2
List of Figures:	7
List of Tables:	13
Acknowledgements:.....	15
Chapter 1: Introduction	17
1.1: Aims:	19
1.2: Objectives:	20
1.3: Background to the Great Estuarine Group:	21
1.3.1: Isotopic analysis and the GEG.....	24
1.4: The clumped isotope paleothermometer:.....	26
Chapter 2: Methods	28
2.1: Introduction to clumped isotopes:	28
2.2: Pre-Preparation:.....	28
2.3: Preparation line:	30
2.3.1: 87°C acid digestion:.....	30
2.3.2: CO ₂ purification line:.....	31
2.3.2.1: April 2018 line configuration:	32
2.3.2.2: September 2018 – January 2019 line configuration:.....	33
2.3.2.3: January 2019 – March 2019 line configuration:	33
2.3.2.4: April 2019 – March 2020:	35
2.3.2.5: March 2020 – March 2021.....	36
2.3.2.6: End of March 2021- 7 th May 2021	37
2.3.2.7: 10 th May 2021 – March 2022	37
2.4: The MIRA mass spectrometer:.....	38
2.4.1: Reference gas:.....	39
2.5: Data Processing:.....	39
2.5.1: Instrument linearity	39
2.5.2: Δ_{47} standardisation:	40
2.5.3: Acid fractionation Δ_{47} correction:	42
2.5.4: Temperature derivation:.....	42
2.5.5: $\delta^{18}\text{O}_{\text{CARBONATE}}$:	43
2.5.6: $\delta^{18}\text{O}_{\text{FLUID}}$:	43
2.5.7: Additional data corrections:	44
2.5.7.1: Reference gas experiment corrections:.....	44
2.5.7.2: Reference gas drift corrections:.....	46
2.6: Uncertainties:.....	46
2.7: Sample derived contamination and additional sample preparation:.....	49

2.7.1: Investigation of sample derived contaminants:	50
2.7.2: Water vapour contamination effects:	53
2.8: Limitations with clumped isotope analysis:.....	53
2.8.1: Considerations regarding data processing and comparisons between labs.	53
2.8.2: Additional factors influencing our analysis:.....	54
Chapter 3: Taking the heat out of British Jurassic septarian concretions	55
3.1: Introduction:	55
3.1.1: Study materials	58
3.2: Methods:.....	60
3.2.1: Sample preparation	60
3.2.2: Measurement and data handling	62
3.2.3: Temperature calculation.....	62
3.2.4: Sample contexts.....	63
3.3: Results:.....	64
3.4: Interpretation and discussion:.....	66
3.4.1: Comparison with earlier work:	69
3.5: Conclusions:	72
Chapter 4: Early Paleocene cementation of Middle Jurassic sandstone by hot, meteoric water	74
4.1: Introduction:	74
4.1.1: Carbonate concretions and Clumped Isotopes:.....	74
4.1.2: Great Estuarine Group	75
4.1.3: Valtos Sandstone Formation and its Concretions.....	78
4.1.4: Burial History:	81
4.1.5: Concretion Petrography.....	87
4.1.6: Models of formation	88
4.1.7: Stable isotopes.....	88
4.1.8: Spherical concretions from Valtos:	91
4.2: Methods:.....	93
4.2.1: Samples:	93
4.2.1.1: Main Valtos Sandstone Concretion:	93
4.2.1.2: Additional samples from Valtos, Skye:	93
4.2.1.3: Other Valtos Sandstone Formation Concretions:	97
4.2.1.4: Other cements from Skye and Eigg:.....	98
4.2.1.5: Eigg Lava Formation amygdales:.....	100
4.2.2: Sample preparation	102
4.2.2.1: VR1 Concretion samples:	102
4.2.2.2: Other samples:.....	102
4.2.3: Clumped isotope measurement and data handling	103
4.2.4: Δ_{47} Temperature calculation	103

4.2.3: Sr isotope analysis.....	104
4.3: Results:.....	105
4.4: Discussion:	114
4.4.1: Concretion VR1:	114
4.4.1.1: Zone 1: Early cementation	115
4.4.1.2: Zone 2:	119
4.4.1.3: Zone 3:	129
4.4.1.4: Summary of concretion VR1:	130
4.4.2: Wider context: other cements Valtos Cliffs.....	131
4.4.2.1: Summary of wider context: other cements Valtos Cliffs:	136
4.4.3: Wider context: other concretions of the Valtos Sandstone Formation	136
4.4.3.1: Comparison with previous work:.....	140
4.4.3.2: Summary of wider context: other concretions of the Valtos Sandstone Formation:	142
4.4.4: Wider context: Other cements from Skye and Eigg.....	143
4.4.4.1: Trotternish, Skye:.....	143
4.4.4.2: Eigg:.....	145
4.4.4.3: Eigg Lava Formation amygdales:.....	145
4.5: Conclusions:	146
Chapter 5: Clumped isotopes in Middle Jurassic molluscan aragonite: time for a reset?.....	148
5.1: Introduction:	148
5.1.1: The Kildonnán Member and <i>Praemytilus strathairdensis</i>	149
5.2: Methods:.....	153
5.2.1: Sampling and sample pre-preparation:	153
5.2.2: XRD measurements:.....	156
5.2.3: Clumped isotopes:	156
5.2.3.1: Clumped isotope preparation and measurement:	156
5.2.3.2: Data handling:.....	159
5.2.3.3: Uncertainty:	159
5.2.4: SEM	161
5.2.5: CHN:	161
5.3: Results.....	161
5.3.1: XRD:.....	161
5.3.2: Clumped isotopes: <i>Praemytilus strathairdensis</i> - '159-' collection:	161
5.3.3: Clumped isotopes: <i>Praemytilus strathairdensis</i> Holmden and Hudson (2003) samples:	162
5.3.4: Clumped isotopes: Other shells:	164
5.3.5: SEM:	166
5.4: Discussion:	169

5.4.1: <i>Praemytilus strathairdensis</i> : High temperatures	169
5.4.1.1: Mixing:	172
5.4.1.2: Vital effects and stress	172
5.4.1.3: Measurement variability.....	175
5.4.1.4: Organic contaminants.....	176
5.4.1.5: Aragonite to calcite neomorphism	177
5.4.1.6: Carbonate-Fluid interaction:.....	179
5.4.1.7: Solid-State Resetting.....	182
5.4.1.8: Summary of <i>Praemytilus strathairdensis</i> : High temperatures	185
5.4.2: Environmental conclusions from <i>P. strathairdensis</i> data	188
5.4.3: Wider context:	189
5.5: Conclusions:	191
Chapter 6: Conclusion.....	194
6.1: Future work:.....	197
Chapter 7: References.....	200

List of Figures:

Figure 1.1: The middle to Upper Jurassic succession of the Hebrides of Scotland, after Hesselbo and Coe (2000).	22
Figure 1.2: After Hudson and Andrews (1987); interpretation of $\delta^{18}\text{O}_{\text{CARBONATE}}$ results from a range of carbonate material (Tan and Hudson, 1974; Andrews, 1986), using the temperature equation of Anderson and Arthur (1983) to derive temperature and $\delta^{18}\text{O}_{\text{FLUID}}$ values.	25
Figure 2.1: Schematic of the preparation line before March 2019	33
Figure 2.2: Schematic of the preparation line after March 2019	34
Figure 2.3: Schematic of the preparation line after April 2019	36
Figure 2.4: Relationship between $\Delta 47$ (LRF) and $\Delta 47$ (CDRS @87) for standards measured between September 2018 and October 2018. Gradient and constant of linear equation are the basis for the data transfer function.	41
Figure 2.5: Comparison of corrected and uncorrected data for the standards: A) UEACMST; B) ETH1; C) ETH3. Also shown for comparison is data collected in a time-period where the reference gas aliquot was changed daily (Everyday RG).	45
Figure 2.6: Measured Δ_{48} vs. Δ_{49} values from YSC (yellow sparry calcite), BFC (brown fibrous calcite) and CBC (concretion body cement) from 4 concretions from the Oxford Clay and Amphill Clay formations. Box A shows uncontaminated samples, box B shows contaminated samples. Data collected in September/October 2018.	50
Figure 3.1: Line drawing from a slab of Staffin Shale Formation concretion showing the various calcite phases described in this chapter.	57
Figure 3.2: Sample locations. C = Calvert; CAS = Cassington; P = Peterborough; S = Staffin.	57
Figure 3.3: Geological map of the sampling locality of Staffin Shale Formation concretions, with Ammonite zones as reference; Point 7, Staffin Bay, Trotternish, Isle of Skye. After Morton & Hudson (1995).	59
Figure 3.4: Concretion from the Staffin Shale Formation at Staffin Bay, Trotternish, Isle of Skye, which is ex situ but likely from bed 40. The brown fibrous calcite and yellow sparry calcite fills of the septarian cracks are weathered to dark brown/black. The calcitic concretion body (light grey) has been bordered by a thick siderite layer (orange) which also has yellow sparry calcite fractures (weathered black here).	60

Figure 3.5: Line drawing of sample 161a, showing sampling sites: black circle = concretion body; red line = fibrous fringe (with inner and outer marked as initials); blue line = spar.	61
Figure 3.6: Cross plots of concretion geochemical and Δ_{47} temperature data. Error bars represent one standard error of the pooled standard deviation (see Table 3.2).	65
Figure 3.7: Box and whisker diagram of: (A) Δ_{47} values and (B) temperatures reported for body, fringe and spar cements of Oxford and Ampthill Clay concretions by Loyd et al. (2014) and this study.	70
Figure 4.1. Stratigraphy of the Great Estuarine Group, with schematic log for Trotternish (Skye). Black and white scale bar divisions represent ~25 m (after Andrews, 1984).	76
Figure 4.2: Map of Skye and the Small Isles, including Eigg, with sampling locations indicated by arrows. Red dashed zone shows extent of hydrothermal influence of the Skye Paleocene igneous centres, based on information from Forester and Taylor (1977). Map adapted from Thrasher (1992).	77
Figure 4.3: Map showing extent of the Sea of the Hebrides and Inner Hebrides basins after Fyfe et al. (2021). IHB = Inner Hebrides basin.	78
Figure 4.4: Graphic log of the Valtos Formation at Valtos (Trotternish) after Harris and Hudson (1980).	79
Figure 4.5: Concretions from the basal Valtos Formation, Valtos Trotternish. A) ‘Spherical’ concretion, bed 3 ; B) ‘Tabular’ concretion, basal part of bed 3. This concretion previously analysed in Wilkinson (1989) – vertical spacing of drill core holes is ~10 cm.	80
Figure 4.6: Concretions from upper part of the Valtos Formation (Division E) of Laig Bay, Eigg. Hammer handle is 35 cm long. A) large concretions in bed 2 similar to the spherical concretions seen at Valtos (Fig. 5a) B) ‘decimetre-scale’ concretions; C) concretions in cemented zone adjacent to Tertiary dyke.	82
Figure 4.7: Calcite-cemented veins that cross cut (post-date) concretions at, A) bed 3 Valtos Cliffs, Trotternish, Skye; and B) bed 2 (Division E) Laig Bay, Eigg.	83
Figure 4.8: Prominent calcite-cemented veins in cemented sandstone adjacent to a dyke margin (dyke now eroded into trench feature (left). The veins run parallel to the dyke. Laig Bay, Eigg.	84
Figure 4.9: Calcite cemented vein within dyke at Valtos Cliffs, bed 2, Trotternish, Skye.	85

- Figure 4.10:** Simplified burial history of the Great Estuarine Group, updated from Hudson and Andrews (1987). The brown envelope shows the complete thickness of the GEG. The plot depicts a theoretical maximum burial as tectonic/erosional disturbances are not accounted for. The pecked lines indicate greater uncertainty post-60 Ma and are a compromise solution from varied data sources. The timing of two phases of land surface erosion is indicated but depth of erosion is not known. The Valtos Sandstone Formation is positioned in the centre of the GEG envelope. 86
- Figure 4.11:** Concretions in bed 3 at Valtos, Trotternish. A) Compaction of sedimentary laminae visible around the concretions, particularly clear on the LHS above concretion. 88
- Figure 4.12:** Comparison of $\delta^{18}\text{O}$ and $\delta^{13}\text{C}$ results for decimetre-scale (E2 to 8) and large (E1) concretions from Eigg measured by Wilkinson (1989, 1992). P1 to 3 indicate zones of the large Eigg concretion referred to in text (reported as P1-3 by Wilkinson, 1989). 90
- Figure 4.13:** Comparison of $\delta^{18}\text{O}$ and $\delta^{13}\text{C}$ results for spherical (VR1 and 2) and basal (VB1 to 3) concretions from Valtos, Skye, measured by Wilkinson (1989, 1993). 90
- Figure 4.14:** Data for concretion VR1 from Wilkinson (1989, 1992), indicating vertical and horizontal transects; A) $\delta^{13}\text{C}$ and $\delta^{18}\text{O}$ (‰, PDB); B) SrCO_3 and MnCO_3 (mol%); C) MgCO_3 and FeCO_3 (mol%). 92
- Figure 4.15:** Concretion VR1, bed 3, Valtos, Trotternish. A) *In situ* as illustrated by Wilkinson (1993) and B) *ex situ* as seen on the foreshore in 2018 (inverted relative to A). 94
- Figure 4.16:** *Neomiodon* limestone blocks, *ex situ* at Valtos Cliffs, Skye. A) Sample 189-8 in the field; B) Sample 18-4 in the field; C) Sample 189-8 with spar fills visible; D) 18-4 vein sample. 95
- Figure 4.17:** Veins associated with a dyke intruding the Valtos Sandstone at Valtos Cliffs, Skye. A) Locations of samples in reference to the dyke; B) Sample 189-5, showing needle-like calcite crystals and association with a brown smectite mineral; C) Sample 189-7a including location of vein subsection; D) Sample 198-6; E) Schematic of the relationship between vein 189-5 and 189-7a. 96
- Figure 4.18:** Sample EG 191015-1, concretion from Dun Dearg, Skye. Field photo courtesy of J. E. Andrews. 97

Figure 4.19: Sampling schematic of ‘large’ concretion from bed 2, Divison E, Laig Bay, Eigg.	98
Figure 4.20: Field photos of decimetre-scale concretions from Laig Bay, Eigg. A) Sample 169-6; B) Sample 169-7; C) Sample 169-6 in situ; D) section of Sample 169-6 taken for hand specimen.	99
Figure 4.21: Cross section of sample 169-1r, a dyke margin concretion from Laig Bay, Eigg. Powder was milled from a well cemented section, seen here as the palest colour.	99
Figure 4.22: Images of veins from the Duntulm Formation at Kilmaluag Bay, Skye; A) veins crosscutting both sedimentary and igneous intrusive rocks; B) Sample 199-1 from bed 3 (an oyster bed); Sample 199-2 from a cemented sandstone (bed 1).	101
Figure 4.23: Clumped isotope results for concretion VR1; A) $\delta^{13}\text{C}$ and $\delta^{18}\text{O}_{\text{CARBONATE}}$ results measured by MIRA, compared to previously measured results from Wilkinson (1993); B) Δ_{47} derived temperatures; C) derived $\delta^{18}\text{O}_{\text{FLUID}}$ results.	107
Figure 4.24: Clumped isotope results for all samples from A) Skye; and B) Eigg.	112
Figure 4.25: XPL petrographic images of the poikilotopic crystal structure of concretion VR1, increasing in size and elongating radially. A) shows a schematic of concretion fabric from Wilkinson (1989) and approximate positions of sample site; B) shows the central, almost equant crystal in extinction at the concretion centre (Z1), highlighted in C); D) shows crystals in Z2 at 46 cm from the concretion centre, annotated in E) to highlight calcite crystal terminations; F) shows a crystal boundary from Z3, the outer edge of the concretion (60.5 cm from the centre), where individual crystals greatly exceed the size of the field of view, highlighted in G).	121
Figure 4.26: XPL petrographic images from concretion VR1. A) shows approximately equant crystals from sample M8604 16.5 from centre (Z1), highlighted in B); C) shows mixture of elongated and approximately equant crystals in Z1 from sample M8614 at 26 cm from concretion centre (horizontal transect, approximately equivalent to M87216), highlighted in D); E) shows elongated crystals from sample M8605, 31.5 cm from centre at Z1 edge, highlighted in F).	122
Figure 4.27: Map of the Inner Hebrides adapted from Thrasher (1992). Red dashed zone shows mapped extent (Forester and Taylor 1977) of hydrothermal influence of the Cuillin/Red Hills Igneous Centres. Blue labels identify localities where	126

Paleocene lava was emplaced directly on the eroded surface of the Valtos Formation. Note that these localities are spread across the depositional basin.

- Figure 4. 28:** Sr isotope results for concretion VR1 and dyke vein 189-7a from Valtos Cliffs, Skye, in comparison to a suite of other Sr results from the Jurassic sediments and shells of the Inner Hebrides (data from Andrews et al., 1987; Hamilton et al., 1992; Holmden and Hudson, 2003) and Paleocene Lava from Skye (data from Scarrow, 1992). In B, the results of Jurassic clays from the Duntulm Formation (DF) and Kilmaluag Formation (KF) are omitted for ease of comparison. 128
- Figure 4.29:** Petrography of sparry calcite cements in the shelter cavity of an articulated *Neomiodon* sp. shell (Sample 76861, equivalent to Sample 189-8) Valtos Cliffs, Skye. A) PPL image of stained thin section; note pink colour of the final cavity filling cement (non-ferroan) versus the blue colour (ferroan) of the penultimate cement generation; B) CL image of centremost cements showing bright orange CL colour of the final cement fill. It is assumed that drilling for Δ47 sampled mainly the bright orange CL final cement fill as drilling was targeted in the centre of the cavity; C) bright orange CL colour of vein cements in Sample 18-4 similar to that in B). 135
- Figure 4.30:** Clumped isotope results for all concretions from the Valtos Sandstone of Skye and Eigg. Error bars represent one standard error of the pooled standard deviation. The $\delta^{18}\text{O}_{\text{CARBONATE}}$ errors are < symbol dimensions. 138
- Figure 4.31:** Decimetre-scale concretion at Laig Bay, Eigg, showing the concretion's proximity to a dyke and its location within the cemented sandstone dyke margin, which therefore must have succeeded concretion formation. 139
- Figure 4.32:** Comparison of $\delta^{13}\text{C}$ and $\delta^{18}\text{O}_{\text{CARBONATE}}$ of Valtos concretions from Skye and Eigg for the present study and Wilkinson (1989, 1992, 1993) and Tan and Hudson (1974). Figure includes values for original aragonite and calcite replaced *Neomiodon* shells from Tan and Hudson (1974). 141
- Figure 5.1:** Map of Skye and the Small Isles, including Eigg, with sampling locations indicated by arrows. Map adapted from Thrasher (1992). 150
- Figure 5.2:** Graphic log of the Kildonnan Member at the type section (Eigg) after Hudson et al. (1995). 151
- Figure 5.3:** Shell plaster of *P. strathairdensis* in bed 5e of the Kildonnan member at the type section (Eigg). Note the distinctive pink colour of the skeletal aragonite. Hand lens is 6 mm long. Photo courtesy of Julian Andrews. 153

Figure 5.4: Measured $\delta^{13}\text{C}$ and $\delta^{18}\text{O}_{\text{CARBONATE}}$ values of suite '159-' <i>P. strathairdensis</i> shells, in comparison with shells previously measured by Tan and Hudson (1974) and Holmden and Hudson (2003). 10 °C groupings of Δ_{47} derived temperatures are indicated by colour (MIRA 159: xx-xx °C).	163
Figure 5.5: Clumped isotope results for <i>P. strathairdensis</i> , distinguishing between the '159-' collection and the shells provided by Holmden and Hudson (2003). Contours show $\delta^{18}\text{O}_{\text{FLUID}}$ values (‰, VSMOW).	164
Figure 5.6: Comparison of $\delta^{18}\text{O}$ and $\delta^{13}\text{C}$ of shells measured by Holmden and Hudson (2003) (open markers) and remeasured here (filled markers).	165
Figure 5.7: SEM images of aragonite nacre of shells A) 14a; B) 14c; C) 18a.	167
Figure 5.8: SEM images at increasing magnification of the bottom surface of shell 18b (not otherwise analysed). Possible neomorphism can be seen in the lowermost nacreous layers.	168
Figure 5.9: Covariant trend in $\delta^{13}\text{C}$ and $\delta^{18}\text{O}_{\text{CARBONATE}}$ seen in <i>P. strathairdensis</i> shells, including data previously measured by Tan and Hudson (1974) and Holmden and Hudson (2003). Coloured circles represent data measured by MIRA, with colours corresponding to the percentage of calcite indicated by XRD. The two shells with calcite percentage between 23-25% are clear outliers of this trend.	178
Figure 5.10: Δ_{47} derived temperatures and back calculated $\delta^{18}\text{O}_{\text{FLUID}}$ results of <i>P. strathairdensis</i> and mudstone hosted concretion bodies*, with contours indicating measured $\delta^{18}\text{O}_{\text{CARBONATE}}$. Green box highlights the likely region of original temperature of growth and ambient $\delta^{18}\text{O}_{\text{FLUID}}$ of shells with $\delta^{18}\text{O}_{\text{CARBONATE}}$ close to -2‰ (VPDB).	190

List of Tables:

Table 2.1: schematic indicating the sections of this chapter that describe the methods used for sample gas preparation (Section 2.3.2.X) and additional data corrections (Section 2.5.7.X) to different periods of data acquisition.	31
Table 2.2: Transfer functions used to correct local reference frame data to the CDES reference frame, with reference to their time periods of use.	42
Table 2.3: Pooled standard deviation of each standard, for each chapter.	48
Table 2.4: Standard error for each standard in each period of measurement, using the standard deviation of standards from individual time periods.	48
Table 2.5: Details of tests of pre-preparation technique trials for contamination reduction, using concretion body cement (SC8 CBC) and a standard (UEACMST). Treatment time is in minutes. Orange highlights indicate that change is greater than +1 standard deviation of the mean, and blue highlights indicate that change is greater than -1 standard deviation of the mean.	52
Table 3.1: Equivalence of sample numbering across the different studies for the concretions used in this study.	59
Table 3.2: Geochemical data and δ_{47} temperature results of chapter 3	64
Table 4.1: Stable isotope data from concretions from the Valtos Sandstone Formation from Tan and Hudson (1974) showing average, minimum and maximum values.	89
Table 4.2: Clumped isotope results from concretion VR1. All \pm values represent one standard error of the pooled standard deviation.	106
Table 4.3: Clumped isotope results from other Valtos Sandstone Formation concretions from Skye and Eigg. All \pm values represent one standard error of the pooled standard deviation.	109
Table 4.4: Clumped isotope results from other samples from Skye and Eigg. All \pm values represent one standard error of the pooled standard deviation, except for 189-8bulk* where standard error of sample repeats is used.	111
Table 4.5: Estimates of meteoric $\delta^{18}\text{O}_{\text{WATER}}$ values for Middle Cretaceous from modelling.	116
Table 4.6: Sr isotope results for samples from concretion VR1 and a sample from a vein within a dyke at Valtos Cliffs, Skye (189-7a).	129

Table 5.1: Clumped isotope results from <i>P. strathairdensis</i> shell collection '159-'. When N>1, average values are presented above data from individual measurement repeats. All ± values represent one standard error of the pooled standard deviation.	154
Table 5.2: Results from Holmden and Hudson (2003) for the shells remeasured in this chapter. *Sr concentration estimated using figures within Holmden and Hudson (2003).	155
Table 5.3: Clumped isotope results from <i>P. strathairdensis</i> shells that were also previously analysed by Holmden and Hudson (2003). For all shells average values are presented above data from individual measurement repeats. All ± values represent one standard error of the pooled standard deviation.	155
Table 5.4: Location, age and species information for other biogenic samples measured with clumped isotopes.	157
Table 5.5: Clumped isotope results from all other biogenic material. When N>1, average values are presented above data from individual measurement repeats. All ± values represent one standard error of the pooled standard deviation. Formation abbreviations refer to Table 5.4.	158
Table 5.6: Clumped isotope results from mudstone hosted concretions. For all concretions, average values are presented above data from individual measurement repeats. All ± values represent one standard error of the pooled standard deviation.	159
Table 5.7: Results of XRD analysis of <i>P. strathairdensis</i> and <i>unionids</i> .	162
Table 5.8: A survey of published thermal tolerances for modern <i>Mytilus</i> species. Note – often these experiments included a sharp transition in temperature, rather than a continuous high temperature	170
Table 5.9: All ± values represent one standard error of the pooled standard deviation. Water content are an approximation that does not take into account alternate sources of hydrogen. *sample E 218 results are from Hudson (1967).	182

Acknowledgements:

Firstly, thank you to my funders EnvEast and NERC, and the University of East Anglia, for the opportunity and means to undertake and complete this PhD.

I would like to thank my supervisory team: Prof. Julian Andrews, thank you for the huge amount of help, understanding and guidance you have given me throughout the last 5 years. Thank you for your great help with fieldwork and for providing some of the samples in this thesis. Prof. Paul Dennis, thank you for being the reason MIRA works and keeps working, and for your help and support. Thank you for your help with the method chapter and data processing, and for your patience when sharing your knowledge with me. Dr Alina Marca, thank you for all of the help you have given me through all stages of working with MIRA, for running many samples for me, for your help with the cleaning experiments and for improving the methods chapter. Thank you for going above and beyond for me and for your support in and out of the lab. Thanks to Dr Jim Hendry for your kind emails, help with fieldwork, for providing concretions and thin sections, and for your assistance with Chapter 3. Thanks also to Dr Nikolai Pedentchouk for your help and support in the early stages of the project, and particularly for your methodological guidance.

Thank you to John Hudson (University of Leicester) for providing several samples and for the incredibly helpful discussion throughout, particularly for Chapter 3.

Thanks to Vicky Ward (University of Leicester archives) and Mark Wilkinson (The University of Edinburgh) for the use of samples and thin sections for Chapter 4, and additional thanks to Mark for useful discussions. Thank you to Matthew Wakefield for the collection of concretion and lava samples from Eigg, Andy Johnson (University of Derby) and Colin Mettam (St Andrews University) for providing Gryphaea samples, and Eileen Gallacher (University of East Anglia) and Lisa Reynolds for additional sample provision. Thank you to Chris Holmden (University of Saskatchewan) for providing samples for Chapter 5 and for running Sr isotopes. Thanks for Bill Patterson (University of Saskatchewan) for providing unpublished isotope data to assist in Chapter 5. Thank you to Tim Atkinson (University College London) for help in the field.

Thanks to Amber Vaughan for running pilot study of clumped isotopes, Bertrand Lézé for running the XRD and SEM work and microscope training, and Antony Hinchliffe for running the CHN analysis. Thank you to Graham Chilvers, Alina Mihailova, and Robert

Utting for the additional lab help, training and support, and thanks to Sarah Wexler for help with labwork and your company. Many thanks also to Simon Ellis, Nick Garrard & Andy Macdonald for lab support.

Thanks to Bridie and James, for your friendship, support, email proof reading and offers for hugs particularly through the last year. Emma, Jade, Miles, Nicola, thank you for your company, patience and friendship in our tiny office and out. Thanks to David for your friendship, snacks and company. Thank you, Abbi and family for huge support and company writing up. Charlotte, thank you for your support, entertainment and for your grammar help. Thanks to Alison for ever-present kindness and support and for all of the exciting adventures out of Norwich.

Finally, thanks to Mum and Dad for being so supportive and wonderful, always.

Acknowledgements for Chapter 3 (published as Paxton et al., 2021):

Paul Dennis, Alina Marca, James Hendry and particularly Julian Andrews proofread and offered improvement to the text. John Hudson provided additional intellectual input. Paul Dennis contributed to discussion on the methodological differences between Paxton et al. (2021) and Loyd et al. (2014), helped make Figure 3.6, produced much of the paper's supplemental data file and provided initial formatting of Appendix 1.

Chapter 1: Introduction

Since the earliest development of the technique in the 1940s-50s (e.g. Urey, 1947; Urey et al., 1951), the oxygen isotope paleothermometer has been used to facilitate better understanding of many subjects and problems in low temperature geochemistry. Among others, these include the study of paleoclimates (e.g., Emiliani 1978; Hayes and Grossmann, 1991; Zachos et al., 2001); paleo-seawater composition (Veizer et al., 1999; Prokoph et al., 2008) diagenetic cementation, including concretion formation (e.g., Mozley and Burns, 1993; Hudson et al., 2001), paleosols (e.g. Cerling and Quade, 1993) and as a tool to understand the diagenetic history of sedimentary basins (e.g. Given and Lohmann, 1986; Hudson and Andrews, 1987); see also the review of Swart (2015).

However, the oxygen isotope paleothermometer is based on measurements of $\delta^{18}\text{O}$ in carbonate mineral precipitates from solution, and any derived value is influenced both by the thermodynamic fractionation of oxygen isotopes (temperature dependent) and the $\delta^{18}\text{O}$ composition of the fluid that the carbonate precipitated from. For calcite, the relationship can be theoretically or empirically derived (using carbonates of known temperature and $\delta^{18}\text{O}_{\text{FLUID}}$) and is often depicted in the format of Equation 1.1:

$$T = a - b(\delta^{18}\text{O}_{\text{CALCITE}} - \delta^{18}\text{O}_{\text{FLUID}}) + c(\delta^{18}\text{O}_{\text{CALCITE}} - \delta^{18}\text{O}_{\text{FLUID}})$$

Equation 1.1

Where T is temperature and a, b and c are constants.

Therefore, utilising oxygen isotopes as a paleothermometer requires information or assumptions about the original $\delta^{18}\text{O}_{\text{FLUID}}$ composition. This is possible if complementary methods, such as fluid inclusion data, are available, or if well-constrained estimates can be made. For example, the $\delta^{18}\text{O}$ composition of seawater through geological time is commonly estimated as a function of the supposed polar ice volume (the composition of which is strongly depleted in ^{18}O) at any given time (Shackleton and Kennett, 1975).

Where there is ambiguity in both temperature and fluid isotope composition, as typified by terrestrial and other meteoric-sourced environments (soils, lakes, rivers and lagoons) the use of oxygen isotopes as a paleothermometer is much more difficult and must be treated with great caution (see, for example, Leng and Marshall, 2004).

The development of clumped isotope palaeothermometry, a technique that uses the thermodynamically controlled preferential bonding of 'heavy' carbon and oxygen isotopes (^{13}C – ^{18}O) to allow temperature derivation without the need of any assumption, resolves, in theory, the aforementioned issues of oxygen isotope paleothermometry by decreasing the unknowns in Equation 1.1. As such, it has opened up possibilities for isotopic studies of the paleoclimate and geological processes that were previously not possible.

Following the earliest work on clumped isotopes (Eiler and Stauble, 2004; Ghosh et al, 2006; Eiler, 2007), and despite the considerable analytical difficulties of the technique (e.g., Eiler, 2007; Huntington et al., 2009; Affek, 2012), many laboratories now have the capability to measure clumped isotopes, and there has been a proliferation of clumped isotope studies, concerned with both the theoretical aspects (e.g., Guo et al., 2009; Dennis et al., 2011; Bernasconi et. al., 2018; Bajnai et al., 2020; Guo, 2020; Anderson et al., 2021; Fiebig et al., 2021; Hemingway and Henkes, 2021), and the application of the theory (e.g., Finnegan et al., 2011; Huntington et al., 2011; Dennis et al., 2013; Loyd et al., 2012; 2014; Petersen et al., 2016; Dennis et al., 2019; Vickers et al., 2021).

Despite the wide user base, the technique is still undergoing development, with improvements in (among others) interlaboratory standardization (Bernasconi et al., 2018) and calibration (Anderson et al., 2021), and investigation into relevant processes such as solid-state reordering (Hemingway and Henkes, 2021) and kinetic fractionation (Guo, 2020) within the last 5 years.

At the University of East Anglia, clumped isotopes are measured on the Multi-Isotopologue Ratio Analyser (MIRA) mass spectrometer, which was custom built for the purpose (Dennis et al., 2014). This thesis focuses on the application of the clumped isotope paleothermometer in deep geological time, using material primarily derived from the Middle Jurassic Great Estuarine Group (GEG) of the Inner Hebrides of Scotland, UK. These first clumped isotope data from Scottish Jurassic sedimentary carbonates are framed by a well characterised sedimentary system with more than seventy years history of geochemical, sedimentological and palaeontological research. The new clumped isotope data could thus be used to test existing well-founded interpretations while improving or understanding of the technique as a whole.

The following case studies were identified:

- Early diagenetic carbonate concretions within mudstones;
- Sandstone-hosted carbonate concretions of burial diagenetic origin;
- Well-preserved skeletal carbonate, particularly bivalve fossils with aragonite shells.

Such targets serve not only as case studies of the British Jurassic world, but also help inform our wider understanding of sedimentary environments and systems.

1.1: Aims:

- The first aim of this study was to use clumped isotopes to help understand the conditions under which early diagenetic cementation proceeds.
- The second aim was to use the clumped isotope technique to better understand the paleoenvironmental conditions under which lagoonal and marine Jurassic organisms lived.
- The third aim was to build upon previous geochemical work where challenges or contradictions had arisen that could be solved or elucidated by the application of clumped isotope paleothermometry:
 - Early clumped isotope work on mudstone-hosted concretions had provided unreasonably high temperatures for cements previously thought to have formed under shallow burial conditions.
 - There was unsatisfactory explanation for highly negative $\delta^{18}\text{O}$ values measured from calcite cements at the centre of supposedly Jurassic aged sandstone-hosted concretions.
 - Pristine Jurassic bivalve aragonite shell material had been characterised as showing a freshwater-marine mixing trend, until a breakthrough paper caused a major change in interpretations brought about by the use of Sr isotope data. Clumped isotopes could be used to investigate the temperature and lagoon water $\delta^{18}\text{O}$ composition of this system.

1.2: Objectives:

The objectives of this work were as follows:

In Chapter 3:

- To use clumped isotopes to analyse the calcitic cements of concretion bodies and septarian fracture fills of mudstone hosted concretions from the Late Jurassic aged Ampthill and Oxford Clay formations of the South of England. Long thought to be diagenetic products formed under shallow burial conditions, a previous study utilising clumped isotopes on concretions of the same units gave much hotter temperatures for the bodies of concretions than had previously been proposed (Loyd et al., 2014). Performing clumped isotope analysis on additional concretions will help corroborate or clarify previous results.
- To extend the study to mudstone hosted concretions of the Kimmeridgian aged Staffin Shale Formation (Skye, UK), in order to compare the above to another locality of similar age with identical diagenetic features.

In Chapter 4:

- To use clumped isotopes to understand the diagenetic history of large sandstone hosted concretions of the Valtos Sandstone Formation, part of the Bathonian aged GEG of the Inner Hebrides, UK. A particular objective was to unravel the history of previously unexplainably negative $\delta^{18}\text{O}$ values found in the centre of a concretion from Valtos, Skye (UK) analysed by Wilkinson (1993).
- To place these concretions in a regional, basinal context by analysing similar concretions from the same formation at Laig Bay, on the Isle of Eigg (UK).

In Chapter 5:

- To analyse with clumped isotopes, pristine aragonite shells from the well-studied Kildonnan member of the Lealt Shale Formation (GEG), sourced from the type section at Kildonnan foreshore, Eigg (UK), in order to further investigate the growth/depositional environment and temperature recorded by these shells. Doing so will complement previous studies of this lagoonal system, which last received an updated interpretation twenty years ago (Holmden and Hudson 2003).

1.3: Background to the Great Estuarine Group:

The Jurassic of the Inner Hebrides, particularly the GEG, is an excellent natural laboratory for completing the aims of this thesis.

Globally, the Jurassic period is thought to have been warmer than present, with high atmospheric CO₂ levels (e.g., Hallam, 1993; Sellwood and Valdes, 2008; Ruebsam et al., 2020) and lacking significant polar ice masses (e.g., Hallam, 1993; 2001; Sellwood and Valdes, 2008; Donnadieu et al., 2011).

The Jurassic succession within the Hebridean basin is one of the more complete sections of the British Jurassic (Fig. 1.1) and is described in detail by Morton and Hudson (1995) and Hesselbo and Coe (2000). Briefly, the Lower Jurassic sediments are marine offshore sequences, transitioning to shallow water sand waves (Barreraig Sandstone) and mixed marine-freshwater lagoons in the Middle Jurassic, followed by a transgression to shallow marine conditions in the Callovian and into the Upper Jurassic (Hudson and Trewin, 2002). The GEG, of Bathonian age, is a paralic sequence of sediments deposited in shallow lagoonal, fluvial and deltaic environments (Morton and Hudson, 1995) which are described in detail by Harris and Hudson (1980).

Preceded by the fully marine Barreraig Sandstone Formation, the lowest unit of the GEG is a non-marine organic rich shale (the Cullaidh Shale Formation), which transitions into the Elgol Sandstone, a delta system with some lateral facies variation but predominantly fluvially dominated in Strathaird, Skye (Harris, 1989). There is a sharp transition into the overlying Lealt Shale Formation, a freshwater-brackish lagoonal system which is divided into the Kildonnan Member (older) and the Lonfearn Member (younger), distinguished by the prevailing molluscan fauna (Hudson, 1966) and an algal (microbial) stromatolite which caps the Kildonnan Member throughout the basin (Harris and Hudson, 1980). The second deltaic sandstone facies, the fluvial Valtos Sandstone Formation, overlies the Lealt Shale Formation; this is the thickest unit within the group and is interspersed with abundant bivalve-rich shell beds of the freshwater genera *Neomiodon* sp. (Harris, 1992). The sandstone is notable for the occurrence of large diagenetic concretions (e.g. Wilkinson, 1993). Next is the Duntulm Formation, representing a marine-brackish lagoonal system (Andrews and Walton, 1990), which is followed by a regressive sequence of freshwater lagoonal facies (the Kilmaluag Formation; Andrews, 1985) and finally the alluvial plain sediments of the Skudiburgh Formation (Andrews, 1985). The GEG is succeeded by the

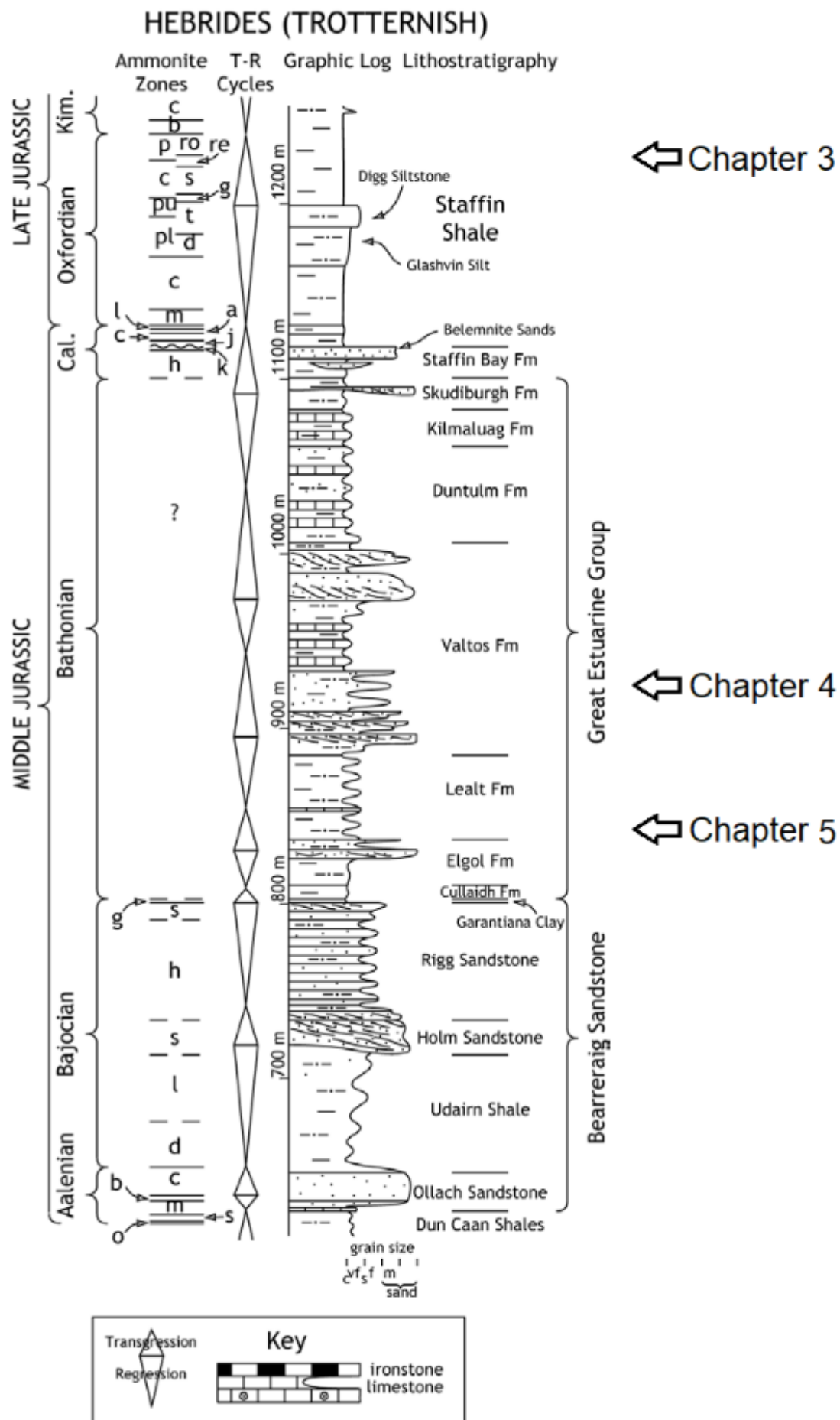


Figure 1.1: The middle to Upper Jurassic succession of the Hebrides of Scotland, after Hesselbo and Coe (2000).

transgressive Staffin Bay Formation, which marks a return to marine conditions, followed by the Staffin Shale Formation which is fully marine (Morton and Hudson, 1995).

There is a major unconformity between the youngest Jurassic sediments and Upper Cretaceous rocks, representing a period of uplift and erosion (e.g., Hudson, 1983; Hudson and Andrews, 1987). The preserved Upper Cretaceous sediments of the Inner Hebrides are thin, and are all of shallow marine origin (Harker, 2002). The presence of any substantial thickness of Cretaceous cover is not thought likely (Hudson and Andrews 1987), and following this there was a period of early Paleocene faulting and erosion (Hudson, 1983).

The Hebridean Igneous Province, part of the wide ranging North Atlantic Igneous Province, developed in the Paleocene. The Mesozoic rocks of the Inner Hebrides were buried by lavas, numerous dykes and sills were emplaced within the sedimentary rocks and igneous centres developed across the region, notably in Skye, Mull, Rum and Ardnamurchan (Emeleus and Bell, 2005).

The Mesozoic rocks of Skye were rapidly buried by up to 1200 m of Paleocene Lava (England, 1994; Emeleus and Bell, 2005), the extrusion of which preceded the development of the Skye Central Complex (Emeleus and Bell, 2005, and references therein). On Skye, the Little Minch Sill Complex intrudes the Jurassic sediments of the Trotternish peninsula, post-dating the lava emplacement (Gibson, 1990; Emeleus and Bell, 2005), but predating the intrusive centres (Fowler et al., 2004; Emeleus and Bell, 2005).

The igneous intrusive and extrusive material have not in the past been thought to have majorly altered the Jurassic sediments – for example, there was not thought to be any evidence for an additional heating component when the sediments were buried by the lava pile (e.g., Hudson, 1983; Hudson and Andrews, 1987). In fact, the Paleocene lavas and intrusives probably helped preserve the softer underlying Jurassic sediments from subsequent erosion, particularly in the Quaternary.

The Jurassic mudstones show low thermal maturity when greater than 15 km from the Skye Central Complex (Thrasher, 1992) and the effects of major hydrothermal circulation driven by the complex is thought to only extend to approximately 6.5 km away from the igneous centres (Taylor and Forester, 1971; Forester and Taylor, 1977). There are contact metamorphic effects where sills and dykes intrude into the sediments, but

these effects do not extend further than several metres; Bishop and Abbott (1995) showed that the thermal effects of dykes within shales were proportional to dyke thickness and only had a local effect on the sediments.

The apparently good preservation of the Jurassic GEG makes the sequence highly attractive for the application of isotopic analysis, and the subsequent, very well documented, Paleocene igneous activity makes for a fascinating and potentially unique geological basin history.

1.3.1: Isotopic analysis and the GEG

The first comprehensive study of carbonates from the GEG utilising $\delta^{18}\text{O}$ and $\delta^{13}\text{C}$ was by Tan and Hudson (1974), who analysed both skeletal and diagenetic carbonates from the succession. For the biogenic (skeletal) carbonate, this approach was used to interpret the temperature of growth for some of the organisms, and interpretations of inferred $\delta^{18}\text{O}_{\text{FLUID}}$ values assisted in the identification of growth environmental conditions and wider depositional environments. This initial analysis was further developed subsequently; extensive palaeontological and geochemical work was undertaken on the Kildonnan Member of the Lealt Shale Formation to better characterise the lagoonal system (e.g. Hudson, 1980; Hudson et al., 1995; Holmden and Hudson, 2003) expanding the range of organisms studied using stable isotopes (e.g. Patterson et al. 1999). This research area is explored more thoroughly in Chapter 5.

Detailed isotopic studies of early diagenetic carbonates including microbialites (Andrews, 1986) and dolostones (Andrews et al., 1987) had developed from the early work of Tan and Hudson (1974), who had also studied mudstone-hosted concretions. Their pioneering data supported the hypothesis that such concretions formed during shallow burial, in equilibrium with connate fluids. In the Scottish Jurassic, geochemical work on mudstone-hosted concretions paused for thirty years until in-depth investigations of those in the Staffin Shale Formation by Hendry et al. (2006) and Pearson et al. (2005). This research thread is revisited in Chapter 3.

Due to the aforementioned ambiguities of the oxygen isotope paleothermometer when interpreting $\delta^{18}\text{O}_{\text{carbonate}}$ data, the interpretation of later, burial diagenetic cements by Tan and Hudson (1974) rested on their assumption that the timing of cementation (for many of the cements they analysed) occurred under no more than 200 m of burial, from

meteoric-sourced fluids during the late Jurassic. The burial diagenesis of the GEG was discussed further by Hudson and Andrews (1987), a review that incorporated new isotopic data that had been produced in the 1980s; $\delta^{18}\text{O}$ values from various carbonate cements and biogenic material was used to construct Figure 1.2, which provided estimates of likely depositional and burial temperatures and $\delta^{18}\text{O}_{\text{FLUID}}$ values. Significantly, this study included a refined estimate of likely Jurassic meteoric $\delta^{18}\text{O}_{\text{FLUID}}$ compositions, between -4‰ to -6‰ SMOW (Hudson and Andrews, 1987).

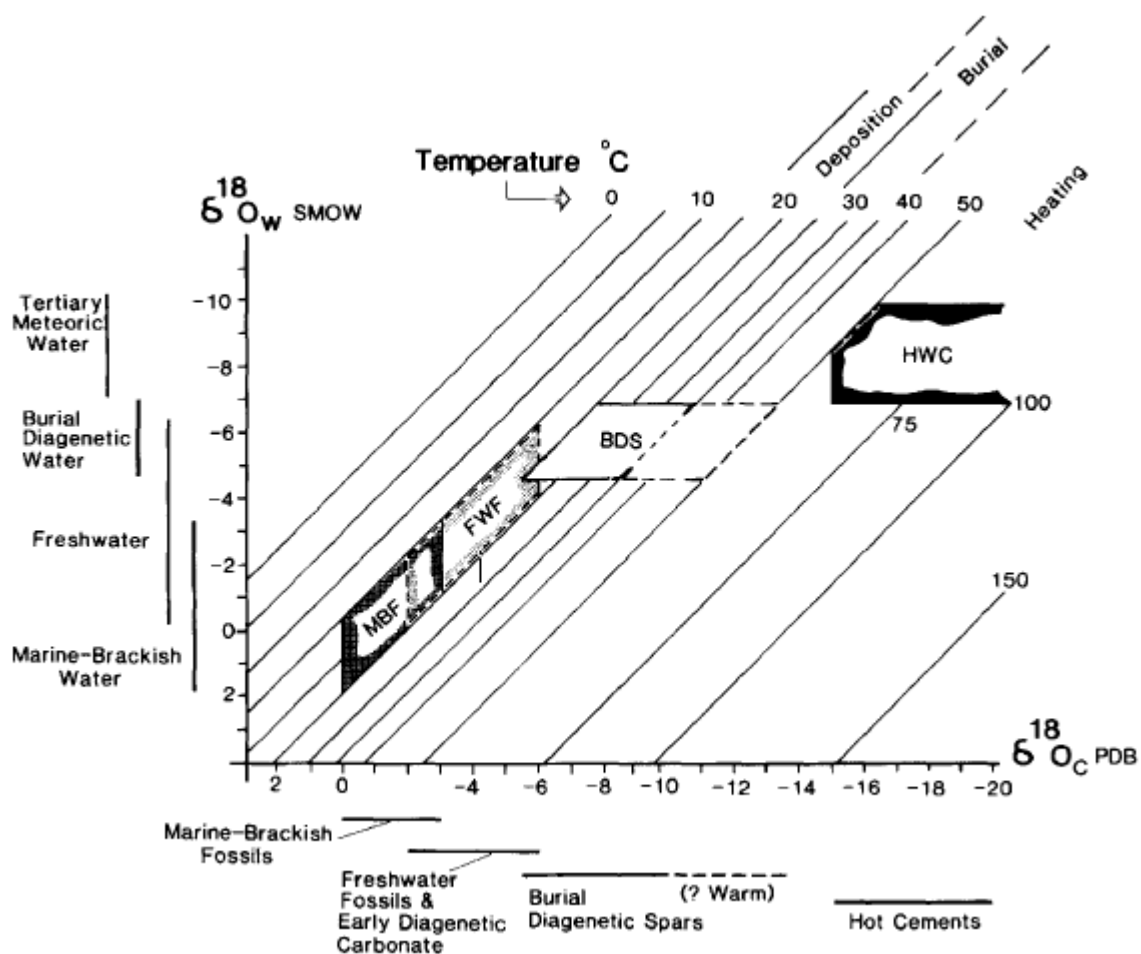


Figure 1.2: After Hudson and Andrews (1987); interpretation of $\delta^{18}\text{O}_{\text{CARBONATE}}$ results from a range of carbonate material (Tan and Hudson, 1974; Andrews, 1986), using the temperature equation of Anderson and Arthur (1983) to derive temperature and $\delta^{18}\text{O}_{\text{FLUID}}$ values.

First analysed by Tan and Hudson (1974) and interpreted by Hudson and Andrews (1987) as late (burial) diagenetic cements, the sandstone hosted carbonate concretions of the Valtos Sandstone Formation were subsequently the focus of more detailed isotopic analysis by Wilkinson (1989; 1992, 1993). Discussed thoroughly in Chapter 4, these large metre-scale carbonate concretions were concluded to have formed from pore fluids from a Middle or Upper Jurassic meteoric groundwater 'lens', the carbonate sourced from

dissolution of aragonite *Neomiodon* sp. shells; cementation timing was thought to have been completed before the end of the Upper Jurassic (Wilkinson, 1993). $\delta^{18}\text{O}$ measurements of the interior of one concretion from the Valtos Formation in Trotternish provided the initial impetus for Chapter 4, as the results were markedly negative (Wilkinson, 1993) and difficult to explain.

1.4: The clumped isotope paleothermometer:

The measurement of ^{13}C – ^{18}O clumped isotopes was first performed by Eiler and Schauble (2004) on atmospheric CO_2 , and further developed by Ghosh et al. (2006), Schauble et al. (2006) and Eiler (2007). The first published application to carbonates was by Ghosh et al. (2006) who created a Δ_{47} temperature calibration using a range of carbonate material precipitated at different temperatures, which was then used to derive the sea-surface temperature of a coral from the northern Red Sea.

This successful application appeared to be proof of concept for the utility of clumped isotope palaeothermometry, and the potential for use in paleoclimate studies in particular was emphasised by Eiler (2011). Crucially, the technique provided an independent temperature estimation and could be used with measurements of $\delta^{18}\text{O}_{\text{CARBONATE}}$ to back-calculate the precipitating fluid $\delta^{18}\text{O}$ values. It was also initially thought that clumped isotope measurements from skeletal carbonates were largely free from organism specific disequilibrium effects, or ‘vital effects’, an issue that had clouded the interpretation of stable isotope data in many fossil groups (Eiler, 2011). This would later be proven untrue, with some taxa displaying clear Δ_{47} disequilibrium effects; for example, lower-than-actual growth temperatures were derived from some cold water (Saenger et al., 2012) and shallow water (Spooner et al., 2016) corals. A fuller discussion of vital effects on Δ_{47} is given in Chapter 5. Despite this complication, many useful investigations of paleoclimate/palaeoenvironment have been attempted, using both biogenic (e.g., Finnegan et al., 2011; Price and Passey, 2013; Petersen et al., 2016; Breitenbach et al., 2018; Price et al., 2020; Vickers et al., 2020, 2021; De Winter et al., 2021; Barney and Grossman, 2022; Letulle et al., 2022; among many others) and non-biogenic carbonate material (Affek et al., 2008; Passey et al., 2010; Kluge et al., 2013; Snell et al., 2014; Burgener et al., 2019; Matthews et al., 2021; and many others).

Clumped isotope paleothermometry has also been used to investigate a wider range of low-temperature (non-metamorphic) geochemical topics including;

paleoelevation (e.g. Snell et al., 2014; Huntington and Lechler, 2015 and references therein); fluid source and flow characterisation in fault systems (Bergman et al., 2013; Dennis et al., 2019); geospeedometry (Bristow et al., 2011; Passey and Henkes, 2012; Mangenot et al., 2019); and diagenetic studies which are discussed further in Chapters 3 and 4.

Recently the clumped isotope technique has been extended further to include combined Δ_{47} - Δ_{48} measurements (Bajnai et al., 2020; Fiebig et al., 2021), which, despite the challenges of the analysis, due to the required high precision, have great potential for applications where kinetic disequilibrium is either suspected or observed in Δ_{47} data. The combination of Δ_{47} and U-Pb measurements have also emerged as a potential thermochronometer, which may further improve the utility of clumped isotope analysis for carbonate cementation studies (e.g., Methner et al., 2016; Mangenot et al., 2018; Brigaud et al., 2020; Hoareau et al., 2021).

In the following chapters I first describe the methods used during the operation of the Multi-Isotopologue Ratio Analyser mass spectrometer (MIRA) at the University of East Anglia (UEA). This is followed by three case study chapters and a final brief overall conclusion. All of the primary data is given in Appendix 1-3, which are included as a CD.

Chapter 3 has been published as: Paxton, R. B., Dennis, P. F., Marca, A. D., Hendry, J. P., Hudson, J. D., & Andrews, J. E. (2021). Taking the heat out of British Jurassic septarian concretions. *The Depositional Record*, 7(2), 333-343.

Chapter 2: Methods

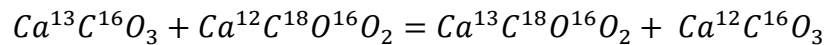
This chapter describes the preparation, analysis and data processing used throughout the time period of data acquisition, which lasted from April 2018 to March 2022.

2.1: Introduction to clumped isotopes:

Carbonate clumped isotope thermometry is a technique that concerns the preferential ordering and abundance of $^{13}\text{C}-^{18}\text{O}$ bonds with temperature within the processes of calcium carbonate precipitation, recrystallization and reordering, compared to the stochastic abundance of $^{13}\text{C}-^{18}\text{O}$ bonds; measured as Δ_{47} (Ghosh et al., 2006) and expressed as the following equation (Eiler and Schauble, 2004):

$$\Delta_{47} = \left(\frac{R_{\text{measured}}^{47}}{R_{\text{stochastic}}^{47}} - 1 \right) \times 1000 \quad \text{Equation 2.1}$$

Ordering occurs between the carbonate anion in a homogenous system:



This thermodynamically controlled ordering is independent of ambient water isotopic composition, and therefore temperature can be derived by the measurement of Δ_{47} . This enables $\delta^{18}\text{O}_{\text{FLUID}}$ compositions to be back calculated using the relationship between $\delta^{18}\text{O}_{\text{CARBONATE}}$, $\delta^{18}\text{O}_{\text{WATER}}$ and temperature; allowing all variables of the standard $\delta^{18}\text{O}$ paleothermometer to be obtained (Eiler, 2011; Affek, 2012).

2.2: Pre-Preparation:

For the MIRA system, at least 4 mg of pure carbonate is required to be acid reacted to produce sufficient volume of gas for clumped isotope measurement. Smaller sample sizes have been trialled but were hindered by a size effect relating to the preparation line (Umbo, 2020). Where the material has a lower % of carbonate and more impurities (e.g., in a sandstone hosted carbonate concretion) the mass required is greater.

Before 2020, the sample size chosen for measurement of a pure carbonate was between 3.9 and 4.2 mg. After 2020 this was increased by 1/3, typically using 5.9 to

6.2 mg of a pure carbonate sample. Both samples and standards were scaled as such, and this change was not thought to have affected Δ_{47} .

Three methods have been used to prepare powdered carbonate samples for clumped isotope analysis:

- Hand drilling with an electric multi-tool drill, using short bursts and gentle pressure and various diamond drill heads
- Grinding of more friable material with a pestle and mortar
- Filing samples into powder using a small diamond file

Δ_{47} is more susceptible to resetting than $\delta^{18}\text{O}_{\text{CARBONATE}}$ and $\delta^{13}\text{C}$ (Eiler, 2011), thus care must be taken when preparing powdered samples for isotopic analysis, as it is possible that the pressure and temperature of drilling or crushing samples may cause resetting of C-O bonds. The technique used was decided for each sample individually so pressure and heat were minimised in the process, to avoid geochemical variations caused by preparation technique alone.

The large mass required for analysis of a carbonate has to be taken into account when preparing the sample, particularly when many repeat measurements are required. The large volume of material required for repeat analysis raises the risk of isotopic heterogeneities being encountered. Defliese and Lohmann (2015) found that in samples composed of two end-members with heterogeneities greater than 2‰ for both $\delta^{13}\text{C}$ and $\delta^{18}\text{O}_{\text{CARBONATE}}$, Δ_{47} values could be detectably offset from equilibrium.

For the mudstone hosted concretions whose results are reported in Chapter 3, wherever possible powders were drilled from areas close to where high resolution bulk stable isotope measurements were made, thus giving an indication of the homogeneity of the sample – for example, high resolution isotopic analysis across fibrous calcite layers gave an indication of whether sub-sampling would be appropriate. For samples where high-resolution oxygen isotopes were not taken, visual assessment of sample area was carefully done, to ensure the correct phase was measured.

If additional powder had to be obtained after the first material drilled had been exhausted, typically it was obtained as close to the original site as possible.

Sample powders were either taken from cut surfaces or freshly broken surfaces. When this could not be achieved, the top layer of the rock was shaved off using a file or a drill and discarded, then drilling proceeded from the resultant surface.

For fossils such as bivalves and ammonites, shell fragments were highly fragile and tended to be embedded in a muddy matrix, so for these samples mud was carefully removed using needles and a thorough visual assessment of fragments was done through a magnifying glass prior to crushing.

2.3: Preparation line:

2.3.1: 87°C acid digestion:

For clumped isotope analysis, carbonate material is acid digested to release CO₂. Other gases may also be released in this process; therefore, the gas is passed through a preparation line to remove contaminants (see Section 2.3.2), allowing pure CO₂ to be measured by the MIRA mass spectrometer.

Carbonate samples are reacted by dropping powder held in a small glass or silver vial into a common acid bath containing ~105% phosphoric acid heated to 87°C. Samples with low purity requiring larger sample volumes were occasionally dropped in 2 vials. At 87°C total reaction can be completed within 30 minutes for calcite.

The common acid bath is usually pumped for >30 minutes between samples. This is sufficient to eliminate 'memory effects' between samples. However, powder spillage can occur when samples are dropped into the acid bath; in this instance, the yield tends to be lower and there may be contamination in later samples. This scenario is monitored for and attempted to be avoided, powder is removed where possible, and any occurrence is noted in log-books to avoid erroneous results.

Carbonate material that is not pure (particularly material that is high in clay and organics) may release 'contaminant' gases upon acid digestion. The composition and reaction rate of these additional reactions are not known. For this reason, samples of higher purity were typically reacted at the beginning of an acid run, although memory effect or gradual contamination within the acid bath was not seen for the samples measured here.

Until 2020, the acid (of ~30 ml volume) was replaced after 15-20 sample capsules had been reacted. After 2020, experiments took place on both the capsules and acid volume; with glass capsules replaced with smaller silver capsules, the acid vessel modified (typical acid volume increased to ~60 ml) and a high acid volume (~90 ml) trialled for a period, which allowed much greater numbers of samples to be run before acid required changing.

2.3.2: CO₂ purification line:

The aim of the preparation line is to isolate CO₂ and remove all other gases that may be released in the acid digestion process, or introduced through the presence of acid itself (e.g., water vapour and other gases dissolved in the acid). The CO₂ preparation line went through several changes during the period of data acquisition. These are detailed below for the start to end of data acquisition, including periods where data was not measured but changes were made which then affected future measurements and line alterations. Table 2.1 relates the data in Chapters 2-5 to the methods detailed below.

Time period	Section describing method used:		Chapter			
	Prep. line	Corrections	2	3	4	5
Sept 2018 - Oct 2018	2.3.2.2			■		
Nov 2018 - Dec 2018	2.3.2.2		■		■	■
Jul 2019 - Aug 2019	2.3.2.4			■	■	■
Aug 2019 - Oct 2019	2.3.2.4		■			
Oct 2019 - Feb 2020	2.3.2.4			■	■	■
Apr 2021 - Jun 2021	2.3.2.6, 2.3.2.7	2.5.7.1			■	■
Jun 2021 - Aug 2021	2.3.2.7				■	■
Oct 2021	2.3.2.7				■	■
Nov 2021 - Dec 2021	2.3.2.7					■
Jan 2022 - Feb 2022	2.3.2.7	2.5.7.2			■	■
Feb 2022 - Mar 2022	2.3.2.7				■	■

Table 2.1: schematic indicating the sections of this chapter that describe the methods used for sample gas preparation (Section 2.3.2.X) and additional data corrections (Section 2.5.7.X) to different periods of data acquisition. The chapters in which data from these time periods were used is indicated by filled boxes in the columns to the right.

2.3.2.1: April 2018 line configuration:

Initial data (not included in later chapters but relevant to the development of the clumped isotope methodology used after April 2018) was collected using the following preparation system (Fig. 2.1):

- Stage 1: Acid digestion and water removal:
 - After 20 minutes of vacuum evacuation of the acid bath headspace, acid digestion of carbonates was given 20 minutes, with released gas passing through two spiral traps (held at -110°C) to remove water, with CO_2 frozen above liquid nitrogen in cold finger 1 (CF1).
- Stage 2: Gas measurement and transfer:
 - Gas pressure was measured using the barocel in CF1, then CO_2 transferred to cold finger 2 (CF2) for 5 minutes, trapping in liquid nitrogen.
- Stage 3: Porapak Trap:
 - The sample gas is then cryodistilled into CF3 using liquid nitrogen – passing through a trap (L: 24 cm, i.d.: 4 mm) packed with Porapak Q, a sorbent material which sequesters hydrocarbons, for 90 minutes at -20°C .
- Stage 4: Transfer to MIRA:
 - The sample was then transferred to a cold finger on MIRA for 5 minutes using liquid nitrogen.

After each stage, liquid nitrogen was used to trap CO_2 and non-condensable gases (NC) were removed using the vacuum system. At this point the vacuum system consisted of one Pfeiffer HiCube pumping station with a pump speed of 70 l/s; consisting of drag stage turbo pumps backed by diaphragm pumps. The vacuum was connected to a back manifold, which was linked to the glass preparation line at 3 locations (Fig. 2.1).

Between samples, the water traps were heated to 75°C for at least 15 minutes to remove the frozen-out water, and the Porapak Q trap was heated to 140°C for 30 minutes and evacuated. At the end of the working day all traps were heated for at least an hour.

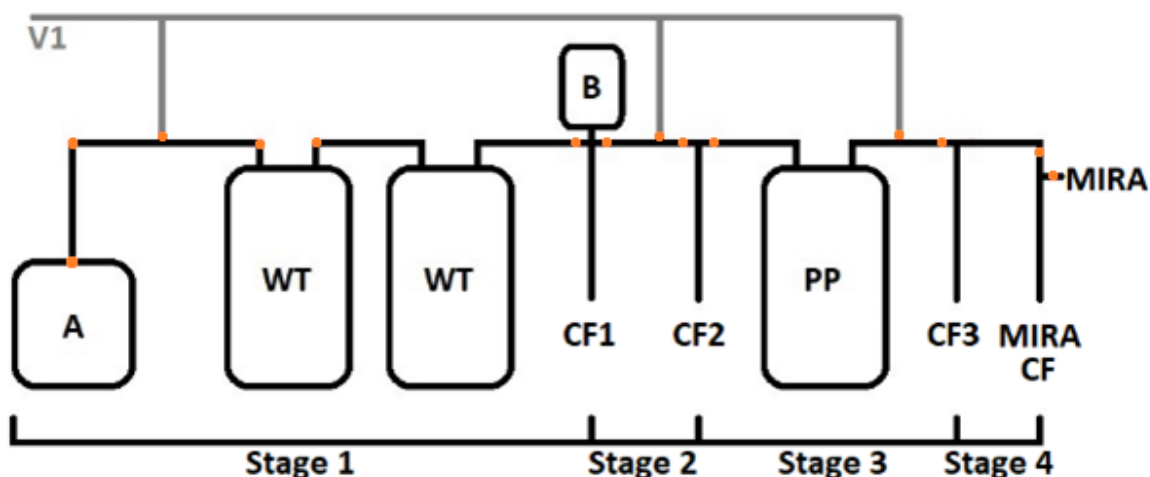


Figure 2.1: Schematic of the preparation line before March 2019. A = common acid bath; WT = water trap; B = Barocel; CF = Cold finger; PP = Porapak Q trap; MIRA = Multi-Isotopologue Ratio Analyser mass spectrometer; V= Vacuum line

2.3.2.2: September 2018 – January 2019 line configuration:

Improvements were made to this line after April 2018:

- Stage 1: Acid digestion time was raised from 20 to 30 minutes
- Stage 1: Water trap temperatures were raised from -110 to -80°C
- Water traps baking temperatures were raised to 80°C
- Stage 3: The Porapak Q trap was replaced with a shorter trap (L:12 mm, i.d: 4 mm) and the required transfer time was therefore shortened to 30 minutes
- Porapak Q bake out temperature was raised to 160°C

These changes affected some of the temperatures and timings of the different stages, but the overall processes remained the same as described previously.

2.3.2.3: January 2019 – March 2019 line configuration:

In January 2019 a quadrupole mass spectrometer was added to the line, positioned between CF2 and the Porapak Q trap, and was used to investigate the ‘background gas’ constituents. It was found that water vapour was a significant component, despite the quadrupole MS being positioned after the traps used to remove water. Water vapour and related ions can interact with CO₂, causing scrambling and re-equilibration. As illustrated in Figure 2.1, the preparation line and acid bath described above were evacuated by one vacuum line, linked to the preparation line by three valves; one positioned before the water traps, one between CF1 and CF2, and one between the Porapak Q trap and CF3. It was observed that the opening of the latter two valves was

allowing water vapour to move back into the line through the vacuum line manifold, bypassing the water traps (P. Dennis, pers. comm., 2019).

To reduce this backflow of water vapour into the line, two additional traps were added between the preparation line and the manifold of the vacuum system, positioned between the 2nd and 3rd vacuum outlet. These traps are kept cooled with liquid nitrogen over the course of a working week and can be isolated from both the preparation and vacuum line manifold using valves when not cooled.

Additionally, a similar (isolatable) trap was added between the common acid bath and a second Pfeiffer HiCube vacuum pump (see Section 2.3.2.1) was added immediately after the acid vessel. A third water trap, hereby referred to as 'WT1', was added between the acid vessel and the glass preparation line. This configuration is illustrated in Figure 2.2.

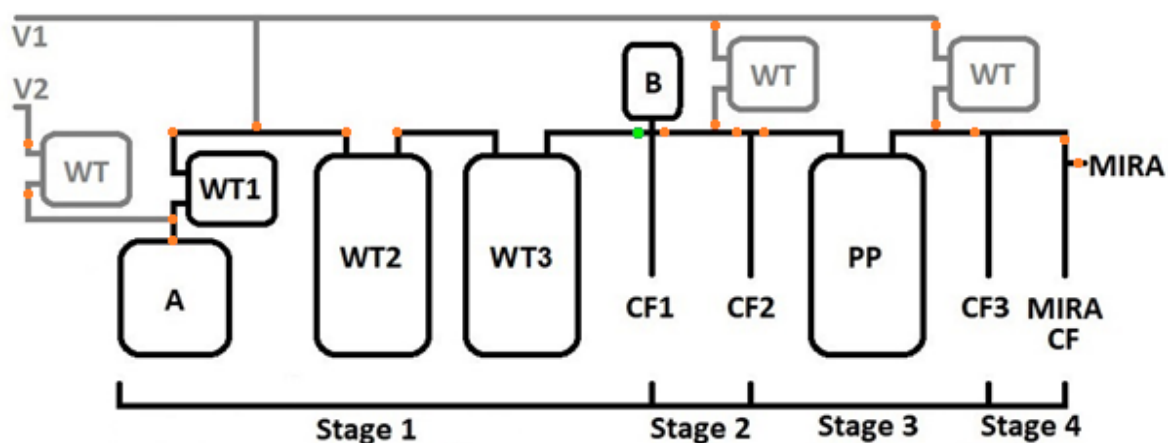


Figure 2.2: Schematic of the preparation line after March 2019. A = common acid bath; WT = water trap; B = Barocel; CF = Cold finger; PP = Porapak Q trap; MIRA = Multi-Isotopologue Ratio Analyser mass spectrometer; V= Vacuum line.

Stage 1, between March 2019 and June 2019, therefore had three water traps, with the first held at $\sim -74^{\circ}\text{C}$ using a dry-ice ethanol slush, and the subsequent two held at -100 to -105°C . After acid digestion took place, WT1 was isolated from the line, unfrozen and evacuated through the second vacuum pump. The second vacuum pump was also used to evacuate the acid between samples, further avoiding the addition of water vapour to the line. The low level of water vapour reaching water traps 2 and 3 removed the necessity for heating these traps between sample runs, instead maintaining their cooled temperature for the entire working day, heated to 80°C for several hours overnight to evacuate.

In order to further reduce transfer of water vapor to the Porapak Q trap, the valve between the third water trap and the Barocel cold finger now was to be only opened during the acid step, remaining closed at all other points including periods when the line was not in use.

Stage 3 was also altered - the Porapak Q trap was to be maintained throughout the day at a constant temperature of $\sim -20^{\circ}\text{C}$ (no higher than -20°C but usually above -22°C) and baked at 200°C overnight.

These modifications to the line achieved a significant improvement in background vacuum pressure within the line, from an average of 4×10^{-7} reduced to 2×10^{-7} hPa, and subsequently the effect from background contamination reduced to levels enabling measurement of meaningful temperature trends in Δ_{48} for standards (P. Dennis, pers. comm., 2020). Further discussion regarding water vapour contamination is found in Section 2.7.2.

2.3.2.4: April 2019 – March 2020:

While most changes above were maintained in this period, an additional stage was added. The protocol (see Fig. 2.3) therefore was as following:

- Stage 1: 30 minute acid digestion at 87°C , gas trapped by liquid nitrogen in 'WT1'. NC are pumped through acid vacuum (V2).
- Stage 2: 10 minute sublimation from WT1, through WT2 and WT3 into CF1 (Barocel cold finger): the liquid nitrogen is removed from WT1 and replaced with ethanol cooled to -115°C ; WT2 & 3 are also held at -115°C . NC are removed through V1 upon completion and pressure is measured by the barocel. If pressure is lower than expected, this process is repeated for 5 minutes.
- Stage 3: 5 minute transfer to CF2, followed by removal of NC.
- Stage 4: 30 minute transfer through PPK held below -20°C , frozen with LN into to CF3. NC are removed through V2 upon completion.
- Stage 5: 5 minute transfer of gas from CF3 to MIRA cold finger. NC are removed through V1 upon completion.

Between samples, the acid was evacuated for 5 minutes. WT1 was heated to 40°C after use, and overnight.

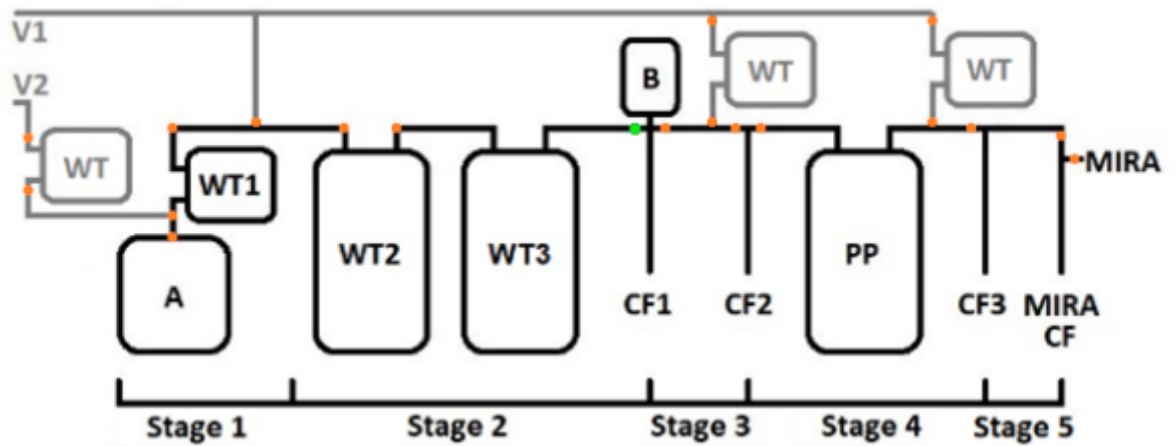


Figure 2.3: Schematic of the preparation line after April 2019. A = common acid bath; WT = water trap; B = Barocel; CF = Cold finger; PP = Porapak Q trap; MIRA = Multi-Isotopologue Ratio Analyser mass spectrometer; V= Vacuum line.

2.3.2.5: March 2020 – March 2021

Throughout this time period, results from analyses were poor in comparison to the previous period. Many changes were made to the line and to the MIRA mass spectrometer during this time. The most prominent changes to the preparation line which affected later measurements are summarised here:

- Acid vessel: There was an issue of scattering of sample powder in the reaction vessel – in the first seconds after the sample vials were dropped, large CO₂ gas bubbles were formed by the first powder to be reacted, with some of the unsubmerged sample powder remaining on the bubble surface until the bubbles burst, where a portion of this powder was flung unreacted into the neck of the vessel (leading to slightly lower yields). To attempt to resolve this problem, several acid vessels were trialled, the volume of acid was increased by double (causing a visible difference in the appearance of the reaction), and weights (gold pieces and silver rods) were added to sample vials. Sample vials were also changed from glass capsules to silver capsules, which were also weighted.
- A carousel system was subsequently added to the acid vessel, and the neck lengthened significantly. This meant that the sample vials dropped vertically, but also meant that the acid was exposed to air upon loading, unlike in the past when a valve maintained vacuum in the acid vessel. There was still issues with powder backflow. Smaller silver vials were used in this carousel.

- Acid was now evacuated for ~1 hour in between samples. The vessel was also pumped hot and with a spinner for several hours in the evening and continued to be pumped cold (no spinner) overnight.
- The sublimation step was removed, returning to a one stage acid reaction-water removal step (combined stage 1 & 2 of Fig. 2.2). WT1 was heated up to 80°C between use and evacuated at 80°C overnight.
- Degradation of the 2nd Vacuum pump (to the gas preparation line) meant that the background vacuum pressure of the line increased from 2×10^{-7} to $\sim 2 \times 10^{-6}$ MBar. This reduced the sensitivity of the vacuum gauge to NC gas evacuations, therefore when there was no visible pressure raise (particularly after stage 3, 4 and 5) the vacuum was opened for 20 seconds (chosen as NC removal to background levels before this issue took <20 seconds).

2.3.2.6: End of March 2021- 7th May 2021

After several alterations to MIRA in the previous time period, there were improvements in the results, with better repetition and internal precision. The gas preparation line was as following (with reference to Fig. 2.2):

- Stage 1: 40 minute acid digestion of 6 mg samples (for pure carbonates) at 87°C in a deep acid, gas trapped by liquid nitrogen in 'CF1'. WT1 is held at -90°C using cooled ethanol, WT2 and WT3 are held at -115°C. NC are pumped through Line vacuum for 20 seconds.
- Stage 2: 5 minute transfer to CF2, followed by removal of NC (20 seconds).
- Stage 3: 60 minute transfer through PPK held below -20°C, frozen with LN into to CF3. NC are removed through V1 upon completion (20 seconds).
- Stage 4: 5 minute transfer of gas from CF3 to MIRA cold finger. NC are removed through V1 upon completion (20 seconds).

2.3.2.7: 10th May 2021 – March 2022

From 10th May 2021 the process included sublimation, as in Figure 2.3. Several changes to the protocol were made:

- Stage 1: 30 minute acid reaction at 87°C. The volume of acid was halved. Acid digestion still occurred at 87°C, gas trapped by liquid nitrogen in 'WT1'. NC are pumped through acid vacuum (V2) for >1 minute (referring to pressure gauge to judge NC removal).
- Stage 2: 20 minute sublimation from WT1, through WT2 and WT3 into CF1 (Barocel cold finger): the liquid nitrogen is removed from WT1 and replaced with ethanol cooled to -90°C; WT2 & 3 are held at -115°C. NC are removed through V1 upon completion and pressure is measured by the barocel.
- Stage 3: 5 minute transfer to CF2, followed by removal of NC (20 seconds).
- Stage 4: 30 minute transfer through PPK held below -20°C, frozen with LN into to CF3. NC are removed through V2 upon completion (20 seconds).
- Stage 5: 5 minute transfer of gas from CF3 to MIRA cold finger. NC are removed through V2 upon completion (20 seconds).

Acid was pumped for ~50 minutes between samples. As before, WT1 is heated up to 80°C between samples and overnight.

Samples were loaded into the carousel at the end of every day, and the acid was evacuated hot for >1 hour in the evening (spinner on) and pumped cold overnight (spinner off).

2.4: The MIRA mass spectrometer:

Clumped isotope measurements are taken on the MIRA mass spectrometer. MIRA is a dual inlet 120° magnetic sector isotope ratio mass spectrometer with a high sensitivity ion source. 6 faraday cups allow simultaneous collection of CO₂ masses $m/z = 44 - 49$. Magnetic field strength is monitored and manually adjusted if necessary before each analysis to maintain peak centring at ~8000 volts.

With a major ion beam strength of 7.5×10^{-8} A for mass 44, MIRA takes 4 acquisitions of 20 sample-reference gas pairs, with a 20 second integration period for each sample or reference cycle, after a 10 second change over delay time. Bulk $\delta^{45} - \delta^{49}$ values of the sample are calculated with respect to the reference gas. $\delta^{18}\text{O}$ (VSMOW), $\delta^{13}\text{C}$ (VPDB) and Δ_{45-49} are calculated using the calibrated composition of the working reference gas values for $R_{13/12}$, $R_{18/16}$ and $R_{17/16}$ of VPDB and VSMOW. Routine internal measurement precision of Δ_{47} is $\pm 0.008\text{‰}$ (Dennis et al., 2014).

Additional information can be found within the supplementary data of Paxton et al. (2021); including information on the handling of ^{17}O .

2.4.1: Reference gas:

Reference gas is made on site by reaction of Carrara marble at 87°C , which is equilibrated with Norwich tap water (NTW) at room temperature for more than 6 months before cleaning it on the gas preparation line. The purpose of equilibrating reference gas with NTW is twofold; i) to bring the reference gas into clumped isotope equilibrium at the lab temperature, and ii) to produce a reference gas close in bulk isotopic composition to most carbonates measured at UEA. NTW has an oxygen isotopic composition of approximately -7‰ VSMOW; CO_2 equilibrated with NTW at 25°C will have an oxygen isotope composition of approximately $+33\text{‰}$ VSMOW, close to typical marine carbonates. The reference gas is stored in a 500 mL stainless steel cylinder, which is attached to the MIRA reference gas side of the dual inlet.

Throughout the majority of the data acquisition period, at the start of the working day the internal and external bellows of both sides of the inlet were evacuated, and then a small aliquot of reference gas was expanded, via a metering volume, into the reference inlet. However, between 15th April 2021 and 15th June 2021, an experiment was run where one aliquot of reference gas was used for up to several weeks at a time, held in the mass spectrometer reference bellows. It was discovered by examining Δ_{49} of the standards that over these extended periods the reference gas in the bellow became gradually contaminated, affecting Δ_{47} (P. Dennis, pers. comm. 2021). A correction was calculated for the samples run during this time period, as described in Section 2.5.7.1. From 16th June 2021 onwards the reference gas was once again changed daily as described above.

2.5: Data Processing:

2.5.1: Instrument linearity

For analyses of clumped isotopes, most laboratories require raw data to be corrected for 'non-linearity', an instrument dependant artefact, where measured Δ_{47} values differ from true Δ_{47} values with variations in δ_{47} (bulk isotopic composition) (Huntington et al., 2009).

Correction takes place using linear regression of a ‘heated gas line’, composed of different gases of known bulk composition equilibrated at a common temperature, where the measured values of Δ_{47} (HG vs. WRG) are plotted against δ_{47} (HG vs WRG) (Dennis et al., 2011). The intercept of this line is taken as the true Δ_{47} value.

MIRA does not display such linearity issues (Dennis, 2014; Dennis et al., 2014) therefore no correction is required. Further information reflecting this subject can also be found in the supplemental material of Paxton et al. (2021).

2.5.2: Δ_{47} standardisation:

Raw Δ_{47} data, named ‘ Δ_{47} (LRF)’ for ‘local reference frame’, is converted to the carbon dioxide equilibrium scale of Bernasconi et al. (2018), ‘ Δ_{47} (CDES-25)’. This accounts for the effect of lab specific mass spectrometric artefacts arising from processes such as scrambling in the ion source in order to ensure reported data is comparable between labs (Dennis et al., 2011). To do this, an empirical transfer function is constructed in each lab using a suite of common carbonate standards (Bernasconi et al., 2018).

Δ_{47} (CDES-25) transfer functions applied to the raw data were created by projecting Δ_{47} (LRF) measurements of ETH1 and ETH3 carbonate standards (Bernasconi et al., 2018) and the UEA Carrara Marble standard (UEACMST), against the UEA derived ‘ Δ_{47} (CDES @87)’ values of the same standards, the equation of the relationship allowing calculation of the transfer function (Fig. 2.4).

An example of a transfer function used is:

$$\Delta_{47}(\text{CDES @}87^{\circ}\text{C}) = 1.1867 \times \Delta_{47}(\text{LRF@}87) + 0.8105 \quad \text{Equation 2.2}$$

Transfer functions are calculated from standards acid digested at 87°C, and thus a correction is added to allow equivalence at 25°C, see Section 2.5.3, below.

The UEA empirically derived Δ_{47} (CDES @87) values of the standards used are as follows:

- ETH1 = 0.218‰
- ETH3 = 0.613‰.
- UEACMST = 0.322‰

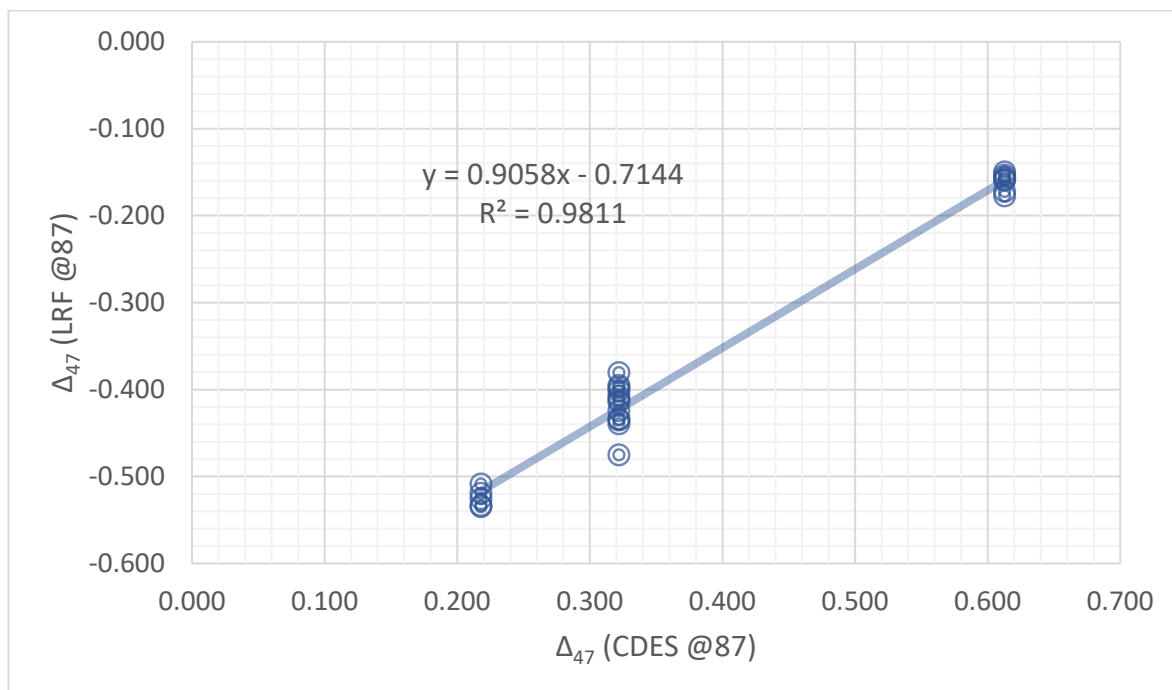


Figure 2.4: Relationship between Δ_{47} (LRF) and Δ_{47} (CDES @87) for standards measured between September 2018 and October 2018. Gradient and constant of linear equation are the basis for the data transfer function.

The above values were measured at an acid digestion temperature of 25°C against a suite of heated gasses and corrected represent reaction at 87°C using the UEA empirically derived acid fractionation correction value (-0.062; see Section 2.5.3) for comparison with Δ_{47} (LRF@87) values.

UEA derived ETH values are close to those provided by a recent interlaboratory comparison (Bernasconi et al., 2021); the difference in Δ_{47} calculated utilising the ETH Δ_{47} (CDES-90°C) values of Bernasconi et al. (2021) versus valued derived at UEA (corrected to represent reaction at 90°C) is lower than measurement precision for samples between 0-100°C.

ETH1, ETH3 and UEACMST have significantly different precipitation temperatures.

Transfer functions were not constant and were calculated for several time periods when data was collected. All transfer functions used for data in this thesis are displayed in Table 2.2.

Measurements of ETH2 and ETH4 were also used to monitor instrument linearity, which remained linear throughout the duration of analysis (P. Dennis, pers. comm. 2018; see also the supplementary data of Paxton et al., 2021).

Time period	CDES@87°C Calibration
Sept 2018 - Oct 2018	$\Delta_{47}(\text{CDES @87}^\circ\text{C}) = 1.1034 \times \text{LRF@87} + 0.7887$
Nov 2018 - Dec 2018	$\Delta_{47}(\text{CDES @87}^\circ\text{C}) = 1.08861 \times \text{LRF@87} + 0.71326$
Jul 2019 - Aug 2019	$\Delta_{47}(\text{CDES @87}^\circ\text{C}) = 1.1598 \times \text{LRF@87} + 0.8125$
Aug 2019 - Oct 2019	$\Delta_{47}(\text{CDES @87}^\circ\text{C}) = 1.1598 \times \text{LRF@87} + 0.8125$
Oct 2019 - Feb 2020	$\Delta_{47}(\text{CDES @87}^\circ\text{C}) = 1.1506 \times \text{LRF@87} + 0.8243$
Apr 2021 - Jun 2021	$\Delta_{47}(\text{CDES @87}^\circ\text{C}) = 1.15287 \times \text{LRF@87} + 0.85566$
Jun 2021 - Aug 2021	$\Delta_{47}(\text{CDES @87}^\circ\text{C}) = 1.13302 \times \text{LRF@87} + 0.84353$
Oct 2021	$\Delta_{47}(\text{CDES @87}^\circ\text{C}) = 1.06621 \times \text{LRF@87} + 0.8486$
Nov 2021 - Dec 2021	$\Delta_{47}(\text{CDES @87}^\circ\text{C}) = 1.10473 \times \text{LRF@87} + 0.82888$
Jan 2022 - Feb 2022	$\Delta_{47}(\text{CDES @87}^\circ\text{C}) = 1.06564 \times \text{LRF@87} + 0.83717$
Feb 2022 - Mar 2022	$\Delta_{47}(\text{CDES @87}^\circ\text{C}) = 1.1469 \times \text{LRF@87} + 0.99404$

Table 2.2: Transfer functions used to correct local reference frame data to the CDES reference frame, with reference to their time periods of use.

2.5.3: Acid fractionation Δ_{47} correction:

Typically, the reporting of Δ_{47} data is based on acid digestion at 25 °C. For data reacted at different temperatures, a correction factor has to be applied to the measured Δ_{47} values. In accordance with Guo et al. (2009), a 1 °C change in temperature from 25 °C is equivalent to 0.001‰ difference in Δ_{47} , therefore for acid digestion at 87 °C a sample should have a difference of -0.062‰ compared to the Δ_{47} value measured at 25 °C. Measurements of samples at UEA using both offline reaction at 25 °C and online at 87 °C show an offset of 0.062‰. This value is in excellent agreement with the theoretical fractionation reported in Guo et al. (2009). Therefore, for acid digestion at 87°C, a correction factor of 0.062‰ is added to the Δ_{47} values of each sample.

$$\Delta_{47}(\text{CDES } 25) = \Delta_{47}(\text{CDES@87}) + 0.062\text{‰} \quad \text{Equation 2.3}$$

2.5.4: Temperature derivation:

The following equation, empirically derived at UEA (Kirk, 2017; Dennis et al., 2019), was used to derive the carbonate formation temperatures of each sample:

$$\Delta_{47}(\text{CDES } 25) = \frac{(0.0389 \times 10^6)}{T^2} + 0.2139 \quad \text{Equation 2.4}$$

Where T = Temperature in Kelvin.

See Section 2.8.1 for further discussion of temperature equations.

2.5.5: $\delta^{18}\text{O}_{\text{CARBONATE}}$:

In addition to Δ_{47} , MIRA provides a value of $\delta^{18}\text{O}_{(\text{VSMOW})}$ of the measured CO_2 gas, which can be converted into $\delta^{18}\text{O}_{\text{CARBONATE}(\text{VSMOW})}$ using the following equation:

$$\delta^{18}\text{O}_{\text{CARBONATE}(\text{VSMOW})} = \frac{1000 \times \delta^{18}\text{O}_{\text{CO}_2(\text{VSMOW})}}{1.0084} - 1000 \quad \text{Equation 2.5}$$

Where the constant 1.0084 is the acid fractionation factor (Swart et al., 1991), which corrects for the fractionation caused by the conversion of the carbonate sample into CO_2 at 87°C .

For aragonite samples, a correction of -0.289 (Lachniet et al., 2015) is used when converting measured values for $\delta^{18}\text{O}_{(\text{VSMOW})}$ of CO_2 into $\delta^{18}\text{O}_{(\text{VSMOW})}$ of carbonate in order to take into account the aragonite acid fractionation factor.

The $\delta^{18}\text{O}_{\text{CARBONATE}}$ values are reported with respect to VPDB, allowing comparison with published data, converted using the equation:

$$\delta^{18}\text{O}_{(\text{VPDB})} = \frac{\delta^{18}\text{O}_{(\text{VSMOW})} - 30.86}{1.0386} \quad \text{Equation 2.6}$$

2.5.6: $\delta^{18}\text{O}_{\text{FLUID}}$:

Using the calculated values of T (K) and $\delta^{18}\text{O}_{\text{CARBONATE}(\text{VSMOW})}$, an approximation of the original oxygen isotopic composition of the fluid that the carbonate was precipitated from can be back calculated. The equation of Kim and O'Neil (1997) was chosen for calcite samples, as it is appropriate for inorganic calcite:

$$1000 \ln \alpha_{\text{CARBONATE-FLUID}} = 18.03(10^3 T^{-1}) - 32.42 \quad \text{Equation 2.7}$$

Where T is in Kelvin, and

$$\alpha_{\text{CARBONATE-FLUID}} = \frac{\delta^{18}\text{O}_{\text{CARBONATE}(\text{VSMOW})} + 1000}{\delta^{18}\text{O}_{\text{FLUID}(\text{VSMOW})} + 1000} \quad \text{Equation 2.8}$$

For aragonite shells the mollusc specific equation of Grossman and Ku (1986) is used, as the majority of aragonite material studied was from the *Mollusca* phylum:

$$T(^{\circ}\text{C}) = 21.8 - 4.69(\delta^{18}\text{O}_{(\text{ARAGONITE})}(\text{VPDB}) - \delta^{18}\text{O}_{(\text{FLUID})}(\text{VSMOW})) \quad \text{Equation 2.9}$$

2.5.7: Additional data corrections:

2.5.7.1: Reference gas experiment corrections:

As mentioned above in Section 2.4.1, between 15/04/21 and 15/06/21 an experiment was run to investigate the effects of using one reference gas aliquot over periods of several days to weeks, rather than evacuating the mass spectrometer after every day of use. The experiment was repeated several times for between 4 and 14 days. An incremental contamination of the reference gas over these time periods became apparent which strongly affected masses 47-49. This resulted in a depletion in Δ_{47} over time for both samples and standards.

Due to the daily measurement of the standard UEACMST and measurement of ETH1 and ETH3 either daily or on alternate days, the linear trend of Δ_{47} depletion due to contamination was observed and corrected for.

Each standard and sample measured in each time period were labelled from 0-13, representing days surpassed since reference gas aliquot change (n_{days}). Δ_{47} (LRF) of UEACMST, ETH1 and ETH3 were then plotted against n_{days} and the gradients for the depleting trends found.

Due to the varying length of time for each experiment, some time periods incorporated very few standards, making linear correlations difficult. It was therefore decided that for each standard, results from all 5 experiments would be combined as one trend, maintaining their original $n_{\text{days}}=x$, meaning, for example, that there were 5 UEACMST results for $n_{\text{days}} = 1$ but only one for $n_{\text{days}} = 13$.

Using an average of the gradients for UEACMST, ETH1 and ETH3, a correction factor was created, which was subsequently applied to all samples and standards that were run during the duration of the experiments:

$$\Delta_{47}(\text{LRF corrected}) = \Delta_{47}(\text{LRF uncorrected}) + (n_{\text{days}} \times 0.00907)$$

Equation 2.10

The improvement to results can be seen on Figure 2.5. This appeared to adequately correct for the contamination related depletion.

The $\Delta_{47}(\text{LRF corrected})$ values for standards were subsequently used to create the $\Delta_{47}(\text{CDES-25})$ transfer function for this time period.

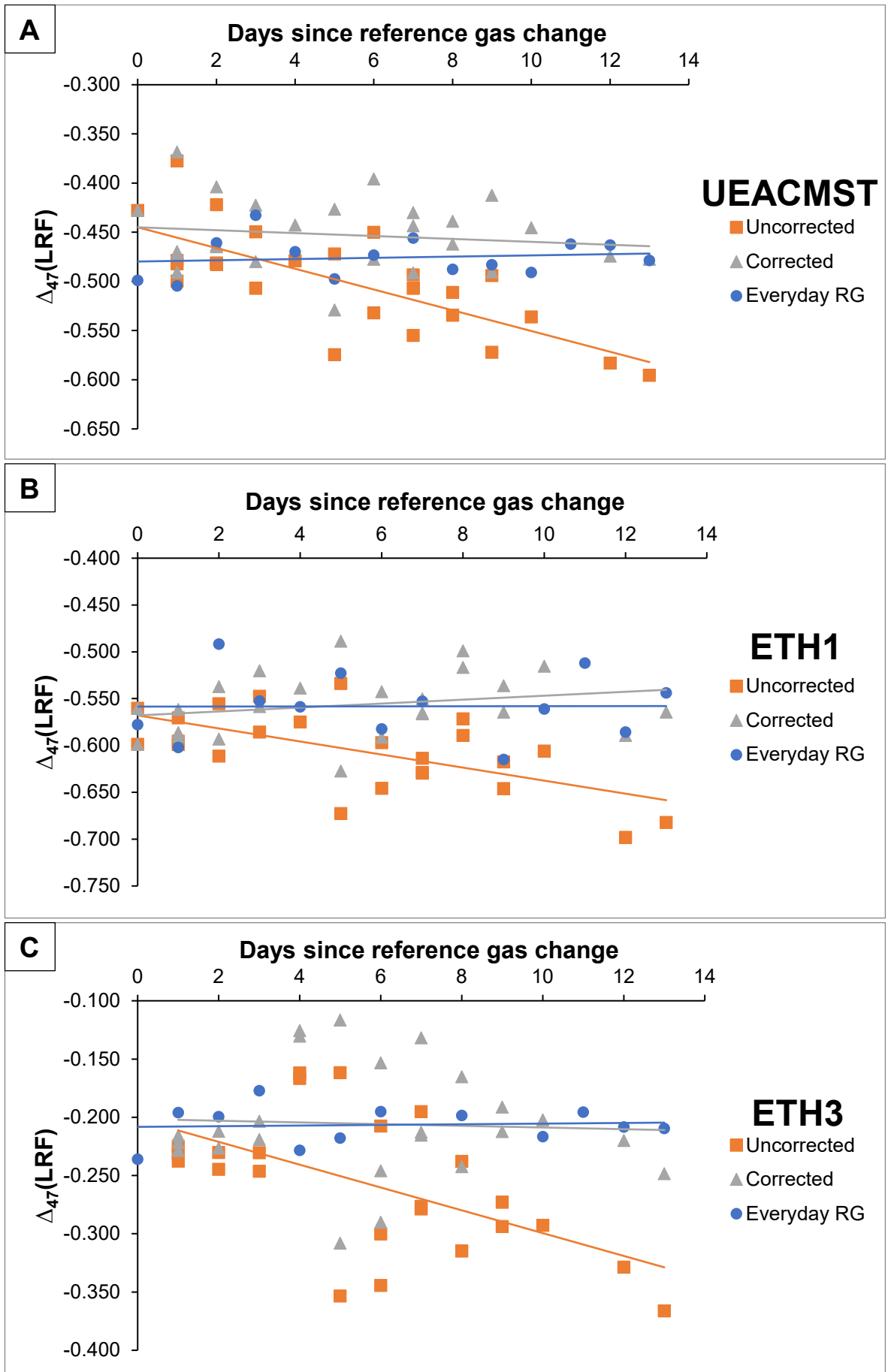


Figure 2.5: Comparison of corrected and uncorrected data for the standards: A) UEACMST; B) ETH1; C) ETH3. Also shown for comparison is data collected in a time-period where the reference gas aliquot was changed daily (Everyday RG).

2.5.7.2: Reference gas drift corrections:

Between 18/01/22 and 23/02/22 the reference gas reservoir (which supplies the daily reference gas aliquots) gradually shifted Δ_{47} composition for reasons which we don't yet fully understand. There was no evidence of fractionation, and it is possible that a changing lab temperature during this period resulted in some reequilibration of the reference gas (P. Dennis, pers. comm., 2022). The cause of the change in Δ_{47} is still being investigated.

This caused a shift in Δ_{47} values for all measurements similar to that seen in Section 2.5.7.1 above. The systematic nature of the transition allowed creation of a correction factor to be applied to data measured for this time period.

The method is the same as described above, with n_{days} calculated since initiation of the drift. Once again, the gradients derived from the 3 standards were averaged, providing a correction factor that was applied to all samples and standards:

$$\Delta_{47}(LRF_{corrected}) = \Delta_{47}(LRF_{uncorrected}) + (n_{days} \times 0.0051) \quad \text{Equation 2.11}$$

2.6: Uncertainties:

Many labs report uncertainties for clumped isotope measurements as standard deviation or standard error; however, as the number of repetitions is commonly only 3 this standard deviation or standard error may misrepresent the true uncertainty of the data (Fernandez et al., 2017).

It can be assumed that between each individual measurement, there will be differences caused by human variances in preparation, differences in components of the preparation line and by differences in performance of the mass spectrometer itself. These differences can occur within one day of measurements, and perhaps to a greater extent, between different measurement days.

Assuming there are no cumulative systematic biases (such as cumulative contamination of reference gas, where a trend of increasing or decreasing results might be gathered- see Section 2.5.7), data from many repeat analyses of a single sample might be expected to produce a normal distribution curve around a mean value, for which standard deviation would be a reliable method of indicating reproducibility. The distribution would take into account any sample heterogeneity, as well as non-systematic measurement differences as described above.

However, only 3 repetitions would not be likely to represent the sample's true mean or distribution, even if values appeared to have high precision. This poses difficulties for clumped isotope analysis, as a single measurement takes several hours to prepare and run, so many repeat analyses are not feasible.

In order to achieve a more reliable representation of uncertainty and repeatability, for $\delta^{13}\text{C}$, $\delta^{18}\text{O}_{\text{CARBONATE}}$ and Δ_{47} measurements the pooled standard deviation of samples of similar composition was calculated (s_{pooled}), where possible. This parameter relates the standard deviation of several samples, where repeated analysis can be as low as 2, to a common mean; assuming that the standard deviations are not significantly different (*Equation 2.12*).

$$s_{\text{pooled}} = \sqrt{\frac{(n_1-1)s_1^2 + (n_2-1)s_2^2 + \dots + (n_k-1)s_k^2}{n_1 + n_2 + \dots + n_k - k}} \quad \text{Equation 2.12}$$

n_x is the number of measurements made for sample x ; s_x is the standard deviation of the repeated measurements of sample x ; and k is the total number of samples.

This method can be used to estimate the reproducibility of similar samples (for example; 5 concretion body samples measured 3 times each), and can also be used to track the long term reproducibility within the lab - as we commonly measure UEACMST, ETH1 and ETH3 regularly, the pooled standard deviation of these three standards can be calculated to give an indication of reproducibility over long time periods (Table 2.3). Standard error of standards from specific time periods can also be used to monitor repeatability (Table 2.4).

For samples where pooled standard deviation was not appropriate (such as when there were no other similar samples); the standard deviation of measurement repeats were calculated. The standard error of these pooled and non-pooled standard deviations were then calculated, which provides the uncertainty estimates for $\delta^{13}\text{C}$, $\delta^{18}\text{O}$ and Δ_{47} values provided in the text.

When calculating uncertainty for temperature and $\delta^{18}\text{O}_{\text{FLUID}}$ results, the standard error of Δ_{47} were used, in addition to uncertainties related to the UEA temperature equation, and these were fully propagated to provide values of temperature and $\delta^{18}\text{O}_{\text{FLUID}}$ uncertainty (See Part II of Appendixes 1, 2 and 3).

Time period	ETH1				ETH3				UEACMST			
	N	SD			N	SD			N	SD		
		$\delta^{13}\text{C}$	$\delta^{18}\text{O}$	Δ_{47}		$\delta^{13}\text{C}$	$\delta^{18}\text{O}$	Δ_{47}		$\delta^{13}\text{C}$	$\delta^{18}\text{O}$	Δ_{47}
All	133	0.043	0.072	0.029	133	0.044	0.072	0.028	280	0.121	0.104	0.026
Chapter 2	16	0.044	0.058	0.020	20	0.051	0.084	0.024	30	0.058	0.048	0.022
Chapter 3	38	0.054	0.072	0.030	43	0.057	0.051	0.028	81	0.214	0.059	0.029
Chapter 4	108	0.043	0.072	0.030	102	0.044	0.074	0.028	219	0.134	0.113	0.026
Chapter 5	119	0.042	0.070	0.030	114	0.042	0.075	0.030	246	0.127	0.109	0.026

Table 2.3: Pooled standard deviation of each standard, for each chapter.

Time period	ETH1				ETH3				UEACMST			
	N	SE			N	SE			N	SE		
		$\delta^{13}\text{C}$	$\delta^{18}\text{O}$	Δ_{47}		$\delta^{13}\text{C}$	$\delta^{18}\text{O}$	Δ_{47}		$\delta^{13}\text{C}$	$\delta^{18}\text{O}$	Δ_{47}
Sept 2018 - Oct 2018	5	0.008	0.049	0.005	7	0.012	0.011	0.004	12	0.010	0.014	0.007
Nov 2018 - Dec 2018	7	0.007	0.012	0.007	8	0.006	0.041	0.007	8	0.007	0.010	0.008
Jul 2019 - Aug 2019	9	0.019	0.023	0.007	12	0.019	0.013	0.007	22	0.014	0.011	0.005
Aug 2019 - Oct 2019	9	0.019	0.023	0.007	12	0.019	0.013	0.007	22	0.014	0.011	0.005
Oct 2019 - Feb 2020	24	0.012	0.013	0.007	24	0.012	0.012	0.007	47	0.040	0.009	0.005
Apr 2021 - Jun 2021	21	0.010	0.019	0.006	18	0.010	0.020	0.006	23	0.011	0.014	0.005
Jun 2021 - Aug 2021	20	0.006	0.017	0.008	16	0.006	0.015	0.004	25	0.007	0.018	0.005
Oct 2021	12	0.012	0.018	0.010	11	0.009	0.022	0.014	23	0.010	0.060	0.005
Nov 2021 - Dec 2021	11	0.010	0.018	0.007	12	0.009	0.024	0.011	27	0.007	0.013	0.004
Jan 2022 - Feb 2022	6	0.007	0.009	0.007	9	0.009	0.034	0.008	45	0.004	0.011	0.004
Feb 2022 - Mar 2022	9	0.011	0.032	0.008	4	0.008	0.028	0.011	26	0.008	0.015	0.004

Table 2.4: Standard error for each standard in each period of measurement, using the standard deviation of standards from individual time periods.

2.7: Sample derived contamination and additional sample preparation:

Due to the measurement sensitivity required for analysis of Δ_{47} , measurements can be susceptible to effects of contamination. Contamination in this context is the presence of a gas other than the target CO_2 , particularly at the point of measurement by MIRA. Contaminant gases can be released by the acid digestion process of a sample, and if they are not removed before entering the mass spectrometer, contaminants can cause issues with measurement as a result of isobaric interferences at the cardinal masses of the CO_2 isotopologues. The effect will be most pronounced for interferences at mass 47 (Eiler and Schauble, 2004).

While the preparation line has been designed to remove common 'contaminant' gases (cryogenic traps for water vapour, a Porapak Q trap for the removal of hydrocarbons/halocarbons, silver wool to remove sulphur compounds and frequent removal of non-condensable gases), in 2018, measurements of less pure samples, including samples thought to have high volumes of organic matter and presence of clay minerals (e.g. mudrock-hosted concretion body cement and brown fibrous calcite septarian fracture fills; Chapter 3), produced results that showed evidence of contamination.

At UEA, contaminated samples are distinguished from non-contaminated samples using measurement of Δ_{48} , and occasionally, Δ_{49} . Δ_{48} in particular is highly sensitive to the presence of contaminant gases (Eiler and Schauble, 2004; Huntington et al., 2009).

Other institutions use a parameter called $\Delta_{48 \text{ offset}}$ (or $\Delta_{48 \text{ excess}}$) as a contamination indicator; samples are thought to be contaminated when their $\delta_{48}-\Delta_{48}$ deviates from the $\delta_{48}-\Delta_{48}$ best fit lines of heated gases (where δ_{48} = isotope ratio of sample vs. standard) (Huntington et al., 2009). A $\Delta_{48 \text{ offset}}$ threshold is set, below which, samples are considered uncontaminated (e.g., 1.5‰ used by Imperial College London; Davies and John, 2017). As MIRA is a linear mass spectrometer this parameter is not applicable to our samples. Instead, in the past we have looked at our raw Δ_{48} and Δ_{49} measurements.

For concretion body and brown fibrous fringe data (Chapter 3), there were several lines of evidence suggesting contamination for the more organic rich calcite phases in the earliest results measured. While the majority of the data had reasonable Δ_{48} values, the temperatures derived for these data were unrealistically negative; in addition, when comparing Δ_{48} with Δ_{49} , another component sensitive to contaminants, the data for the organic rich phases fell outside the range seen for the purer samples and standards (Fig. 2.6). These data were therefore discarded. Comparisons of Δ_{47} , Δ_{48} and Δ_{49} of similar

samples were used to investigate contamination in other samples, although these parameters could vary systematically as well, and the clear covariance seen for the results of Figure 2.6 is unusual.

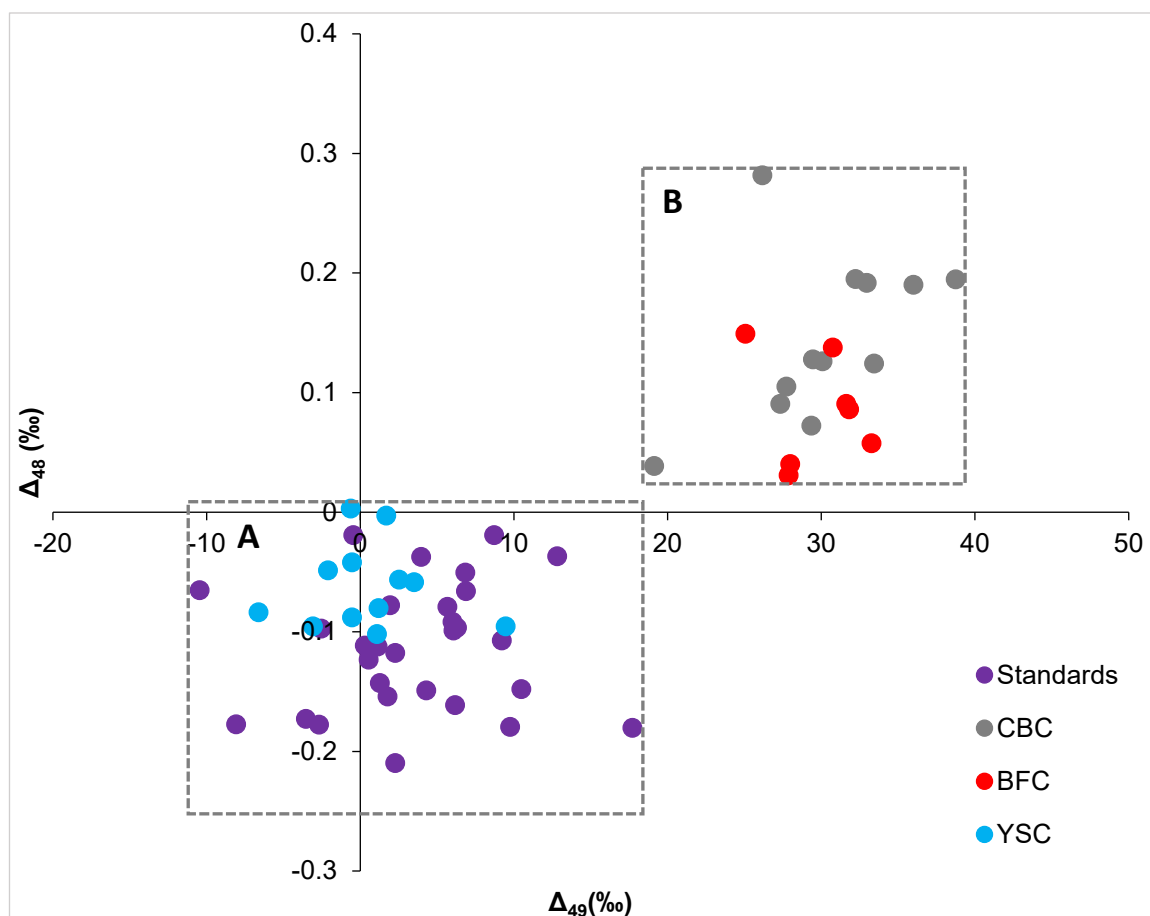


Figure 2.6: Measured Δ_{48} vs. Δ_{49} values from YSC (yellow sparry calcite), BFC (brown fibrous calcite) and CBC (concretion body cement) from 4 concretions from the Oxford Clay and Amphill Clay formations. Box A shows uncontaminated samples, box B shows contaminated samples. Data collected in September/October 2018.

2.7.1: Investigation of sample derived contaminants:

Due to the preliminary results shown in Figure 2.6, it was apparent that despite effective gas purification for other samples, for the concretion bodies and early brown spars, a contaminant gas was not being removed by the preparation line. The potential sources were thought to be either the organic material or clay minerals - Mucciarone and Williams (1990) had observed contaminant peaks at masses 47 and 48 that stemmed from NO_2 gas released from clay adsorbed ammonium.

Several pre-preparation techniques were trialled in order to attempt to prevent the release of contaminant gases from the acid digestion process. Experiments took place using powdered concretion body from 'SC8', a Staffin Shale concretion ascribed to Bed 40 provided by Jim Hendry and previously analysed in Hendry et al. (2006), also analysed in Chapter 3 and Paxton et al. (2021). A control (UEACMST) was also used to check that these methods did not affect the $\delta^{18}\text{O}$, $\delta^{13}\text{C}$ and Δ_{47} of a pure standard.

These tests were informed by previous results of tests done at UEA using MIRA (Saha, 2013). The methods are detailed below:

1. Reacting concretion body powder with sodium hydroxide (NaOH)

Rationale: As applied by Saha (2013), NaOH is used for the purpose of ion exchange, exchanging Na^+ with ammonium (NH_4^+).

NaOH can also dissolve kaolinite (Kämpf and Schwertmann, 1982; Yapp, 1991), which, along with illite-smectite, is dominant in the clay mineral fraction of the Staffin Shale Formation (Hendry et al. 2006).

Method:

- ~50 mg of carbonate material placed in a small glass beaker
- <15 mL of 1M NaOH added to cover sample and left for required amount of time.
- Samples are vacuum filtered with deionised water and dried in a vacuum oven with no heat.

This method was used for 'Method 3' (190 minute submersion) and 'Method 7' (340 minute submersion) of Table 2.5.

2. Reacting concretion body powder with sodium hypochlorite (NaOCl)

Rationale: NaOCl removes organic matter from carbonate (e.g., Devereux, 1967).

Method:

- ~50 mg of carbonate material placed in a small glass beaker
- <15 mL of 10-15% NaOCl added to cover sample and left for required amount of time.
- Samples are vacuum filtered with deionised water and dried in a vacuum oven with no heat.

This method was used for 'Method 1' (>1440 minute submersion) and 'Method 4' (4360 minute submersion) of Table 2.5.

3. A combination of methods 1 and 2, with NaOCl treatment followed by NaOH, using the same methods as above consecutively.

These include ‘Method 2’ (>1440 minute submersion in NaOCl, 60 minute submersion in NaOH), ‘Method 5’ (4370 minute submersion in NaOCl, 60 minute submersion in NaOH) and ‘Method 6’ (1440 minute submersion in NaOCl, 85 minute submersion in NaOH) of Table 2.5.

The results for these experiments are shown in Table 2.5. No results for SC8 CBC gave temperatures >5°C, which are considered too negative to record shallow burial temperatures, despite varying treatment time. In addition, even a 3-hour NaOH treatment of UEACMST caused a measured change $\delta^{18}\text{O}$ in UEACMST. Moreover, it was found that extended immersion in NaOCl caused a significant negative shift in $\delta^{18}\text{O}$ for both sample and standard. It was concluded that such pre-treatment was not appropriate for the samples showing contamination; and indeed, the issue was resolved as described in Section 2.7.2, requiring no pre-treatment.

Sample	Method	n	NaOCl treatment time (mins)	NaOH treatment time (mins)	Average		
					$\delta^{13}\text{C}$ (‰)	$\delta^{18}\text{O}$ (‰)	T(Δ_{47}) (°C)
SC8 CBC	Untreated	3			-15.31	-0.81	-24
	1	2	>1440 †		-15.23	-0.84	-24
	2	2	>1440 †	60	-15.13	-0.71	-9
	3	2		190	-14.99	-0.52	-10
	4	1	4360		-14.84	-1.97	-14
	5	1	4370	60	-14.90	-1.92	2
	6	2	1440	85	-14.93	-0.67	-26
UEACMST	Untreated	17			1.95	-2.04	180
	3	4		190	1.95	-2.20	140
	4	2	4360		1.53	-2.57	104
	5	3	4370	60	1.69	-2.42	127
	6	4	1440	85	1.85	-2.25	136
	7	4		340	1.97	-2.22	141

† NaOCl evaporated overnight

Table 2.5: Details of tests of pre-preparation technique trials for contamination reduction, using concretion body cement (SC8 CBC) and a standard (UEACMST). Treatment time is in minutes. Orange highlights indicate that change is greater than +1 standard deviation of the mean, and blue highlights indicate that change is greater than -1 standard deviation of the mean. Note that UEACMST average is calculated from 17 results measured at the time period when most results here were also analysed, and SC8 CBC result is from data collected in April 2018, before improvement of contamination issue, and not as reported in Chapter 3.

2.7.2: Water vapour contamination effects:

As described in Section 2.3.2, above, the presence of traces of water vapour in the gas preparation line was discovered in early 2019, and after changes to the preparation line in March 2019 this issue was improved significantly. After this point, 'organic rich' concretion body and brown fibrous fringe calcites gave reasonable temperatures, and the apparent contamination issue was solved.

Prior to March 2019, the presence of water vapour may have allowed water to coat some of the surfaces within the preparation line; particularly those made of metal. This may have facilitated re-equilibration of CO₂ molecules if they came into contact with coated surfaces. Water vapour is also thought to have reduced the effectiveness of the Porapak Q trap, allowing organic derived contaminants to enter the mass spectrometer. There is also the potential that water may have been reacting with contaminant gases causing release of a contaminant species that caused interference at mass 47 (P. Dennis, pers. comm., 2022).

2.8: Limitations with clumped isotope analysis:

2.8.1: Considerations regarding data processing and comparisons between labs.

Understanding the limitations of clumped isotope data processing methodology is important in particular when comparing data from different labs.

While calibrating Δ_{47} measurements to the CDES-25 reference frame allowing data to be comparable between labs, variations in the calculations used for data processing can affect the comparability of reported results. Δ_{47} (CDES-25) is expressed relative to an acid digestion temperature of 25 °C, and correction is required when digestion takes place at different temperatures. The source of the acid reaction correction factor used varies within the literature, which means that different corrections are applied for the same digestion temperature between studies. The correction factor used at UEA is described above and was derived empirically within the lab but is also in agreement with the Guo et al. (2009) theoretical fractionation relationship.

Another source of uncertainty in data comparison comes from the range of equations used by workers to derive the carbonate formation temperature from Δ_{47} ; which in turn influences the $\delta^{18}\text{O}_{\text{FLUID}}$ value calculated. A variety of different temperature equations are used, which means that even if results have identical Δ_{47} (CDES-25) values,

the temperatures reported may be different. For example, a temperature of 24.1°C calculated using Equation 2.4 (Kirk, 2017; Dennis et al., 2019) would be calculated as 39.8 °C using Equation 9 of Dennis et al. (2011).

The UEA temperature Equation (Equation 2.4) is, however, nearly identical to the recently published calibration of Anderson et al. (2021), which was calibrated to carbonate standards and was in agreement with several other studies. The use of the UEA temperature equation is therefore justified for use and comparable to other labs.

2.8.2: Additional factors influencing our analysis:

In addition to the issues with water vapour that have been described above, several other factors may have affected our analyses.

The Porapak Q trap temperature was not always consistent between different samples. This may have particularly affected early analysis as, in early 2018, the cooling devices were struggling to reach the ideal temperature of -20°C. Temperatures ranged from -16.8°C to -21°C throughout the initial period of work in April 2018, and between -19.7 to -26°C for subsequent analyses, with most falling between -20 to -22°C. The initial higher temperatures may have reduced the Porapak Q effectiveness; however, it is uncertain if the later inconsistency of temperatures lower than 20°C between samples affected the precision or repeatability of results.

The water traps can face the same issue as above, with starting temperatures for each trap ranging by up 9°C, although stability was increased over time.

Detailed notes were made on the initial temperatures of each step for each sample (where the majority of gas transfer between cold fingers occurs), but temperature varied within the duration of time given for each stage of the preparation process, which could not be tracked for each sample. Therefore, even though no apparent relationship between logged temperatures is seen between samples, it is unknown if there were relationships with this unrecorded variability.

Chapter 3: Taking the heat out of British Jurassic septarian concretions

This chapter has been published as the following paper: Paxton, R. B., Dennis, P. F., Marca, A. D., Hendry, J. P., Hudson, J. D., & Andrews, J. E. (2021). Taking the heat out of British Jurassic septarian concretions. *The Depositional Record*, 7(2), 333-343.

3.1: Introduction:

There is considerable interest in the application of clumped isotope palaeothermometry for reconstructing temperatures from carbonate rocks and fossils from a range of Earth-surface palaeoenvironmental and diagenetic settings (Ghosh et al., 2006; Eiler, 2007, 2011; Huntington et al., 2011). While clumped isotope palaeothermometry does not require prior assumptions regarding temperature or water isotopic compositions, a potential drawback is that many earth surface biotic and abiotic carbonates probably crystallize too rapidly to achieve the complete isotopic equilibrium (Daëron et al., 2019) required to apply the technique quantitatively. This said, some abiotic carbonates, particularly slowly growing sparry calcite cements in basinal sediments, should be excellent targets for clumped isotope analysis. These sparry cements typically formed under shallow to deep burial conditions where warmer temperatures (e.g. 20-50 °C; Defliese & Lohmann, 2016; Purvis et al., 2020) ensure isotope exchange reaction rates are fast, and dissolved inorganic carbon (DIC)-calcite equilibrium is more likely to be achieved.

Ancient carbonate concretions (Raiswell & Fisher, 2000) are obvious targets for clumped isotope palaeothermometry and the first Δ_{47} data (Loyd et al., 2012) showed that concretion body cements were influenced by post-depositional fluid alteration, driven by either silica diagenesis (Miocene, Monterey Formation) or meteoric-water influx (Cretaceous Holz Shale Formation).

This was followed by clumped isotope palaeothermometry on septarian concretions (Dale et al., 2014; Loyd et al., 2014) of various ages, attractive targets because a single decimetre-sized concretion can contain a variety of carbonate cements that record changes in the geochemical environment and temperature from initial formation through progressive burial in sedimentary basins over millions of years. Both studies reconstructed cementation temperatures and the fluid types involved in

concretion cementation. Their results showed that some concretion bodies gave temperatures indicative of formation at shallow depths (Loyd et al., 2014), while other concretion-body data indicated much higher temperatures (Dale et al., 2014; Loyd et al., 2014), apparently resolving some of the uncertainty inherent in traditional stable isotope data (Mozley & Burns, 1993). However, clumped isotope paleothermometry is not a panacea; each case study needs careful evaluation of all supporting data. For example, clumped isotope data show that negative $\delta^{18}\text{O}$ values in sparry calcite cements filling septarian fractures may not indicate meteoric water input (Dale et al., 2014), although they often do (Loyd et al., 2014).

This study concentrates on British Jurassic concretions which have a history of detailed previous research (Hudson 1978; Hudson et al., 2001; Hendry et al., 2006) allowing the new clumped isotope information to be constrained in a tight framework of supporting data. These Jurassic concretions are thought to have formed in unconsolidated, organic-rich, marine muds (Duff, 1975; Kenig et al., 1994) within a few metres of the sea floor (Hudson, 1978; Hendry et al., 2006). Concretion bodies (Fig. 3.1) may have initiated from a biomineralization of a bacterial extra-cellular polysaccharide framework (Hendry et al., 2006) which was rapidly entombed by microsparry calcite cement. The pore water from which this cement precipitated was essentially seawater, while bacterial sulphate reduction (BSR) caused the incorporation of isotopically negative C in calcite, and S in pyrite (Irwin et al., 1977; De Craen et al., 1999).

The lithifying concretion bodies contracted at an early stage of cementation, forming septarian cracks (Fig. 3.1) or more irregular breccias within an otherwise unconsolidated sediment. Mobile clays, intruded into cracks at both Calvert and Staffin (Fig. 3.2), are direct evidence of this, and pyrite coating breccia fragments are evidence this happened in the BSR zone (Hudson, 1978; Hudson et al., 2001). In many cases, brown fibrous cements nucleated on crack walls forming distinct cement fringes (Fig. 3.1).

The Sr isotope compositions of early calcite phases (concretion bodies and fibrous cement fringes) in the English concretions are very close to those of Callovian seawater (Hudson et al., 2001). Moreover, the $\delta^{18}\text{O}$ values of these phases are similar to those from well-preserved benthic fossils, which led Hudson et al. (2001) to infer early calcite cementation temperatures of *ca* 15 °C, assuming the widely accepted $\delta^{18}\text{O}$ composition for Jurassic seawater of $-1\text{‰}_{\text{VSMOW}}$ (Shackleton & Kennett, 1975). The last stage of concretion development resulted in the precipitation of ferroan sparry calcite in the

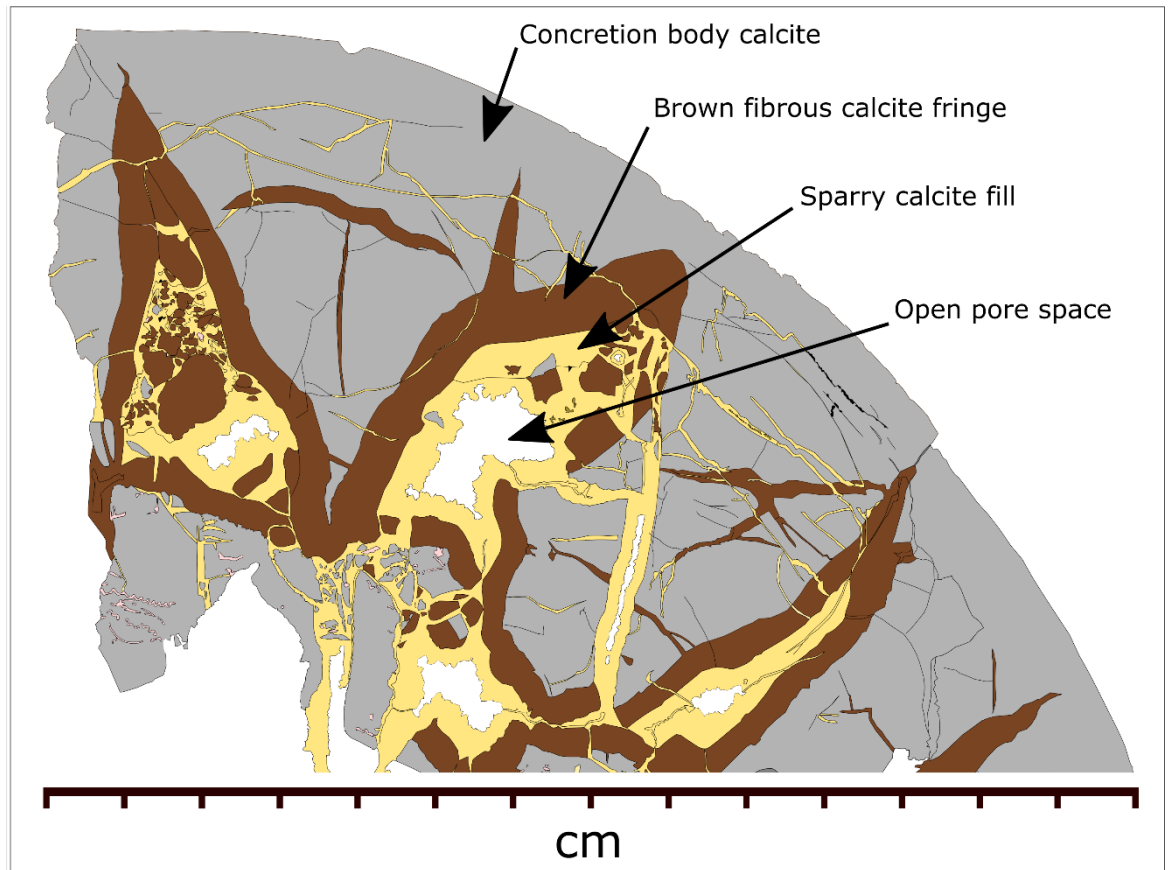


Figure 3.1: Line drawing from a slab of Staffin Shale Formation concretion showing the various calcite phases described in this chapter.

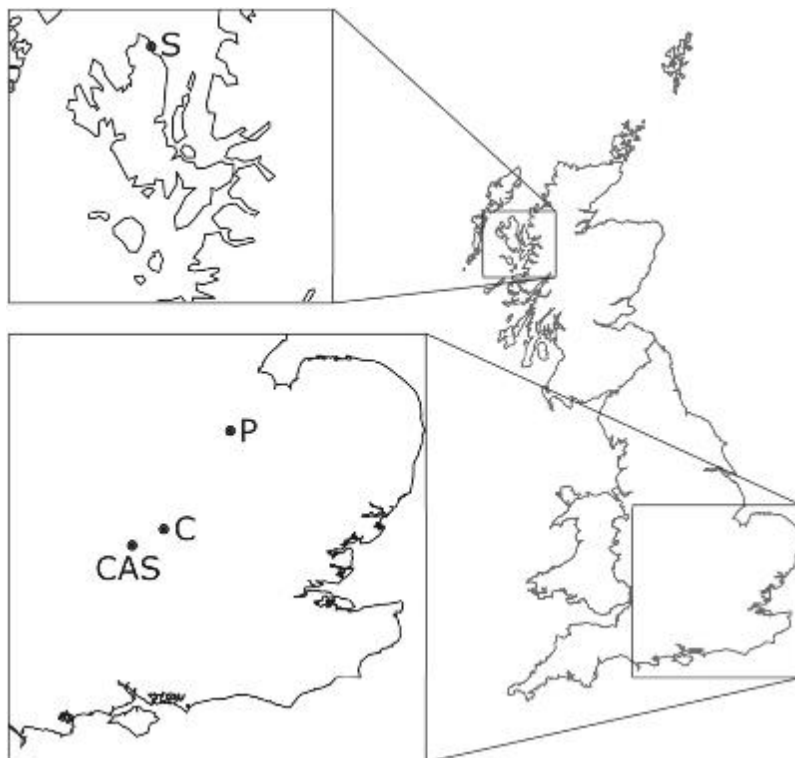


Figure 3.2: Sample locations. C= Calvert; CAS = Cassington; P = Peterborough; S = Staffin.

septaria (Fig. 3.1), cements that have distinctly negative $\delta^{18}\text{O}$ values (mean $\delta^{18}\text{O}$ of $-7.4\text{‰}_{\text{VPDB}}$) indicative of a meteoric fluid (Hudson, 1978). Likewise, at Staffin, Hendry et al. (2006) derived minimum concretion body and fibrous calcite cementation temperatures *ca* 10°C , with ferroan sparry calcites displaying a wide range in $\delta^{18}\text{O}$ values ascribed to variable mixing of marine and highly ^{18}O -depleted meteoric pore fluids.

This study is timely because Loyd et al., (2014) reported clumped isotope temperatures from English Jurassic concretion body calcites and brown fibrous cement fringes that were *ca* 20 to 30 $^{\circ}\text{C}$ warmer than those inferred from geological and traditional geochemical evidence (Hudson et al., 2001). They resolved the temperature mismatch by suggesting the shallow burial precursor calcites had undergone pervasive reaction with heated basinal fluids with $\delta^{18}\text{O}$ compositions around $+3.2\text{‰}_{\text{VSMOW}}$; a scenario that is the opposite of the typical 'meteoric water-alteration pathway' proposed for calcitic concretions based on an ensemble of stable isotope data (Mozley & Burns, 1993).

3.1.1: Study materials

Middle and Upper Jurassic concretions were analysed from a range of localities (Fig. 3.2) and stratigraphic horizons as indicated by ammonites in the concretions (see Cox et al., 1994). These included concretions from brick pits (now back-filled) at Calvert (Jason Subzone, Jason Zone, middle Callovian, Buckinghamshire), Norman Cross Quarry near Peterborough (Obductom Subzone, Coronatum Zone, middle Callovian, Cambridgeshire) and a former gravel pit at Cassington (Obductom Subzone, Coronatum Zone, middle Callovian, Oxfordshire) all described in Hudson (1978) and Hudson et al. (2001). An *ex situ* concretion derived from the Ampthill Clay (Serratum Subzone, Serratum Zone, upper Oxfordian) was collected from Pleistocene till at Norman Cross quarry (Hudson, 1978). The lower Kimmeridgian Staffin Shale Formation concretions (Densicostata/Normandia Subzone, Baylei Zone) are from the Hebridean Isle of Skye (Hendry et al., 2006) (Fig. 3.3 and 3.4). Equivalence of material sampled in earlier published research is shown in Table 3.1.

This study	Hudson (1978)	Hudson et al. (2001)	Loyd et al. (2014)	Hendry et al. (2006)	Pearson et al. (2005)
C5	C5-X*	c595XX*			
CAS1095-6		CAS1095X*			
P1AB	P1A-X*	P1ABXX*			
P35-95	P3-X*	P595 A	P3-4r		
SC8				SC8	SC8-XX*
151-7					
161a					

* X and XX signifies an alpha-numeric extension to the sample number dependent on the cement type (e.g. concretion body cement, fringing cement, fracture fill spar).

Table 3.1: Equivalence of sample numbering across the different studies for the concretions used in this study.

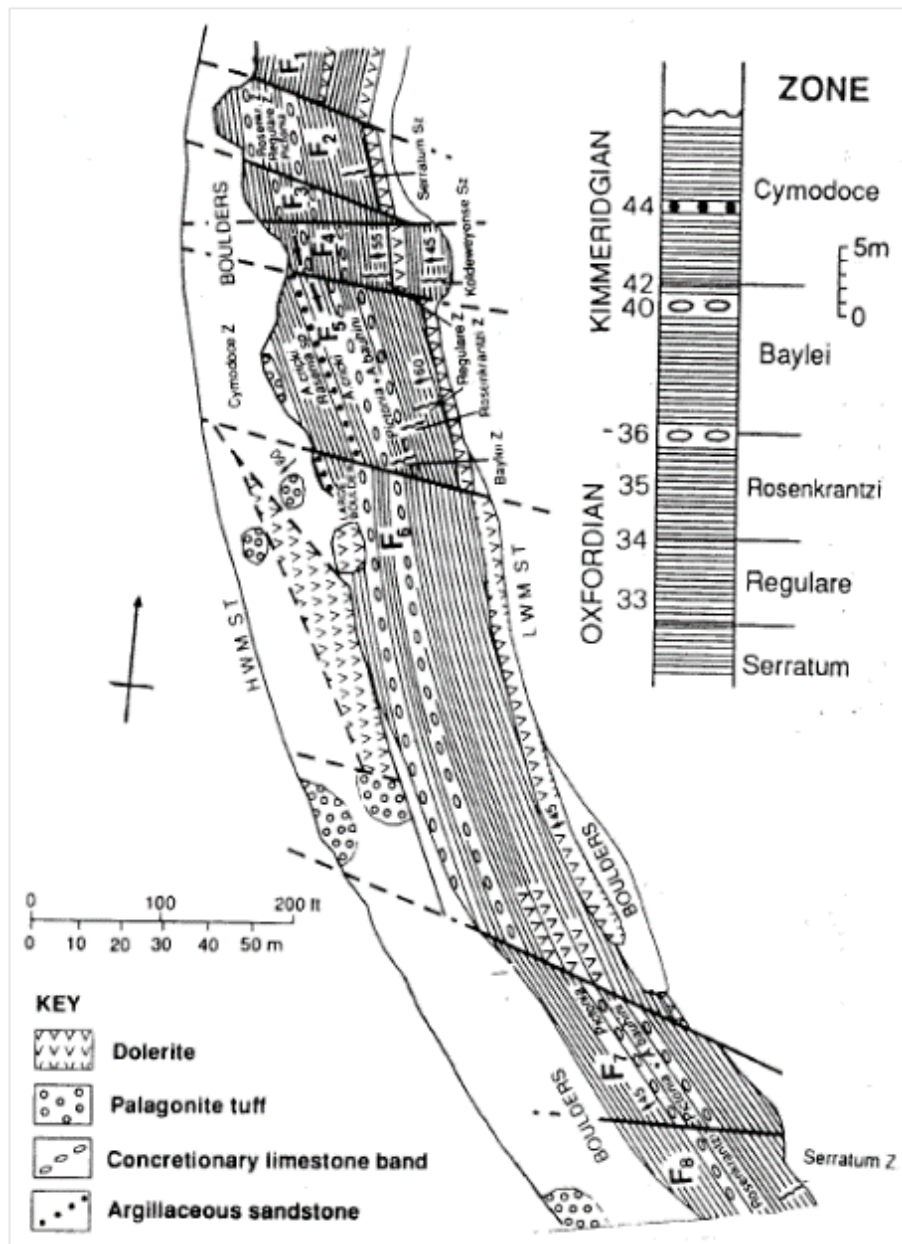


Figure 3.3: Geological map of the sampling locality of Staffin Shale Formation concretions, with Ammonite zones as reference; Point 7, Staffin Bay, Trotternish, Isle of Skye. After Morton & Hudson (1995).



Figure 3.4: Concretion from the Staffin Shale Formation at Staffin Bay, Trotternish, Isle of Skye, which is *ex situ* but likely from bed 40. The brown fibrous calcite and yellow sparry calcite fills of the septarian cracks are weathered to dark brown/black. The calcitic concretion body (light grey) has been bordered by a thick siderite layer (orange) which also has yellow sparry calcite fractures (weathered black here).

3.2: Methods:

3.2.1: Sample preparation

Sample powders from concretion body cements, brown fibrous fringes and void-filling spars were either drilled from cut slices, or produced by crushing fragments (broken from hand specimen) in a pestle and mortar. In all cases areas of sample with visible microfractures or other obvious inhomogeneities were avoided. For three concretions where brown fibrous fringes were >4 mm thick subsamples were obtained by drilling two trenches (1 mm wide x 1.5 mm deep x 15-20 mm long), one parallel to the inner margin adjacent to the concretion body, and another parallel to the outer margin close to the contact with the succeeding sparry calcite cement (E.g., Fig. 3.5).

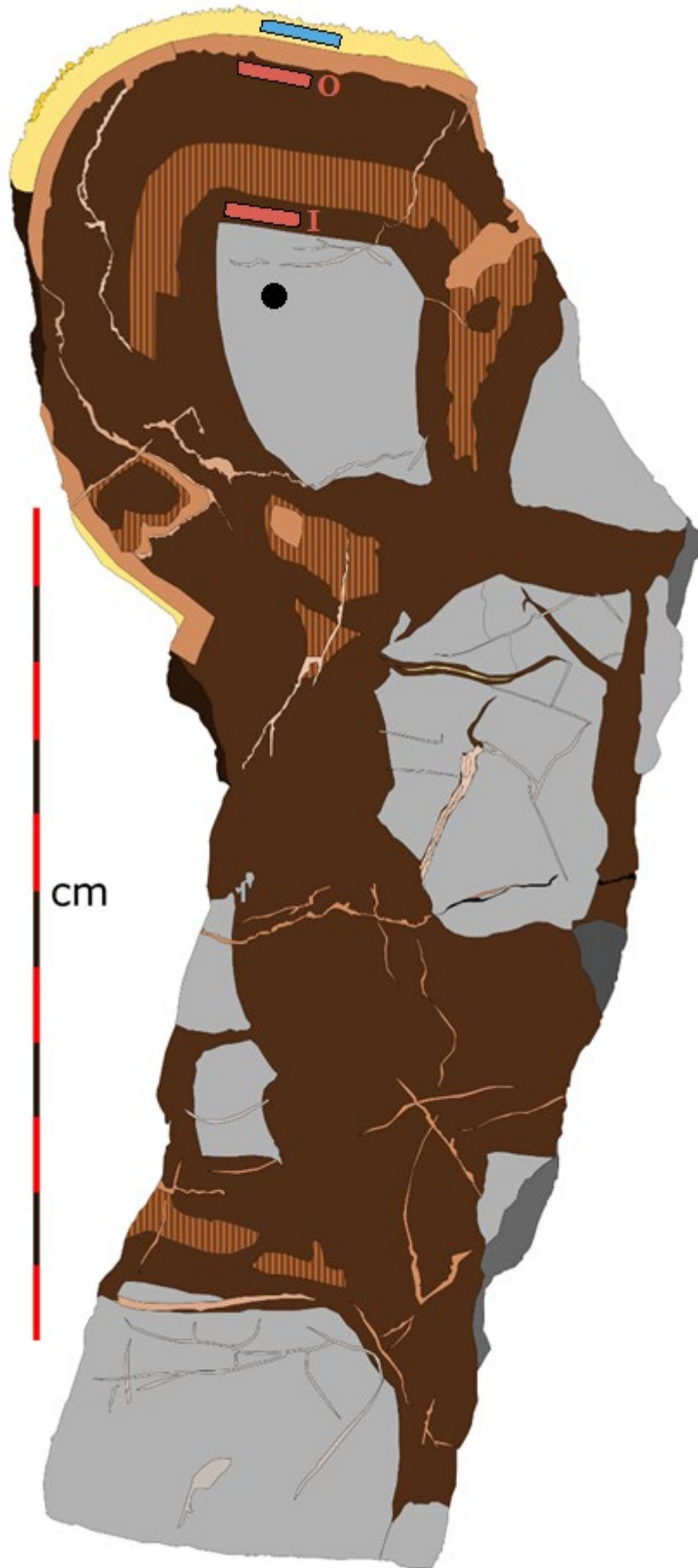


Figure 3.5: Line drawing of sample 161a, showing sampling sites: black circle = concretion body; red line = fibrous fringe (with inner and outer marked as initials); blue line = spar.

Sample powders (*ca* 4-6 mg) were reacted in vacuo at 87°C for 30 minutes with 102% ortho-phosphoric acid in a common acid bath, dynamically collecting the evolved CO₂ by freezing into a spiral trap immersed in liquid nitrogen (-196°C). Next the trap was isolated from the reaction vessel, keeping it immersed in liquid nitrogen whilst removing non-condensable gases by vacuum pumping. Then, warming the trap to -120°C, the CO₂ was sublimated at low pressure, cryodistilling it into a manometer via two further water traps also held at -120°C. After carrying out a second step of removing non-condensable gas, the gas amount was measured to estimate reaction yield. In the last stages of gas purification the CO₂ was transferred through a static Porapak-Q trap (120 mm long x 9 mm diameter) held at -20 °C, freezing it into a cold finger for 30 minutes before a final step of removing non-condensable gas.

3.2.2: Measurement and data handling

Sample CO₂ was measured as described in Chapter 2.

3.2.3: Temperature calculation

The empirical clumped isotope calibration of Kirk (2017) based on measurements made in the UEA laboratory using the MIRA mass spectrometer (Dennis et al., 2019) was used to calculate temperatures (Equation 2.4 of Chapter 2). The calcite-water isotope fractionation factor calibration of Kim and O'Neil (1997), which is appropriate for abiotic carbonates, is used to determine water oxygen isotope compositions (Equation 2.7 of Chapter 2).

The isotope values reported here are the mean of 3-6 measurements of replicate samples, with the measurement uncertainty reported as ± 1 standard error of the pooled standard deviation of measurements for each of the three phases: concretion bodies, fibrous fringes and spars. In using the pooled standard deviation it is necessary to ensure that there is a sufficient number of samples to determine a representative distribution of the measurement uncertainty. The standard deviations and errors for 'individual' samples are also reported in Appendix 1: Part II. Temperature and fluid isotope compositions are calculated using the mean Δ_{47} and $\delta^{18}\text{O}$ values with full propagation of the measurement and calibration uncertainties. The $\delta^{13}\text{C}$ and $\delta^{18}\text{O}$ values are reported for carbonates with

respect to Vienna-Pee Dee Belemnite (VPDB) and $\delta^{18}\text{O}$ values for water with respect to Vienna-standard mean ocean water (VSMOW).

3.2.4: Sample contexts

The sedimentology, petrography and paragenesis of the various calcites sampled here have been reported before, principally by Hudson (1978) and Hudson et al. (2001; English concretions) and Hendry et al. (2006; Staffin). Salient points are summarised here, discussing published stable isotope data in context with this new data in subsequent sections.

Concretion body calcites are mostly non-ferroan microspars that grew into the pore space of peloidal host sediment. These concretions have pyritic rims consistent with formation in the BSR zone; pyrite formation sequestered available Fe^{2+} explaining the low iron content in the microspars. The Amphill Clay and Staffin concretions are different; in these the body microspars are ferroan, and the concretions lack pyritic rims. This indicates availability of excess Fe^{2+} for incorporation into calcite either from; (1) iron-reduction under sub-oxic conditions while rates of BSR (and thus pyrite formation) were low; or (2) from upward diffusion of methanogenic Fe^{2+} when BSR had effectively ceased, the latter implying growth near the base of the BSR zone. The ferroan microspars from Staffin have resultant dull-orange cathodoluminescence (CL).

Brown fibrous cement fringes, oriented normal to septarian fracture walls are best described in the Staffin and Amphill Clay samples (Hudson, 1978; Hendry et al., 2006), comprising radiating palisades (50 μm wide and up to 5,000 μm long), some with fascicular-optic textures. The brown body colour is imparted by polar organic inclusions (Pearson et al., 2005). The earliest phases of growth (Staffin) are non-ferroan and non-luminescent, becoming dull orange luminescent distally, then passing into more ferroan compositions with dull brown to very dull brown CL, which is interpreted as evidence of initial suboxic conditions resulting from a pause in sedimentation, followed by renewed burial and ingress of methanogenic Fe^{2+} . Iron content of the English brown fibrous calcites is similarly variable but has not been studied systematically.

The fracture-hosted sparry cements are variably white or yellow ferroan calcites with dull to very dull brown CL. Crystals are typically 0.5 to 4 mm in size, variously equant to elongate with steep terminations into open spaces.

3.3: Results:

Stable and clumped isotope results for the calcite phases in the concretions are summarised in Table 3.2 and Figure 3.6.

Sample	Phase	<i>n</i>	$\delta^{13}\text{C}$ (‰, VPDB)	$\delta^{18}\text{O}_{\text{Carbonate}}$ (‰, VPDB)	Δ_{47} (CDES)*	$T(\Delta_{47})$ (°C)	$\delta^{18}\text{O}_{\text{Fluid}}$ (‰, VSMOW)
<u>Staffin Shale Formation, Skye[†]</u>							
151-7	Body	3	-17.47 ± 0.06	-1.04 ± 0.03	0.703 ± 0.012	9 ± 5	-2.2 ± 1.1
	Fibrous fringe	4	-15.68 ± 0.09	-0.70 ± 0.02	0.673 ± 0.012	18 ± 5	0.1 ± 1.1
	Spar	4	-10.69 ± 0.11	-10.74 ± 0.07	0.677 ± 0.011	17 ± 5	-10.1 ± 1.0
161a	Body	4	-17.34 ± 0.05	-0.89 ± 0.03	0.690 ± 0.011	13 ± 5	-1.2 ± 1.0
	Inner fibrous fringe	3	-16.81 ± 0.11	-0.27 ± 0.03	0.677 ± 0.013	17 ± 5	0.3 ± 1.2
	Outer fibrous fringe	4	1.66 ± 0.09	-0.93 ± 0.02	0.654 ± 0.012	24 ± 5	1.2 ± 1.1
	Spar	4	-5.62 ± 0.11	-11.74 ± 0.07	0.653 ± 0.011	25 ± 5	-9.5 ± 1.1
SC8	Body	5	-14.89 ± 0.04	-0.75 ± 0.02	0.658 ± 0.009	23 ± 5	1.2 ± 1.0
	Inner fibrous fringe	3	-14.95 ± 0.11	-0.30 ± 0.03	0.677 ± 0.013	17 ± 5	0.3 ± 1.2
	Outer fibrous fringe	3	-2.34 ± 0.11	-0.40 ± 0.03	0.629 ± 0.013	33 ± 6	3.5 ± 1.2
	Spar	5	-7.46 ± 0.10	-3.38 ± 0.07	0.672 ± 0.010	18 ± 5	-2.5 ± 1.0
<u>Amphill Clay, Peterborough[§]</u>							
P35-95	Body	3	-19.50 ± 0.06	-0.70 ± 0.03	0.683 ± 0.012	15 ± 5	-0.5 ± 1.1
	Inner fibrous fringe	3	-19.80 ± 0.11	-0.68 ± 0.03	0.683 ± 0.013	15 ± 5	-0.5 ± 1.1
	Outer fibrous fringe	4	-20.10 ± 0.09	-1.21 ± 0.02	0.670 ± 0.012	19 ± 5	-0.1 ± 1.1
	Spar	3	-0.47 ± 0.13	-9.55 ± 0.08	0.630 ± 0.013	33 ± 6	-5.7 ± 1.2
<u>Oxford Clay, Peterborough[§]</u>							
P1AB	Body	3	-15.69 ± 0.06	-0.80 ± 0.03	0.697 ± 0.012	11 ± 5	-1.5 ± 1.1
	Spar	4	-0.15 ± 0.11	-9.53 ± 0.07	0.602 ± 0.011	43 ± 6	-3.7 ± 1.1
	Spar	3 [#]	-0.16 ± 0.14	-9.52 ± 0.09	0.616 ± 0.011	38 ± 6	-4.7 ± 1.1
<u>Oxford Clay, Calvert^{**}</u>							
C5	Body	3	-14.25 ± 0.06	-0.66 ± 0.03	0.673 ± 0.012	18 ± 5	0.2 ± 1.1
	Spar	3	-0.41 ± 0.13	-7.34 ± 0.08	0.638 ± 0.013	30 ± 6	-4.1 ± 1.2
<u>Oxford Clay, Cassington^{††}</u>							
CAS1095-6	Body	3	-14.72 ± 0.06	-0.76 ± 0.03	0.675 ± 0.012	17 ± 5	0.0 ± 1.1
	Spar	3	0.86 ± 0.13	-7.93 ± 0.08	0.650 ± 0.013	26 ± 6	-5.5 ± 1.1
All ± values represent one standard error of the pooled standard deviation.							
*CDES is Carbon Dioxide Equilibrium Scale							
[†] Location: 57.661774 -6.246455 (WGS84)							
[§] Location: 52.509702 -0.274535 (WGS84)							
[#] Same sample as above, excluding one high temperature measurement; see text.							
^{**} Location: 51.903016 -0.991232 (WGS84)							
^{††} Location: 51.794775 -1.318454 (WGS84)							

Table 3.2. Geochemical data and Δ_{47} temperatures

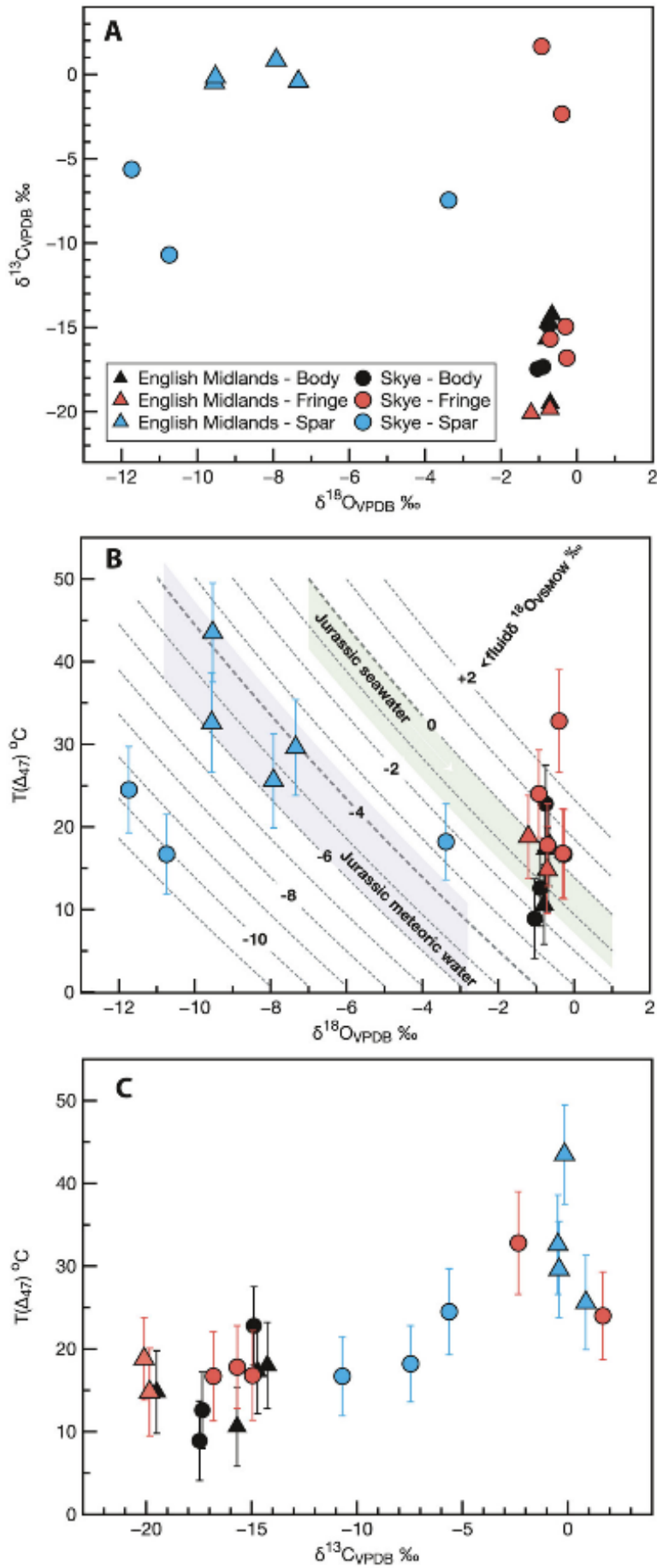


Figure 3.6: Cross plots of geochemical and Δ_{47} temperature data. Error bars represent one standard error of the pooled standard deviation (see Table 3.2). The $\delta^{18}\text{O}_{\text{VPDB}}$ and $\delta^{13}\text{C}_{\text{VPDB}}$ errors are < symbol dimensions.

The $\delta^{13}\text{C}$ and $\delta^{18}\text{O}_{\text{carbonate}}$ values (Fig. 3.6 A) are broadly consistent with previous data from the same Oxford and Amptill Clay concretions (Hudson, 1978; Hudson et al., 2001); similarly, the data from newly sampled Staffin Shale concretions are mainly comparable to data in Hendry et al. (2006). The clumped isotope data (Table 3.2) mostly show similar paragenetic trends despite being from different geographic areas and stratigraphic units.

Concretion body cements gave temperatures between 9 ± 5 °C and 18 ± 5 °C, and pore fluid values between 0.2 ± 1.1 ‰ and -2.2 ± 1.1 ‰_{VSMOW}, excepting concretion SC8 body which gave a temperature of 23 ± 5 °C and a pore fluid value of 1.2 ± 1.0 ‰_{VSMOW} (Fig. 3.6 B).

The brown fibrous cement fringes mostly gave temperatures between 15 ± 5 °C and 19 ± 5 °C, and pore fluid values between -0.5 ± 1.1 ‰ and 0.3 ± 1.2 ‰_{VSMOW} (Fig. 3.6 B). Two Skye concretions with thick fibrous calcite fringes that were sub-sampled display increasing temperatures and more ^{18}O -enriched pore fluid compositions from the inner to outer edges (Table 3.2).

Temperatures and pore fluid compositions for void filling spars are variable in both geographic regions (Fig. 3.6 B), 151-7 (Skye) having the lowest (17 ± 5 °C) and P1A-B (Peterborough) the highest at 43 ± 6 °C. Spars from the Oxford and Amptill Clays gave fluid compositions between -3.7 ± 1.1 ‰ and -5.7 ± 1.2 ‰_{VSMOW}, whereas two concretions from the Staffin Shale had spar fluid compositions of -10.1 ± 1.0 ‰ and -9.5 ± 1.1 ‰_{VSMOW}. SC8 (Skye) was again an exception, with a pore fluid value of -2.5 ± 1.0 ‰_{VSMOW}.

3.4: Interpretation and discussion:

The variance of individual sample replicates (Appendix 1: Part II) is typically close to, or less than the overall pooled uncertainties and are similar between different calcite phases, and are also commensurate with the long-term uncertainty associated with measurement of the standards. This is believed to indicate that sampling resulted in homogeneous powders for analysis. However, it is possible that some of the sample internal variance might reflect original inhomogeneity in the sediments including minor variation in the timing of cementation of residual porosity in the concretion bodies. There is no petrographic evidence to suggest the latter is likely in these sampled concretions (Hudson et al., 2001; Hendry et al., 2006) although electron backscatter data in Loyd et al. (2014) imply <10% 'pseudospars' patches in some of their British concretion bodies. Other

causes of variance could be due to inclusion of undetected cements in micro-fractures and the possibility of crystal face disequilibrium effects (Dickson, 1991) in the coarser sparry calcites. However, simple mixing modelling (Paxton et al., 2021: Supplemental Information, section 5) indicates that all phase mixing can be excluded other than a very small fraction of spar cement.

For most concretions, the clumped isotope data from the earliest-formed calcites (body, cement fringe) gave temperatures between $9\pm 5^\circ\text{C}$ and $19\pm 5^\circ\text{C}$ (Table 3.2). In addition, all but one concretion body sample (151-7 from Staffin; Table 3.2) gave derived water $\delta^{18}\text{O}$ values of $ca -1\text{‰}_{\text{VSMOW}}$ $\delta^{18}\text{O}$, consistent with the values for Jurassic seawater proposed by Shackleton and Kennett (1975). The data thus indicate calcite precipitation from marine pore fluids, consistent with the Sr isotope compositions (Hudson et al., 2001). There is little evidence that the concretion bodies were pervasively altered by meteoric waters (cf. Mozley & Burns, 1993) and no evidence for pervasive alteration by a secondary phase of hot ($33\text{--}46^\circ\text{C}$) ^{18}O -enriched pore water, which Loyd et al. (2014) proposed for some of the same material.

Taken together the concretion body results are a new measure of mean bottom water temperatures of $ca 15^\circ\text{C}$ (range 9 to 18°C) in British Callovian-Kimmeridgian seas, in agreement with earlier Callovian benthic (Hudson et al., 2001; Mettam et al., 2014) and Kimmeridgian water column (belemnite rostra $\delta^{18}\text{O}$, Staffin Shale Formation) temperature estimates between 14 and $<20^\circ\text{C}$ (Wierzbowski et al., 2006; Nunn et al., 2009). Moreover, these abiogenic concretion body calcites are probably a more secure guide to bottom water temperatures than fossil skeletal carbonates because assumptions about biogenic vital effects are not required. In this context, note both the high variability in $\delta^{18}\text{O}$ values from Staffin Shale Formation belemnite rostra (Wierzbowski et al., 2006; Nunn et al., 2009) and their remarkably high clumped isotope temperatures (Vickers et al., 2020), suggesting undetected disequilibrium effects. Only the coolest belemnite apical-line clumped isotope temperature of $18.7\pm 5^\circ\text{C}$, thought to reflect benthic or syndepositional conditions in the Staffin Shale Formation (Vickers et al., 2020), overlaps the concretion body temperature range reported here.

These results align well with established views that British Jurassic concretion body calcites precipitated under very shallow marine burial conditions (Raiswell, 1976; Hudson, 1978; Hudson et al., 2001; Hendry et al., 2006) within the BSR zone, as supported by negative $\delta^{13}\text{C}$ compositions (Fig. 3.6 C; see also Irwin et al., 1977; Mozley & Burns,

1993; Hudson et al., 2001). The similarity of the data from the concretion bodies and the fracture-hosted fibrous cement fringes also supports the inference that septarian fracture initiation and subsequent fringe cementation was penecontemporaneous with formation of the concretion body under marine shallow burial conditions (Hudson et al., 2001; Hendry et al., 2006).

The rates of crystallization of these earliest-formed calcite phases are not known so assumptions regarding isotopic equilibrium are difficult to substantiate. This noted, it is striking that the clumped isotope temperatures are consistent with the wider geological context of concretion growth (Hudson, 1978; Sellés-Martínez, 1996; Hendry et al., 2006), suggesting that they did form under near isotopic equilibrium.

In most cases the fibrous cement fringes formed from seawater-derived pore fluids between 4 and 9 °C warmer than the fluid from which the concretion bodies formed. Sub-samples of a cement fringe from the Amphill Clay concretion did not record significant changes in temperature or fluid composition from inner to outer edge (Table 3.2). However, two concretions from the Staffin Shale of Skye both show a transition from initial precipitation at 17 ± 5 °C from pore fluids with a $\delta^{18}\text{O}$ value of $0.3 \pm 1.2\text{‰}$, to significantly warmer temperatures and slightly more evolved pore fluids close to the outer edge of the cement (Table 3.2). This is consistent with initial growth at shallow burial within, and perhaps near the base, of the BSR zone (Hendry et al., 2006), followed by deeper burial (warmer pore water) and transition beyond the BSR zone, as suggested by gradually increasing $\delta^{13}\text{C}$ values (Hendry et al., 2006). The enrichment of ^{18}O in these Staffin Shale fluids (Table 3.2) suggests some near-closed system, water/sediment interaction; limited reaction with a silicic sediment component like volcanic ash (Knox, 1977) would achieve this (cf. Noh & Lee, 1999). It is noteworthy that the ^{18}O enrichment and temperature increase have opposing effects on the $\delta^{18}\text{O}_{\text{carbonate}}$ value (Table 3.2), such that without Δ_{47} data little if any change in the conditions of precipitation would be apparent.

Sparry calcites that partially or wholly fill void spaces are the final carbonate cement phases in all the studied concretions. Clumped isotope temperatures for these cements are variable (from 26 ± 6 °C to 43 ± 6 °C for the English concretions; and 17 ± 5 °C to 25 ± 5 °C from the Skye concretions; Table 3.2), but usually higher than the corresponding concretion body temperature, consistent with formation under relatively deeper burial. The Oxford and Amphill Clay spars precipitated from pore fluids with $\delta^{18}\text{O}$ values

between $-3.7 \pm 1.1\%$ and $-5.7 \pm 1.2\%$ VSMOW, while spars in two of the Skye concretions precipitated from fluids with $\delta^{18}\text{O}$ values between $-9.5 \pm 1.1\%$ and $-10.1 \pm 1.0\%$ VSMOW (Table 3.2). These fluid compositions indicate the presence of meteoric waters, confirming conclusions of earlier studies (Hudson, 1978; Hudson et al., 2001; Hendry et al., 2006; Loyd et al., 2014).

In one Skye concretion (SC8) the fringe cement data is comparable with other concretions in this study but the body yielded a temperature of 23 ± 5 °C (Table 3.2), warmer than any of the others. As the SC8 $\delta^{18}\text{O}$ value is not anomalous, it is suggested that the higher temperature results from disequilibrium effects on Δ_{47} . In addition, while the spar from SC8 had a comparable precipitation temperature (18 ± 5 °C) to that of other concretions, the derived pore water composition was much more ^{18}O -enriched ($-2.5 \pm 1.0\%$ VSMOW compared to between $-9.5 \pm 1.1\%$ and $-10.1 \pm 1.0\%$ VSMOW for the other Skye concretions; Table 3.2). The reason for this difference is not clear; however, Hendry et al. (2006) recorded a large range in Staffin Shale concretion sparry calcite $\delta^{18}\text{O}_{\text{carbonate}}$, ranging from -1.5% to -17% VPDB, suggesting substantial heterogeneity in pore fluid composition between concretions. This variation might be due to spars precipitating from fluids at different stages of burial and uplift, including progressive displacement by Palaeocene meteoric water (Hendry et al., 2006).

The clumped isotope temperatures for all concretion calcite phases are below the maximum burial temperature estimates for their locations (<60 °C for the Staffin Shale; Pearson et al., 2005; Lefort et al., 2012; Vickers et al., 2020; ≤ 50 °C for Southern England; Green et al., 2001). The highest temperature measured (43 ± 6 °C) was for a spar from P1A-B. This value is a mean of four repeats, one of which gave much higher temperatures (Table 3.2); excluding this outlier gives a temperature of 38 ± 6 °C and a fluid $\delta^{18}\text{O}$ composition of $-4.7 \pm 1.1\%$ VSMOW (Table 3.2), more in line with data from the other English concretions. However, since there is no evidence for contamination at mass 48 in this outlier all the data in the mean temperature reported is retained.

3.4.1: Comparison with earlier work:

The clumped isotope temperatures reported here from sparry fracture fills are similar to those of Loyd et al. (2014); they report temperatures of 32 ± 2 to 48 ± 2 °C from Oxford and Ampthill Clay spars. However, Loyd et al. (2014) also report elevated temperatures for the earlier diagenetic phases (body, cement fringe); in contrast this

study shows that the earlier cements were precipitated at, or close to Earth surface temperatures. This difference is clear in the reported Δ_{47} values (Fig. 3.7). There are a number of factors, mostly methodological, that may account for this difference, which are explored below.

The most obvious difference between the spars and the earlier diagenetic phases is a *ca* 15‰ depletion in $\delta^{13}\text{C}$ values for the Oxford and Amphill Clay concretions body cements (-14.3 to -19.5‰_{VPDB}) when compared to the spars (0.9 to -0.5‰_{VPDB}). As has

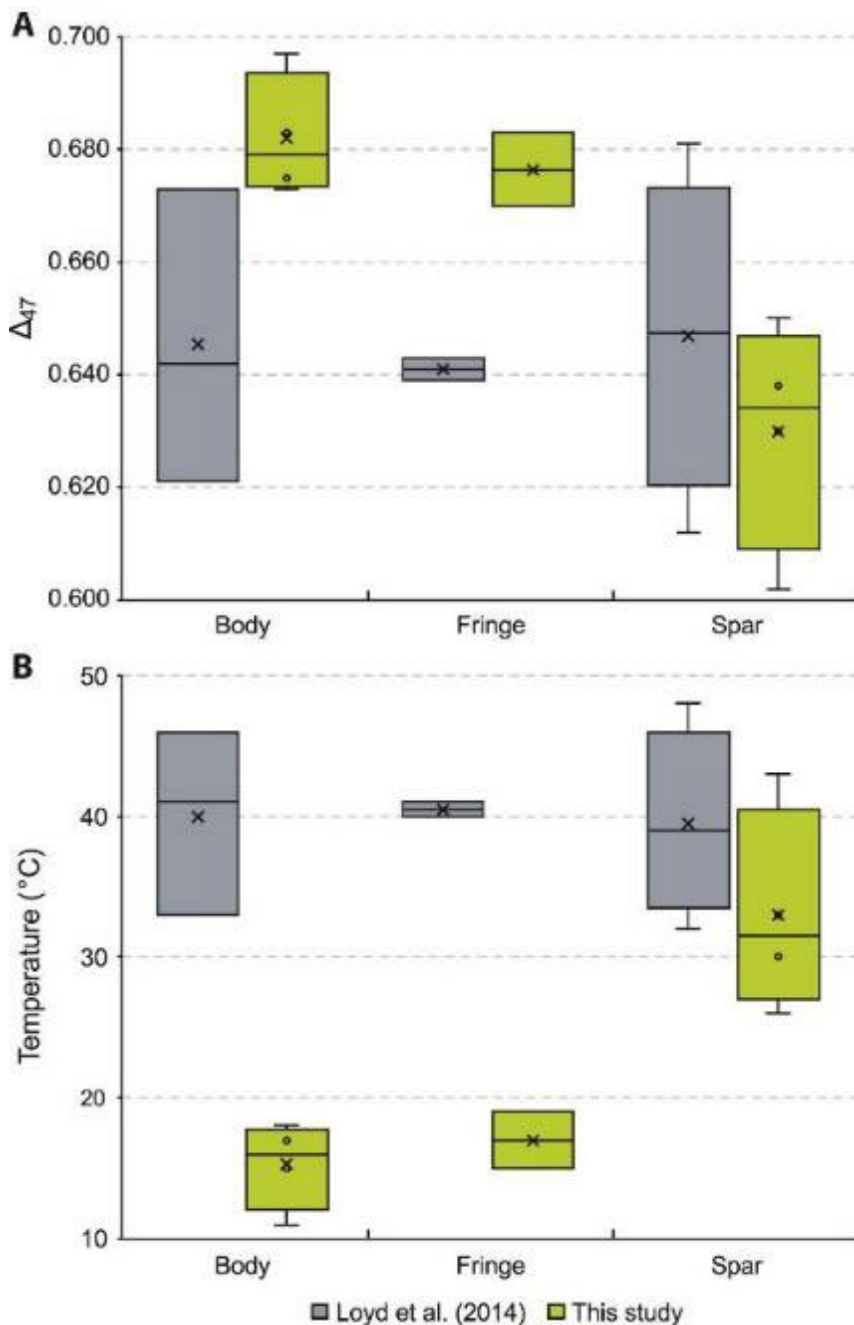


Figure 3.7: Box and whisker diagram of: (A) Δ_{47} values and (B) temperatures reported for body, fringe and spar cements of Oxford and Amphill Clay concretions by Loyd et al. (2014) and this study.

been shown by Schauer et al. (2016) and Daëron et al. (2016) there is a subtle but significant effect of the ^{17}O correction algorithm on reported Δ_{47} values when using different values for R^{17}_{VSMOW} and λ , the gradient of the oxygen isotope mass dependent fractionation line. Early studies typically used values of $R^{17}_{\text{VSMOW}} = 0.0003799$ and $\lambda = 0.5164$. Using these values, concretion body cement samples with depleted $\delta^{13}\text{C}$ values compared to spar cements will record Δ_{47} values that are too low, and thus higher apparent temperatures. The parameters used in the ^{17}O correction algorithm by Loyd et al. (2014) were not reported but, since their work precedes recognition of the importance of parameters employed, it is likely that they are now out-dated.

Other methodological differences between this study and that of Loyd et al. (2014) include the following. (1) The use of different temperature calibrations. Loyd et al. (2014) used the Ghosh et al. (2006) calibration as transformed onto the CDES by Dennis et al. (2011). This is at marked variance with virtually all other published calibrations. (2) Loyd et al. (2014) used the Passey et al. (2010) correction of $+0.08\text{‰}$ Δ_{47} in order to correct their results to an acid reaction temperature of 25 °C . It is likely that this correction value varies between reaction systems and schemes; for example, a value of $+0.062\text{‰}$ is reported here. (3) A significant correction for linearity is required in the Loyd et al. (2014) study. Since there is a large difference in the δ_{47} value of body and spar cements then small errors in the linearity correction will translate into variable offsets of the reported true Δ_{47} value as a function of the bulk δ_{47} value. It is likely that a contribution of one, or more of these methodological factors can explain the apparent elevated body cement temperatures reported by Loyd et al. (2014) when compared to the data reported here.

Additionally, there are possible effects associated with sample mineralogy and organic matter content, as well as possible mixing effects. The major difference between the spars and the earlier diagenetic phases (body, cement fringe) is that spars are largely free of non-carbonate impurities. In comparison, the concretion body cements have cemented pore space in host shales that include siliciclastic minerals, organic matter and pyrite framboids (Hendry et al., 2006; Hudson, 1978), while the early fibrous fringes contain abundant high molecular weight organic inclusions (Pearson et al., 2005). It is thus possible that non-carbonate derived contaminant molecules at the cardinal masses of the CO_2 isotopologues could cause inter-laboratory differences in results from impure carbonate samples. When experienced at UEA, such contamination invariably leads to elevated Δ_{48} and Δ_{47} values and the reporting of too low a temperature (Chapter 2.7). This

is not consistent with the observation in Loyd et al. (2014) that body cements precipitated at similar temperatures to the spar cements (see Figure 3.7). However, contaminants at masses 46 and 48 have been reported to lead to a lowered Δ_{47} and too high apparent temperatures (Snell et al., 2019). Potential contaminants include NO_2 arising from ammonium adsorbed on clay particles which has been previously identified as causing significant shifts in measured $\delta^{18}\text{O}$ (δ_{46}) values of carbonate cements (Mucciarone & Williams, 1990).

An additional effect may be caused by the mixing of cement phases. It is possible to include a component of spar cement when sampling body cements if small veins of microspar are not identified. Mixing of these two phases can lead to lowered Δ_{47} and higher apparent temperatures. Note, however, that Loyd et al. (2014) report taking great care during sampling to avoid mixing of phases.

Ultimately, it is thought most likely that the methodological differences between this study and that of Loyd et al. (2014), notably the ^{17}O correction, go a long way to explaining the different conclusions regarding the comparative temperatures of body and spar cements. The differences in data and interpretation are entirely understandable given the still novel nature of the clumped isotope method and the on-going rapid development of the technique. As clumped isotope mass spectrometry evolves, and our understanding of the subtleties improves, convergence of results should follow.

3.5: Conclusions:

New clumped isotope data from British Jurassic septarian concretions demonstrate:

1. that earliest-formed (syndimentary) concretion body calcites mostly precipitated at temperatures between $9\pm 5^\circ\text{C}$ and $18\pm 5^\circ\text{C}$, from fluids with $\delta^{18}\text{O}$ values between $0.2\pm 1.1\text{‰}$ and $-2.2\pm 1.1\text{‰}_{\text{VSMOW}}$. The fluid compositions indicate Jurassic seawater and the temperatures are recording bottom water/in-sediment conditions.
2. early diagenetic, brown, fibrous cement fringes mostly gave temperatures between $15\pm 5^\circ\text{C}$ and $19\pm 5^\circ\text{C}$, and pore fluid values between $-0.5\pm 1.1\text{‰}$ and $0.3\pm 1.2\text{‰}_{\text{VSMOW}}$. These results again imply a marine fluid under very shallow burial conditions.

3. later diagenetic sparry calcite cements formed between 17 ± 5 °C and 43 ± 6 °C with fluid compositions between $-2.5\pm 1.0\text{‰}$ and $-10.1\pm 1.0\text{‰}_{\text{VSMOW}}$, indicating precipitation from meteoric-influenced fluids under shallow burial conditions.

These data are consistent with established views on the formation of Jurassic septarian concretions and also demonstrate their potential to provide robust sea floor palaeotemperatures, free from assumptions about “vital effects” associated with biogenic carbonates. While the data on early diagenetic phases presented in this study differ from an earlier clumped isotope study on similar concretions (Lloyd et al., 2014), the disparity is probably caused by methodological differences.

Chapter 4: Early Paleocene cementation of Middle Jurassic sandstone by hot, meteoric water

4.1: Introduction:

4.1.1: Carbonate concretions and Clumped Isotopes:

Carbonate concretions are common features in the sedimentary rock record (McBride et al., 1985, 2003; Wilkinson, 1991, 1992, 1993; Mozley and Burns, 1993; Selléz-Martínez, 1996; Raiswell and Fisher, 2000; and others). Mudstone hosted carbonate concretions have been extensively studied and are usually thought to have initiated during early diagenesis, resulting from microbial reactions in the sediment (e.g., Raiswell and Fisher 2000 and references therein). Sandstone hosted concretions are less commonly reported, but are important due to their occurrence in reservoir rocks where they can reduce porosity, decrease permeability and impede fluid flow, hence lowering reservoir quality (e.g., Morad et al., 2010; Nyman et al., 2014). These concretions have been explored in relation to their nucleation, distribution (Bjørkum and Walderhaug, 1990) growth rates (Wilkinson and Dampier 1990) and carbonate source e.g., redistribution of calcite from dissolution of fossils within the host sand bodies. Others have explored the use of concretions as indicators of palaeo-groundwater flow (e.g., Johnson, 1988), fluid flow relating to faults and deformation (Balsamo et al., 2012; Del Sole and Antonellini, 2019) and as records of pore fluid evolution through their geochemistry (e.g., Wilkinson 1991, 1993; Noh and Lee, 1999; McBride et al., 2003).

The clumped isotope paleothermometer has become a powerful geochemical method for investigating carbonate material, as discussed in Chapter 1. As the abundance of ^{13}C - ^{18}O bonds in a carbonate formed at equilibrium is a function of temperature (Ghosh et al., 2006) it is now an important tool in diagenetic studies where it helps elucidate the temperature and pore water composition of diagenetic calcite (Chapter 1; also e.g., Huntington et al., 2011; Purvis et al., 2020; Paxton et al., 2021).

The technique has been used to investigate several diagenetic scenarios, including: to constrain the timing of sedimentary diagenetic events (Huntington et al., 2011); to investigate pore fluid sources and temperatures for cements in fault systems (e.g., Swanson et al., 2012; Bergman et al., 2013), to identify reactivation of syndepositional fracture networks in a carbonate platform (Budd et al., 2013) and to improve understanding of diagenetic recrystallization and alteration (e.g., Suarez and

Passey, 2014; Stolper et al., 2018; Guo et al., 2021; and others). Clumped isotopes have also been used in studies of cementation, for assessing the utility of early meteoric diagenetic cements in paleoclimate studies (Defliese and Lohmann, 2016) and for investigating the cementation and recrystallisation of authigenic carbonates at subduction zones with implications for geothermal gradients (Sample et al., 2017).

Mudrock hosted concretions have been targets of several clumped isotope studies (Lloyd et al., 2012; 2014; Dale et al., 2014; Heimhofer et al., 2017; Paxton et al., 2021 and Chapter 3). The application of clumped isotopes to sandstone hosted concretions and cements should significantly improve our understanding of the temperatures at which cementation proceeded (e.g. Methner et al., 2016; Purvis et al., 2020), provide insights into porewater evolution during concretion growth (e.g., Fan et al., 2014), and help better constrain the burial depth of cementation through the link between temperature and geothermal gradients (e.g., Purvis et al., 2020; Cui et al., 2019; 2021; Jimenez-Rodriguez et al., 2022).

The value of performing clumped isotope analysis on diagenetic carbonates is clear. Analysis of sandstone hosted carbonate concretions using clumped isotopes will help understand further the diagenetic processes leading to their formation, give insights into the porewater evolution and through interpretation of temperature, may help constrain depth and timing within a burial profile, constraining basin history.

4.1.2: Great Estuarine Group

This chapter focuses on concretions hosted in the Valtos Sandstone Formation of the Middle Jurassic Great Estuarine Group (GEG; Fig. 4.1) which outcrops on the islands of Skye and other Inner Hebridean islands, in particular the Isle of Eigg (Fig. 4.2). The GEG Sediments are Bathonian in age, deposited in two half graben, the Sea of the Hebrides Basin and the Inner Hebrides Basin (Fig. 4.3). The GEG is preceded by the Bearreraig Sandstone Formation, shallow, open-marine sand wave deposits (Morton, 1976) and succeeded by the marine Staffin Bay Formation (Hudson, 1962; Riding and Thomas, 1997; see Fig. 4.1). Unlike the other Jurassic aged sediments of the Inner Hebrides, which are fully marine (for summary see Morton and Hudson, 1995), the GEG represents a paralic, mainly freshwater to brackish lagoonal sequence with no wholly marine fossils (Hudson, 1963; 1980) (Fig. 4.1).

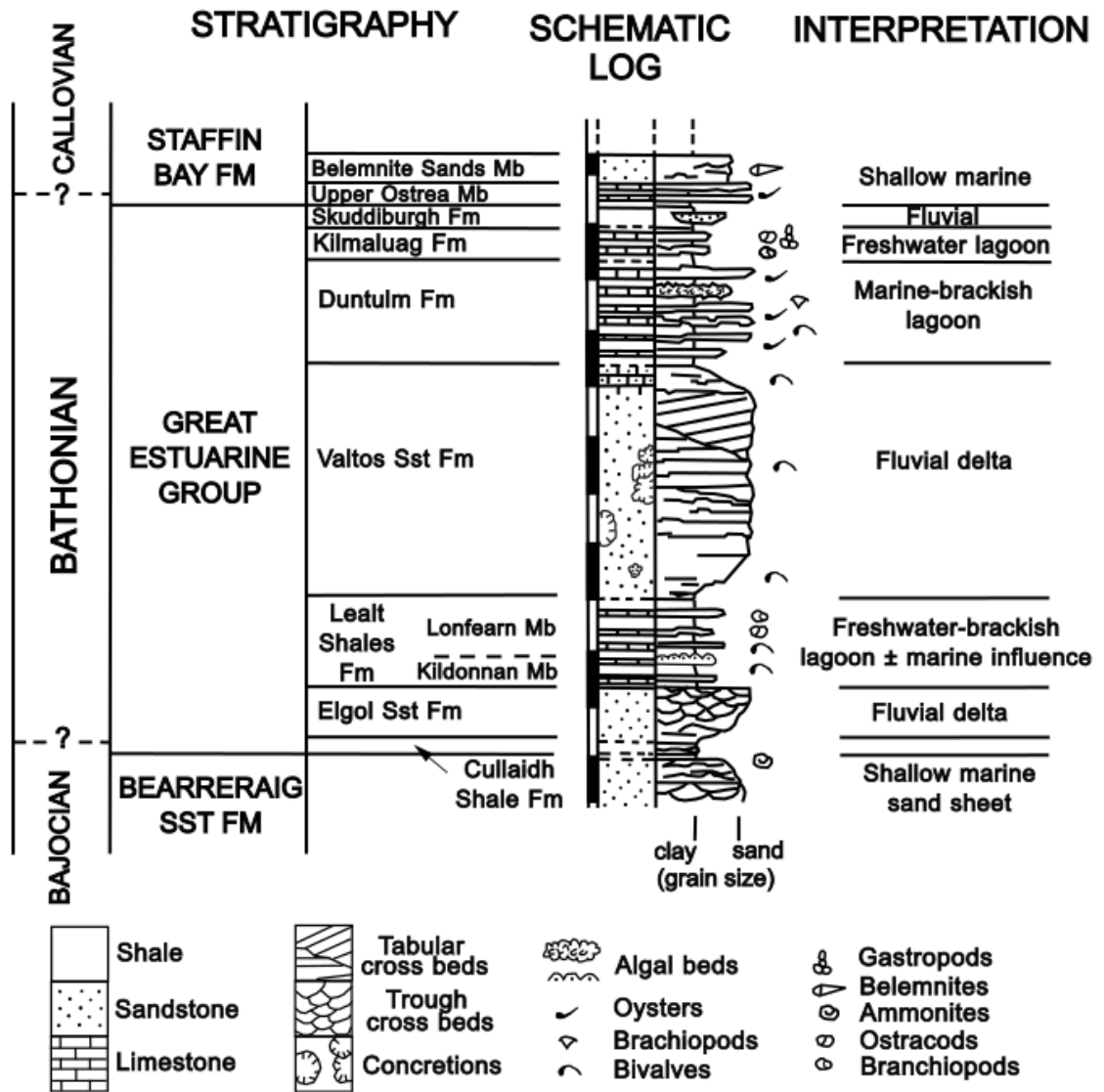


Figure 4.1. Stratigraphy of the Great Estuarine Group, with schematic log for Trotternish (Skye). Black and white scale bar divisions represent ~25 m (after Andrews, 1984).

Two formations within the GEG are dominated by sandstone; the older Elgol Sandstone Formation and younger Valtos Sandstone Formation, both of which are fluvial deltaic sediments.

The Elgol Sandstone is a Gilbertian deltaic coarsening upward sequence (Harris and Hudson, 1979; Harris, 1989). It is largely unfossiliferous (Harris and Hudson, 1980; Harris, 1989), and besides localised silicic cementation (Harris, 1989) caused by hydrothermal reactions relating to the Cullin igneous centre (Harris and Hudson, 1980) at Port na Cullaidh, Elgol, there is little cementation.

The Valtos Sandstone Formation (Fig. 4.4) is the thickest formation within the GEG and represents fluvial deltaic deposition as detailed by Harris (1992). The formation outcrops in Trotternish, Waternish and Strathaird on the Isle of Skye, and on the isles of

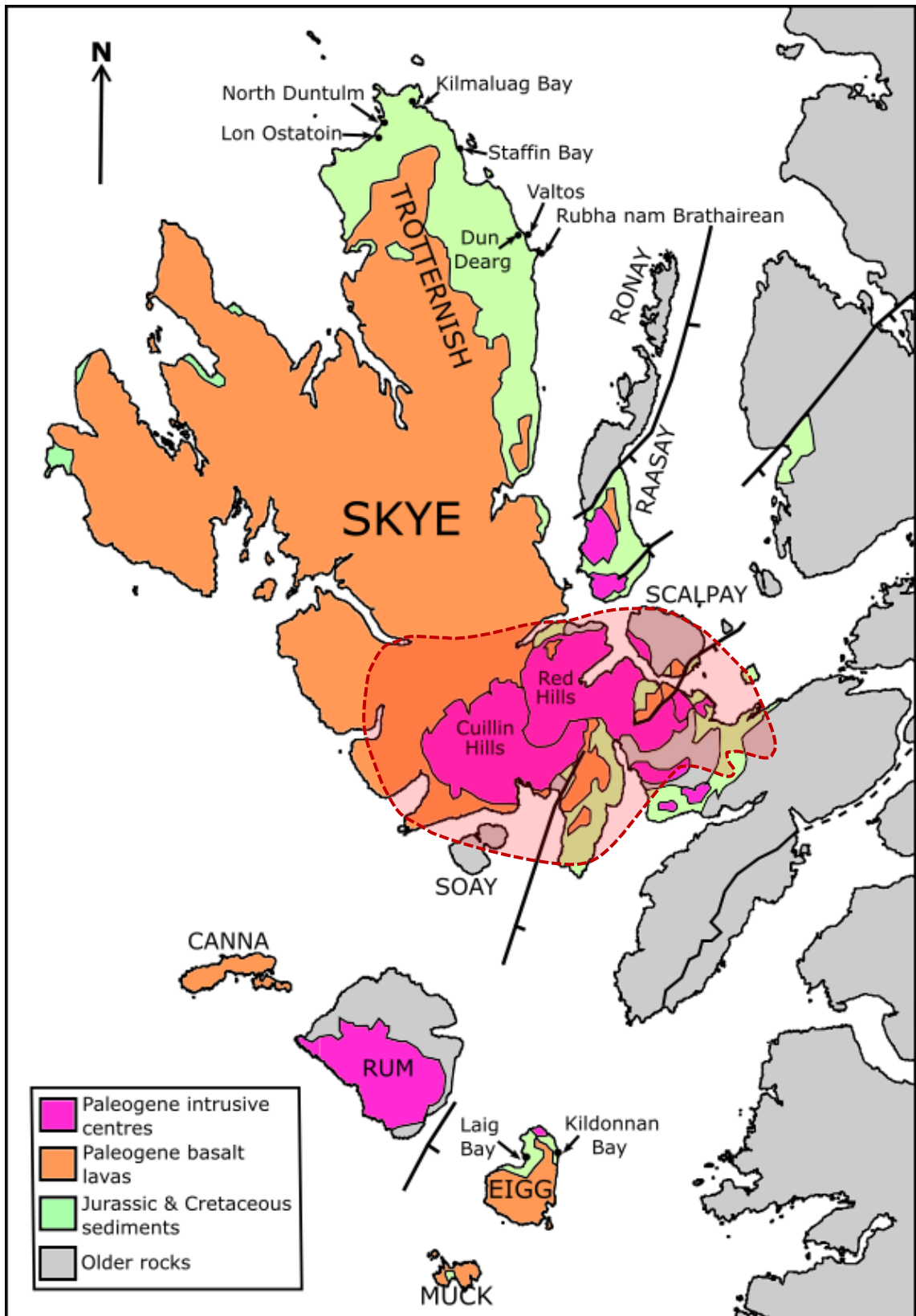


Figure 4.2: Map of Skye and the Small Isles, including Eigg, with sampling locations indicated by arrows. Red dashed zone shows extent of hydrothermal influence of the Skye Paleocene igneous centres, based on information from Forester and Taylor (1977). Map adapted from Thrasher (1992).

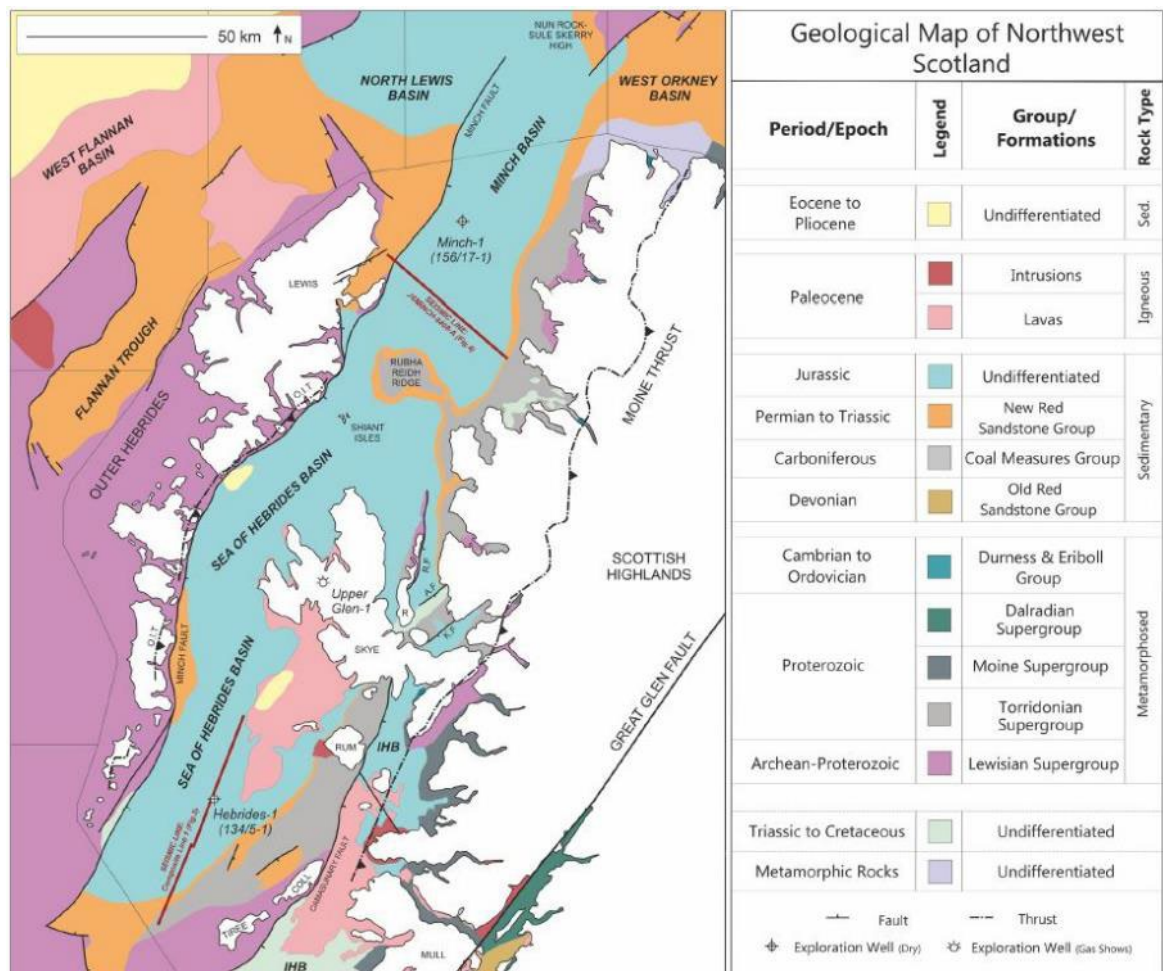


Figure 4.3: Map showing extent of the Sea of the Hebrides and Inner Hebrides basins after Fyfe et al. (2021). IHB = Inner Hebrides basin.

Raasay and Eigg, with some lateral variation between localities (Harris and Hudson, 1980). The lithologies are broadly medium/coarse grained concretionary sandstones, usually capped by *Neomiodon* biosparite limestones, with further *Neomiodon* limestones and silty shales interbedded with the sandstones (Harris and Hudson, 1980). *Neomiodon sp.*, the most common fossil found in the Formation, was a small freshwater burrowing bivalve (Hudson, 1963; 1980).

4.1.3: Valtos Sandstone Formation and its Concretions

The Valtos Sandstone is unlike the Elgol Sandstone as fossils are preserved within cemented concretions and limestone beds, although outside of these layers there is sparse cementation.

An overview of the diagenesis and cementation of the Valtos Sandstone, as understood in the mid-1980s, is given in Hudson and Andrews (1987). Sandstone beds

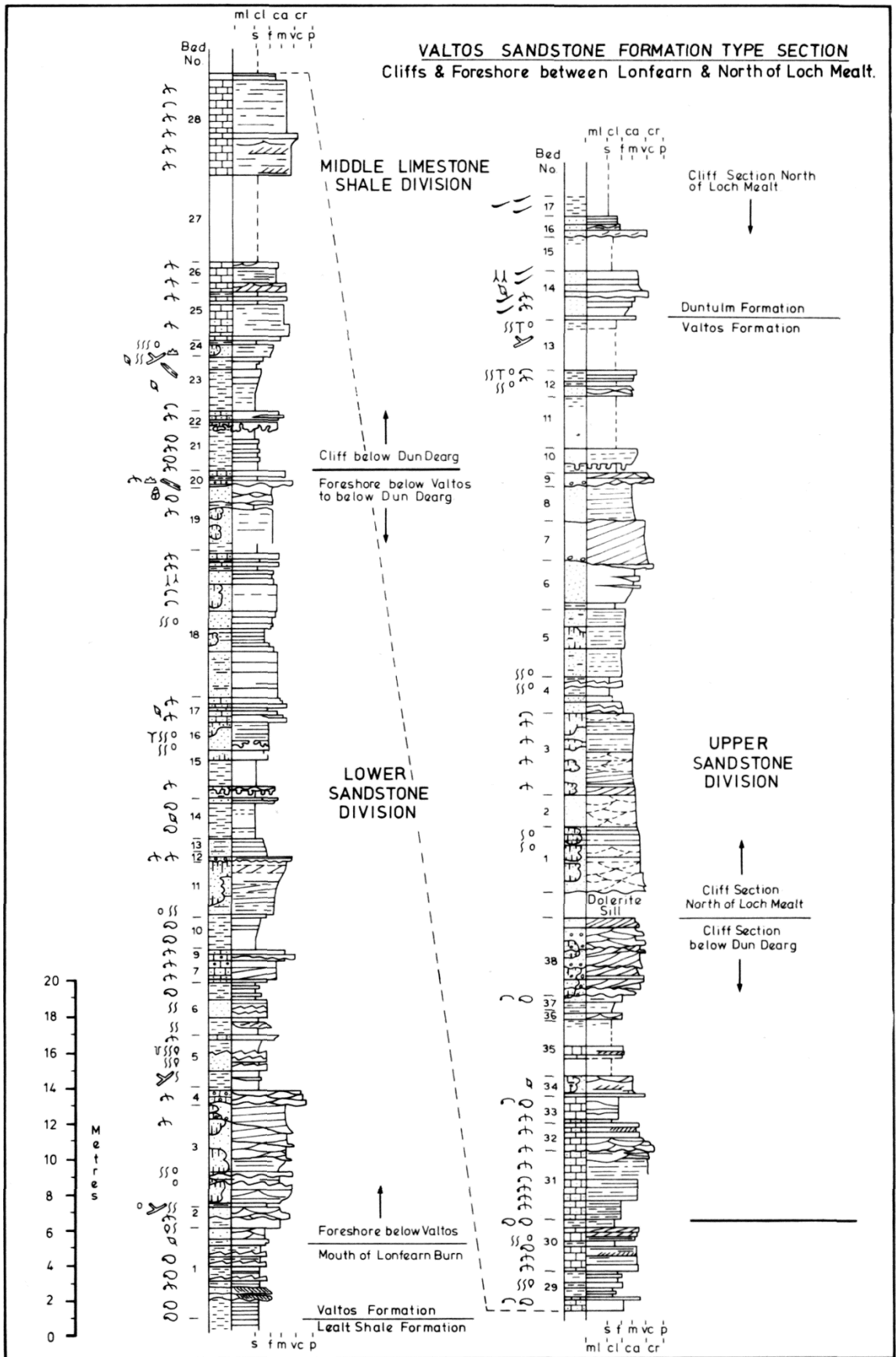


Figure 4.4: Graphic log of the Valtos Formation at Valtos (Trotternish) after Harris and Hudson (1980).

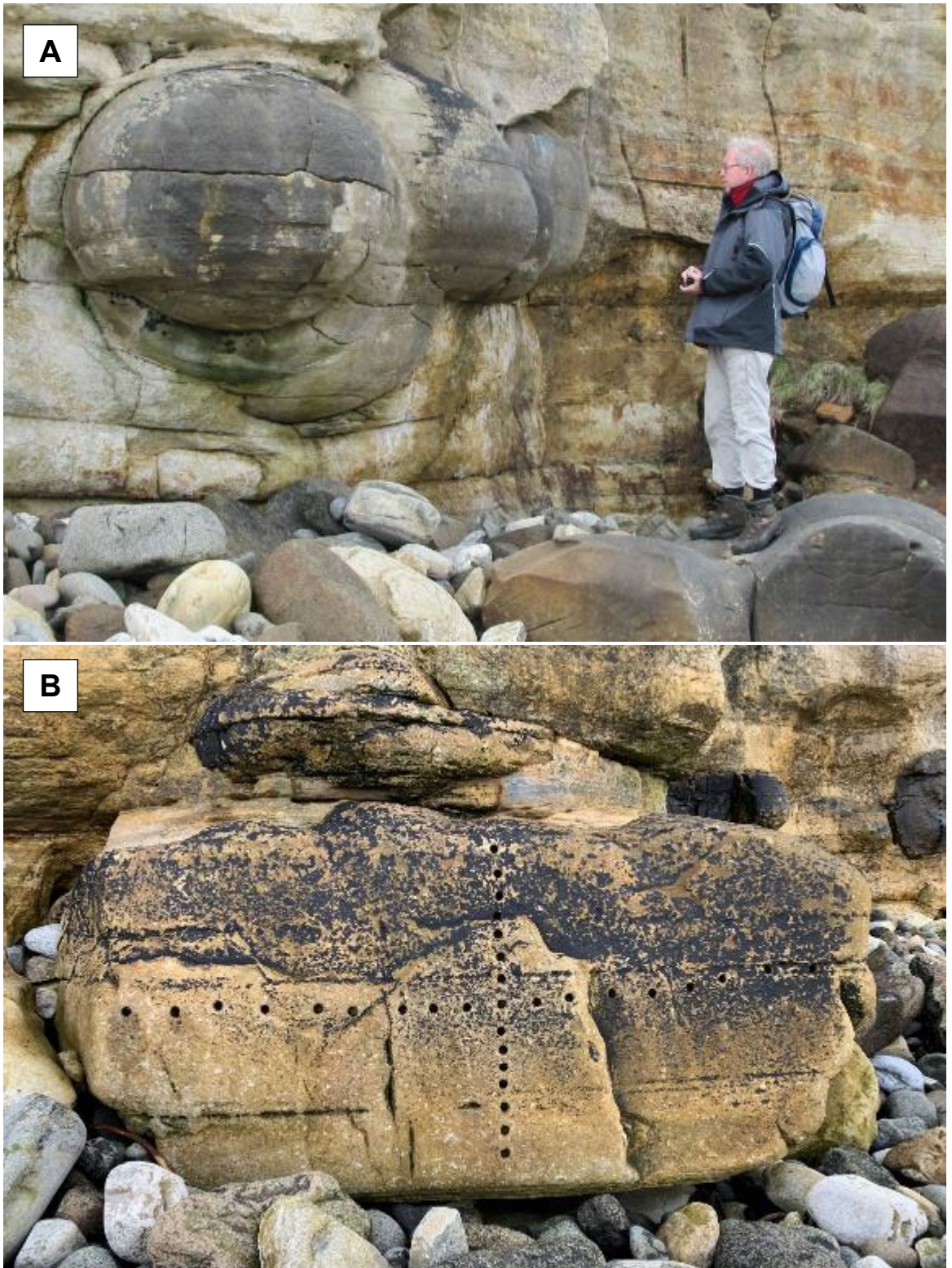


Figure 4.5: Concretions from the basal Valtos Formation, Valtos Trotternish. A) 'Spherical' concretion, bed 3; B) 'Tabular' concretion, basal part of bed 3. This concretion previously analysed in Wilkinson (1989) – vertical spacing of drill core holes is ~10 cm.

with thicknesses <1 m are almost always cemented fully. At the type section (Valtos, Trotternish; Harris and Hudson, 1980) within bed 3 there is a lower concretionary unit which contains tabular concretions bounded by bedding (Fig. 4.5). Above this, large spherical concretions first occur, many >1 m in diameter (Fig. 4.5) although the host sandstone is otherwise very poorly cemented. While *Neomiodon* shells, originally aragonitic, but preserved as neomorphic calcite, are found within the concretions, the surrounding uncemented sandstones are unfossiliferous (Hudson and Andrews, 1987), suggesting that total bioclast dissolution occurred.

On Eigg, there are three concretionary morphologies; i) large concretions (some >1 m in diameter) occurring in Division E (Hudson and Harris, 1979; Harris, 1992), which appear sub-spherical (elongated parallel to bedding) similar to those described at Valtos, Trotternish; ii) highly spherical concretions, radius averaging 12 cm (Wilkinson, 1992) which also occur in Division E (bed 2); iii) centimetre sized concretions that line the contacts of intrusive dykes (Fig. 4.6) (Hudson and Andrews, 1987). The coarser sands of Eigg have few shells and are sparsely concretionary (Hudson and Andrews, 1987).

At both Valtos and on Eigg there are also veins of calcite that post-date the concretions (Fig. 4.7), and the lower cemented *Neomiodon* limestones of Valtos (most likely bed 7 or bed 17; Harris and Hudson, 1980), Trotternish. Veins of cement are also common subparallel to dykes on Eigg (Fig. 4.8) and also post-date dykes (in one case filling a fracture within a dyke) at Valtos (Fig. 4.9).

4.1.4: Burial History:

The burial history of the GEG has been presented by Hudson and Andrews (1987) and Morton (1987) and an updated representation is summarised in Figure 4.10. It is thought that the Jurassic sediments underwent <500 m burial prior to uplift which occurred before the Late Cretaceous (Hudson, 1983; Morton, 1987). There is no evidence for significant sedimentation in the Upper Cretaceous; preserved outcrops do not exceed ~25 m (Hudson, 1983).

In the Paleocene, regional igneous activity buried the Mesozoic sediments rapidly (within 1.6 Ma; Hamilton et al., 1998) under a lava pile of up to 1200 m thickness (England, 1994; Emeleus and Bell, 2005). Emplacement of intrusive of sills and dykes also occurred during this igneous activity; significantly, the Little Minch Sill complex of

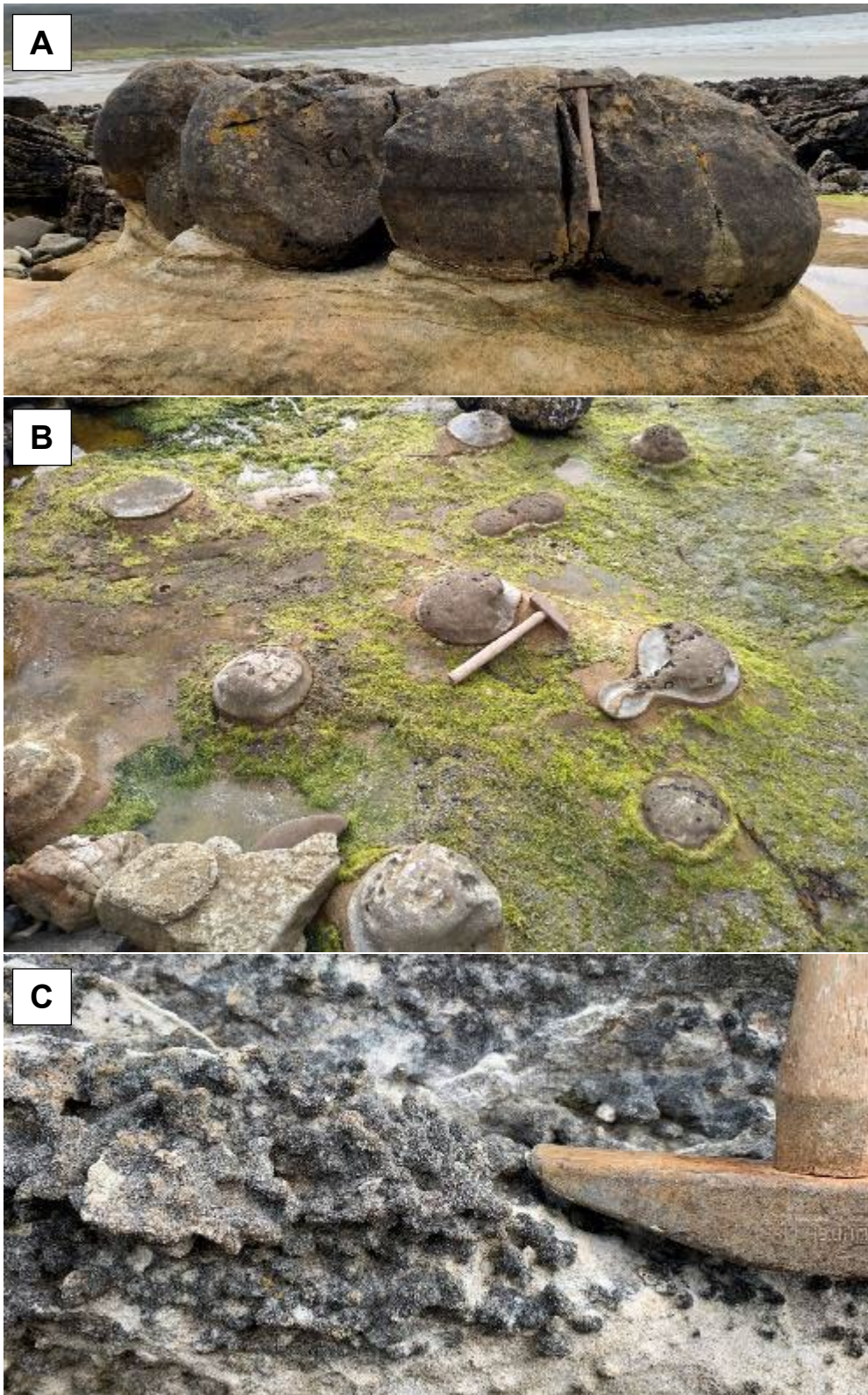


Figure 4.6: Concretions from upper part of the Valtos Formation (Division E) of Laig Bay, Eigg. Hammer handle is 35 cm long. A) large concretions in bed 2 similar to the spherical concretions seen at Valtos (Fig. 5a) B) 'decimetre-scale' concretions; C) concretions in cemented zone adjacent to Tertiary dyke.

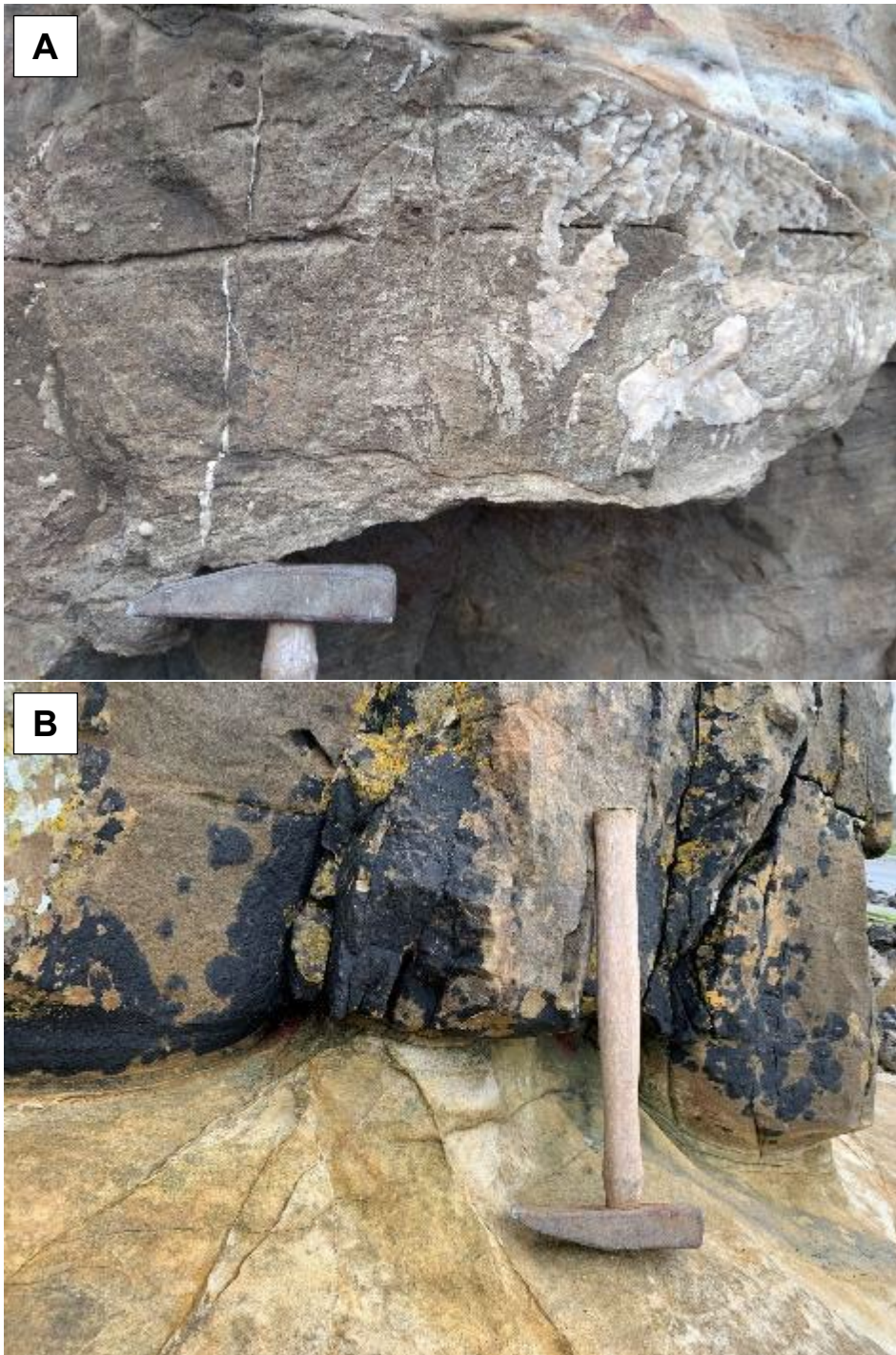


Figure 4.7: Calcite-cemented veins that cross cut (post-date) concretions at, A) bed 3 Valtos Cliffs, Trotternish, Skye; and B) bed 2 (Division E) Laig Bay, Eigg. Hammer handle is 35 cm long.

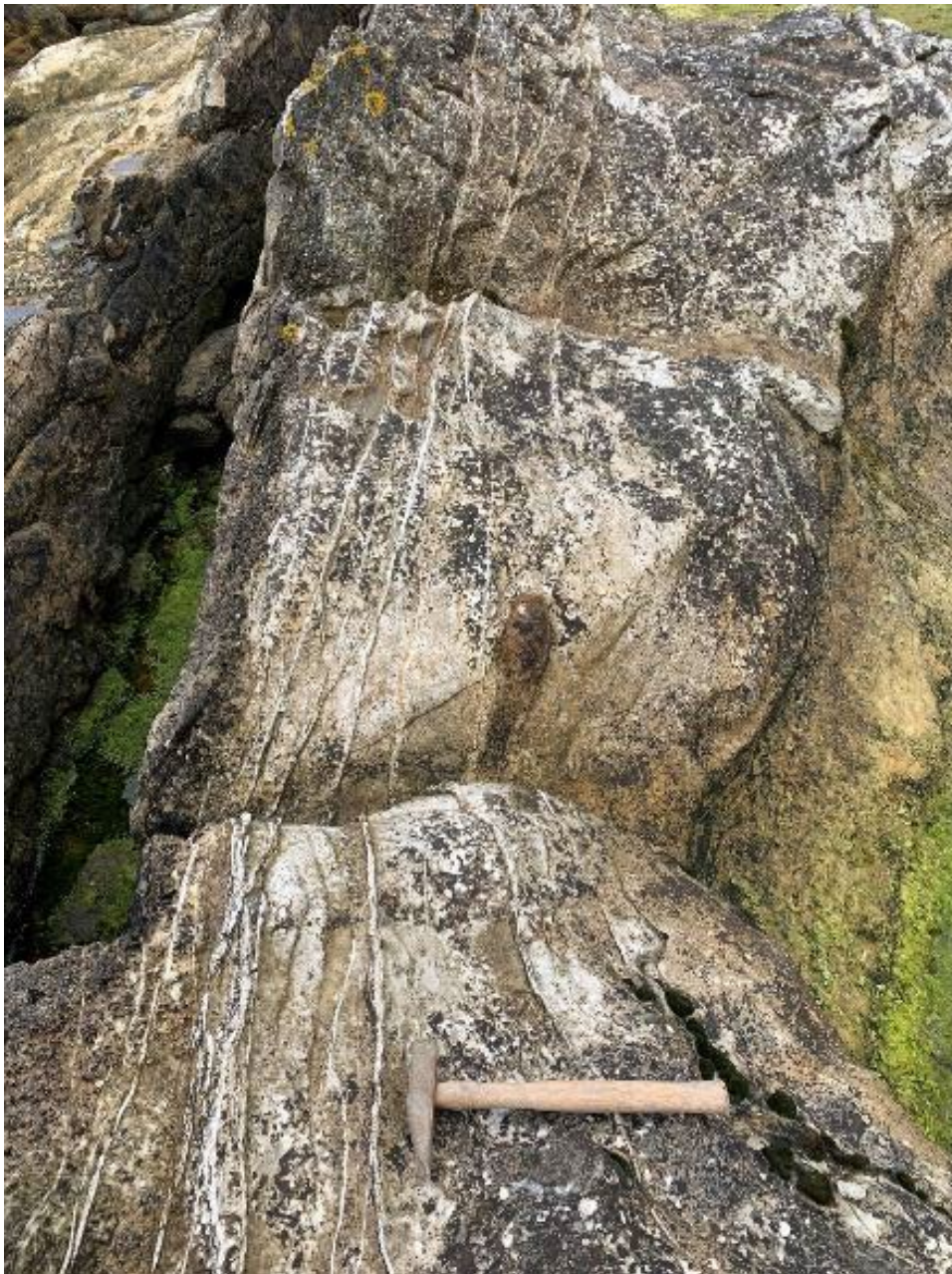


Figure 4.8: Prominent calcite-cemented veins in cemented sandstone adjacent to a dyke margin (dyke now eroded into trench feature (left)). The veins run parallel to the dyke. Laig Bay, Eigg. Hammer handle is 35 cm long.

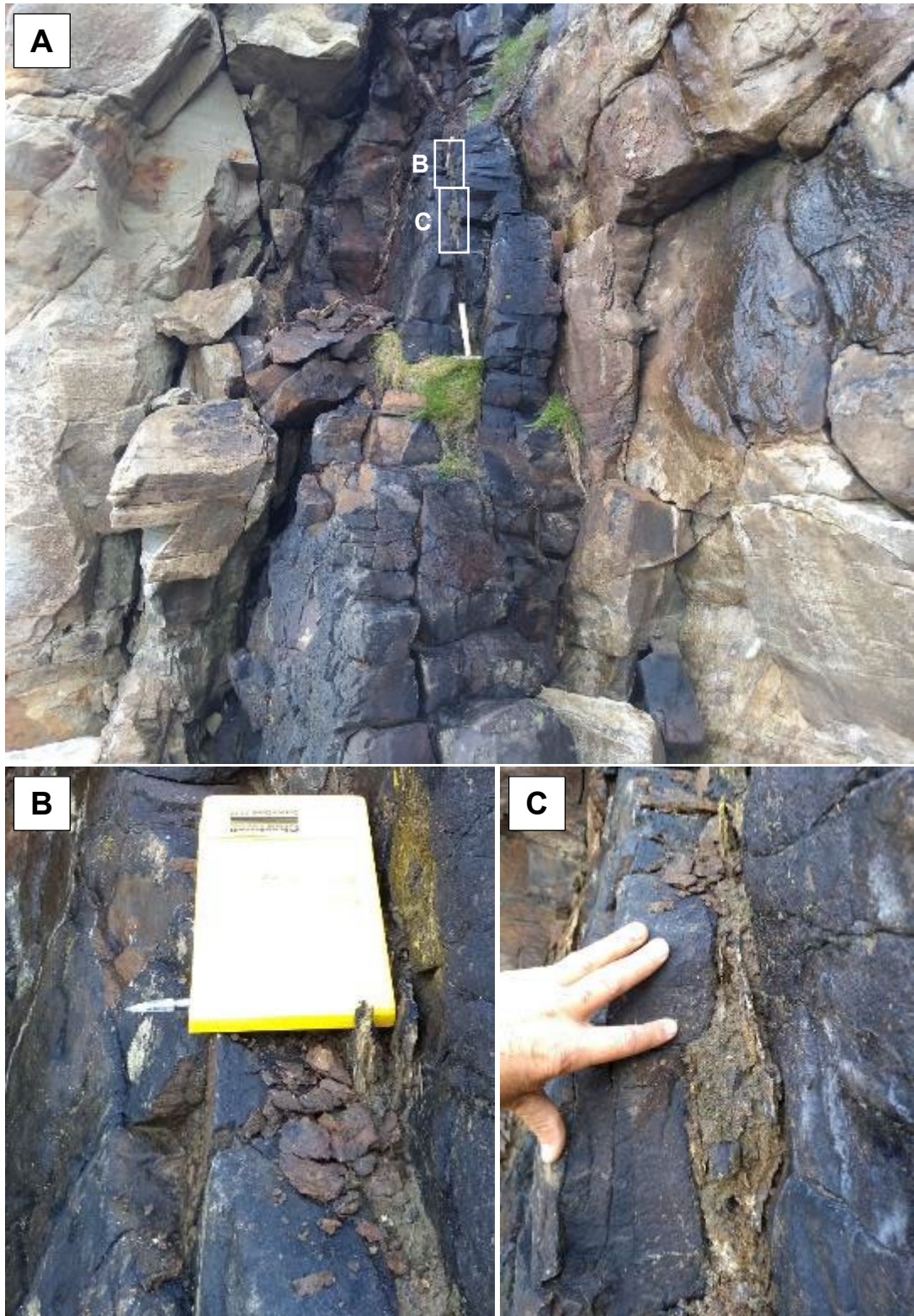


Figure 4.9: Calcite cemented vein within dyke at Valtos Cliffs, bed 2, Trotternish, Skye. Photo A showing positions of photos B & C. Hammer handle in A is 35 cm long. Notebook in B is 13 cm wide.

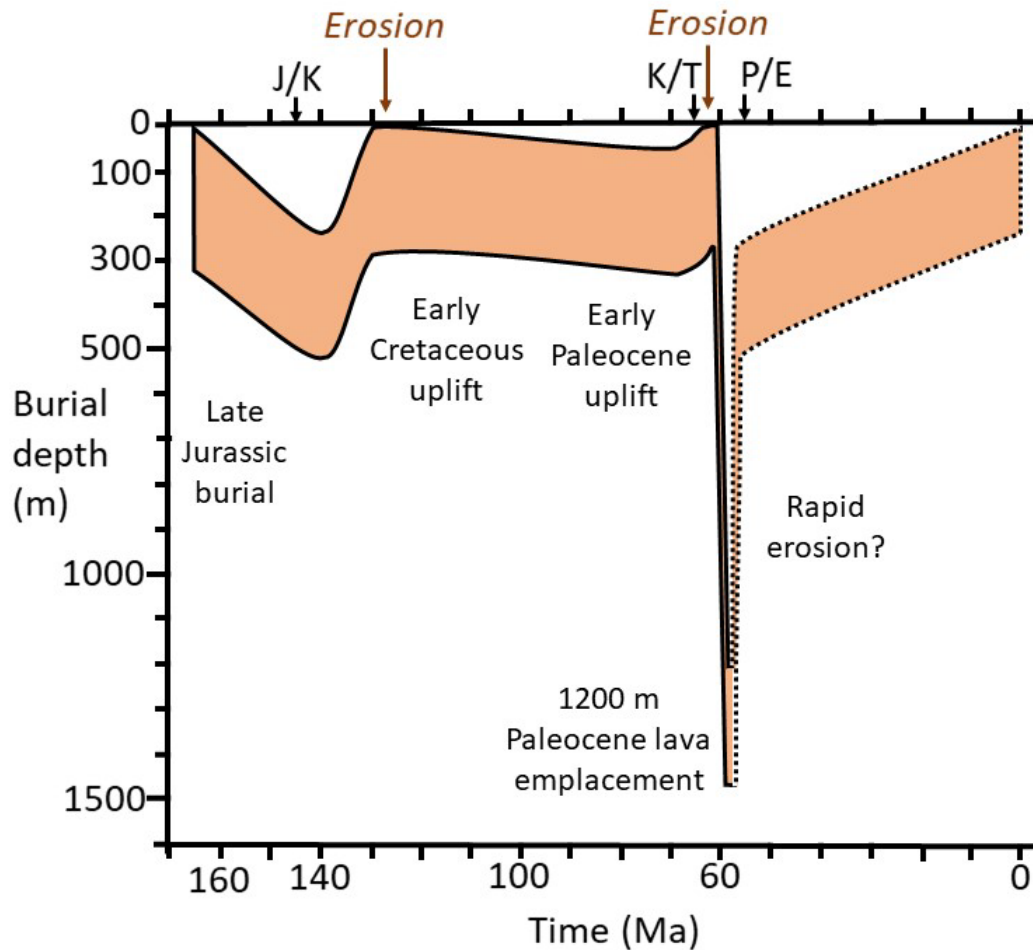


Figure 4.10: Simplified burial history of the Great Estuarine Group, updated from Hudson and Andrews (1987). The brown envelope shows the complete thickness of the GEG. The plot depicts a theoretical maximum burial as tectonic/erosional disturbances are not accounted for. The pecked lines indicate greater uncertainty post-60 Ma and are a compromise solution from varied data sources. The timing of two phases of land surface erosion is indicated but depth of erosion is not known. The Valtos Sandstone Formation is positioned in the centre of the GEG envelope.

Trotternish was emplaced some time after the lavas were deposited (Gibson, 1990; Emeleus and Bell, 2005), and dyke emplacement is thought to have occurred throughout the duration of the igneous event (England, 1994; Emeleus and Bell, 2005). However, the effects of both burial and thermal alteration on the GEG are minimal in many localities; aragonitic shells are still preserved in shales (Hudson and Andrews, 1987; Holmden and Hudson, 2003), and there is very good organic preservation within the Jurassic succession generally (e.g., Lefort et al., 2012). The thermal effects of the Skye Central Complex are limited to a zone about 6.5 km from the margin of the complex; this alteration zone is mostly due to hydrothermal effects (Taylor and Forester, 1971; Forester and Taylor, 1977) (Fig. 4.2). Outside this hydrothermally influenced zone organic matter in Jurassic rocks is

extremely immature (Thrasher, 1992). In such immature shales, the thermal influence of smaller igneous intrusions on organic maturity is a local effect that is proportional to intrusion width (Bishop and Abbott, 1995) and marked in the field by darker coloration and lack of shale fissility.

Apatite fission-track analysis (AFTA) samples from Skye are typically >85 °C; however, it is likely that they do not represent burial temperatures alone, but also regional thermal influence from the igneous activity (Holford et al., 2010).

4.1.5: Concretion Petrography

The petrography of the Valtos concretions was described by Hudson and Andrews (1989) and Wilkinson (1993) and is summarised here with additional observations made during this study. The large spherical concretions from Valtos are formed by one generation of ferroan calcite, with no inter crystal zoning (Wilkinson, 1993), growing concentrically from an (assumed) initial nucleus. At the centre of the concretion, crystals are equant, ~ 0.25 mm diameter, and increase in both size and elongation radially to >50 mm (Wilkinson, 1993), with a poikilotopic texture which is clearly visible in hand specimen. Wilkinson (1993) recognised the remains of feldspars preserved within the cemented concretions, which had undergone significant degradation into illite and minor kaolinite.

Hudson and Andrews (1987) reported that in addition to replacement of aragonite shells by calcite, pressure solution of these shells was common, with some shells being reduced to 'films' between quartz grains. Such shells are only preserved in concretions, showing that pressure solution took place prior to concretion growth (Hudson and Andrews, 1987).

Wilkinson (1989) estimated by point counting that, at present, ~30% porosity is preserved within the sandstone, reduced from an estimated original porosity of 45-50%. At Valtos, sediments around some concretions show clear deflection of lamination (e.g., Fig. 4.11; Hudson and Andrews, 1987; Wilkinson, 1993) although others do not. Using this compactional 'deflection' Wilkinson (1993) estimated that the host sandstone framework is $20 \pm 4\%$ more compacted than the concretions.

The petrography of the small decimetre-scale concretions from Eigg division E are also formed by a single generation of ferroan calcite cement, with poikilotopic texture common; no zoning was observable under cathodoluminescence (CL) (Wilkinson, 1992).

4.1.6: Models of formation

The concretions of both Eigg and Skye are thought to have formed through the redistribution of calcium carbonate from dissolution of originally aragonite *Neomiodon* shells (Wilkinson, 1992, 1993). This conclusion is supported by the preservation of shell debris within the concretion bodies but absence in the host sands at Valtos (Tan and Hudson, 1974; Hudson and Andrews, 1987) and the observation that the preservation of shell material decreases from centre to edge within concretions (Wilkinson, 1993). Wilkinson (1992) hypothesised that each small concretion from Eigg section E was nucleated around one *Neomiodon* shell.



Figure 4.11: Concretion in bed 3 at Valtos, Trotternish. Compaction of sedimentary laminae visible around the concretion is particularly clear on the LHS above concretion. Notebook is 20 cm long.

4.1.7: Stable isotopes

The concretions of the Valtos sandstone have been investigated by stable isotope geochemistry for almost 50 years, starting in the 1970s when Tan and Hudson (1974) measured single values from 27 individual concretions collected on Skye and Eigg (Table 4.1).

Locality	No. of samples	$\delta^{13}\text{C}$ (‰; PDB)			$\delta^{18}\text{O}$ (‰; PDB)		
		Mean	Min	Max	Mean	Min	Max
Eigg	8	2.38	1.1	3.2	-7.53	-10.2	-5.3
Trotternish	18	0.86	-0.8	3	-10.7	-13.7	-6.2
Waternish	1	2.25			-8.5		

Table 4.1: Stable isotope data from concretions from the Valtos Sandstone Formation from Tan and Hudson (1974) showing average, minimum and maximum values.

Although Tan and Hudson (1974) reported a wide range of values, particularly from Trotternish, it appears that for both $\delta^{13}\text{C}$ and $\delta^{18}\text{O}$ the Trotternish concretions were on average more negative compared to those from Eigg.

This early work was followed by more detailed studies of Jurassic concretions in the Valtos Sandstone at Laig Bay, Eigg (Wilkinson, 1992) and at Valtos, Trotternish (Wilkinson, 1993), and also concretions in the older Bearreraig Sandstone (Wilkinson, 1991).

Transects were taken through several small concretions from bed 2 of Division E, Eigg (Wilkinson, 1992). Oxygen isotope compositions (excluding two outliers) were between -11.1‰ to -9.4‰ (mean -10.1‰), with a range in $\delta^{13}\text{C}$ from \sim -6.2‰ to -3.7‰ (mean -5.2‰; Fig. 4.12). Wilkinson (1989) also measured a transect of one large (metre scale) concretion from Division E, Eigg (Fig. 4.12). The results were different from the smaller concretions, with a centre to edge trend that had three distinct zones. In particular, carbon isotopes were almost all between +3.3‰ and +2.3‰ except measurements from the third zone, towards the outer edge of the concretion, which reached -5.22‰. For $\delta^{18}\text{O}$ there is a transition from \sim -7‰ in the core of the concretion (P1) towards more negative values, around \sim -9‰ to -10‰ (P2), then maintaining this -10‰ in zone 3 (P3). Wilkinson hypothesised that this was due to burial and temperature changes, with P1 at a constant temperature due to aquifer flow, despite progressive burial; aquifer flow ceased in P2, allowing temperature to increase as burial continued; and finally, formation of P3 after reaching a constant burial depth.

For Valtos concretions at Trotternish, transects of 5 concretions were analysed, 2 spherical concretions (Wilkinson 1989, 1993) and 3 tabular from the basal concretionary bed (Wilkinson, 1989; see Fig. 4.13). Similar to the largest concretion from Eigg, these concretions showed large variation in isotope values within one concretion, particularly for oxygen isotopes: $\delta^{18}\text{O}$ values ranging from -18.2‰ to -6.0‰ were reported (Wilkinson, 1989). $\delta^{13}\text{C}$ values varied less, ranging from -3.5‰ to +1.6‰.

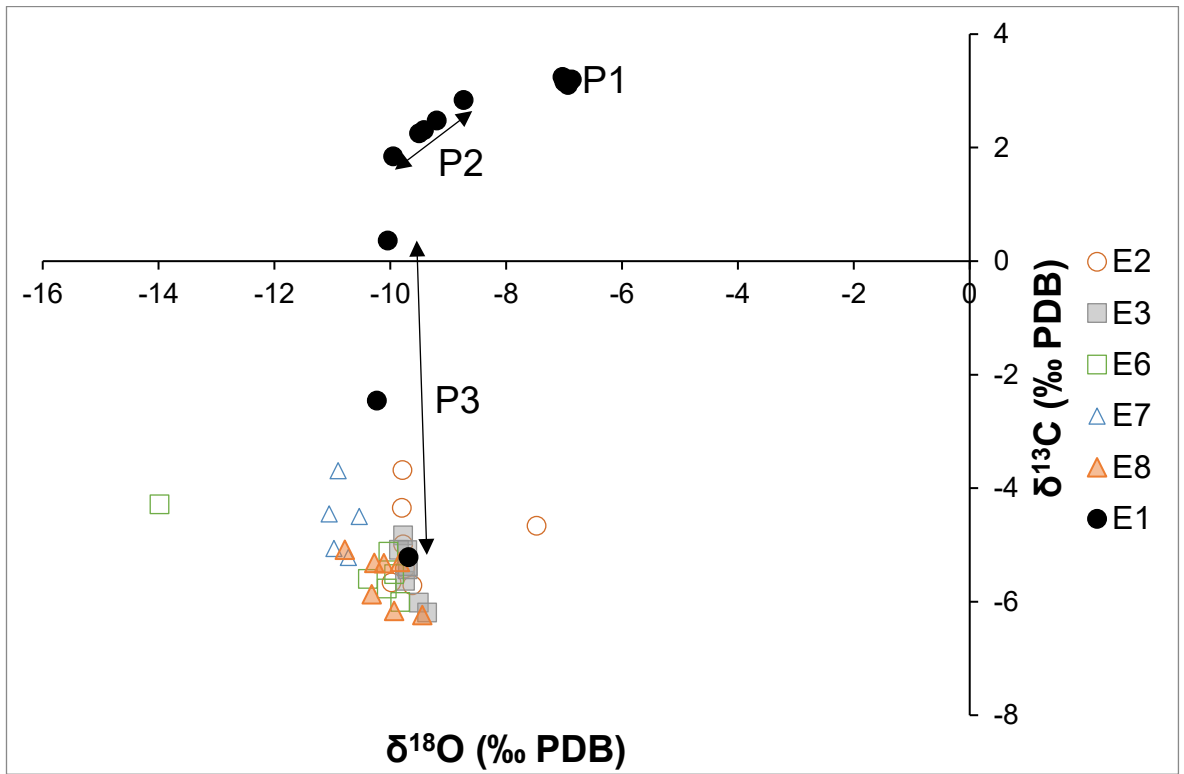


Figure 4.12: Comparison of $\delta^{18}\text{O}$ and $\delta^{13}\text{C}$ results for decimetre-scale (E2 to 8) and large (E1) concretions from Eigg measured by Wilkinson (1989, 1992). P1 to 3 indicate zones of the large Eigg concretion referred to in text (reported as P1-3 by Wilkinson, 1989).

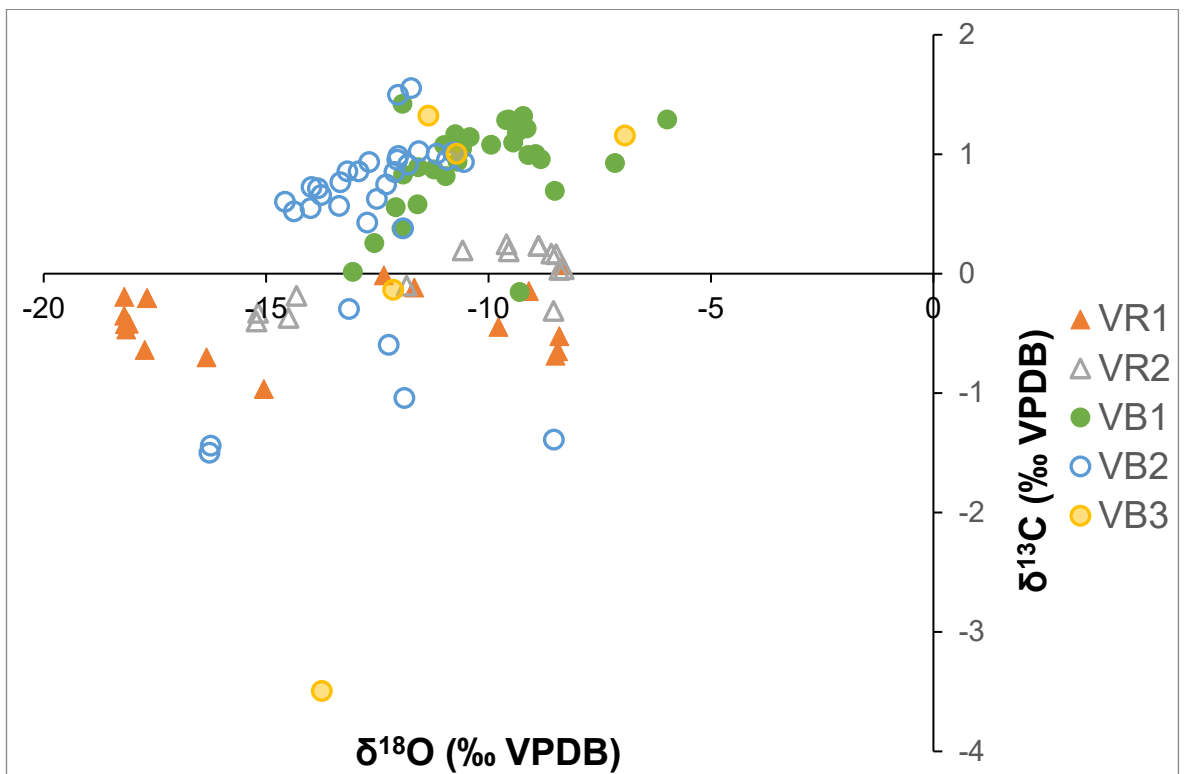


Figure 4.13: Comparison of $\delta^{18}\text{O}$ and $\delta^{13}\text{C}$ results for spherical (VR1 and 2) and basal (VB1 to 3) concretions from Valtos, Skye, measured by Wilkinson (1989, 1993).

4.1.8: Spherical concretions from Valtos:

Focusing on the spherical concretions from Valtos, Trotternish, two concretions were analysed by Wilkinson (1993). Of particular interest was a near spherical concretion of assumed concentric growth which had been bisected, more or less in half, by modern weathering/coastal erosion, providing two centre-to-edge transects, oriented vertically and horizontally from the centre. $\delta^{13}\text{C}$ in this concretion (VR1) did not vary by more than 1.0‰ but was concentrically zoned with respect to $\delta^{18}\text{O}$ (see Fig. 4.14):

1. Zone 1 (Z1): The centre to ~26 cm radius had strongly negative values (-18.2‰ to -17.7‰ PDB);
 - a. At the edge of Zone 1, sampled on each transect at ~30 cm, there is a transition zone which had values between -16.3‰ and -15.0‰;
2. Zone 2 (Z2): There were less negative values (-9.8‰ to -8.3‰ PDB) from ~40 cm to 53 cm (vertical transect) or 58 cm (horizontal transect);
3. Zone 3 (Z3): The outermost edge, sampled at 60 cm (vertical transect) and 66 cm (horizontal transect), showed $\delta^{18}\text{O}$ once again becoming more negative (-12.4‰ and -11.7‰ PDB respectively) (Wilkinson 1993).

Wilkinson (1993) hypothesised that these changes in $\delta^{18}\text{O}$ were caused by changing porewater isotopic compositions rather than temperature effects. However, the most negative values, found at the centre of the concretion, were difficult to interpret and not satisfactorily explained.

The clumped isotope paleothermometer, by providing an independent temperature estimate, allows derivation of the $\delta^{18}\text{O}_{\text{FLUID}}$ values of the precipitating pore fluids, thus removing ambiguity. This new information enables us to interpret the pore fluid and temperature evolution captured in the concentric cementation of sandstone hosted concretions. This in turn allows better understanding of the cementation and diagenesis of the Valtos Sandstone Formation, and carbonate concretion precipitation as a whole.

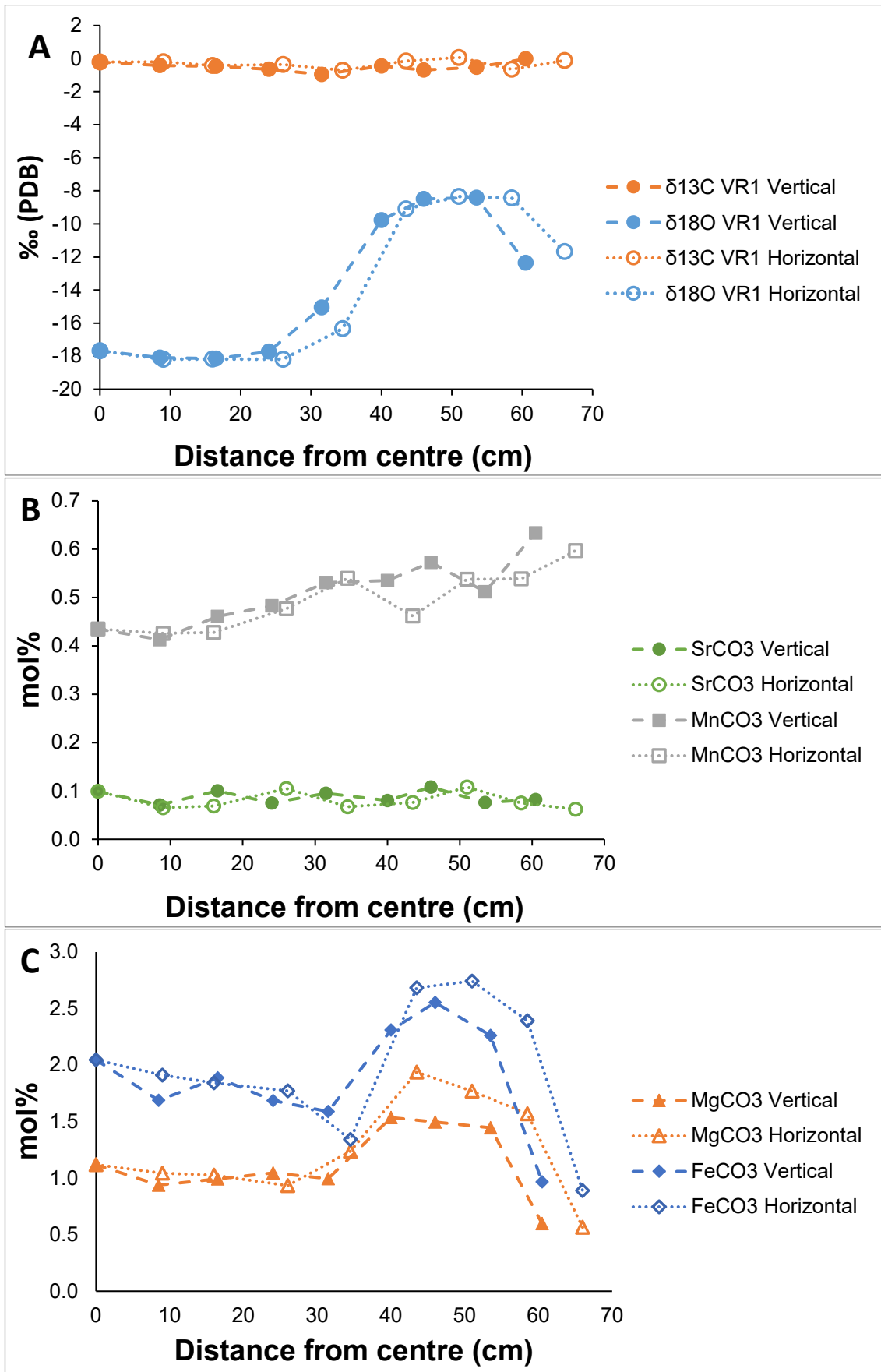


Figure 4.14: Data for concretion VR1 from Wilkinson (1989, 1992), indicating vertical and horizontal transects; A) $\delta^{13}\text{C}$ and $\delta^{18}\text{O}$ (‰, PDB); B) SrCO_3 and MnCO_3 (mol%); C) MgCO_3 and FeCO_3 (mol%).

4.2: Methods:

4.2.1: Samples:

The main focus of this chapter is one large spherical concretion from Skye, VR1, although data from other cements from both Skye and Eigg are included. Full location details and sample notes are included in Appendix 2: Part V.

4.2.1.1: *Main Valtos Sandstone Concretion:*

Concretion VR1 (Fig. 4.15) is from bed 3 of the Valtos Sandstone Formation (Fig. 4.4; Harris and Hudson, 1980); a wave deposited sandstone (described as Facies 4 in Table 2 of Harris, 1992). The concretion is close to spherical, with a slight horizontal elongation (Wilkinson, 1992). This concretion is no longer *in situ* but was originally sampled by Mark Wilkinson at the Valtos Cliffs, Trotternish, Skye (approximate grid reference: NG 516 642) (Fig. 4.2).

4.2.1.2: *Additional samples from Valtos, Skye:*

Several vein samples were collected at Valtos Cliffs (Trotternish, Skye). One vein was collected from the base of a large concretion (189-1; Fig. 4.7a); one from a large loose block of *Neomiodon* limestone (18-4; Fig. 4.16); and three which were associated with a dyke which bisected the sandstone (189-5v, 189-6, 189-7a; Fig. 4.9 and Fig. 4.17).

A *Neomiodon* limestone with shelter porosity-filling spar (within articulated shells) was also collected from a small loose block (189-8 spar and bulk; Fig. 4.16).

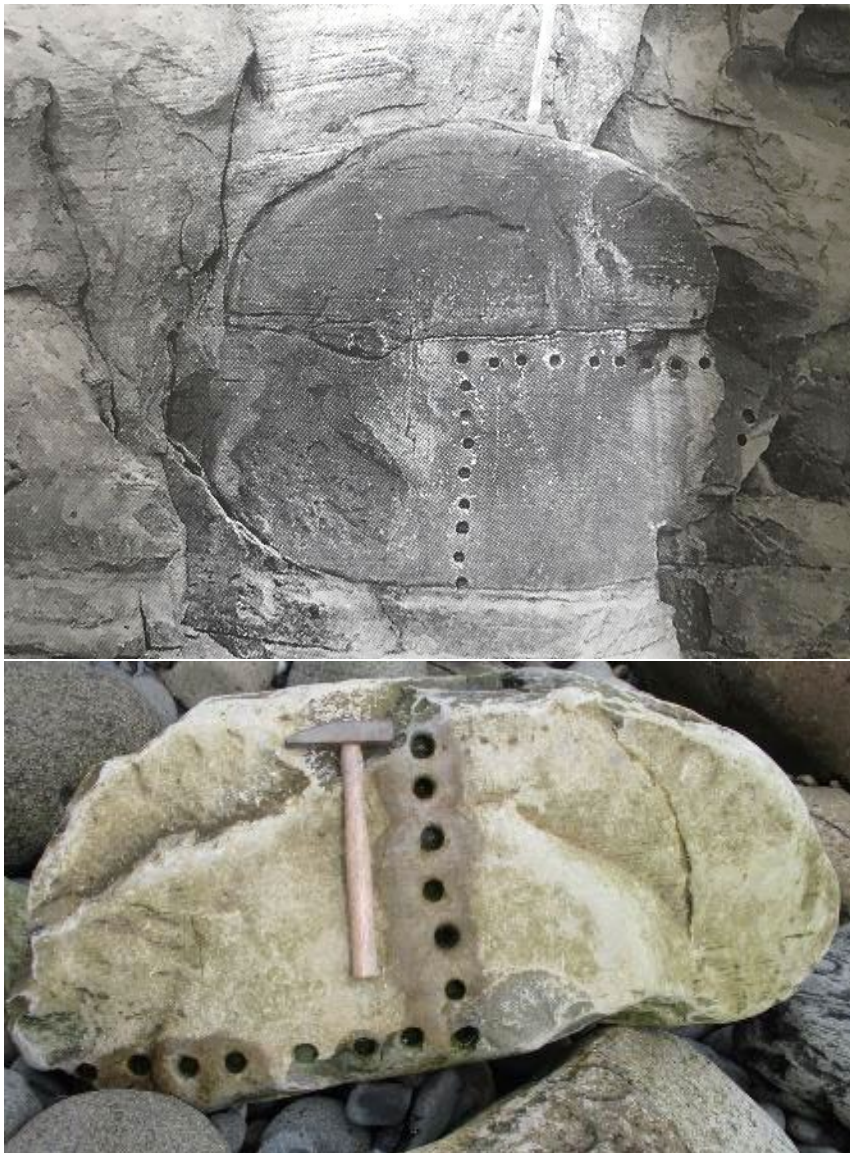


Figure 4.15: Concretion VR1, bed 3, Valtos, Trotternish. A) *In situ* as illustrated by Wilkinson (1993) and B) *ex situ* as seen on the foreshore in 2018 (inverted relative to A). Hammer handle is 35 cm long.



Figure 4.16: *Neomiodon* limestone blocks, ex situ at Valtos Cliffs, Skye. A) Sample 189-8 in the field; B) Sample 18-4 in the field; C) Sample 189-8 with spar fills visible; D) 18-4 vein sample. Notebook in A is 20 cm long.

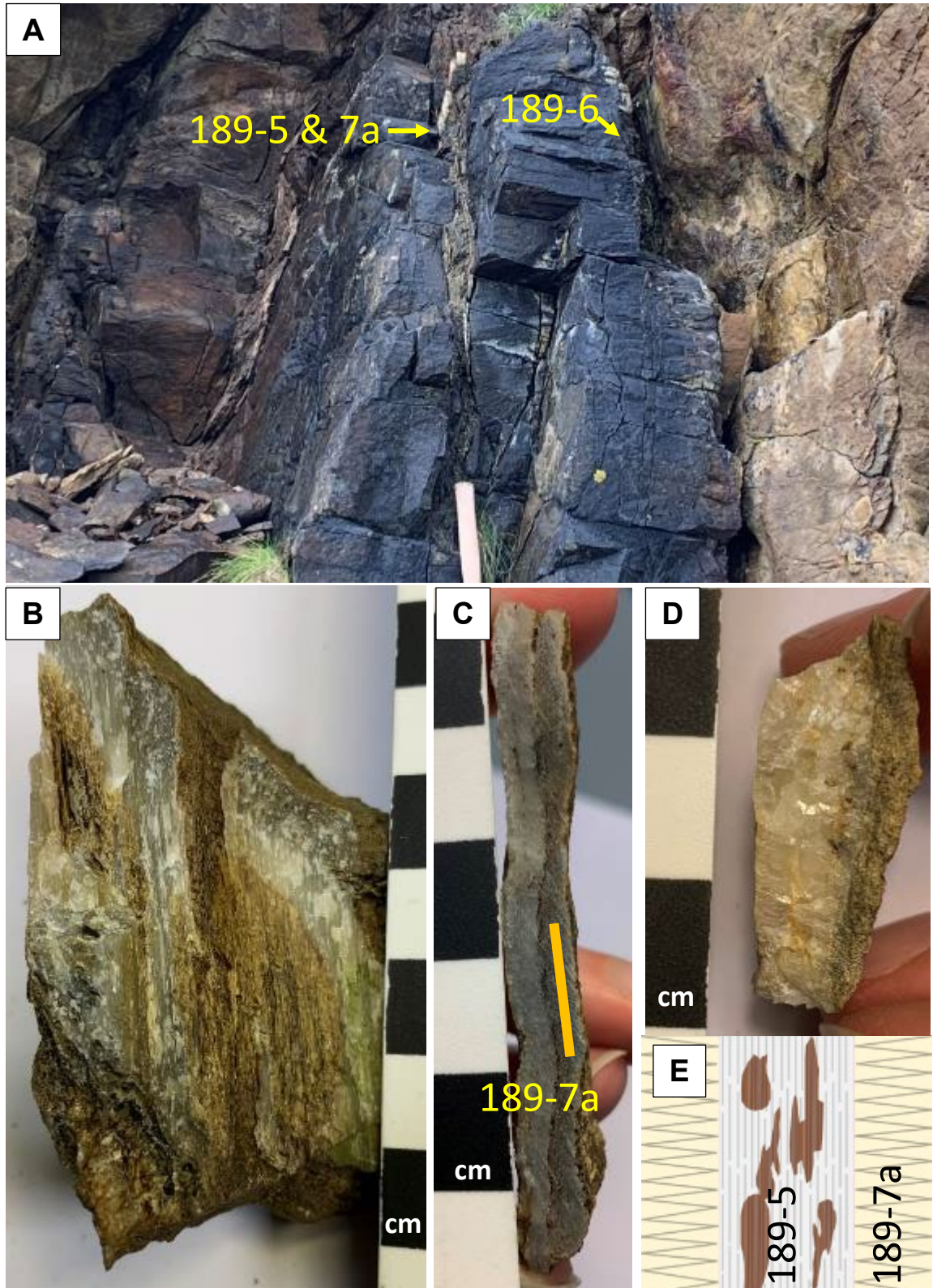


Figure 4.17: Veins associated with a dyke intruding the Valtos Sandstone at Valtos Cliffs, Skye. A) Locations of samples in reference to the dyke; B) Sample 189-5, showing needle-like calcite crystals and association with a brown smectite mineral; C) Sample 189-7a including location of vein subsection; D) Sample 198-6; E) Schematic of the relationship between vein 189-5 and 189-7a.

4.2.1.3: Other Valtos Sandstone Formation Concretions:

Dun Dearg, Skye:

A concretion (EG191015-1) from bed 38 (Harris and Hudson, 1980) was sampled from the Valtos Sandstone at Dun Dearg, Trotternish, Skye, which is stratigraphically above the Valtos cliff section (Fig. 4.18).

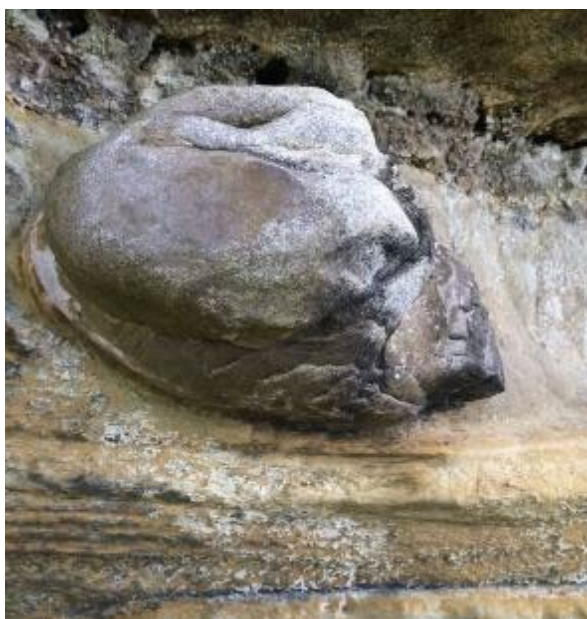


Figure 4.18: Sample EG 191015-1, concretion from Dun Dearg, Skye. Field photo courtesy of J. E. Andrews.

Laig Bay, Eigg

One metre scale, sub-spherical concretion from bed 2 of Division E (Harris, 1992) of the Valtos Sandstone at Laig Bay, Eigg was subsampled from near the centre (169-9), edge (169-10), and at an intermediate point (169-11), all at ~30-35 cm from the top of the concretion. See Figure 4.19 for the horizontal sampling scheme.

Sections of three decimetre-scale concretions were taken from the concretion bed described in detail by Wilkinson (1992). All concretions were highly wave eroded, and the vertical profile of these concretions is not known. Sample 169-6 was from a concretion with a 16 cm radius and was sampled 8 cm from the centre (Fig. 4.20). Sample 169-7 was from close to one nucleus of a concretion that had once had two nuclei (Fig. 4.20). Sample 169-8 was from a concretion that appeared sub-spherical with an 8 cm 'radius'; it was subsampled once at ~2 cm from the apparent 'centre' and once at the edge of the

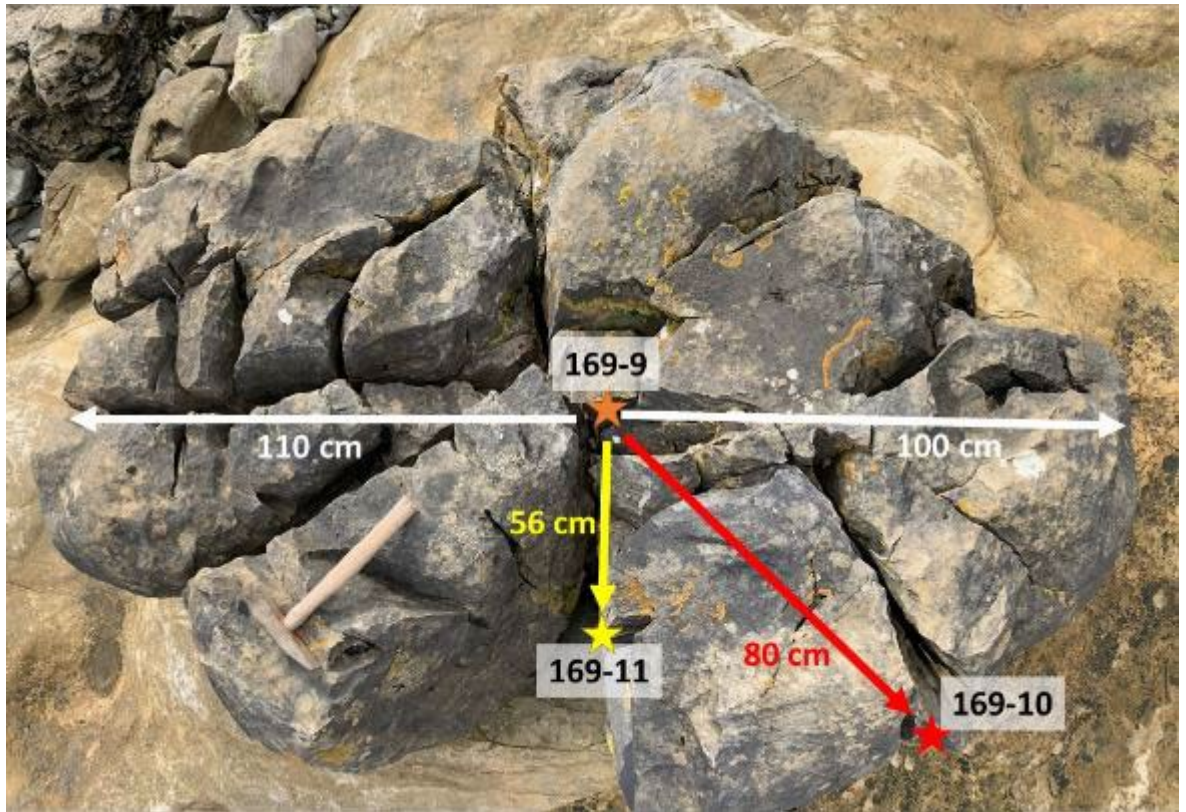


Figure 4.19: Sampling schematic of ‘large’ concretion from bed 2, Division E, Laig Bay, Eigg. Hammer handle is 35 cm long.

concretion; however, this concretion may have not been zoned concentrically due to its sub spherical nature (Fig. 4.20).

A concretion nodule from the margin of a Paleocene dyke was also sampled (Fig. 4.21). Cementation decreases from the margins of the dykes and most of the beds of Division E are very poorly cemented, although cemented veins that run parallel to dykes can be observed (Fig. 4.8) – measurement was attempted on one such vein, but the gas volume produced was extremely low.

4.2.1.4: *Other cements from Skye and Eigg:*

Lealt Shale Formation – Kildonnann Member

Three samples were collected at Kildonnann Bay, Eigg from the Kildonnann Member of the Lealt Shale Formation. Two (JEA-159-3 and JEA-159-4) were sandstone cements from bed 4A (Hudson, 1966) – JEA-159-3 is from Hudson’s ‘Complex Bed’ (Hudson, 1966), while JEA-159-4 is from 30 cm above the base of the Complex Bed.

The sparry infill of a septarian fracture from a mudstone hosted concretion (bed 5F; Hudson, 1966) was also measured.

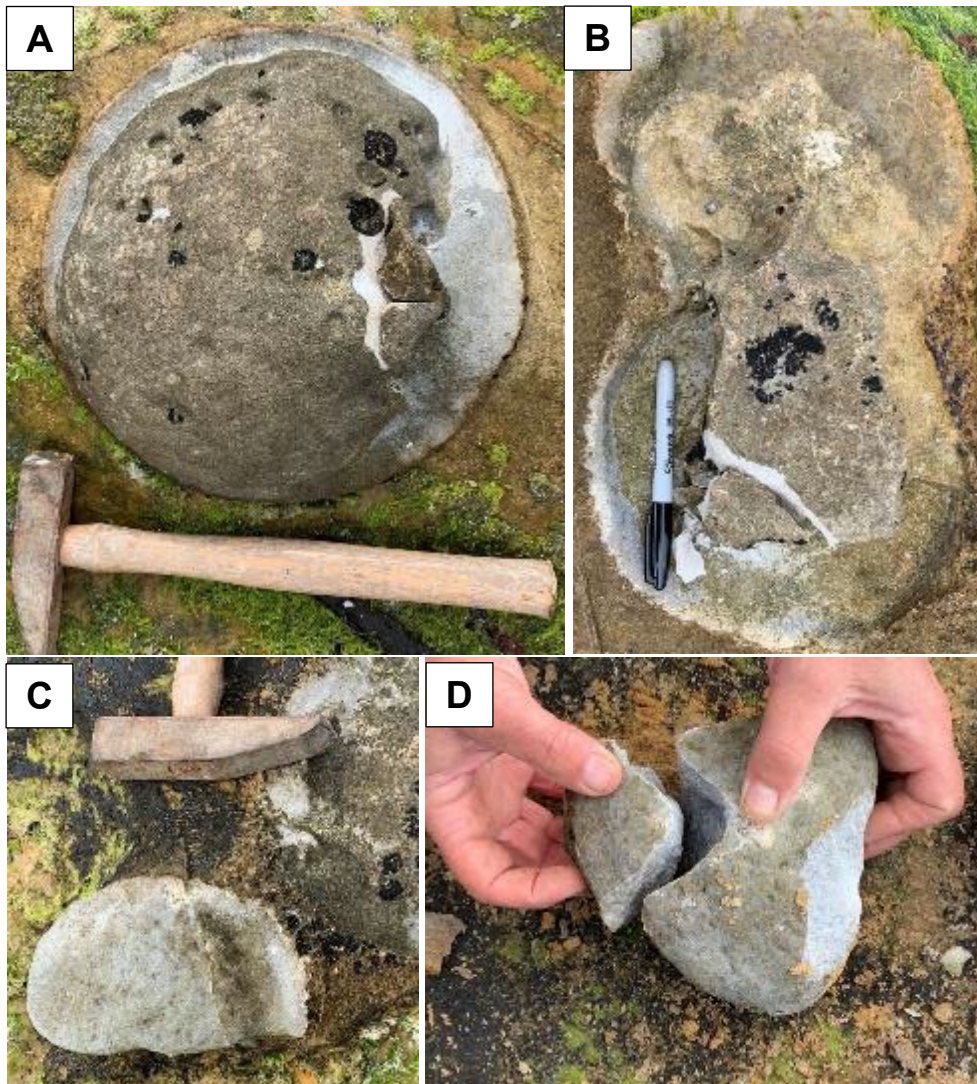


Figure 4.20: Field photos of decimetre-scale concretions from Laig Bay, Eigg. A) Sample 169-6; B) Sample 169-7; C) Sample 169-6 in situ; D) section of Sample 169-6 taken for hand specimen.



Figure 4.21: Cross section of sample 169-1r, a dyke margin concretion from Laig Bay, Eigg. Powder was milled from a well cemented section, seen here as the palest colour.

Lealt Shale Formation – Lonfearn Member

Two samples were taken from the Lonfearn Member at Rubha nam Brathairean (Brothers Point), Trotternish, Skye. A fibrous calcite vein (samples 18-9X) from bed 4 (Harris and Hudson, 1980) was subsampled at the base, centre and edge. The yellow sparry calcite septarian fracture fill of a mudstone hosted concretion (bed 3) was also sampled (sample 18-7y5c). The sample locality is close to a sill and is 0.5 to 1 m from mudstone that is friable and visibly baked.

Duntulm Formation

Two samples of sandstone cement were obtained from beds 5 (17-1) and 23 (17-2) of the Duntulm Formation (Andrews and Walton, 1990) at Lon Ostatoin, Trotternish, Skye. It should be noted that the succession here is overlain by a Paleocene igneous sill, though these beds are not close to the sill. Sparry vug infills of an oyster-rich (*Praeexogyra hebridica*) limestone bed (bed 19; Andrews and Walton, 1990) from Lon Ostatoin were also analysed.

At Kilmaluag Bay, two late-stage sparry calcite veins – that cross-cut a sill which here is in very close proximity – were sampled. Sample 199-1 was within an oyster bed (bed 3; Andrews and Walton, 1990) directly next to the sill (Fig. 4.22), while Sample 199-2 was within a cemented sandstone (bed 1; Andrews and Walton, 1990) 2 m from the sill (~1.5 m from the sill stratigraphically) (Fig. 4.22).

The sample TR-1609, sparry infills of a fractured algal limestone was sourced from bed 20 (Andrews and Walton, 1990) of the Duntulm Formation at North Duntulm, Trotternish, Skye by John Hudson.

4.2.1.5: *Eigg Lava Formation amygdales:*

Amygdales from one hand sample of the Eigg Lava Formation, kindly collected by Matt Wakefield from a loose block of basalt at the south-west side of Laig Bay were also analysed. Sample SA-1 was calcite taken from one large vug, while SA-2 was drilled from many small vugs.

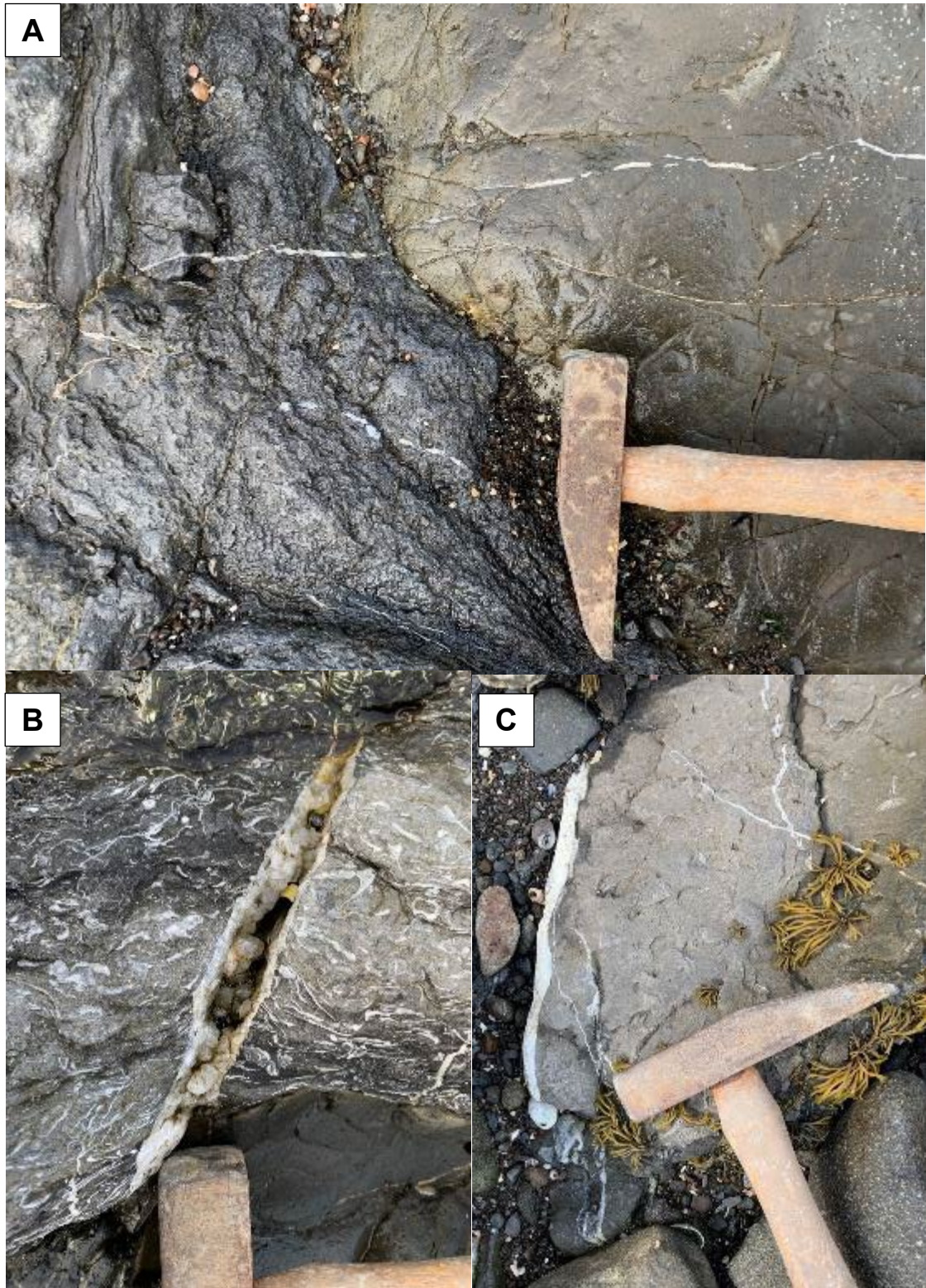


Figure 4.22: Images of veins from the Duntulm Formation at Kilmaluag Bay, Skye; A) veins crosscutting both sedimentary and igneous intrusive rocks; B) Sample 199-1 from bed 3 (an oyster bed); Sample 199-2 from a cemented sandstone (bed 1).

4.2.2: Sample preparation

4.2.2.1: *VR1 Concretion samples:*

Core plugs of concretion VR1, collected by Mark Wilkinson, were made available from the Leicester University archive collection; the complete vertical transect of concretion VR1 (Wilkinson, 1993), was measured. Sample powders were drilled from each core plug, taking care to avoid heating and pressure. The percentage of carbonate material was found to be ~40%, therefore >40 mg of sample powder was drilled from each sample. Within the results presented by Wilkinson (1993), the 5th sample in the transect (M8605) appears to give a $\delta^{18}\text{O}$ composition intermediate between the extremes in $\delta^{18}\text{O}_{\text{CARBONATE}}$; >100 mg was drilled for this sample to allow daily measurement (see below). Powder was drilled from fresh surfaces with no visible discolouration. Where weathered surfaces were unavoidable, a 'fresh' surface was uncovered by drilling a top layer away, which was discarded. Samples were homogenised by shaking to mix the sample powder within the vial.

For each measurement, 9.45-10.19 mg of sample were reacted, in order to achieve a gas volume proportionate to the yield of a pure carbonate sample of 4 mg. Refer to methods (Chapter 2.3) for the preparation system setup.

With the exception of sample M8605, samples were measured 3-4 times. Sample M8605 was measured once each day providing 10 values in order to establish a representative distribution of error.

4.2.2.2: *Other samples:*

Samples of sandstone cements, veins (including fibrous calcite veins), sparry vug fills within shelter porosity in articulated shells, lava amygdales and other concretions were also sampled for analysis (see Appendix 2: Part V for description and locality detail). Samples were all carefully milled using a fine drill bit to ensure sampling of the desired carbonate phase.

Some veins were subsampled parallel to their margins, relying on visual definition of zones (refer to Appendix 2: Part IV, where inner and outer measurements are indicated for such samples).

For impure sandstone-hosted calcite cements, approximate carbonate percentage was deduced and sample size scaled up as described for VR1 above, with the aim to match the gas yield of a 4 or 6 mg sample, depending on MIRA preparation method.

Some samples were analysed as 4 mg or 4 mg gas yield equivalent with a preparation method identical to VR1 (Chapter 2.3). Others were measured at 6 mg or equivalent. The change in gas volume used between the two methods is not thought to have affected the Δ_{47} values measured, although a size effect has been observed for samples <4 mg, relating to the Poropak step of the gas preparation line (Umbo, 2020) – see Chapter 2.2.

4.2.3: Clumped isotope measurement and data handling

Sample CO₂ was measured as described in Chapter 2.

4.2.4: Δ_{47} Temperature calculation

The temperature calibration is as described in Chapter 2. The calcite-water isotope fractionation factor calibration of Kim and O’Neil (1997) is used for all samples, as it is appropriate for abiotic carbonates (Equation 2.7).

The samples of VR1 were each repeated 3-10 times as described above. The measurement uncertainty for $\delta^{18}\text{O}_{\text{CARBONATE}}$, $\delta^{13}\text{C}$ and Δ_{47} of VR1 is reported as ± 1 standard error of the pooled standard deviation of all VR1 measurements. Pooled standard deviation was used as the sample composition is comparable for all 10 core plugs.

Uncertainty for the $\delta^{18}\text{O}_{\text{CARBONATE}}$, $\delta^{13}\text{C}$ and Δ_{47} of sandstone concretion EG191015-1 is also calculated as ± 1 standard error of the pooled standard deviation of all VR1 measurements, as the concretion was effectively from the same locality (bed 38 at Dun Dearg, above the Valtos Cliffs) and the same material.

Uncertainties for $\delta^{18}\text{O}_{\text{CARBONATE}}$, $\delta^{13}\text{C}$ and Δ_{47} for the majority of the other samples were also calculated by grouping samples with similar materials and calculating the ± 1 standard error of the pooled standard deviation of each group. The groupings were as follows:

- The 3 sub-samples of the large Eigg concretion
- The 4 samples from the 3 decimetre-scale Eigg concretions
- All other sandstone cements (including the Eigg dyke margin nodule)

- Non-fibrous calcite veins
- Spar infills of shell vugs, septarian fractures, amygdales and a baked Callovian belemnite (Staffin Shales) (upon the assumption that these are likely to be almost 100% pure calcite)
- Fibrous calcite vein subsamples (sample 18-9)

Samples where $n = 1$, could not be included in the calculation of pooled standard deviation of a group; however, a representative uncertainty was assumed by applying the pooled standard deviation from other samples in the group. This compromise allows a notional uncertainty to be assigned. By definition using the pooled standard deviation method, a sample with $n = 1$ will have the highest representative standard error of the group.

The final sample (189-8bulk) was thought to be comparatively different to all other samples, being the only sample of 'bulk' limestone (non-discriminatory shells/cement mix) thus $\delta^{18}\text{O}_{\text{CARBONATE}}$, $\delta^{13}\text{C}$ and Δ_{47} uncertainty for this sample is shown as ± 1 standard error of the individual sample replicates ($n = 5$).

Temperature and fluid isotope compositions were calculated using the mean Δ_{47} and $\delta^{18}\text{O}_{\text{CARBONATE}}$ values with full propagation of the measurement and calibration uncertainties. The $\delta^{13}\text{C}$ and $\delta^{18}\text{O}_{\text{CARBONATE}}$ values are reported for carbonates with respect to Vienna-Pee Dee Belemnite (VPDB) and $\delta^{18}\text{O}_{\text{FLUID}}$ values with respect to Vienna-standard mean ocean water (VSMOW).

All calculations are provided in Appendix 2: Part II. A summary table with all data and both their sample replicate and pooled standard deviation derived standard errors is included in Appendix 2: Part IV.

4.2.3: Sr isotope analysis

Sr isotope analysis was kindly completed by Chris Holmden from the University of Saskatchewan. Carbonate powders were dissolved twice were dissolved in twice the stoichiometric volume of 1.0 N HCl required to completely dissolve the sample. After the effervescence ceased, the solution was centrifuged, and the supernatant was separated from any residues and dried down on a hot plate. The sample was purified from Ca, Rb and other trace elements using conventional cation exchange chromatography. The purified Sr aliquot was then loaded onto single Ta filaments with phosphoric acid and Ta-gel to increase the ionization efficiency of Sr in the mass

spectrometer. The $^{87}\text{Sr}/^{86}\text{Sr}$ measurements were performed using a thermal ionization mass spectrometer (Thermo-Elemental Triton instrument) operating in static multi-collection mode. An exponential law was used to correct the measured $^{87}\text{Sr}/^{86}\text{Sr}$ ratios for instrumental mass fractionation against measurements of $^{88}\text{Sr}/^{86}\text{Sr}$ with a true ratio of 8.375209. Isobaric interference of ^{87}Rb on ^{87}Sr was monitored using ^{85}Rb , and corrections made if necessary. The external reproducibility of $^{87}\text{Sr}/^{86}\text{Sr}$ was better than ± 15 ppm (2σ), based on multiple runs of SRM 987 performed throughout the course of this work, which yielded a mean $^{87}\text{Sr}/^{86}\text{Sr}$ ratio of 0.710259.

4.3: Results:

Stable and clumped isotope results for the vertical transect of VR1 are displayed in Table 4.2 and Figure 4.23. Stable $\delta^{13}\text{C}$ and $\delta^{18}\text{O}$ as reported by Wilkinson (1993) are also shown in Figure 4.23a for comparison. There are slight differences in our newly measured stable isotope results compared to those measured by Wilkinson, (1993), which may be explained by the sampling of different poikilotopic crystals, or sides of the core plug. The trends, however, are consistent with those previously reported.

From the centre to the edge of the concretion, there are distinct changes in both temperature and back-calculated pore water isotopic composition, with both of these following the zonal trend previously seen in $\delta^{18}\text{O}$ measurements.

Temperatures at the concretion centre have been measured as 45 ± 6 °C, increasing to ~ 50 °C at 24-31.5 cm from the centre. After this there is a sharp transition to higher temperatures, reaching 73 ± 8 °C at 40 cm, which is reduced to 63 ± 8 °C at 46 cm from centre but increased again to 73 ± 7 °C by 53.5 cm. The outermost measurement at the edge of the concretion gave a much-reduced temperature of 57 ± 7 °C.

Back calculated $\delta^{18}\text{O}_{\text{WATER}}$ compositions mimic the temperature trend fairly closely. From 0-25 cm the fluid composition is between $-11.1 \pm 1.1\text{‰}$ and $-12.6 \pm 1.1\text{‰}$ VSMOW. For the pore fluid, a transition begins one measurement earlier than for temperature, but is also the transition point of $\delta^{18}\text{O}_{\text{CARBONATE}}$ (31.5 cm) – water compositions have risen to $-7.7 \pm 0.9\text{‰}$ VSMOW. The measurements that gave very hot temperatures (40-53.5 cm) give positive $\delta^{18}\text{O}_{\text{WATER}}$ compositions, between $0.0 \pm 1.2\text{‰}$ and $+2.1 \pm 1.1\text{‰}$ VSMOW, before the pore fluid composition becomes more negative at the concretion edge ($-4.4 \pm 1.1\text{‰}$ VSMOW), corresponding with the decrease in temperature.

Sample	N	Zone	Distance from centre (cm)	$\delta^{13}\text{C}$ (‰, VPDB)	$\delta^{18}\text{O}_{\text{CARBONATE}}$ (‰, VPDB)	Δ_{47} (CDES-25)	T(Δ_{47}) (°C)	$\delta^{18}\text{O}_{\text{FLUID}}$ (‰, VSMOW)
M8603	4	Z1	0	-0.19 ± 0.03	-18.5 ± 0.0	0.598 ± 0.011	45 ± 6	-12.4 ± 1.1
M87215	4		8.5	-0.32 ± 0.03	-18.5 ± 0.0	0.601 ± 0.011	44 ± 6	-12.6 ± 1.1
M8604	4		16.5	-0.64 ± 0.03	-17.8 ± 0.0	0.597 ± 0.011	45 ± 6	-11.7 ± 1.1
M87216	4		24	-0.64 ± 0.03	-18.0 ± 0.0	0.587 ± 0.011	50 ± 6	-11.1 ± 1.1
M8605	10		31.5	-0.35 ± 0.02	-14.4 ± 0.0	0.590 ± 0.007	48 ± 5	-7.7 ± 0.9
M87217	3	Z2	40	-0.35 ± 0.03	-10.0 ± 0.0	0.539 ± 0.013	73 ± 8	0.7 ± 1.3
M8606	3		46	-0.80 ± 0.03	-9.0 ± 0.0	0.559 ± 0.013	63 ± 8	0.0 ± 1.2
M87218	5		53.5	-0.67 ± 0.02	-8.6 ± 0.0	0.539 ± 0.010	73 ± 7	2.1 ± 1.1
M8607	4	Z3	60.5	-0.16 ± 0.03	-12.6 ± 0.0	0.570 ± 0.011	57 ± 7	-4.4 ± 1.1

Table 4.2: Clumped isotope results from concretion VR1. All ± values represent one standard error of the pooled standard deviation.

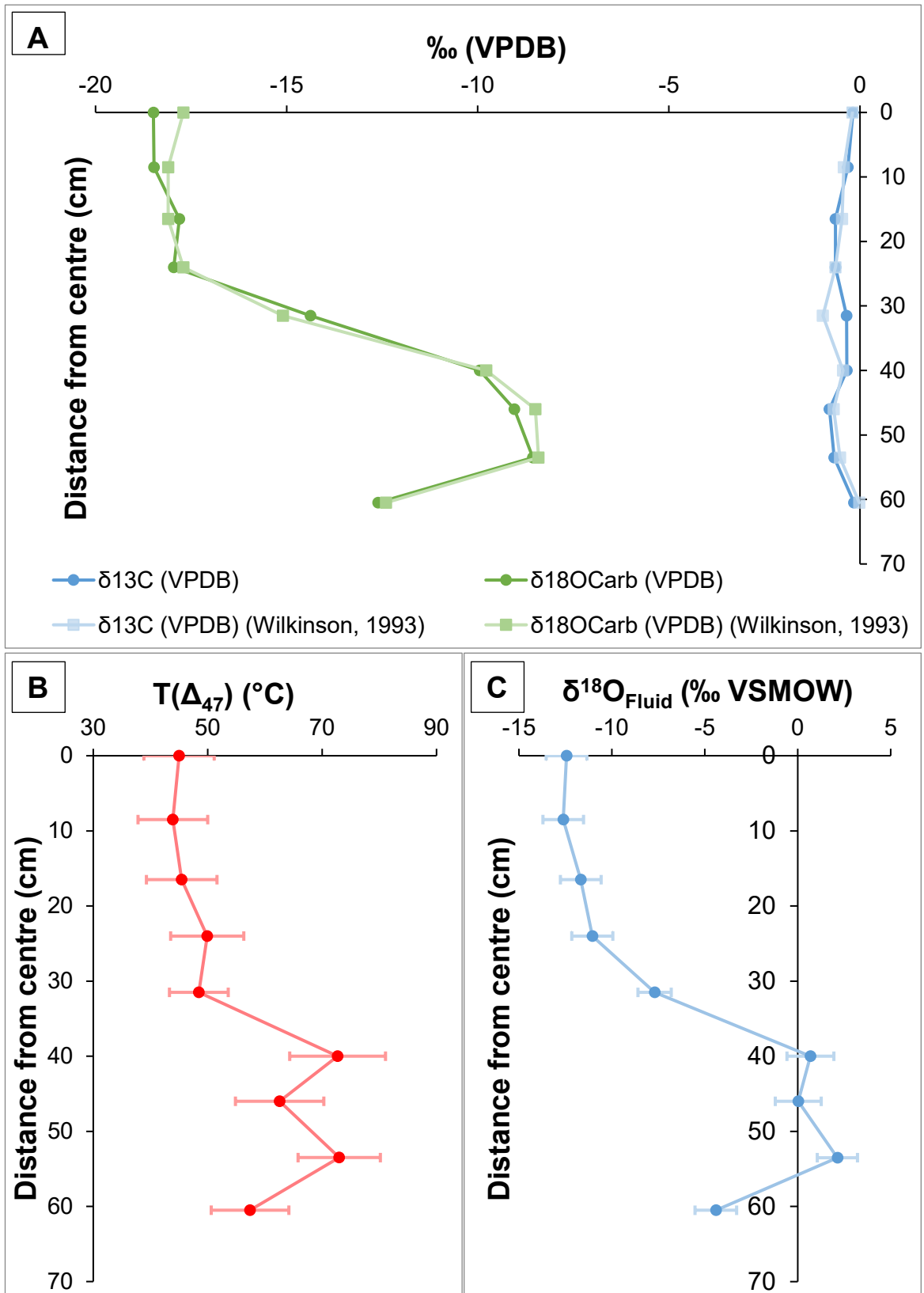


Figure 4.23: Clumped isotope results for concretion VR1; A) $\delta^{13}\text{C}$ and $\delta^{18}\text{O}_{\text{CARBONATE}}$ results measured by MIRA, compared to previously measured results from Wilkinson (1993); B) Δ_{47} derived temperatures; C) derived $\delta^{18}\text{O}_{\text{FLUID}}$ results.

The concretion from bed 38 (Dun Dearg) gives a temperature of 64 ± 9 °C and a $\delta^{18}\text{O}_{\text{FLUID}}$ composition of -1.8 ± 1.4 ‰ (Table 4.3).

The results from Eigg's large and small concretions are not similar to one another (Table 4.3). The large concretion has $\delta^{13}\text{C}$ values between $+1.5$ ‰ and $+3.3$ ‰ VPDB and $\delta^{18}\text{O}_{\text{CARBONATE}}$ values between -6.7 ‰ and -7.2 ‰ VPDB. The decimetre scale concretions have negative $\delta^{13}\text{C}$ values (-3.0 ‰ to -5.6 ‰ VPDB) and lower $\delta^{18}\text{O}_{\text{CARBONATE}}$ values than the large concretion (-10.0 ± 0.1 ‰ to -10.4 ‰ VPDB).

The large and small Eigg concretions also have very different clumped isotope derived results. Towards the centre of the large concretion, the temperature is 79 ± 8 °C, with a pore fluid value of $+4.9 \pm 1.1$ ‰ VSMOW. This changes to 98 ± 9 °C and $+7.2 \pm 1.2$ ‰ VSMOW at 63 cm from the previous measurement, and the outermost sample gave measurements of 68 °C, and fluid $\delta^{18}\text{O}$ values of $+2.7 \pm 1.1$ ‰ VSMOW. In contrast, the results from the decimetre-scale concretions of division E were much cooler, with temperatures ranging from 13 ± 6 to 35 ± 6 °C. Fluid compositions range from -6.2 ± 1.1 ‰ to -10.1 ± 1.3 ‰ VSMOW.

A comparison of all concretions and spar data from Skye and Eigg is shown on Figure 4.24. Data for other samples measured are shown in Table 4.4, ordered by Formation.

Several veins from the Valtos Cliff section give $\delta^{13}\text{C}$ results close to 0 ‰ VPDB ($+0.2 \pm 0.1$ ‰ to -0.3 ± 0.1 ‰). Exceptions include the two central dyke veins (189-5v and 189-7a) which gave slightly more negative results; -2.0 ‰ and -3.4 ‰ VPDB respectively. The spar infill from a *Neomiodon* Limestone had values of $+1.1$ ‰ VPDB. $\delta^{18}\text{O}$ results were also largely consistent for both spar and veins – all but one (detailed below) gave values between -18.6 ± 0.1 ‰ and -20.0 ± 0.1 ‰ VPDB.

Most Valtos Sandstone Formation veins and spar infills from Valtos Cliffs give temperatures between 30 ± 13 °C to 52 ± 10 °C and fluid values between -12.1 ± 2.7 ‰ and -15.4 ± 2.5 ‰ VSMOW. Exceptions include a vein from the base of a large concretion (189-1) which gave a temperature of 67 ± 10 °C and a $\delta^{18}\text{O}_{\text{FLUID}}$ value of $+4.1 \pm 1.5$ ‰ VSMOW; the vein from the margin of the dyke (189-6; 24 ± 8 °C; -16.5 ± 1.6 ‰ VSMOW) and the 'bulk' *Neomiodon* Limestone (189-8bulk), which gave a value of 94 ± 8 °C and fluid values of $+5.5 \pm 1.1$ ‰ VSMOW. The concretion vein (189-1) also gives an unusual $\delta^{18}\text{O}_{\text{CARBONATE}}$ value of -5.8 ± 0.1 ‰ VPDB, although the carbon value is not unusual.

Type	Locality	Sample	N	Location in concretion	$\delta^{13}\text{C}$ (‰, VPDB)	$\delta^{18}\text{O}_{\text{CARBONATE}}$ (‰, VPDB)	Δ_{47} (CDES-25)	T(Δ_{47}) (°C)	$\delta^{18}\text{O}_{\text{FLUID}}$ (‰, VSMOW)
Large Sandstone Concretion	Dun Dearg, Skye	EG191015-1	2	Base	2.05 ± 0.04	-11.09 ± 0.04	0.556 ± 0.016	64 ± 9	-1.8 ± 1.4
	Laig Bay, Eigg	169-9	3	Centre	1.52 ± 0.04	-6.72 ± 0.05	0.528 ± 0.011	79 ± 8	4.9 ± 1.1
		169-11	3	64 cm	3.25 ± 0.04	-7.08 ± 0.05	0.496 ± 0.011	98 ± 9	7.2 ± 1.2
		169-10	3	Edge	3.08 ± 0.04	-7.23 ± 0.05	0.549 ± 0.011	68 ± 7	2.7 ± 1.1
Small Sandstone Concretion	Laig Bay, Eigg	169-6	3		-5.50 ± 0.03	-10.07 ± 0.06	0.648 ± 0.016	26 ± 7	-7.5 ± 1.3
		169-7	6		-3.04 ± 0.02	-10.39 ± 0.04	0.625 ± 0.011	35 ± 6	-6.2 ± 1.1
		169-8	3	'Edge'	-5.63 ± 0.03	-9.97 ± 0.06	0.688 ± 0.016	13 ± 6	-10.1 ± 1.3
			3	'Centre'	-5.51 ± 0.03	-10.25 ± 0.06	0.659 ± 0.016	22 ± 6	-8.5 ± 1.3
Dyke margin nodule	Laig Bay, Eigg	169-1r	3		-0.10 ± 0.02	-20.08 ± 0.02	0.606 ± 0.020	42 ± 9	-14.6 ± 1.7

Table 4.3: Clumped isotope results from other Valtos Sandstone Formation concretions from Skye and Eigg. All ± values represent one standard error of the pooled standard deviation.

The sample of concretion nodule from the dyke margin in the Valtos Sandstone at Laig Bay, Eigg (169-1) gives a temperature of 42 ± 9 °C and fluid value of -14.6 ± 1.7 ‰ VSMOW, comparable with veins from the Valtos Sandstone of Skye. The $\delta^{13}\text{C}$ and $\delta^{18}\text{O}_{\text{CARBONATE}}$ values are also very comparable to veins, giving results of -0.1 ‰ and -20.1 ‰ VPDB respectively.

From the Lonfearn Member of the Lealt Shale Formation, the three subsamples of the fibrous calcite vein (18-9x) show a trend from their base to upper edge of the vein in both $\delta^{13}\text{C}$ ($+2.1$ to $+2.7$ ‰ VPDB) and $\delta^{18}\text{O}_{\text{CARBONATE}}$ (-13.2 to -11.8 ‰ VPDB). A trend in temperature is not observed; values are between 29 ± 9 °C and 32 ± 9 °C with the lowest value at the centre, but high measurement uncertainty and low replicate number ($n = 2$ for each) means that a trend may have been poorly represented by the measurements taken here. Derived fluid compositions show a slight trend of -9.6 ± 1.7 ‰ VSMOW at the base and -8.3 ± 1.7 ‰ VSMOW at the top of the vein.

The other sample from the Lonfearn Member, a sparry septarian fracture fill from a mudstone hosted concretion (18-7ysc) gave $\delta^{13}\text{C}$ results of $+1.8$ ‰ and $\delta^{18}\text{O}_{\text{CARBONATE}}$ results of -8.6 ± 0.1 ‰ VPDB. This cement was hotter than the fibrous calcite vein, giving Δ_{47} derived temperatures of 59 ± 8 °C. $\delta^{18}\text{O}_{\text{FLUID}}$ values were at -0.2 ± 1.3 ‰ VSMOW, a value distinct from most other results from Skye reported in this chapter – there is discussion of the range in $\delta^{18}\text{O}_{\text{FLUID}}$ values shown in concretions from the later Staffin Shale in Chapter 3.4 which may also be relevant in this instance.

The samples collected from the Duntulm Formation were from a range of localities, indicated in Table 4.4, and results will be described in relation to these localities.

The sandstone cements, sample 17-1 (bed 5) and 17-2 (bed 23) both from Lon Ostatoin, give $\delta^{13}\text{C}$ values of -5.2 ‰ and -3.8 ‰ VPDB, with corresponding $\delta^{18}\text{O}_{\text{CARBONATE}}$ values of -15.8 ‰ and -19.4 ‰ VPDB. Temperatures increase moving up the succession from 28 ± 7 °C to 58 ± 9 °C, and fluid values change slightly (but within error) from -12.8 ± 1.4 ‰ to -11.1 ± 1.4 ‰ VSMOW.

Sparry vug fills from bed 19 at Lon Ostatoin (P22-LR; Andrews and Walton, 1990) give lower temperatures than the bed 23 sandstone cement, 23 ± 6 °C. The $\delta^{13}\text{C}$ value of this sample is similar to sandstone cement 17-2, at -3.4 ‰ VPDB, and $\delta^{18}\text{O}_{\text{CARBONATE}}$ gave

Location	Formation	Type	Sample	N	$\delta^{13}\text{C}$ (‰, VPDB)	$\delta^{18}\text{O}_{\text{CARBONATE}}$ (‰, VPDB)	Δ_{47} (CDES-25)	T(Δ_{47}) (°C)	$\delta^{18}\text{O}_{\text{FLUID}}$ (‰, VSMOW)
Laig Bay, Eigg	Eigg Lava	Amygdale	SA-1	4	-6.08 ± 0.04	-16.58 ± 0.07	0.643 ± 0.013	28 ± 6	-13.7 ± 1.2
			SA-2	4	-5.84 ± 0.04	-17.79 ± 0.07	0.646 ± 0.013	27 ± 6	-15.1 ± 1.1
Lon Ostaoin, Skye	Duntulm Formation	Sandstone cement	17-1	4	-5.21 ± 0.02	-15.80 ± 0.02	0.642 ± 0.018	28 ± 7	-12.8 ± 1.4
			17-2	5	-3.81 ± 0.02	-19.35 ± 0.02	0.568 ± 0.016	58 ± 9	-11.1 ± 1.4
Spar infill		P22-LR	4	-3.35 ± 0.04	-14.71 ± 0.07	0.658 ± 0.013	23 ± 6	-12.8 ± 1.1	
Kilmaluag Bay, Skye		Calcite Vein	199-1	3	-2.87 ± 0.04	-15.86 ± 0.12	0.633 ± 0.020	32 ± 8	-12.3 ± 1.6
			199-2	4	-1.07 ± 0.03	-16.39 ± 0.10	0.606 ± 0.017	42 ± 8	-10.9 ± 1.5
North Duntulm, Skye				TR-1609	1	-0.19 ± 0.07	-18.18 ± 0.21	0.631 ± 0.034	32 ± 13
Valtos, Skye	Valtos Sandstone Formation	Calcite Vein	18-4bulk	3	0.06 ± 0.04	-19.33 ± 0.12	0.611 ± 0.020	40 ± 9	-14.2 ± 1.6
			189-1	4	-0.06 ± 0.03	-5.79 ± 0.10	0.549 ± 0.017	67 ± 10	4.1 ± 1.5
			189-5v	3	-1.98 ± 0.04	-19.96 ± 0.12	0.581 ± 0.020	52 ± 10	-12.7 ± 1.7
			189-6	3	0.08 ± 0.04	-18.63 ± 0.12	0.654 ± 0.020	24 ± 8	-16.5 ± 1.6
			189-7a	2	-3.39 ± 0.05	-18.90 ± 0.15	0.611 ± 0.024	40 ± 10	-13.8 ± 1.9
		Spar infill	189-8spar	5	1.07 ± 0.04	-20.01 ± 0.07	0.606 ± 0.011	42 ± 6	-14.5 ± 1.1
		Limestone	189-8bulk*	5	3.31 ± 0.00	-8.20 ± 0.06	0.502 ± 0.010	94 ± 8	5.5 ± 1.1
Rubha nam Brathairean, Skye	Lonfearn Member	Fracture fill	18-7ysc	3	1.75 ± 0.05	-8.64 ± 0.09	0.567 ± 0.015	59 ± 8	-0.2 ± 1.3
		Fibrous Calcite Vein	18-9base	2	2.08 ± 0.01	-13.23 ± 0.04	0.633 ± 0.022	32 ± 9	-9.6 ± 1.7
			18-9centre	2	2.39 ± 0.01	-12.63 ± 0.04	0.639 ± 0.022	29 ± 9	-9.4 ± 1.7
			18-9edge	2	2.75 ± 0.01	-11.81 ± 0.04	0.634 ± 0.022	31 ± 9	-8.3 ± 1.7
Kildonnan Bay, Eigg	Kildonnan Member	Sandstone cement	JEA-159-3	4	1.94 ± 0.02	-7.66 ± 0.02	0.592 ± 0.018	48 ± 9	-1.1 ± 1.5
			JEA-159-4	4	1.88 ± 0.02	-6.98 ± 0.02	0.593 ± 0.018	47 ± 9	-0.5 ± 1.5
		Fracture fill	159-24ysc	4	4.03 ± 0.04	-4.75 ± 0.07	0.603 ± 0.013	43 ± 7	1.0 ± 1.2

Table 4.4: Clumped isotope results from other samples from Skye and Eigg. All ± values represent one standard error of the pooled standard deviation, except for 189-8bulk* where standard error of sample repeats is used.

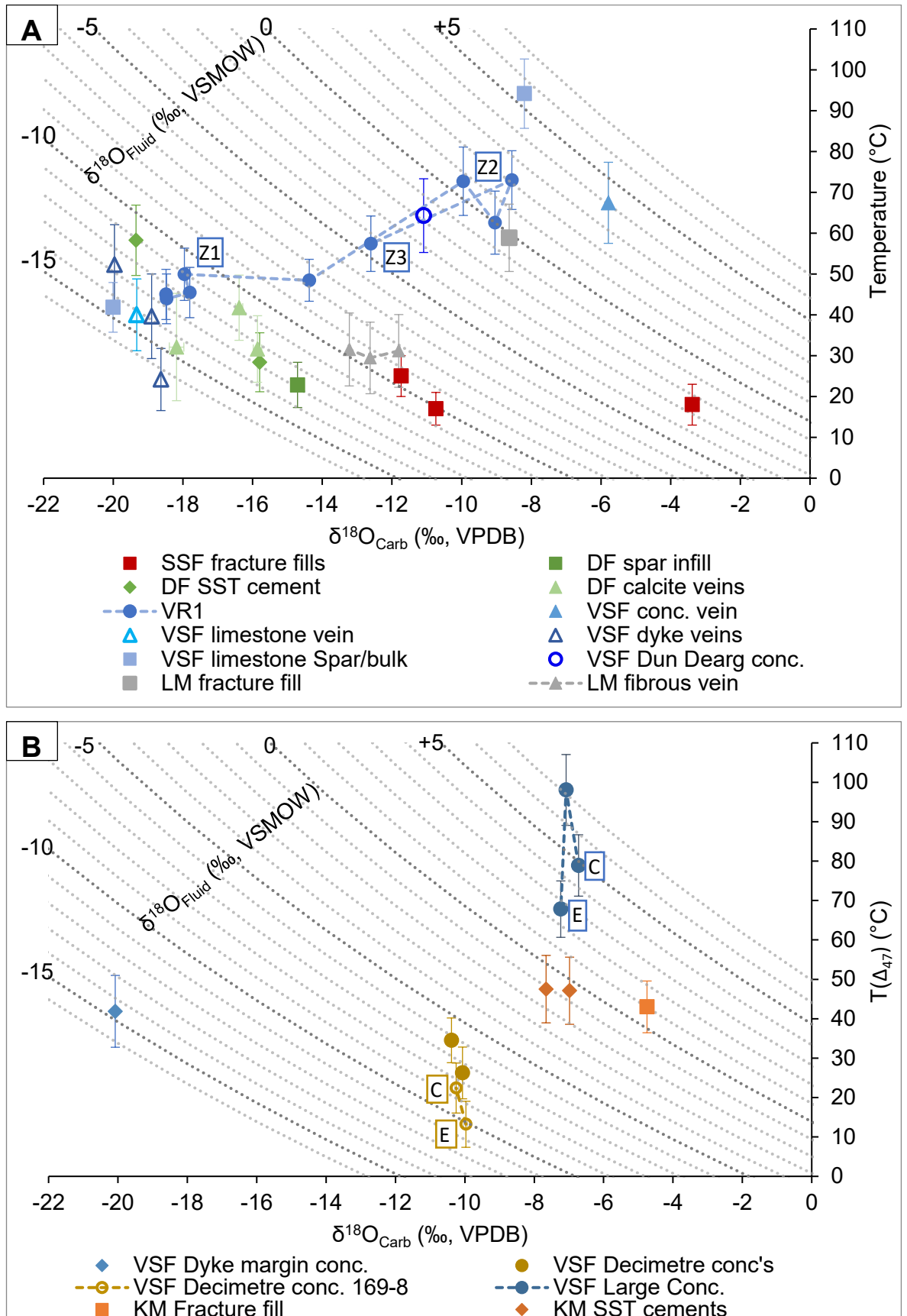


Figure 4.24: Clumped isotope results for all samples from A) Skye; and B) Eigg. Contours show $\delta^{18}\text{O}_{\text{FLUID}}$ values (‰, VSMOW). Abbreviations are as follows: SSF – Staffin Shale Formation; DF – Duntulm Formation; VSF – Valtos Sandstone Formation; LM – Lonfearn Member; KM – Kildonnann Member; SST – Sandstone. Z1 to Z3 indicate zones for concretion VR1; C and E correspond to centre and edge.

similar values to 17-1; $-14.7 \pm 0.1\text{‰}$ VPDB. The derived fluid value for this spar is $-12.5 \pm 1.1\text{‰}$ VSMOW, very similar to the other cements from this locality.

Two calcite veins (199-1, 199-2) sampled at Kilmaluag Bay, Skye, which unequivocally post-date the sill that is intruded into the Duntulm Formation at this locality, give $\delta^{13}\text{C}$ values of -2.9‰ and -1.1‰ , and $\delta^{18}\text{O}_{\text{CARBONATE}}$ values of $-15.9 \pm 0.1\text{‰}$ and $-16.4 \pm 0.1\text{‰}$ VPDB. Temperatures are different by 10 °C ($32 \pm 8\text{ °C}$ and $42 \pm 8\text{ °C}$) and pore fluid values are calculated to be $-12.3 \pm 1.6\text{‰}$ and $-10.9 \pm 1.5\text{‰}$ VSMOW.

Fracture fills from bed 20 of the Duntulm Formation sampled at North Duntulm Foreshore (TR-1609) give higher temperatures than the Lon Ostatein bed 19 spar fills, at $32 \pm 13\text{ °C}$. The $\delta^{13}\text{C}$ value of this sample is the highest of the samples from this formation at $-0.2 \pm 0.1\text{‰}$ VPDB. $\delta^{18}\text{O}_{\text{CARBONATE}}$ give values of $-18.2 \pm 0.2\text{‰}$ VPDB. The derived fluid value for this sample is $-14.5 \pm 2.5\text{‰}$ VSMOW, very similar to many of the other Skye samples but more negative than any other from the Duntulm Formation (with the caveat that this sample was only measured once).

The Kildonnan Member of the Lealt Shale Formation was sampled at Kildonnan Bay, Eigg, and results from this member appear quite distinct from the other data collected. The two different sandstone cements from bed 4A (JEA-159-3 and JEA-159-4) give similar results. Both have $\delta^{13}\text{C}$ measurements of $+1.9\text{‰}$ VPDB, and $\delta^{18}\text{O}_{\text{CARBONATE}}$ values are -7.7‰ and -7.0‰ VPDB for JEA-159-3 and JEA-159-4 respectively. Δ_{47} derived temperatures are $48 \pm 9\text{ °C}$ and $49 \pm 9\text{ °C}$, with $\delta^{18}\text{O}_{\text{FLUID}}$ values of $-1.1 \pm 1.5\text{‰}$ and $-0.5 \pm 1.5\text{‰}$ VSMOW. The sparry septarian fracture filling cement from a mudstone hosted concretion in bed 5f is different, with a $\delta^{13}\text{C}$ of $+4.0\text{‰}$ and $\delta^{18}\text{O}_{\text{CARBONATE}}$ of $-4.7 \pm 0.1\text{‰}$ VPDB. Temperatures are similar ($43 \pm 7\text{ °C}$) to the other samples and give fluid values of $+1.0 \pm 1.2\text{‰}$ VSMOW.

In order to establish Paleocene $\delta^{18}\text{O}_{\text{FLUID}}$ values at or close to the timing of Lava emplacement and cooling, calcite from within amygdales from the Eigg Lava Formation were analysed by clumped isotopes (SA-1 and SA-2). These samples gave the lowest $\delta^{13}\text{C}$ values measured here (-6.1‰ and -5.8‰ VPDB) while $\delta^{18}\text{O}_{\text{CARBONATE}}$ values were comparable to many of the other cements measured here, at $-16.6 \pm 0.1\text{‰}$ and $-17.8 \pm 0.1\text{‰}$ VPDB. Temperatures were consistent, at $28 \pm 6\text{ °C}$ and $27 \pm 6\text{ °C}$, with negative fluid values comparable to many of the other results ($-13.7 \pm 1.2\text{‰}$ and $-15.1 \pm 1.1\text{‰}$ VSMOW).

4.4: Discussion:

4.4.1: Concretion VR1:

Concretion VR1, a spherical concretion from Valtos cliffs, Trotternish, was first investigated by Wilkinson (1993). Horizontal and vertical centre to edge transects indicated that the concretion grew concentrically, with little change from centre to edge for $\delta^{13}\text{C}$ and SrCO_3 , and a slight trend towards increasing values for MnCO_3 . Distinct trends for MgCO_3 , FeCO_3 and $\delta^{18}\text{O}_{\text{CARBONATE}}$ (Fig. 4.14) were found in both transects, which Wilkinson (1993) categorised into three zones:

- Zone 1 (Z1): 0 cm to ~35 cm from centre (vertical transect); zone of relative stability, with lowest $\delta^{18}\text{O}$ values measured.
- Zone 2 (Z2): ~35 cm to ~58 cm (vertical transect); MgCO_3 , FeCO_3 and $\delta^{18}\text{O}_{\text{CARBONATE}}$ transition to higher values.
- Zone 3 (Z3): ~58 cm – 60.5 cm (vertical transect); the outermost edge of the concretion where $\delta^{18}\text{O}_{\text{CARBONATE}}$ decreases and both MgCO_3 and FeCO_3 fall to lowest values.

Of particular note, $\delta^{18}\text{O}$ measurements of the earliest cements in the concretion (Z1) were as negative as -18.2‰, and these ‘anomalously low’ values were difficult to reconcile with the proposed model of concretion formation (Wilkinson, 1993).

Re-measurements of $\delta^{13}\text{C}$ and $\delta^{18}\text{O}_{\text{CARBONATE}}$ from the vertical transect of VR1 using the MIRA mass spectrometer (this study) concur with Wilkinson (1993) (Fig. 4.23a). Wilkinson (1993) interpreted the change in $\delta^{18}\text{O}$ as being predominantly controlled by changing pore-fluid composition; variation caused by temperature variation was not perceived to be a significant control in the context of the assumed burial history during the time-span proposed for concretion formation (see also below). Using measurements of Δ_{47} , the $\delta^{18}\text{O}_{\text{CARBONATE}}$ trend within VR1 has now been investigated thoroughly without requiring any assumptions regarding temperature of calcite precipitation and allowing much more confident assignation of fluid $\delta^{18}\text{O}$.

Temperatures and $\delta^{18}\text{O}_{\text{FLUID}}$ compositions, shown on Figure 4.23 (B and C), record zonal centre to edge changes consistent with the zones described by Wilkinson (1993). The concretion cements began precipitating at 45 ± 6 °C, and all measurements within Z1 are within error of the zonal average (47 °C). $\delta^{18}\text{O}_{\text{FLUID}}$ values of Z1 show gradual increase

(Fig. 4.23 C), with earliest values $\sim -12.4 \pm 1.1\%$ VSMOW evolving to $\sim -11.1 \pm 0.9\%$ VSMOW at 24 cm from centre. The final value of Z1 appears to be transitioning to a more positive fluid composition and temperature increased sharply to 73 ± 8 °C between the final value in Z1 and the first value in Z2. Temperature remained high throughout Z2 in comparison to Z1, averaging 69 °C. The change in pore fluid $\delta^{18}\text{O}$ compositions between Z1 and Z2 is also steep, to values as positive as $+2.1 \pm 1.1\%$ VSMOW. Precipitation temperatures and $\delta^{18}\text{O}$ compositions both decrease in Z3.

4.4.1.1: Zone 1: Early cementation

The initiation of cementation was thought by Wilkinson to be due to an influx of a meteoric water into the sand body that reduced (by dilution) any Mg inhibition to calcite nucleation in the connate pore fluids (Wilkinson, 1993). Meteoric water influx was assumed to be either a Bathonian event that also penetrated the stratigraphically lower Berreraig Sandstone, or due to confined aquifer flow after basin inversion in the Late Jurassic/Early Cretaceous (Hudson and Andrews, 1987; Wilkinson 1991). An estimate of the rate of diagenetic feldspar degradation was used to infer that initiation of concretion formation occurred approximately 8 Ma after sandstone deposition, i.e., Upper Jurassic (Wilkinson, 1991; 1993).

While $\delta^{18}\text{O}_{\text{FLUID}}$ values of $\sim -12\%$ VSMOW from the centre of concretion VR1 are consistent with a meteoric water source (e.g., Dansgaard, 1964), the $\delta^{18}\text{O}$ composition of meteoric water of Jurassic age for the Hebrides is thought to have been much less negative. Estimates of -4 to -6% VSMOW by Hudson and Andrews (1987), based on isotope values from freshwater fossils and early diagenetic freshwater precipitates, were also supported by Searl (1992) when interpreting the Hettangian-Sinemurian aged Broadford beds of Skye and Raasay. Similarly, Emery et al. (1988) suggested values of -7% VSMOW for the Bajocian Lincolnshire Limestone of Eastern England. It thus seems unlikely that values $\sim -12\%$ VSMOW represent meteoric pore fluid values of Jurassic origin.

We assume here that replacement of connate pore fluids in the Valtos Sandstone Formation had occurred before precipitation of the concretion began. After deposition of the GEG, the succeeding Jurassic rocks rapidly became fully marine, culminating with the Callovian – Early Kimmeridgian Staffin Shale Formation (Morton and Hudson, 1995). Meteoric water recharge is not likely to have occurred during this globally significant

transgressive episode. More likely, recharge coincided with a period of exposure and erosion. Two possibilities present themselves: (1) pre-upper Cretaceous erosion (Hudson, 1983) before deposition of the thin Upper Cretaceous marine sediments, and (2) after any marine Upper Cretaceous deposition and the onset of Paleocene volcanism (Hudson, 1983 summarises).

There is no direct evidence of meteoric cementation, and thus inferred pore fluid composition, from the rather sparse Inner Hebridean Cretaceous sediments. Elsewhere in the UK, sphaerosiderites from Lower Cretaceous Wealden Facies (southeast England) gave a range of derived pore fluid $\delta^{18}\text{O}$ compositions between -6 to -4‰ VSMOW (Robinson et al., 2010). Pore filling cement in the Lincolnshire Limestone of the Midland Platform provided estimates of $\delta^{18}\text{O}$ around -8‰ (or more -ve) for meteoric water of Early Cretaceous age (via the Late Cimmerian unconformity; Hendry, 1993). Climatic models for the Middle Cretaceous tend to yield more negative estimations – for a latitude of ~40-45 °N (approximate latitude of the Inner Hebrides in Mid Cretaceous; Smith et al., 1994); estimates for meteoric values range from -5.5 to -11‰ VSMOW (see details and references in Table 4.5). Thus, while inferences from direct measurements in UK cements and fossils are not more negative than -8‰, modelling results may allow Cretaceous meteoric water as negative as -11‰ in the study area. It is therefore possible that that Z1 cementation in concretion V1 formed from pore fluids sourced during a period of pre-upper Cretaceous exposure.

Reference	$\delta^{18}\text{O}_{\text{FLUID}}$ Estimation	Description	Further notes:
Poulsen et al. (2007)	~-7‰ to -10‰ VSMOW	Continental precipitation $\delta^{18}\text{O}$ at 40-45°N	Atmosphere general circulation model with transportation and fractionation of water isotopes; four different CO ₂ concentrations
Zhou et al. (2008)	~-5.5‰ to -7‰ VSMOW	Precipitation $\delta^{18}\text{O}$ at 40-45°N	Ocean-atmosphere general circulation model with transportation and fractionation of water isotopes
Suarez et al. (2011)	-7.5‰ to -11‰ VSMOW	Groundwater $\delta^{18}\text{O}$ at 40-45°N	Groundwater gradients used in precipitation model as proxies for meteoric composition; matched to meteoric $\delta^{18}\text{O}$ compositions derived from pedogenic carbonates

Table 4.5: Estimates of meteoric $\delta^{18}\text{O}_{\text{WATER}}$ values for Middle Cretaceous from modelling.

Evidence for Paleocene meteoric fluid compositions are better constrained for Skye; using estimations of hydrothermal fluid δD values, Paleocene meteoric $\delta^{18}O$ values were estimated to be -12‰ SMOW (Taylor and Forester, 1971; Forester and Taylor, 1977). There is therefore circumstantial evidence that VR1 precipitation may have commenced from Tertiary pore fluids. Analysis of other cements from Skye and Eigg also support this conclusion and will be discussed in detail in Section 4.4.3 and 4.4.4.

The new clumped isotope data show that cementation of Z1 occurred at temperatures averaging 47 °C. Previous work by Wilkinson (1993) proposed that the concretion formed in the Late Jurassic at cooler temperatures under a burial of less than 400 m (Wilkinson, 1993, his Fig. 9); using a simple model with an assumed 'mean upper crust' geothermal gradient of 30 °C km⁻¹ and a surface temperature of 20 °C following Hudson and Andrews (1987), this would be at <31 °C. However, if initiation of concretion growth was instead after Cretaceous exhumation (Fig. 4.10) but before Paleocene lava emplacement, it must have occurred under <300 m burial. Using a mean geothermal gradient of 30 °C km⁻¹ and a surface temperature of 20 °C, the initial temperature of formation would have been ~29 °C at a proposed 300 m maximum burial. Since the Jurassic/Cretaceous burial history is unlikely to be seriously in error (see Hudson and Andrews 1987; Morton 1987), the new temperature data demand one of the following possibilities: a) that the Paleocene Hebridean geothermal gradient was higher than present; b) pore fluids were the additional source of heat; c) a combination of both a) and b); or d) concretion initiation after lava emplacement.

As discussed below, we can be reasonably confident that Z1 cements formed before emplacement of the Skye Lava Group. This means that Z1 cementation started either in the Paleocene (just before lava emplacement) or possibly late in the latest Cretaceous. What is certain is that by the time Z1 cementation initiated, temperatures were ~47 °C in the Valtos Sandstone. If precipitation temperature was to be wholly explained by regional geothermal gradient increase, at a surface temperature of 20 °C and burial depth of 300 m a geothermal gradient of ~90 °C km⁻¹ would be required which is considered unlikely.

A geothermal gradient of 90 °C km⁻¹ is not impossible in the context of volcanic provinces; for example, Icelandic geothermal gradients (Pálmason and Sæmundsson, 1979) can exceed these values at >40 km from active rifting zones (a similar distance to that of Valtos from the igneous centres on Skye), and at distances greater than this,

values of up to 86 °C are known (Pálmason and Sæmundsson, 1979). In a survey of drill hole geothermal gradients collected throughout Africa, the highest values were up to 90°C but these were related to the Red Sea Rift and otherwise non-typical (Macgregor, 2020). Such geothermal gradients over regional areas are, however, unusual; the Norwegian passive margin has maximum regional Cenozoic crust geothermal gradients of 53-55 °C km⁻¹ (Gholamrezaie et al., 2017) while the passive margin of southwest Africa only reaches 48-50 °C where sediments are thickest (thousands of metres) (Gholamrezaie et al., 2017). It is worth noting that these examples are mostly not directly comparable to the continental passive margin setting being examined from the Hebrides, where a pre-eruptive igneous centre was developing, and where the thermal conductivity of the sedimentary cover and the degree of crustal radiogenic heating affected geothermal gradients in specific ways (e.g., table 2 of Thompson, 1977).

Although a gradient of 90 °C km⁻¹ is unlikely, a higher gradient than that typical for 'mean crust' is considered highly likely for the Paleocene; indeed, the present-day geothermal gradient of an exploration well c. 50 km SW of Skye in the in the Sea of Hebrides Basin (134/5-1) was calculated to be ≤ 43 °C km⁻¹ by Holford et al. (2010). An arbitrary geothermal gradient of 60 °C km⁻¹ for the Paleocene was used by Hudson and Andrews (1987), which may still be a reasonable maximum thermal gradient for this period; and 43 °C km⁻¹ a reasonable minimum value.

We caution, however, that such assumed geothermal gradients are simplifications. They do not, for example, allow for variations of conductivity in different lithologies. They also require assumptions regarding initial surface temperature. For the Jurassic, Hudson and Andrews (1987) assumed a surface temperature of 20 °C. However, surface temperatures may have been different in the Paleocene. Paleoflora from Skye (dated to 60.28 ± 0.45 Ma) suggest a mean annual land surface temperature <13 °C for the Mid-Paleocene (Poulter, 2011). Higher surface temperatures may have prevailed in the early Paleocene; Mull palaeoflora dated at 60.6±0.3 Ma, may have been 1-5 °C warmer than the Mid-Palaeocene (Poulter, 2011). Moreover, laterites from interbasaltic layers of the Antrim Lava Group, Northern Ireland dated between 0.5-1 Ma before the Skye paleoflora, suggest a tropical to sub-tropical monsoonal climate (Hill et al., 2000).

If the elevated temperatures observed in the Valtos Formation were due to heated pore fluids alone, they would need to add about 20 °C to the 'normal' (30 °C km⁻¹; surface temperature 20 °C) geothermal depth profiles (outlined above) to give a

combined temperature of 47 °C. It is difficult to imagine how heated fluids could have been present before the Paleocene igneous centres evolved, which argues against a Late Cretaceous timing. However, once the igneous centres developed, local sources of heated water may well have been common, even before lava emplacement. The earliest evidence for volcanic activity in northern Skye is from the Portree Hyaloclastite Formation, which outcrops at locations on both the Trotternish (including sites near Portree, and on the coast north of Staffin) and Waternish Peninsulas (Anderson and Dunham, 1966). Volcanic material was sourced from explosive vents and deposited subaqueously (Anderson and Dunham, 1966). It is very likely that meteoric water was implicated (and heated) in this phreato-magmatic activity, which would explain how heated groundwater might access and migrate into the porous Valtos Sandstone aquifer.

The most likely scenario may be that that Z1 concretion initiation temperatures were influenced by both a high local geothermal gradient due to the imminent onset of plume volcanism, and the influence of locally heated pore fluids.

It is important to note that a steep geothermal gradient (e.g., up to 60 °C km⁻¹) can only have developed as the Tertiary Igneous Province was becoming established around 61 Ma (Emeleus and Bell, 2005 and references therein). We cannot constrain the geothermal gradient before this time, i.e., in the 100 Ma between deposition of the GEG and early Paleocene. This means that a more 'normal' upper crustal average geothermal gradient of 30 °C km⁻¹ could have prevailed during the late Jurassic and Cretaceous as envisioned by Hudson and Andrews (1987). This said, a present-day maximum thermal gradient of 43 °C km⁻¹ has been measured from the Sea of the Hebrides Basin, as noted above (Holford et al., 2010).

4.4.1.2: Zone 2:

Our results show the transition of $\delta^{18}\text{O}_{\text{CARBONATE}}$ from -18.5‰ to -8.6‰ represent a change in both temperature and $\delta^{18}\text{O}_{\text{WATER}}$ composition (Fig. 4.23). This is contrary to the conclusion reached by Wilkinson (1993) who interpreted the $\delta^{18}\text{O}$ trend to be primarily due to a change in pore fluid composition, inherent in the proposed stability of burial depth in his model of formation.

Such a steep transition between zones may be taken to indicate a pause in cementation; however, this is inconsistent with the petrography of the concretion, which

shows only one generation of ferroan calcite with no evidence of zoning (Wilkinson, 1993). Petrography does, however, show a changing cement crystal morphology from centre to edge of the concretion, with crystal size and degree of elongation increasing radially (Wilkinson 1989, see also Fig. 4.25). Poikilotopic cement texture has been associated with lower supersaturation levels (e.g., Saigal and Bjørlykke, 1987; Wilkinson, 1993) which is compatible with the observation that there is a decrease in preserved shell material from the centre to the edge of the concretion, with only one sample of Z2 containing shell material (0.8%, derived by point counting; Wilkinson, 1993). However, the morphological change from approximately equant crystals to crystals with distinct elongation along the C axis appears to be close in timing to the isotopic compositional transition. Petrography from the third sample from the centre of the concretion (M8604, Z1; 16.5 cm radius) shows equant crystals; a thin section at a radius comparable to the 4th sample (M8614, Z1 vertical transect, 26 cm) has a mixture of approximately equant and elongated crystals, and by the transition point (final measurement of Z1 at 31.5 cm, M8605) calcite crystals have distinct elongation, with crystal short axes ~1 mm and long axes >3 mm in dimension (Fig. 4.26). It is unclear whether the timing of this crystallographic change is coincidental or related to the fluid compositional and/or temperature change.

The temperature difference between outermost Z1 and innermost Z2 is from 53 ± 3 °C to 79 ± 7 °C. Similar to the discussion of temperature in Z1, the reasons for this steep change could be due to:

- Steepening of a geothermal gradient without additional burial
- Input of heated fluids
- Increased burial without change in regional geothermal gradient.

If this change happened entirely due to a regional increase in geothermal gradient (potentially related to the onset of Paleocene plume sourced volcanism), without increasing the 300 m depth of pre-Tertiary burial, the geotherm (with a surface temperature of 20 °C) would be required to reach 180 °C km⁻¹ to increase the temperature of concretion cementation to 73 °C, the maximum recorded in Z2. Although a simplification, this modelled gradient is unrealistic, and if maintained throughout the Paleocene Intrusive Event (particularly after lava emplacement) such high temperatures would have had a metamorphic effect on the surrounding and underlying Jurassic sediments, particularly the formations beneath the Valtos Sandstone. Even with a

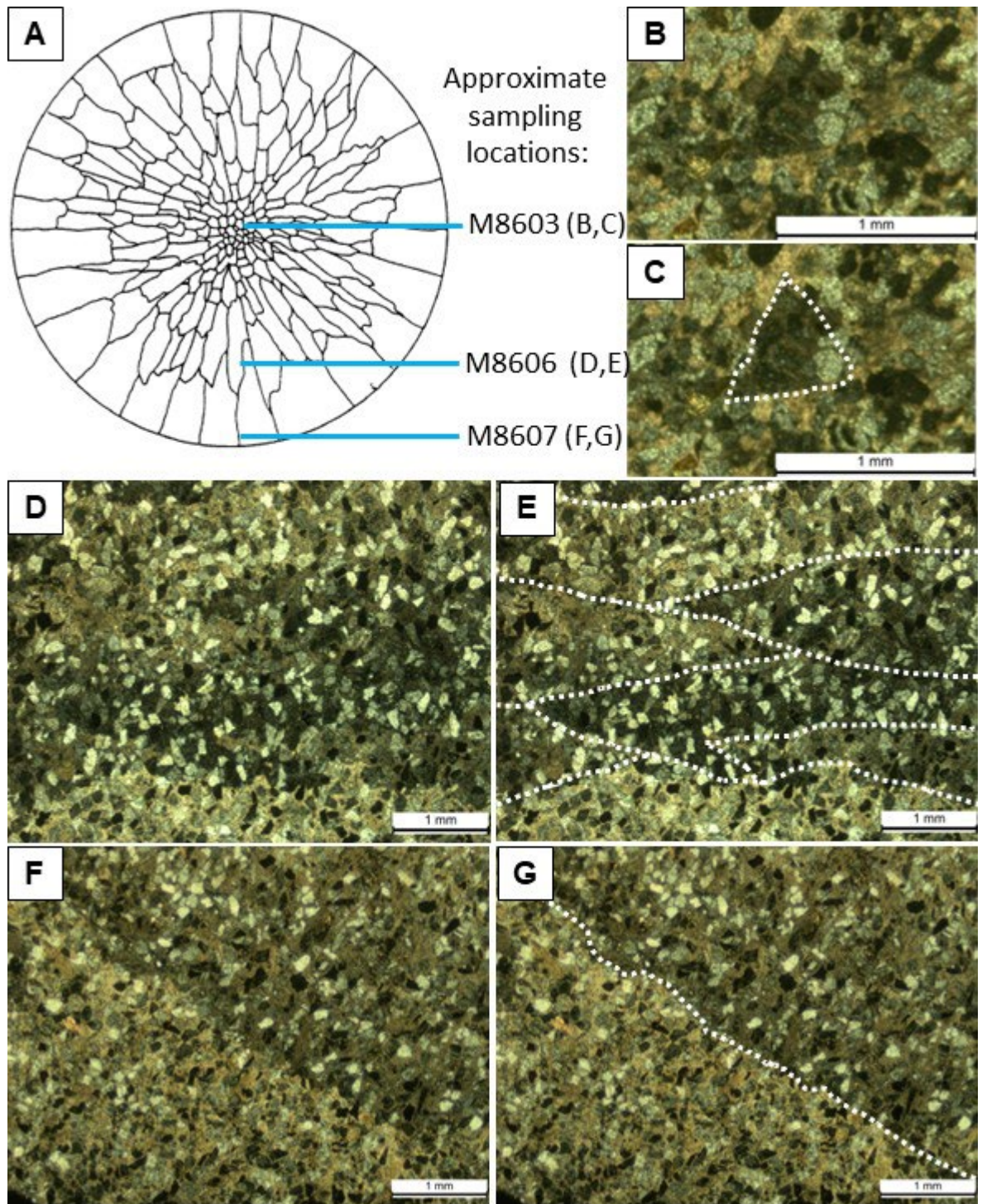


Figure 4.25: XPL petrographic images of the poikilotopic crystal structure of concretion VR1, increasing in size and elongating radially. A) shows a schematic of concretion fabric from Wilkinson (1989) and approximate positions of sample site; B) shows the central, almost equant crystal in extinction at the concretion centre (Z1), highlighted in C); D) shows crystals in Z2 at 46 cm from the concretion centre, annotated in E) to highlight calcite crystal terminations; F) shows a crystal boundary from Z3, the outer edge of the concretion (60.5 cm from the centre), where individual crystals greatly exceed the size of the field of view, highlighted in G).

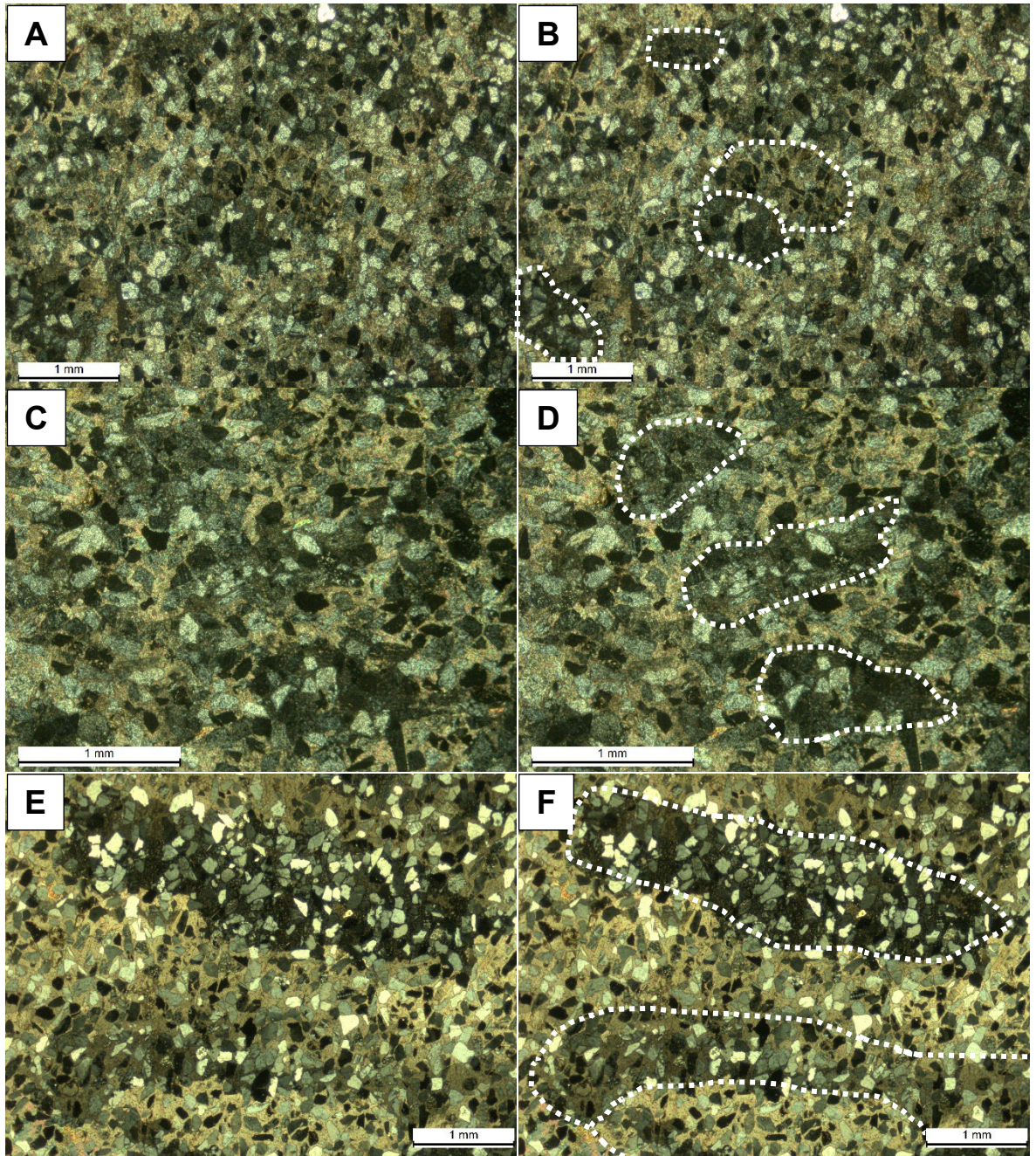


Figure 4.26: XPL petrographic images from concretion VR1. A) shows approximately equant crystals from sample M8604 16.5 from centre (Z1), highlighted in B); C) shows mixture of elongated and approximately equant crystals in Z1 from sample M8614 at 26 cm from concretion centre (horizontal transect, approximately equivalent to M87216), highlighted in D); E) shows elongated crystals from sample M8605, 31.5 cm from centre at Z1 edge, highlighted in F).

minimum estimate of 450 m of lava emplacement on Northern Trotternish (based on the preserved thickness represented in Fig. 10 of Emeleus and Bell, 2005), the buried Valtos Sandstone would be at a temperature of ~ 155 °C (at a geotherm of 180 °C km^{-1} , ignoring lithological controls on thermal conductivity).

Evidence against regional heating to such temperatures are abundant and reviewed in Hudson and Andrews (1987). Aragonite bivalves are preserved in the underlying Lonfearn Member in various localities in northern Skye, as reported in Hudson and Wakefield (2018), who also comment that spore colouration does not support intense heating. More specifically in the local area at Valtos, AFTA data on apatites from the of the Valtos Sandstone Formation at Culnacnoc (NG516629) indicate that the maximum temperature reached in these sandstones in the early Paleocene was ≥ 110 °C (Holford et al., 2010); moreover, these values are likely to be slight overestimates (Holford, pers. comm. 2021). Vitrinite reflectance data from the nearby Lealt Shale at Invertote give R_o values of 0.55 (data in Hudson and Andrews, 1987), while source rock maturity within two wells (Hebrides 1 and Upper Glen 1) show R_o values less than 0.5 for sediments buried up to 1300 m and 1600 m respectively (Fyfe et al., 2021). Organic material from the earliest member of the GEG, the Cullaidh Shale Formation, and the earlier Toarcian aged Dun Caan Shale Member (below the Bearreraig Sandstone Formation) were examined by Thrasher (1992) who concluded that these sediments remain immature unless sampled within 15 km of the main Paleocene Skye Central Complex or close to igneous dyke margins. It is therefore very unlikely that a steep rise in geothermal gradient is the cause of the temperature trend seen in VR1.

Burial might be considered a different potential mechanism for the 26 ± 10 °C temperature change, particularly considering the proposal that Z1 formed close to or contemporaneous with the earliest volcanism on Skye.

The Valtos cliff section (Trotternish) is overlain by the Skye Lava Group. The cumulative thickness of the Skye Lava Group was estimated to be 1200 m by England (1994), although it should be noted that King (1976) used zeolite evidence to estimate a maximum thickness of 2000 m. It is likely that the lava pile was less extensive above Trotternish; mapping of North Skye was undertaken by Anderson and Dunham (1966), who suggested that only the Beinn Edra Group and the Beinn Totaig Group extended to the majority of the Peninsula, estimating approximate thicknesses of these groups as ~ 300 m (1000 ft) and ~ 600 m (2000 ft), ~ 900 m cumulatively. The preserved thickness of

the lavas in northern Skye is given by Emeleus and Bell (2005) as ~450 m, including the underlying Portree Hyaloclastite (30 m), while the zeolite-based thickness map of King (1976) projects that there was around ~1200 m of burial for the location of Valtos Cliffs. Emplacement of 900 to 1200 m of lava could reasonably explain the temperature change within the concretion if the geotherm was $>30\text{ }^{\circ}\text{C km}^{-1}$, as proposed above. After emplacement of 1200 m of lava, a geotherm of $40\text{ }^{\circ}\text{C km}^{-1}$ would give temperatures of $80\text{ }^{\circ}\text{C}$ using a simplified model; a geotherm of $60\text{ }^{\circ}\text{C km}^{-1}$ gives too great an increase ($110\text{ }^{\circ}\text{C}$) to explain the temperature rise, although it would still be consistent with the Holford et al. (2010) AFTA result (see above). A 900 m lava pile would be able to increase temperatures to $80\text{ }^{\circ}\text{C}$ with a geotherm of $50\text{ }^{\circ}\text{C km}^{-1}$.

Zeolite assemblages and zones can be related to temperature estimates; King (1976) identified the zeolites within the lowest part of the lava pile (resting above the Jurassic sediments) as belonging to the Analcime Zone, correlating to approximate temperatures of $75\text{ }^{\circ}\text{C}$ to $90\text{ }^{\circ}\text{C}$. This provides an independent estimate of the maximum burial temperature of the sandstones post lava emplacement and is close to the highest temperature results of Z2 of concretion VR1 ($73 \pm 8\text{ }^{\circ}\text{C}$).

On this basis it is possible to explain the transition to high temperatures in Z2 if this part of the concretion grew after burial by the Skye Lava Group, raising and maintaining the temperature of the pore fluids. However, field evidence argues against this; many, although not all, concretions in the Valtos Cliff section have visible deflection of bedding of the host sandstone around them, where the host rock has deformed around the cemented concretion (Hudson and Andrews, 1987; Wilkinson, 1993; see also Fig. 4.11 and Fig. 4.15). An estimate of $20 \pm 4\%$ compaction of the host rock relative to concretions was calculated by Wilkinson (1989), with no evidence for earlier compaction preserved within the concretion. Our interpretation of Z1, which requires concretion precipitation within the Paleocene, demands that compaction was due to emplacement and thickening of the lava pile as proposed by Wilkinson (1993), which also implies that compaction was complete within the 1.6 Ma (Hamilton et al., 1998) time window of lava emplacement.

As burial and/or changes in the geothermal gradient do not seem to explain the temperature increase, we now consider the introduction of a heated fluid, with a temperature sustained at an average of $69\text{ }^{\circ}\text{C}$ for the duration of the precipitation of Z2. This hypothesis requires a heated water source, as discussed for Z1. It is also important to

note that the temperature change is preceded and then accompanied by a change in $\delta^{18}\text{O}_{\text{FLUID}}$ composition (Fig. 4.23); Z1 averages -11.1% VSMOW, whereas Z2 averages $+0.9\%$ VSMOW, a 12% change, with highest values of $+2.1 \pm 1.1\%$ VMOW at the edge of Z2. There is also a marked increase in calcite Fe and Mg content that follows the temperature and $\delta^{18}\text{O}_{\text{FLUID}}$ trends (Wilkinson, 1993). The meteoric pore fluid of Z1 must have been replaced with a pore fluid that was enriched in ^{18}O and the trend suggests that the composition evolved progressively to such positive values over time.

Heated fluids in hydrothermal systems are known to undergo isotope exchange with surrounding rock units, and such water-rock interaction can result in more positive $\delta^{18}\text{O}_{\text{WATER}}$ values (Craig, 1963; Shepperd, 1986). With the proposed timing of concretion growth, it seems reasonable to explain the progressive positive change in pore fluid values towards the outer edge of the concretion as a result of local meteoric water percolating through, and reacting with, hot basaltic glass and phenocrysts. High levels of seasonal meteoric precipitation (1175.6 mm to 2266.7 mm) are indicated by fossil flora preserved within the Skye Lava Group (Poulter, 2011), and the Skye basalts are known to have $\delta^{18}\text{O}$ values above $+5\%$ SMOW (Taylor and Forester, 1971; Forester and Taylor, 1977). Such a scenario also explains why the Z2 cements have high Fe and Mg contents (about 1.5x higher) relative to Z1. Mg^{2+} is relatively easily leached from basaltic glass and olivine, while rainwater, being naturally acidic (pH 5.6), will facilitate leaching of iron. Initial oxidation reactions between the basalt and water will also consume dissolved oxygen such that the percolating fluid would have been acidic and reducing, conditions that favour the leaching of ferrous Fe (Garrels and Christ, 1965). Heating of the water by the hot basalt would have further promoted Fe solubility (e.g. Seyfried et al., 1991). The Z2 Fe contents are approximately 3x, and the Mg contents approximately 8x, those in limestone-hosted sparry, burial cements from the overlying Duntulm Formation (cf. Andrews 1986; Hudson and Andrews 1987).

We favour heated fluids generated within the lava pile as there are serious spatial and 'timing' issues with other more regional heat sources. For example, it is well known that hydrothermal systems developed around the central igneous complexes of Skye, Mull and Rum (Taylor and Forester, 1971; Forester and Taylor, 1977). However, the effects of these systems are typically limited to a radius of about 6.5 km distance (Forester and Taylor, 1977; Fig. 2.2) from the centre. Also, it is likely that concretion cementation was complete before eruption of the Skye Central Complexes, as they post-date eruption of the Skye Lava Group (Emeleus and Bell, 2005). Similarly, influence of

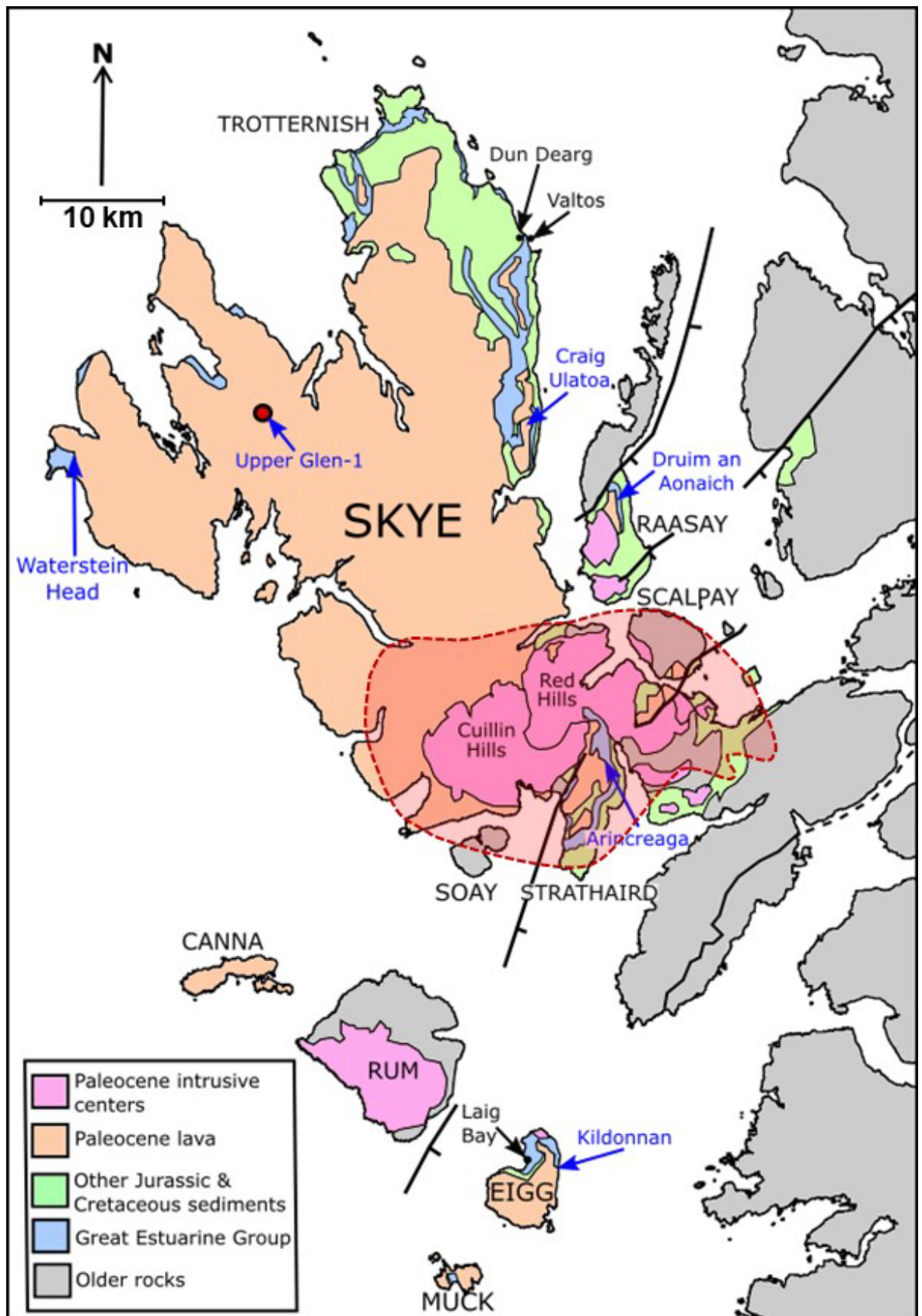


Figure 4.27: Map of the Inner Hebrides adapted from Thrasher (1992). Red dashed zone shows mapped extent (Forester and Taylor, 1977) of hydrothermal influence of the Cuillin/Red Hills Igneous Centres. Blue labels identify localities where Paleocene lava was emplaced directly on the eroded surface of the Valtos Formation. Note that these localities are spread across the depositional basin.

heat from the intrusion of the Little Minch Sill complex into the Valtos Formation at Valtos cannot have been responsible for local heating as it was emplaced after the Skye Lava Group (Anderson and Dunham, 1966; Gibson and Jones, 1991; Emeleus and Bell, 2005).

Taking all the evidence together it seems likely that, while Z1 of the concretion began forming at the earliest stage of effusive igneous activity on Skye, Z2 was forming after extrusion of a small volume of lava pile, the hot lavas being the source for the heated meteoric water. In this scenario, meteoric water passed through the still cooling lava pile, undergoing isotope exchange and leaching Fe and Mg from the mafic minerals. While the concretions were growing the down-bearing pressure of the lava pile was not enough to overcome the supporting litho- and hydro-static pressure in the sandstone; compaction occurred after the concretions had formed, presumably as the overlying lava pile thickened.

There are several areas where lava was emplaced directly onto a land surface where the Valtos Formation Sandstone was outcropping. Localities include the east coast of Eigg (overlain by the Eigg Lava Formation), within the Upper Glen 1 borehole in Waternish (NG299506; see Schofield, 2016; Fyfe et al., 2021), and at Craig Ulatoa near Prince Charles' Cave/Portree (NG51047) (Fig 4.27). At Waterstein Head on Waternish the Lavas are also just above the Valtos Sandstone Formation. These outcrops show that there were multiple points of entry (others may be present in sub-crop) for meteoric-derived fluids to enter the Valtos Sandstone aquifer.

Sr isotope measurements were taken at 3 points of the VR1 transect to investigate the concretion cement in comparison to other Skye rocks (see Table 4.6 for results, and Figure 4.28 for comparison). The outermost measurement of Z2 gave the highest measured values (0.710020 ± 0.000008) which is the only measurement that does not overlap with values for Jurassic shells (Holmden and Hudson, 2003). It is, however, far below values measured for Jurassic clays (Hamilton et al., 1992), and seems to favour the concretion values being representative of the Jurassic shell carbonate source. Values also do not overlap with Sr Isotopes from the Skye lavas (Fig. 4.28), which range from 0.70300 to 0.70531 (Scarrow, 1992). The lack of trace of the lava signal in the concretion may be due to the heated fluids being undersaturated with respects to aragonite, hence allowing further shell dissolution which released Sr and overprinted the lava signature. This is supported by the $\delta^{13}\text{C}$ data for the concretion (Table 4.2 and Fig. 4.23a), which shows no

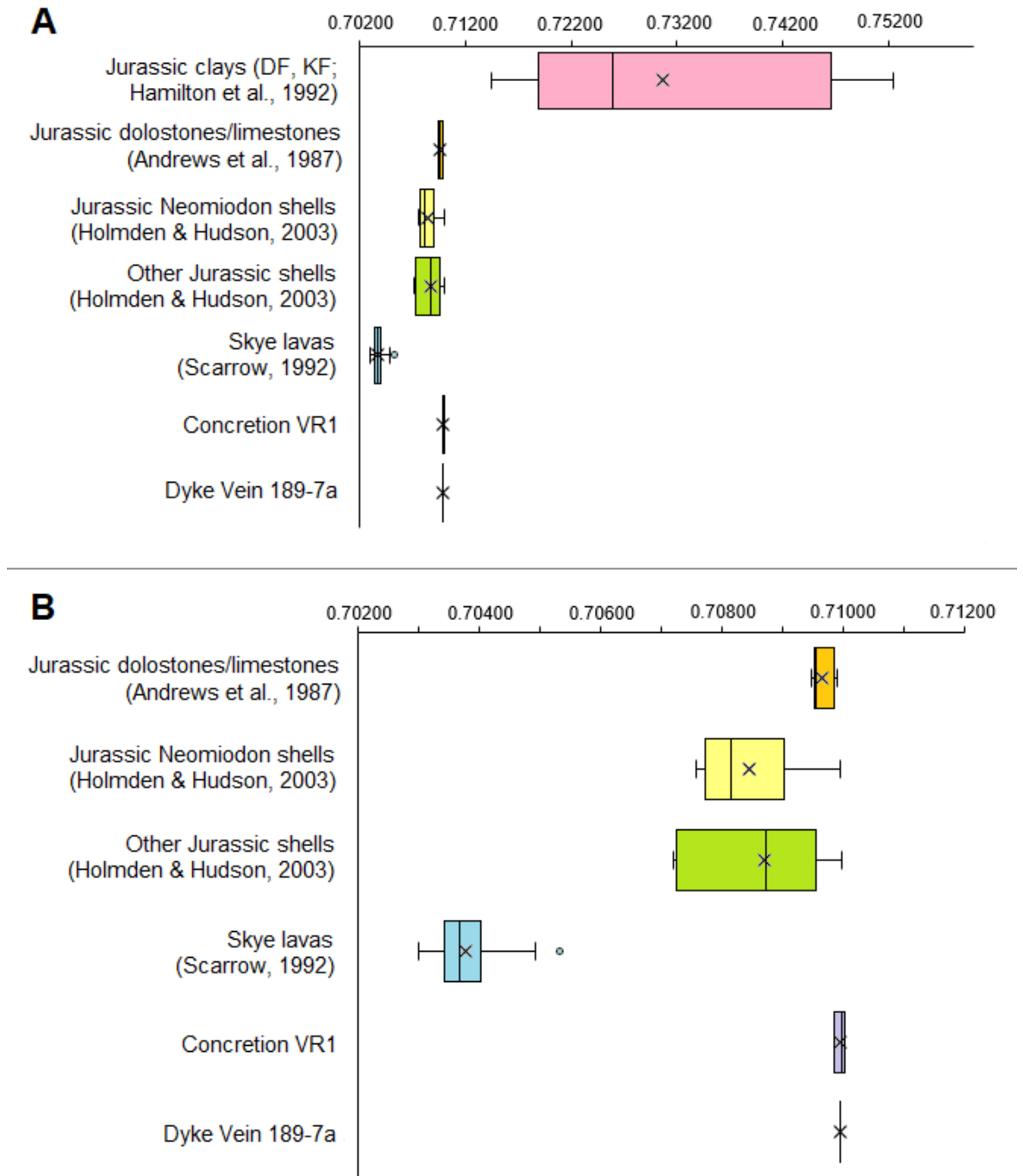


Figure 4.28: Sr isotope results for concretion VR1 and dyke vein 189-7a from Valtos Cliffs, Skye, in comparison to a suite of other Sr results from the Jurassic sediments and shells of the Inner Hebrides (data from Andrews et al., 1987; Hamilton et al., 1992; Holmden and Hudson, 2003) and Paleocene Lava from Skye (data from Scarrow, 1992). In B, the results of Jurassic clays from the Duntulm Formation (DF) and Kilmaluag Formation (KF) are omitted for ease of comparison.

zoning and is consistent with rock buffered values derived by shell dissolution, as suggested by Wilkinson (1993).

The lava water-rock interaction and heating scenario seems most capable of explaining both the temperature and pore fluid compositional change for Z2. The elevated temperatures would have had to been sustained throughout the growth of the zone.

Sample ID	Description	Distance from centre (cm)	$^{87}\text{Sr}/^{86}\text{Sr}$	Error
189-7a	Earliest vein within dyke at Valtos		0.709941	0.000007
M8603	Centre sample, VR1	0	0.709836	0.000006
M87218	2nd outermost sample, VR1	53.5	0.710020	0.000008
M8607	Edge sample, VR1	60.5	0.709961	0.000008

Table 4.6: Sr isotope results for samples from concretion VR1 and a sample from a vein within a dyke at Valtos Cliffs, Skye (189-7a).

4.4.1.3: Zone 3:

The final outer zone of the concretion, Z3, contains only one measurement representing the outermost edge of the concretion, and therefore the youngest region of cementation. Clumped isotope measurements reveal that there is a change in temperature and $\delta^{18}\text{O}_{\text{WATER}}$ between Z2 and Z3, in addition to the changes in $\delta^{18}\text{O}_{\text{CARBONATE}}$, Mg and Fe reported by Wilkinson (1993). The final temperature measurement of Z2 is 73 ± 7 °C, which decreases to 57 ± 7 °C for the Z3 measurement. While distinct from the final measurement of Z2, the Z3 measurement is within error of the second measurement of Z2 (63 ± 8 °C). The change in derived $\delta^{18}\text{O}_{\text{FLUID}}$ is more distinct, with the final value of Z2 of $+2.1 \pm 0.8$ ‰ decreasing to -4.4 ± 1.1 ‰ VSMOW. Mg and Fe both drop to their lowest values of the transect; MgCO_3 drops from 1.5 to 0.60 mol%; FeCO_3 drops from 2.3 to 0.97 mol%; (see also Fig. 4.14) (Wilkinson, 1993).

Zone 3 also represents the termination of cementation and must have formed when carbonate supply from dissolving *Neomiodon* shells was becoming limited. The surrounding sand body remains very friable and poorly cemented, with *Neomiodon* shells only preserved within concretions (Hudson and Andrews, 1987). Petrography shows poikilotopic cement also clearly visible in hand specimen, with distinct elongation, the longest axis of some crystals reaching >50 mm length (Wilkinson, 1993; see also Fig. 4.25).

As with the transition from Z2 to Z3, there is no petrographic evidence for a break in cementation.

With one measurement, it is difficult to interpret this zone due to the limited data; additionally, the second concretion (VR2) measured by Wilkinson (1993) did not show similar zonation. Overall, the decrease in element contents, temperature and isotope ratios either point to a change in the extent of water/rock interaction, or the introduction of another distinct pore fluid with a different composition to that of Z2. The latter scenario is not wholly consistent with petrographic evidence for no break in cementation.

We can be confident that the fluid did not supply any additional carbonate – dissolving *Neomiodon* shells continuing to be the carbonate source, as evidenced by the Z3 Sr isotopes (Table 4.6) which are not distinct from measurements of the other zones (Fig. 4.28 and Table 4.6). Figure 4.24a shows concretion T (°C) vs $\delta^{18}\text{O}_{\text{CARBONATE}}$, with contour lines representing the $\delta^{18}\text{O}_{\text{FLUID}}$ values. The measurement of Z3 falls almost midway between the measurements for Z1 and Z2. This could be evidence that a meteoric fluid of similar composition to that of Z1 infiltrated the sandstone and a mixture of the two fluids precipitated the outer edge of the concretion. Alternatively, a similar composition could have resulted if the Z3 fluid was dominantly fracture fed; meteoric water passing through fractures would interact much less (higher water/rock ratio) with the bulk of the basaltic glass, picking up less Fe, Mg and heat, while retaining a more negative ‘meteoric water’ isotopic composition

With eruption of the Skye Lava Group continuing after the concretion formed, as clear from the bedding lamination deflection observed around some concretions, the source of the heated and altered meteoric fluid that formed Z2 may well have become limited as the lava pile grew. Indeed King (1976) makes the point that vertical fluid movement predominantly through ‘unconnected’ vesicular horizons would have been difficult, a problem that intensifies as the lava pile gets thicker and more non-vesicular aquitards are emplaced.

4.4.1.4: *Summary of concretion VR1:*

The analysis of concretion VR1 utilising clumped isotopes has significantly altered the understanding of the diagenetic history of the concretion. Previously, the $\delta^{18}\text{O}_{\text{CARBONATE}}$ isotopic trend of the concretion had been inferred to be pore-fluid

controlled, but with unexplainably negative initial values (Wilkinson, 1993). We now can see that the isotopic trend is controlled by both temperature and pore-fluid $\delta^{18}\text{O}_{\text{FLUID}}$ changes. The formation of the concretion has been shown to have initiated in the Paleocene, due to the isotopically depleted $\delta^{18}\text{O}_{\text{FLUID}}$ composition of the initial pore fluids, with the influence of heating due to earliest igneous activity influencing the temperature of precipitation of Z1. The subsequent evolution of pore fluids, proposed to be caused by exchange with the earliest Skye Lavas, and associated pore-fluid heating has been recorded in the transition to Z2, which has the greatest volume of cementation. The outermost zone appears to record a reduction in meteoric water-rock exchange with lavas, implying fluid transport through fractures within the lava. This also changes the assumption made by Wilkinson (1993) that pore fluids were near-stagnant; fluid movement within the sand-body was necessary to allow the pore-fluid evolution seen.

As compaction of the Valtos Sandstone by a significant thickness of lava (up to 1200 m; England, 1994; Emeleus and Bell, 2005) must have occurred after most, if not all, of the concretions were formed, including VR1 which had visible deflection of lamination when *in situ* (Fig. 4.11; Fig. 4.15), the rate of concretion cementation must be re-evaluated. Previous modelling by Wilkinson and Dampier (1990) concluded that a Valtos Sandstone concretion of radius 0.5 m would have taken >6 Ma to form if in stationary pore fluids, and ~4 Ma with pore fluids moving at a rate of 5 m a⁻¹. The constraint of precipitation initiation contemporaneous with earliest igneous events on Skye (the Portree Hyaloclastite), then fluid interaction with earliest Lavas in Z2 but termination of growth before compaction due to more significant emplacement of lava, indicates that cement precipitation was much more rapid than previously modelled. The emplacement of the full extent of the lavas is thought to have occurred within 1.6 Ma (Hamilton et al., 1998), thus concretion formation and subsequent sandstone compaction must have occurred within a fraction of this time.

4.4.2: Wider context: other cements Valtos Cliffs.

In order to put the VR1 concretion data into a wider paragenetic context, other samples from the Valtos cliff locality were measured using clumped isotopes. These included vein-fed sparry calcite cements that post-dated concretion formation, but also *Neomiodon* limestones which were analysed as both whole rock and separated sparry calcite cement components. The results are given in Table 4.4 and plotted on Figure 4.24.

Veins from bed 3 (Harris and Hudson, 1980; the horizon of VR1 and associated concretions) with clear cross-cutting relationship to the concretions were sampled. The first (189-1) was from a concretion ~2 m diameter from the same horizon as VR1. Here a sparry calcite filled fracture cross-cuts the concretion, clearly post-dating it. Calcite from this vein gave a Δ_{47} temperature of 67 ± 10 °C and a derived $\delta^{18}\text{O}_{\text{FLUID}}$ value of $+4.1 \pm 1.5$ ‰ VSMOW. These results are similar to those of Z2 in concretion VR1, again indicating a hot, evolved fluid. The $\delta^{13}\text{C}$ was 0.1 ‰ VPDB, again consistent with carbon sourced from dissolving *Neomiodon* shells.

The second vein samples come from the margins and interior of a small dyke (Fig. 4.17) about two metres from the first vein. These veins are filling intrusion-parallel fractures that opened sometime (unconstrained) during or after cooling of the dyke and are likely to postdate concretion formation by a substantial period of time, probably hundreds of thousands of years. Three samples were taken (see Fig. 4.17). Samples 189-5v and 189-7a come from two generations of calcite that filled a fracture 5 cm wide within the dyke, while sample 189-6 comes from a 2-5 mm thick vein filling a fracture between the wall of the dyke and the host sandstone (Fig. 4.17). We assume the opening of the fractures was caused by cooling and contraction. Samples 189-5v and 189-6 gave Δ_{47} temperatures of 52 ± 10 °C and 40 ± 10 °C with pore fluid values of -12.7 ± 1.7 ‰ VSMOW and -13.8 ± 1.9 ‰ VSMOW respectively. This former calcite (sample 189-5v) is intergrown with a brown fibrous smectite (possibly saponite) as identified by X-Ray diffraction (J.E. Andrews, pers. comm., 2021). A Sr isotope measurement was also taken from the earliest part (sample 189-7a) of the vein, giving a value of 0.709941 ± 0.000007 , which overlaps values found in the VR1 cements, suggesting that carbonate was similarly sourced from dissolving Jurassic shell carbonate or limestones (Fig. 4.28). These temperatures indicate that both generations of vein calcite formed after the dyke had cooled substantially from its emplacement temperature; they are also cooler than the maximum cementation temperatures reached during VR1 (Z2) cementation. The pore fluid $\delta^{18}\text{O}_{\text{FLUID}}$ values are consistent with a fracture-fed source from isotopically negative Paleocene meteoric water (Taylor and Forester, 1971), the water having relatively low interaction (high water/rock ratio) with the host sandstone. The presence of smectite suggests that the water interacted with some silicate during transit, either rocks of basaltic composition or mudstones in the overlying GEG. A similar association between calcite cement and smectite has been noted at Duntulm Foreshore/Lon Ostatoin (J.E. Andrews, pers. comm., 2021) and it may be associated with intrusion of the Little

Minch Sill Complex which post-dated lava emplacement (Gibson, 1990; Gibson and Jones, 1991; Fowler et al., 2004). Sample 189-6 was taken from the dyke margin in contact with the host sandstone (Fig. 4.17) and gave the coolest temperatures (24 ± 8 °C) for this locality, and the most negative pore fluid values (-16.5 ± 1.6 ‰ VSMOW). This fracture was clearly cemented after cooling of the lava pile and presumably following some regional exhumation - a geotherm of 40 °C km^{-1} and surface temperature of 13 °C – based on earliest Mid-Paleocene paleoflora evidence from Mull (Poulter, 2011) – suggests burial at ~ 300 m).

Considered together, these vein samples demonstrate a wide range of temperatures and water/rock interaction. While the latter is probably controlled by crack geometry and connectivity, it is likely that the hotter fluids were introduced first, and heating might have been related to intrusion of the Little Minch Sill Complex, which is well developed in this part of Trotternish (Gibson and Jones, 1991; Schofield et al., 2016).

To better understand the spatial context of cementation we also sampled from two fallen blocks of *Neomiodon* limestone, one of which displayed a well-developed ferroan calcite vein. These limestones are inaccessible in the Valtos cliffs but very distinctive lithologies. It is most likely the blocks were from bed 7 which is stratigraphically about 10 m above bed 3 (Harris and Hudson, 1980). Alternatively, the block could have derived from bed 17 about 20 m above bed 3 (Harris and Hudson, 1980).

This limestone allowed for a number of sampling strategies, a whole-rock approach, a cement only approach and also sampling of the vein which clearly post-dated the main phase of shell-bed cementation.

The whole rock sample avoided both vein calcites and vuggy areas of sparry calcite (e.g., in shelter porosity within articulated shells) but integrated calcite from both the calcite-replaced *Neomiodon* shells, and the main phase of post-compactional ferroan sparry calcite cementation (Hudson and Andrews, 1987). This was adopted as it was not possible to separate these components by drilling, but the assumption (based on petrography in Hudson and Andrews, 1987) was that the sample would broadly represent the post-compactional ferroan sparry calcite cement. This sample gave a Δ_{47} temperatures of 94 ± 8 °C, and an enriched $\delta^{18}\text{O}_{\text{FLUID}}$ composition of $+5.5 \pm 1.1$ ‰ VSMOW. These results are most similar to those from Z2 of concretion V1 and we infer that this phase of ferroan spar cementation was essentially coeval with concretion formation.

In the second sampling approach we drilled-out vugs of pure sparry calcite from shelter porosity within articulated *Neomiodon* shells. For this spar the Δ_{47} temperature was 42 ± 6 °C and the $\delta^{18}\text{O}_{\text{FLUID}}$ value was $-14.5 \pm 1.1\%$ VSMOW. These results are essentially identical to those from the post-cementation vein sample (18-4bulk), a ferroan sparry calcite with Δ_{47} temperature of 40 ± 9 °C and a $\delta^{18}\text{O}_{\text{FLUID}}$ values of $-14.2 \pm 1.6\%$ VSMOW. We conclude that the vug-filling and vein cementation were the same phase, an approach borne out by subsequent CL petrography (Fig. 4.29). The cooler temperatures of these vein-fed cements confirm their formation after the main phase of post-compactional cementation described above, presumably later in the Paleocene after a period of cooling, perhaps during basin inversion. The fluid compositions are in keeping with other assumed Paleocene meteoric water sourced values measured in this study (See Table 4.4 and Fig. 4.24).

To try and ensure our interpretations above were robust we also investigated whether the 'hot whole rock' data could be explained as an artefact of mixing calcite phases (cf. Defliese and Lohmann, 2015). These authors showed that mixing two cements with differing $\delta^{13}\text{C}$ and $\delta^{18}\text{O}$ values can have a substantial effect on measured Δ_{47} and thus on temperature estimation. Using their model for Δ_{47} non-linearity by two component mixing, the hypothesis that the 'whole-rock' calcite temperature result was hotter than its true value due to mixing was tested. For a first approach, the vein-hosted vuggy calcite described above was used as one end member (EM1) and calcite-replaced *Neomiodon* shells were the second (EM2), with average $\delta^{18}\text{O}$ and $\delta^{13}\text{C}$ taken from Tan and Hudson (1974) and a Δ_{47} value that corresponded to ~ 70 °C, an estimation that assumes the end member was close in composition to Z2 values (as $\delta^{18}\text{O}_{\text{CARBONATE}}$ values are similar). In a second approach, EM2 was considered an unknown, but $\delta^{18}\text{O}$, $\delta^{13}\text{C}$ and δ_{47} (and thus Δ_{47}) were interpolated due to their linear relationships between endmembers, using values measured from the 'whole-rock' calcite sample and estimates of the percentage of EM1 and EM2 (by area) within the 'whole-rock' sample. Neither experiment indicated that the temperatures derived from Δ_{47} could be explained by two component mixing, all digressions from linearity resulting in negative temperature shifts. We note however, that CL petrography also shows that at least part of the sample contained more than 2 cement generations, beyond the resolution of sampling and beyond the capacity of simple mixing models (Fig. 4.29).

Overall, we conclude our initial interpretation is correct and that this *Neomiodon* limestone was mainly cemented by fluids with high temperature and elevated $\delta^{18}\text{O}_{\text{FLUID}}$

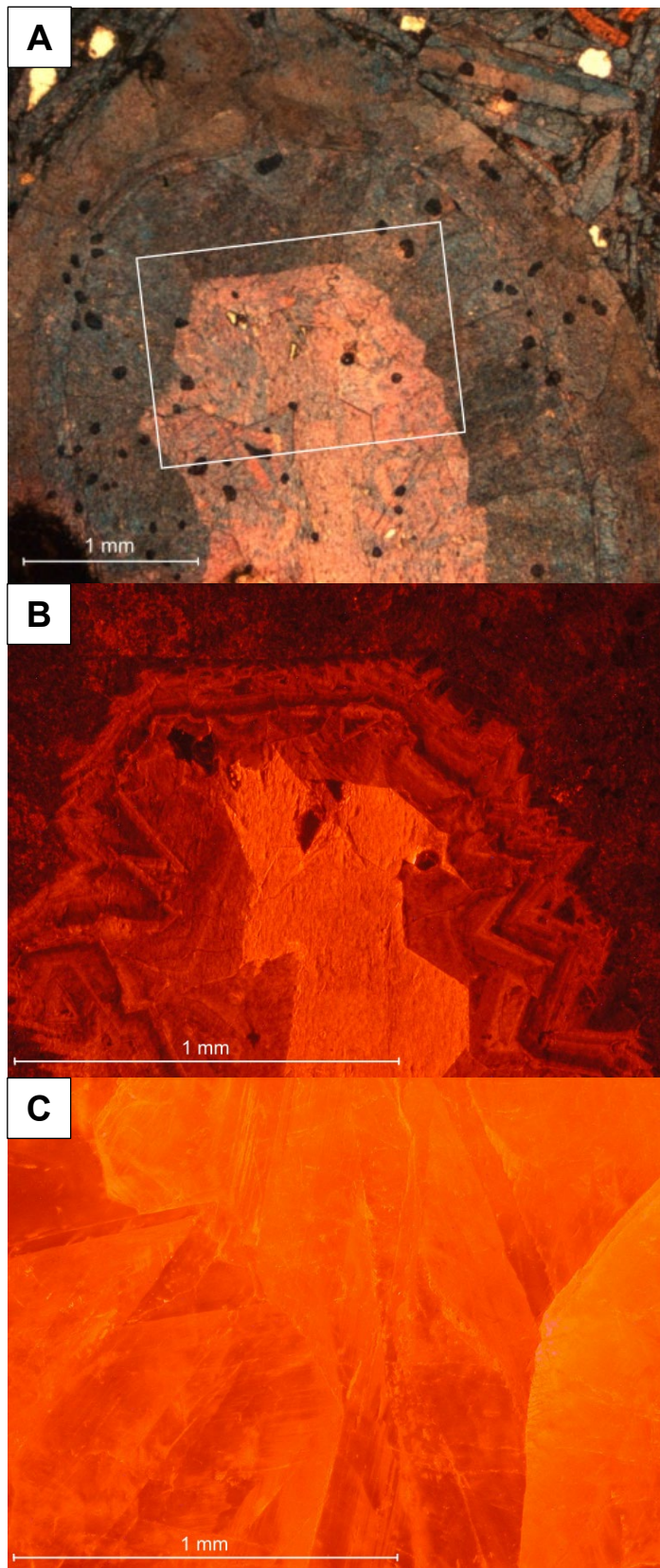


Figure 4.29: Petrography of sparry calcite cements in the shelter cavity of an articulated *Neomiodon* sp. shell (Sample 76861, equivalent to Sample 189-8) Valtos Cliffs, Skye. A) PPL image of stained thin section; note pink colour of the final cavity filling cement (non-ferroan) versus the blue colour (ferroan) of the penultimate cement generation; B) CL image of centremost cements showing bright orange CL colour of the final cement fill. It is assumed that drilling for $\Delta 47$ sampled mainly the bright orange CL final cement fill as drilling was targeted in the centre of the cavity; C) bright orange CL colour of vein cements in Sample 18-4 similar to that in B).

values, a cement precipitated at a similar time to those in Z2 of concretion V1; later, cooler, vein-fed fluids infilled the vuggy-shelter porosity that had been uncemented by the first (hot) phase of ferroan calcite cementation.

4.4.2.1: Summary of wider context: other cements Valtos Cliffs:

Non-concretionary measurements from the Valtos Sandstone at Valtos Cliffs give a range of results; warm and evolved pore fluid is associated with a vein on the edge of a concretion and for the bulk measurement of a well cemented *Neomiodon* spar bed. Other cements have a depleted meteoric pore fluid source, with $\delta^{18}\text{O}_{\text{FLUID}}$ values between $-12.7 \pm 1.7\text{‰}$ and $-14.5 \pm 1.1\text{‰}$ for higher temperature cements ($40 \pm 10\text{ °C}$ to $52 \pm 10\text{ °C}$) and $-16.5 \pm 1.6\text{‰}$ for lower temperature cement ($24 \pm 8\text{ °C}$). These values seem to add to evidence that supports unusually depleted pore fluids for the Paleocene (as suggested by Taylor and Forester, 1971; Forester and Taylor, 1977), and indicates that the $\delta^{18}\text{O}_{\text{FLUID}}$ values seen at the centre of concretion VR1 are not unusual for cements at this locality. The $\delta^{18}\text{O}_{\text{FLUID}}$ values from the majority of veins and vugs are more negative than those proposed by Taylor and Forester (1971) and may imply either an orographic effect or a rainout (amount) effect consistent with a high relief landscape post-lava deposition, with $-16.5 \pm 1.6\text{‰}$ VSMOW as a minimum value measured for Paleocene meteoric water in North Skye.

4.4.3: Wider context: other concretions of the Valtos Sandstone Formation

The Valtos Sandstone Formation has a wide area of outcrop (Fig. 4.2; Harris and Hudson, 1980; Harris, 1992), from Trotternish and Waternish in North Skye, through Raasay and Strathaird to the southern localities of the Small Isles (Eigg and Muck). To better understand the basin-wide context for Valtos concretion VR1, we sampled more concretions in the southern part of the basin on the Isle of Eigg, approximately 75 km south of Valtos. In addition, the Eigg concretions were sampled from near the top of the formation, whereas VR1 was located close to the base of the formation. Earlier stable isotope work on the Valtos concretions (basin-wide) had been performed by Tan and Hudson (1974), followed up by the more detailed studies of Wilkinson (1989, 1992, 1993) who also worked at Valtos and on Eigg.

In this section we mainly describe results (Table 4.3) from concretions collected from Laig Bay (Isle of Eigg) and also a concretion collected from Dun Dearg (Trotternish), near Valtos. This latter sample is from bed 38 (Harris and Hudson, 1980), stratigraphically about 40 m above VR1, so helps constrain any possible stratigraphic variation.

At Laig Bay, there are several different concretionary cementation styles that occur within the concretionary horizon of Division E (Harris and Hudson, 1980): large, spherical concretions similar to VR1 (Fig. 4.6; Fig. 4.19); decimetre-scale spherical concretions (Fig. 4.6, Fig. 4.20; average radius: 11.8 cm; Wilkinson, 1992); cemented dyke margins (Fig. 4.6, Fig. 4.21; described by Hudson and Andrews, 1987). There are also calcitic veins, which, although rather friable due to weathering, occur within the otherwise very poorly cemented sandstones. Some of these veins are closely related to dykes, frequently running parallel to the intrusion (Fig. 4.8). Clumped isotope analysis was undertaken on three parts of one large concretion, three decimetre-scale concretions and a sample of cemented dyke margin.

Results from these concretions are shown on Figure 4.24 and Figure 4.30, while the data is in Table 4.3. Three measurements (roughly centre, intermediate, outer edge, Fig 19) from a large concretion from Eigg give values between 68 ± 7 °C to 98 ± 9 °C, and isotopically enriched pore fluid $\delta^{18}\text{O}$, between $+2.7 \pm 1.1\%$ and $+7.2 \pm 1.2\%$ VSMOW. The single sample from a Dun Dearg concretion (EG191015-1) gave a similar temperature of 64 ± 9 °C, and a derived $\delta^{18}\text{O}_{\text{FLUID}}$ composition of $-1.8 \pm 1.4\%$ VSMOW. These results are consistent with those from Z2 in concretion VR1. They indicate that the high temperatures and enriched pore fluids were a basin-wide phenomenon, or at least, when there were points of entry for hot water, enabled where lava directly overlaid the eroded top of the Valtos sandstone, as in Trotternish and Eigg. These results also show that this style of concretionary cementation occurred throughout the thickness of the Valtos Formation.

The decimetre-scale concretions on Eigg (Wilkinson, 1992) give rather different Δ_{47} values to those from the larger concretions (Fig. 4.30). The Δ_{47} temperatures are generally cooler (13 ± 6 °C to 35 ± 6 °C; averaging 24 °C) with derived pore fluid $\delta^{18}\text{O}$ values of $-6.2 \pm 1.1\%$ to $-10.1 \pm 1.3\%$ VSMOW, averaging -8.1% VSMOW. The pore fluid compositions are not negative enough to be of Paleocene age (-12% , Taylor and Forester, 1971; $-11.1 \pm 1.1\%$ to $-16.5 \pm 1.6\%$, this study), and they are slightly lower than the expected range of Jurassic meteoric pore fluids (-4 to -6% , Hudson and Andrews, 1987; Searl, 1992; -7% ,

Emery et al., 1988). Estimates for Cretaceous pore fluids encompass the range seen (-4 to -6‰, Robinson et al., 2010; -8‰, Hendry, 1993; -5.5 to -11‰ from modelling studies, see references in Table 4.5). We can be sure they formed before the emplacement of the Tertiary dykes as these crosscut the sandstone unit that host the concretions (Fig. 4.31). This suggests that the concretions formed before the Paleocene, (Wilkinson, 1992) possibly during the Lower Cretaceous. It seems likely that these concretions were formed much earlier than the larger concretions, under shallow burial (<200 m), a hypothesis that is supported by the lower temperatures.

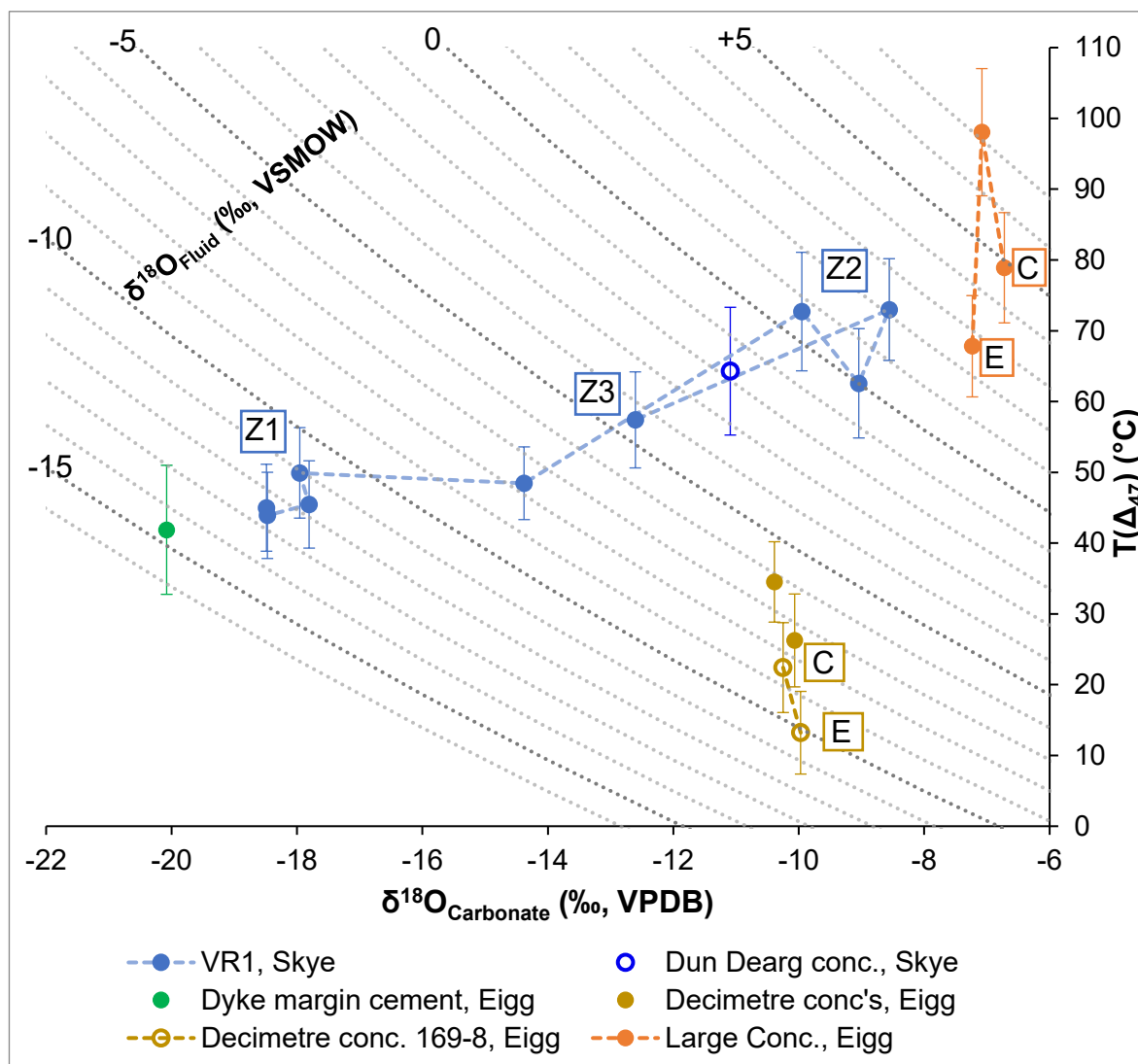


Figure 4.30: Clumped isotope results for all concretions from the Valtos Sandstone of Skye and Eigg. Error bars represent one standard error of the pooled standard deviation. The $\delta^{18}\text{O}_{\text{CARBONATE}}$ errors are < symbol dimensions. Z1 to Z3 indicate zones for concretion VR1; C and E correspond to centre and edge.



Figure 4.31: Decimetre-scale concretion at Laig Bay, Eigg, showing the concretion's proximity to a dyke and its location within the cemented sandstone dyke margin, which therefore must have succeeded concretion formation. Hammer handle 35 cm long.

One small concretion was measured twice, towards the apparent centre of the concretion and towards the outer edge, although this concretion was sub-spherical. Due to the morphology of this concretion, however, it is uncertain without more measurements whether the point taken as 'centre' is true. However, if taken as so, a weak centre to edge trend is recorded, as was found by Wilkinson (1992) for several other concretions, with the centre having a slightly more negative $\delta^{18}\text{O}$ and $\delta^{13}\text{C}$, and possibly a decreasing trend in $\delta^{18}\text{O}_{\text{WATER}}$ and temperature, although the latter results for these are within error of one another. This concretion has the most negative $\delta^{18}\text{O}_{\text{WATER}}$ values of the three measured, with lowest values from the edge of the concretion.

All concretions studied on Eigg in this study (and by Wilkinson, 1992) give distinctly different results to a nodular concretion sampled from a 60 cm wide zone of cementation adjacent to a Tertiary dyke margin (Fig. 4.24 and Fig. 4.30). This cement gave a Δ_{47} temperature of 42 ± 9 °C, and a derived $\delta^{18}\text{O}_{\text{FLUID}}$ value of $-14.6 \pm 1.7\%$ VSMOW. The sample was taken from the fully cemented horizon (see description in Hudson and Andrews, 1987) within a few centimetres of the dyke margin. It had been assumed that this zone of cementation was related to the intense heating from the dyke (Hudson and

Andrews, 1987), an interpretation apparently supported by very negative calcite $\delta^{18}\text{O}$ values (-13.8‰ and -17.2‰; Wilkinson, 1992). However, the Δ_{47} temperatures in this study show that these cements were formed by warm fluids with a negative, Paleocene, meteoric water composition. It seems likely that the zone of cementation is not related to heating effects, but rather to the palaeohydrology of the zone adjacent to the dyke. It is suggested that cementation had been focused along the vertical dyke wall (a vertical aquitard), possibly exploiting fractures that developed in the host sandstone as the dyke cooled. In support of this there are numerous calcite-filled veins that run parallel to the dyke within the zone of cementation, and it is plausible that these fractures were the conduits for the cementing fluid. It is noted that the temperature and fluid composition of this calcite is within the range of the calcites from veins associated with a dyke at Valtos (see above).

4.4.3.1: *Comparison with previous work:*

Previously published $\delta^{18}\text{O}_{\text{CARBONATE}}$ and $\delta^{13}\text{C}$ measurements from Wilkinson (1989, 1992, 1993) are plotted against our concretion results (Fig. 4.32). Through the use of our Δ_{47} derived temperature and fluid measurements we can make interpretations of these results in the context of the constrained temperatures. Tan and Hudson (1974) did not report individual concretion values but provided maximum, minimum and average for the concretions they measured in Trotternish, Waternish and Eigg; these largely overlap the data from Wilkinson and so are not shown on Figure 4.32.

Figure 4.32 shows four distinct data fields that approximately correspond to the measurements of the Valtos Cliffs spherical and basal concretions, the Eigg large concretions and the smaller Eigg decimetre-scale concretions.

Data from the large concretions are overall more complex. Our $\delta^{13}\text{C}$ and $\delta^{18}\text{O}_{\text{CARBONATE}}$ measurements of VR1 Z2, the Dun Dearg concretion and the large Eigg concretion plot in similar isotopic space to previous measurements of large concretions (excluding P3 of the large concretion measured by Wilkinson, 1989). It is unclear whether the results from Trotternish from Tan and Hudson (1974) include a mixture of spherical and 'basal' tabular concretions; basal concretions, which we have not measured with clumped isotopes, mostly give values for $\delta^{18}\text{O}_{\text{CARBONATE}}$ between -8‰ and -15‰, with only a few outliers giving more negative values. Without clumped isotope analysis, further interpretation of these concretions is poorly constrained. However, they plot mostly

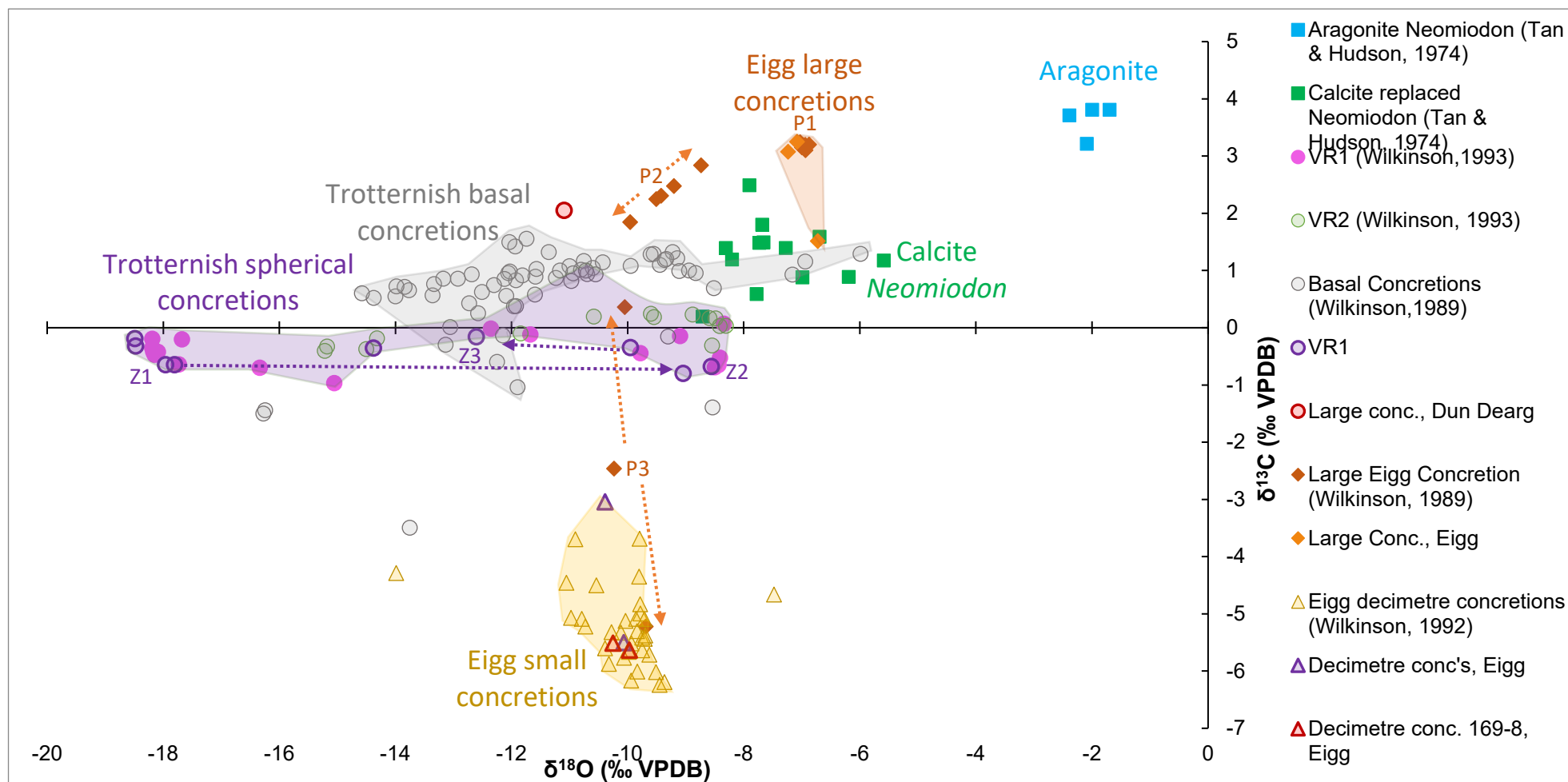


Figure 4.32: Comparison of $\delta^{13}\text{C}$ and $\delta^{18}\text{O}_{\text{CARBONATE}}$ of Valtos concretions from Skye and Eigg for the present study and Wilkinson (1989, 1992, 1993) and Tan and Hudson (1974). Figure includes values for original aragonite and calcite replaced *Neomiodon* shells from Tan and Hudson (1974). P1-3 correspond to zones from the large Eigg concretion analysed by Wilkinson (1989) and Z1-3 correspond to zones within concretion VR1.

between $\delta^{18}\text{O}_{\text{CARBONATE}}$ isotopic values of Z2 and Z3, or possibly the transitional outer edge measurement of Z1, suggesting they would give similar warm temperatures and evolved pore fluid compositions. Definition between Trotternish spherical and basal concretion regions is primarily defined by $\delta^{13}\text{C}$, as the majority of the Basal concretions show higher $\delta^{13}\text{C}$ values, as does the concretion from Dun Dearg.

Data from the large concretions are overall more complex. Our $\delta^{13}\text{C}$ and $\delta^{18}\text{O}_{\text{CARBONATE}}$ measurements of VR1 Z2, the Dun Dearg concretion and the large Eigg concretion plot in similar isotopic space to previous measurements of large concretions (excluding P3 of the large concretion measured by Wilkinson, 1989). It is unclear whether the results from Trotternish from Tan and Hudson (1974) include a mixture of spherical and 'basal' tabular concretions; basal concretions, which we have not measured with clumped isotopes, mostly give values for $\delta^{18}\text{O}_{\text{CARBONATE}}$ between -8‰ and -15‰, with only a few outliers giving more negative values. Without clumped isotope analysis, further interpretation of these concretions is poorly constrained. However, they plot mostly between $\delta^{18}\text{O}_{\text{CARBONATE}}$ isotopic values of Z2 and Z3, or possibly the transitional outer edge measurement of Z1, suggesting they would give similar warm temperatures and evolved pore fluid compositions. Definition between Trotternish spherical and basal concretion regions is primarily defined by $\delta^{13}\text{C}$, as the majority of the Basal concretions show higher $\delta^{13}\text{C}$ values, as does the concretion from Dun Dearg.

No other concretions give $\delta^{18}\text{O}$ results as negative as VR1; it is possible that this concretion nucleated and began cementing earlier than any of the others analysed and is thus the only one which recorded the pore fluid composition before lava emplacement. The large concretion from Eigg measured by Wilkinson (1989) is also an outlier, with three growth 'phases' identified (P1, P2, P3), where both $\delta^{18}\text{O}$ and (particularly) $\delta^{13}\text{C}$ evolve. We do not see such a trend in $\delta^{18}\text{O}_{\text{CARBONATE}}$ from the large concretion we sub-sampled, and although the centre of the concretion has $\delta^{13}\text{C}$ values $\sim 1.5\text{‰}$ lower than measurements closer to the edge, this is the opposite trend to that measured by Wilkinson (1989).

4.4.3.2: *Summary of wider context: other concretions of the Valtos Sandstone Formation:*

Large concretions analysed by clumped isotope analysis from Dun Dearg, Trotternish and Laig Bay, Eigg have similarly enriched pore fluid values and high temperatures to VR1 Z2. In keeping with the interpretations for VR1, this indicates that these concretions formed from fluids that had undergone heating and experienced water

rock interaction with Paleocene lavas. As previously described, both Trotternish and Eigg have locations where lava directly overlies the eroded top of the Valtos Sandstone Formation, providing a potential entry point for such pore fluids. The fact that this composition appears to be the most common, when comparing both new Δ_{47} measurements and previous $\delta^{18}\text{O}_{\text{CARBONATE}}$ measurements (Fig. 4.32), might indicate that at this point in basin evolution there was enhanced pore fluid ingress and conditions that were more propitious for concretion nucleation. This might indicate that the local Paleocene climate was particularly wet, in agreement with paleoflora evidence from Skye (Poulter, 2011). More speculatively, it may be that concretion nucleation was initiated by attainment of a critical (high) temperature; no large concretion records a temperature below 44 ± 6 °C.

4.4.4: Wider context: Other cements from Skye and Eigg

To put the results from the Valtos Sandstone Formation into a basinal, burial diagenetic context, we compare here, results (Table 4.4) from other burial diagenetic cements from Skye and Eigg. These samples were taken from sandstones, limestones and veins in sediments from the Lealt Shale Formation (Lonfearn Member and Kildonnan Member) and the Duntulm Formation stratigraphically below and above the Valtos Sandstone Formation respectively. We focused on samples where it was possible to sample just the cement phase, which for limestones in particular, restricted the sampling to either vuggy or fracture-fill (veins) calcites. Figure 4.24 A shows a comparison of $\delta^{18}\text{O}_{\text{CARBONATE}}$, temperature and $\delta^{18}\text{O}_{\text{FLUID}}$ with results from Skye, and Figure 4.24 B shows results from Eigg.

4.4.4.1: Trotternish, Skye:

Samples from the Duntulm Formation in Trotternish came from Duntulm foreshore, Lon Ostatoin and Kilmaluag Bay (Fig. 4.2). The most complete set of data comes from Lon Ostatoin, sampled from a range of lithologies and using the bed numbers of Andrews and Walton (1990). Two samples of ferroan sparry cement in sandstones (sample 17-1 from bed 5; sample 17-2 from bed 23) gave temperatures of 28 ± 7 °C and a $\delta^{18}\text{O}_{\text{FLUID}}$ value of -12.8 ± 1.4 ‰ VSMOW, and 58 ± 9 °C and -11.1 ± 1.4 ‰ VSMOW respectively. While the bed 23 temperature is consistent with warmer temperatures in concretion VR1, the fluid composition does not reflect extensive water/rock interaction.

The Lon Ostatoin locality is situated within a few hundred metres of a thick dolerite intrusion and it is possible that the warm temperature has been caused by localised heating of groundwater that routed through the permeable sandstone. A sample of vug-filling sparry calcite cement from an intra-shell (*Praeexogyra hebridica*) cavity from bed 19 (oyster-rich limestone), sample P22-LR, gave a temperature of 23 ± 6 °C, with a $\delta^{18}\text{O}_{\text{FLUID}}$ fluid value of -12.8 ± 1.1 ‰ VSMOW. This result shows that the final stage of cementation of this limestone was affected by meteoric water of likely Paleocene origin (fluid $\delta^{18}\text{O}$ composition) and probably at relatively shallow burial depth, perhaps during basin inversion. Spar-filled fractures (TR-1609) in a microbial limestone from nearby North Duntulm (bed 20, Andrews and Walton, 1990) gave a similar ‘cool’ result (single measurement indicates temperatures of 32 ± 13 °C and $\delta^{18}\text{O}_{\text{FLUID}}$ of -14.5 ± 2.5 ‰ VSMOW). The fractures clearly post-date the lithification of this limestone, such that a Paleocene timing for calcite mineralization is considered likely. Distinctive white calcite veins (Fig. 4.22) from bed 3 at Kilmaluag Bay (samples 199-1 and 199-2) must be of Paleocene or younger age as they crosscut the Duntulm Formation sediments, an intruded dolerite Tertiary sill and vuggy mineralization in the dolerite. These calcites gave temperatures of 32 ± 8 °C and 42 ± 8 °C and $\delta^{18}\text{O}_{\text{FLUID}}$ values of -12.3 ± 1.6 ‰ and -10.9 ± 1.5 ‰. The latter is the highest $\delta^{18}\text{O}_{\text{FLUID}}$ result from cements known to be Paleocene or later, although both values are within error of each other, and similar $\delta^{18}\text{O}_{\text{FLUID}}$ values were recorded for a Duntulm Formation sandstone cement (11.1 ± 1.4 ‰ for sample 17-2, discussed above). In addition, a fibrous calcite vein (18-9x) from the Lonfearn Member (Lealt Shale Formation) at Rubha nam Brathairean (Fig. 4.2) gave very similar temperatures (29 ± 9 °C to 32 ± 9 °C) to those from the Duntulm Formation, albeit with less negative $\delta^{18}\text{O}_{\text{FLUID}}$ values (-8.3 ± 1.7 ‰ to -9.6 ± 1.7 ‰ VSMOW), perhaps indicating greater water/rock interaction.

Sparry calcite fills from mudstone hosted concretions, including those reported in Chapter 3 from the lower Kimmeridgian Staffin Shale Formation are also included in Figure 4.24a. As reported in Chapter 3, there is considerable heterogeneity in some of these spars, particularly with respect to $\delta^{18}\text{O}_{\text{FLUID}}$ values. This is possibly due to porosity limitation of both the hosting mudstone sediment and the concretion itself, meaning that pore fluids were able to infiltrate the concretion fractures at different stages of uplift and burial and may have recorded different degrees or episodes of meteoric pore fluid displacement (Hendry et al., 2006; Paxton et al., 2021), regardless of being within the same sedimentary unit. One additional vug-cementing sparry calcite (18-7y) was

sampled from a mudstone hosted concretion in bed 3 of the Lonfearn Member at Rubha nam Brathairean (Fig. 4.2). This spar was the only example of a high temperature and enriched fluid measured outside of the Valtos Sandstone Formation (59 ± 8 °C, $\delta^{18}\text{O}_{\text{FLUID}}$ of $-0.2 \pm 1.3\%$ VSMOW). It is possible that this spar was precipitated from hot waters that have escaped via fractures from the overlying Valtos Sandstone.

4.4.4.2: Eigg:

Samples of cements were collected from the type section of the Kildonnan Member (Lealt Shales) on the east coast of Eigg (Hudson et al., 1995) as part of a wider study (Chapter 5). The data is discussed here (Table 4.4; Fig 4.24b) as it helps further constrain the burial diagenetic conditions of the Valtos Sandstone concretions.

Two samples were collected from bed 4A (Complex Bed of Hudson et al., 1995), both cements from sandstone layers (JEA-159-3, JEA-159-4). A third sample was from the fracture-filling sparry calcite of a bed 5F mudstone hosted concretion. As shown on Figure 4.24b, the results of all three samples are quite consistent, albeit rather distinct relative to most of the other cement data (also see Table 4.4). The Δ_{47} derived temperatures are between 43 ± 7 °C and 48 ± 9 °C, while the derived fluid $\delta^{18}\text{O}$ values are between $-1.1 \pm 1.5\%$ and $+1.0 \pm 1.2\%$. What these data show very clearly is that relatively hot water (up to 48 ± 9 °C) flowed through the fractures and porosity of the Kildonnan Member, even though shale-hosted aragonite shells are well-preserved (Hudson et al., 1995) within their encasing (aquitard) mudstones. The fluid compositions, while not diagnostic of Tertiary meteoric water, most likely represent such waters that had undergone water/rock interaction; one possible explanation is that they reacted with basaltic lithologies, as explained for the Z2 data from concretion VR1 (see above), before routing into the Kildonnan member through fracture and sandstone permeability. The high temperatures may be a remnant of the heated fluids from the Valtos Sandstone but could also represent precipitation at (close to) maximum burial temperature, which seems equally likely based on work in Chapter 5.

4.4.4.3: Eigg Lava Formation amygdaloids:

In a preliminary attempt to measure the temperature and isotopic composition of Paleocene meteoric water from amygdaloidal calcites from the Tertiary lavas, Matthew

Wakefield kindly sampled amygdales in a loose block of basalt from the Eigg Lava Formation at Laig Bay (SA-1 and SA-2). These calcites gave Δ_{47} temperatures of 28 ± 6 °C and 27 ± 6 °C and $\delta^{18}\text{O}_{\text{FLUID}}$ values of $-13.7 \pm 1.2\text{‰}$ and $-15.1 \pm 1.1\text{‰}$ VSMOW, values that help corroborate many of the calcite cement samples discussed above. The calcite precipitated when the lava had cooled considerably, and provides additional confirmation that Paleocene meteoric $\delta^{18}\text{O}$ values in the Inner Hebrides had unusually negative compositions.

4.5: Conclusions:

Clumped isotope analysis on a sandstone hosted concretion (VR1) from the Valtos Sandstone Formation which had 'anomalously low' $\delta^{18}\text{O}$ compositions (Wilkinson, 1993) has presented a more complex picture than previously assumed for concretion genesis. Using Δ_{47} derived temperature estimates and back-calculated pore fluid $\delta^{18}\text{O}$ compositions, a new hypothesis for concretion cementation is proposed.

The centre of the concretion (Z1) formed from Paleocene meteoric pore fluids at ~ 47 °C, under conditions of a higher-than-average geotherm (between 40 to 60 °C km^{-1}) and elevated water temperature due to earliest Paleocene Igneous Event activity. This zone of the concretion gave the most negative $\delta^{18}\text{O}_{\text{CARBONATE}}$ results of any Valtos concretion measurement studied previously by Wilkinson (1989, 1993) and Tan and Hudson, (1974) due to formation from negative meteoric sourced pore fluids ($-12.6 \pm 1.1\text{‰}$ to $-11.7 \pm 1.1\text{‰}$ VSMOW).

At the outermost edge of Z1, a transition began towards Z2 compositions, where evolved $\delta^{18}\text{O}_{\text{FLUID}}$ values (average $+0.9\text{‰}$ VSMOW) and higher temperatures (average 69 °C) were caused by hot water-rock interaction with basalts from the Skye Lava Group, although only a partial lava thickness is plausible, given arguments regarding timing of compaction and constraints relating to lava permeability. As more lavas were emplaced and the pile thickened, vertical fluid movement was controlled more strongly by fractures, increasing the water rock ratio and giving rise to the cooler and less evolved measurements found for Z3 (57 ± 7 °C; $-4.4 \pm 1.1\text{‰}$ VSMOW). Other large concretions from the Valtos Sandstone Formation at Dun Dearg, Trotternish and from the Isle of Eigg also show clumped isotope results similar to Z2. The Eigg decimetre scale concretions are outliers and are presumed to have precipitated pre-Paleocene, with less depleted pore

fluids (avg. -8.1‰ VSMOW) and low Δ_{47} derived temperatures (avg. 24°C) indicating formation at <100 m burial.

The large concretions formed much later than has been proposed in past studies (Wilkinson, 1989; 1993), and must have formed within < 1 Ma, far more rapidly than modelled previously (Wilkinson and Dampier, 1990).

Using a suite of other calcite cements from the associated Great Estuarine Group sediments of Skye and Eigg, the results from VR1 can be placed in a context of predominantly Paleocene cementation. The assumption that Z1 precipitated from meteoric pore fluids with values as low as $-12.6 \pm 1.1\%$, a value for Hebridean meteoric pore fluids previously postulated by Taylor and Forester (1971) and Forester and Taylor (1977), is strongly supported by measurements from other burial diagenetic cements. Most other sparry calcite and fibrous calcite cements within the Valtos Sandstone Formation and Duntulm Formation from Skye gave similar negative results, as negative as $-16.5 \pm 1.6\%$ VSMOW, and with a range of temperatures presumably caused by cooling in the region after the Skye Lava Group cooled. Amygdale calcite cement from the lavas also gave a value of $-13.7 \pm 1.2\%$ to $-15.1 \pm 1.1\%$ VSMOW, corroborating these interpretations.

It is worth noting that most of the high temperatures (>50 °C) come from cements within the large concretions of the Valtos Sandstone Formation: temperatures >50 °C are uncommon in most of the other cements studied. It seems plausible that the Valtos Formation sandstones were a high permeability conduit that transmitted hot, meteoric-sourced, shallow groundwater. It is possible that the hot water promoted calcite nucleation and concretion growth. In contrast, mudstone-dominated units like the Lealt Shale Formation and the Duntulm Formation, acted largely as aquitards, with fluid flow restricted to fractures and permeable sandy beds.

Chapter 5: Clumped isotopes in Middle Jurassic molluscan aragonite: time for a reset?

5.1: Introduction:

Stable isotope analysis of biogenic carbonate has been used to investigate numerous significant issues in geological history (e.g. Urey et al., 1951; Hudson and Anderson, 1989; Veizer et al., 1997, 1999; Zachos et al., 2001; Huck and Heimhofer, 2021). However, as discussed in Chapter 1, without independent constraints on either $\delta^{18}\text{O}_{\text{FLUID}}$ or precipitation temperature, assumptions are required to solve the 'palaeotemperature equation', leading to inherent uncertainties. In addition, some organisms display biogenically mediated disequilibrium isotope effects (vital effects) in the skeletal carbonate they precipitate (Urey et al., 1951). This further complicates the utility of stable isotopes in biogenic carbonates as a reliable record of temperature or other environmental conditions. Vital effects have been identified in a wide range of organisms including corals (e.g., Weber and Woodhead, 1970; Erez, 1978), echinoderms (e.g., Weber and Raup, 1966; Gorzelak et al., 2012), coccoliths (e.g., Ziveri et al., 2003), and foraminifera (e.g. Duplessey et al., 1970; Erez, 1978).

When the clumped isotope technique was pioneered, it was soon applied to paleoclimate/environment studies as it was thought that the abundance of ^{13}C - ^{18}O bonds in the precipitated skeletal carbonate were insensitive to 'vital effects' (Eiler, 2007; 2011). However, as more organisms were analysed, this early conclusion was proven to be untrue. Clear examples of clumped isotope vital effects have been found in some corals (e.g. Saenger et al., 2012; Spooner et al., 2016), echinoids (Davies and John, 2019), adult cephalopods (Davies et al., 2021), brachiopods (Bajnai et al., 2018) and juvenile marine bivalves (Huyghe et al., 2022). Recent developments with combined Δ_{47} and Δ_{48} analysis may allow calculation of 'true' Δ_{47} values from carbonates precipitated with vital effects (Bajnai et al., 2020; Fiebig et al., 2021) but this depends on high precision measurements of Δ_{48} which is not yet achievable in all laboratories.

Nonetheless clumped isotopes in skeletal carbonates remains a promising method to help understand palaeoenvironmental conditions (e.g., Price and Passey, 2013; Petersen et al., 2016; Bergmann et al., 2018; Evans et al., 2018; Henkes et al., 2018; Vickers et al., 2020, 2021; De Winter et al., 2021; Barney and Grossman, 2022; Letulle et al., 2022). Mollusc shells are a commonly analysed fossil due to their prevalence

throughout geological history (e.g., Petersen et al., 2016; Vickers et al., 2021; De Winter et al., 2021; Letulle et al., 2022). Calcitic shells are typically quite well preserved, particularly in Mesozoic and younger rocks, and the preservation of the less stable polymorph aragonite is a clear target if the mineral can be proven to be pristine. Excellent fossil aragonite preservation in limestones is not favoured, due to dissolution-precipitation reactions (neomorphism), which are known to affect $\delta^{18}\text{O}$ values and highly likely to affect Δ_{47} values (e.g., Staudigel and Swart, 2016). However, pristine aragonite shells, typically those encased in an impermeable clay-rich matrix, should preserve their environmental clumped isotope compositions, making them attractive for palaeoenvironmental studies. Recent clumped isotope measurements of unaltered aragonite shells have allowed insights into temperature change at the K-T boundary (Petersen et al., 2016; Tobin et al., 2021), Early Jurassic temperatures from arctic and mid latitudes (Letulle et al., 2022), and late Miocene – Pliocene temperatures of the Tibetan Plateau (Wang et al., 2021), among others.

The application of clumped isotopes to shells with proven pristine preservation from the GEG would therefore be desirable, not only to investigate the environmental conditions of growth, but also to help further evaluate the applicability of clumped isotope data from biogenic carbonates.

5.1.1: The Kildonnán Member and *Praemytilus strathairdensis*

Shells of *Praemytilus strathairdensis* (Anderson and Cox, 1948) are an extinct species of small bivalve molluscs (mussels), found exclusively within the Kildonnán Member of the GEG. The Kildonnán Member represents a lagoonal environment, the nature of which is described below. The shells were described in detail by Hudson (1968), who demonstrated their wholly aragonite composition and nacreous aragonite structure, which, through the observation of excess hydrogen, was also suggested to have trapped free water (Hudson, 1967). Shells are particularly well preserved at the type section, located 1.5 km north of Kildonnán on the Isle of Eigg (Hudson, 1966) (Fig. 5.1).

Shells from this locality have been extensively investigated in previous work. Carbon and oxygen isotope analysis of shells from bed 5 (all bed numbers from Hudson 1966, Hudson et al., 1995; Fig. 5.2) was undertaken by Tan and Hudson (1974), who noted a positive correlation between aragonite $\delta^{13}\text{C}$ and $\delta^{18}\text{O}$, suggesting that this was due to

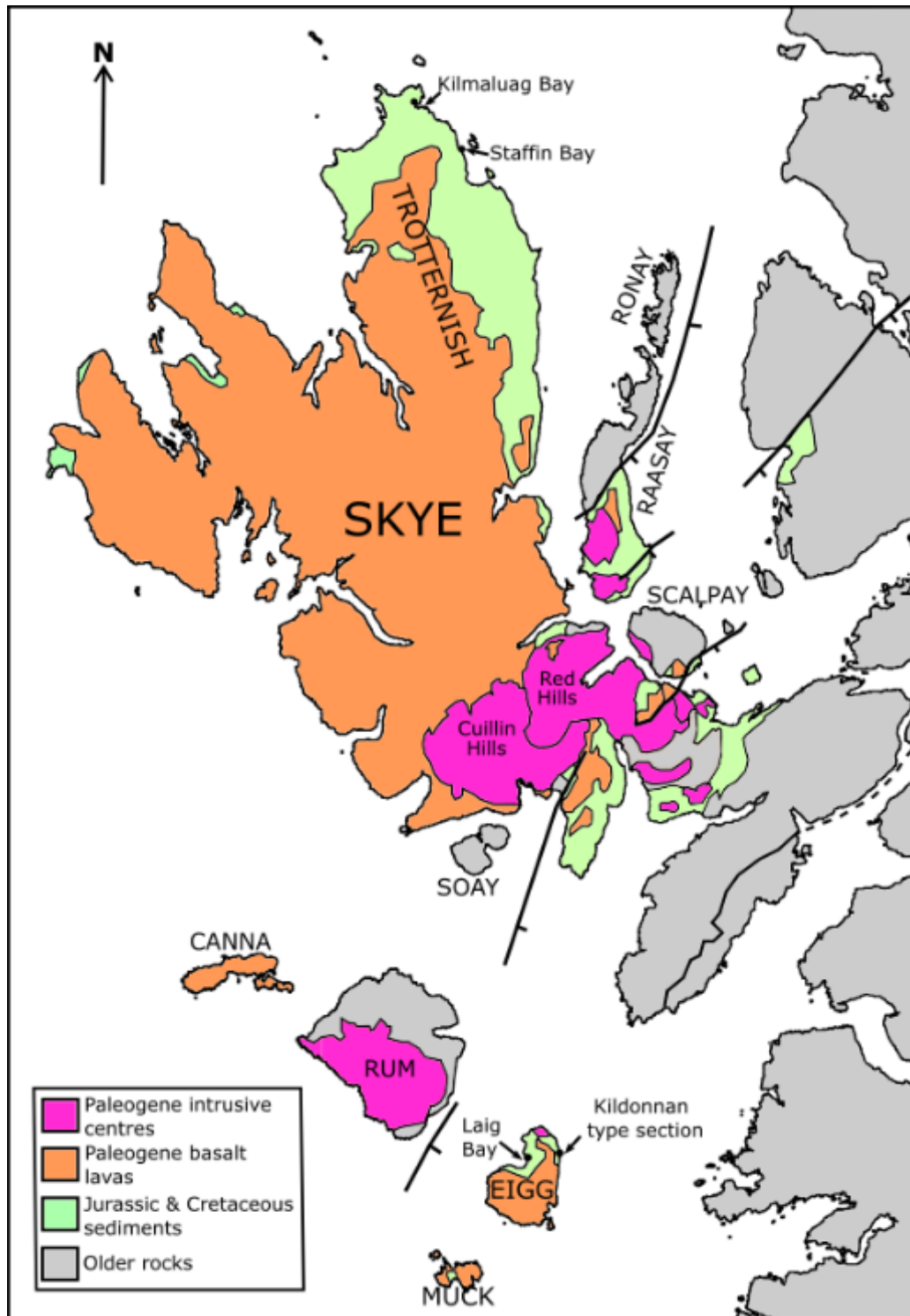


Figure 5.1: Map of Skye and the Small Isles, including Eigg, with sampling locations indicated by arrows. Map adapted from Thrasher (1992).

mixing between marine and less saline, meteoric-derived waters (with more negative $\delta^{18}\text{O}_{\text{WATER}}$ compositions) in a marine-brackish lagoonal system. Hudson (1970) described an algal (microbial) limestone, which contained calcite pseudomorphs after gypsum, which was taken to indicate the potential for the lagoon to become hypersaline as it dried out. Re-examining the previous isotopic data of Tan and Hudson (1974), salinities were

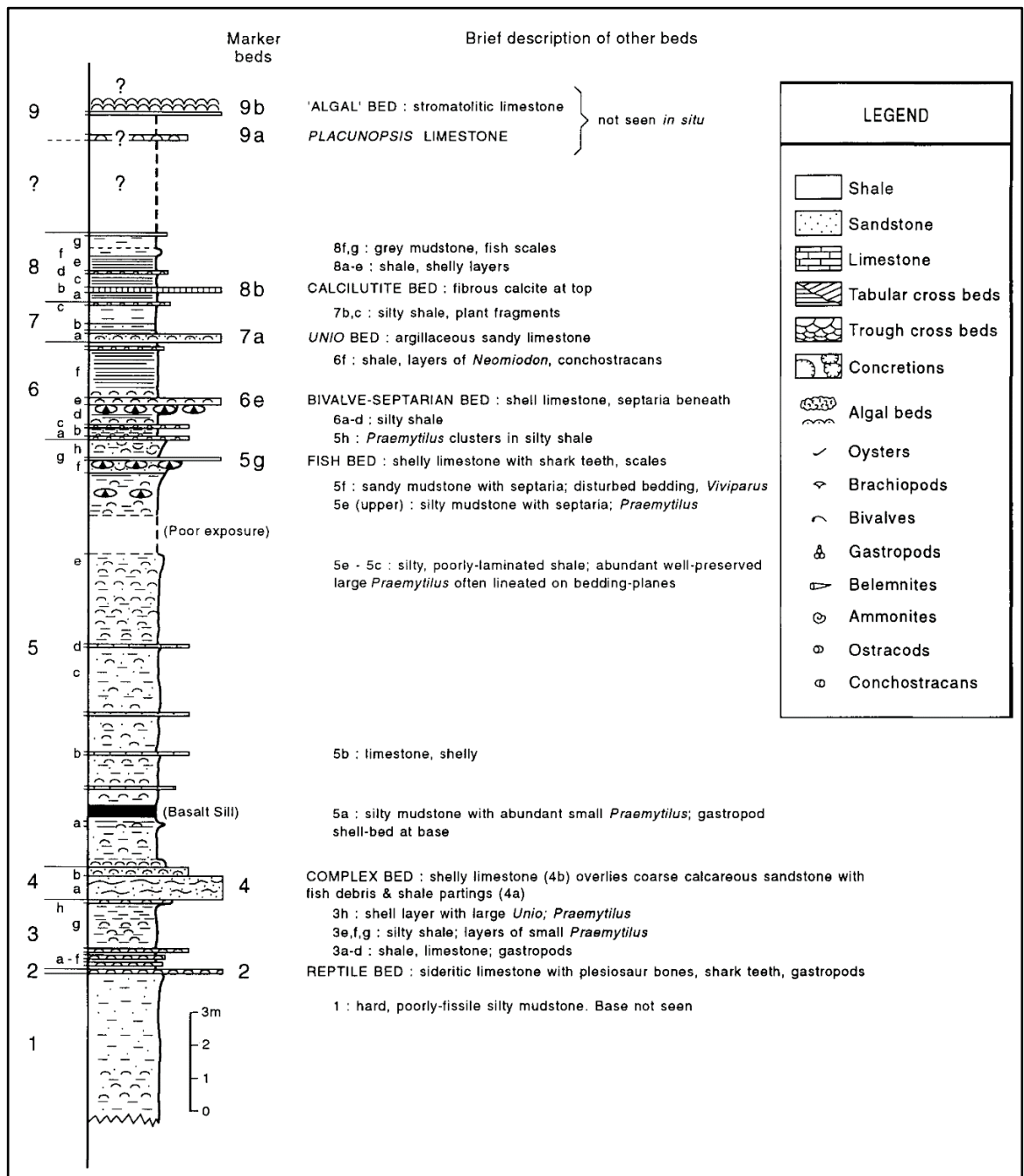


Figure 5.2: Graphic log of the Kildonnan Member at the type section (Eigg) after Hudson et al. (1995).

estimated for the two 'end members' of the positive $\delta^{13}\text{C}$ and $\delta^{18}\text{O}$ relationship, with 34‰ salinity suggested for the 'marine' shells, and 0‰ salinity estimated for freshwater, which was assigned a $\delta^{18}\text{O}_{\text{FLUID}}$ value of -6‰ VSMOW (Hudson et al., 1995).

Work studying other flora and fauna preserved within the Kildonnan Member also supported salinity variation within the lagoon (e.g., Hudson et al., 1995; Wakefield, 1995). Of note, Patterson (1999) studied the $\delta^{18}\text{O}$ and $\delta^{13}\text{C}$ of fish otoliths from bed 3g, finding that samples fell in to two distinct regions of isotopic space. The conclusion reached from

this data segregation was that some fish were able to migrate to the open ocean, recording a marine signature, while a mixed meteoric-marine $\delta^{18}\text{O}$ signature was retained for fish confined to the lagoon system (Patterson, 1999).

This simple salinity control hypothesis was challenged, however, by an investigation into strontium isotope compositions of several shell species from the Kildonnan Member as part of a wider study on Hebridean Middle Jurassic mollusc fossils (Holmden and Hudson, 2003). They found that $^{87}\text{Sr}/^{86}\text{Sr}$ compositions of *P. strathairdensis* were too radiogenic to support aragonite formation from Jurassic seawater. Their data indicated negligible input of marine Jurassic Sr in *P. strathairdensis* shells and suggested that the positive relationship between molluscan $\delta^{18}\text{O}$ and $\delta^{13}\text{C}$ was instead controlled by seasonal variation in evaporation/flooding of a freshwater system, possibly with influence of a marginal marsh environment that was isolated in the dry season but hydrologically connected to the lagoons in the wet season, increasing the input of isotopically depleted fresh water (Holmden and Hudson, 2003). The unstated inference from this interpretation is that the most evaporated, dry season, water compositions reached $\delta^{18}\text{O}$ values more or less identical to Bathonian seawater (i.e., c. -1.5‰ VSMOW).

P. strathairdensis shells from Kildonnan, Eigg were thus chosen for clumped isotopes as they are known to have excellent aragonite preservation in soft mudstones when collected away from minor (cm-scale) igneous sills and dykes. The mudstones have immature vitrinite reflectance values, R_0 averaging 0.56 for both bed 5 and for all measured associated beds (beds 1-6) (Hudson and Andrews, 1987; Hudson, pers. comm. 2021; data courtesy of Brian Cooper). Moreover, the overall environmental and diagenetic conditions of the Kildonnan member are well constrained and framed by the previous work.

The aims for measuring *P. strathairdensis* using clumped isotope analysis were twofold; to derive the ambient temperature of the water of the lagoonal system, allowing an insight into Hebridean Middle Jurassic climate, and to thereby calculate $\delta^{18}\text{O}_{\text{FLUID}}$ values which would corroborate (or otherwise) the environmental model of Holmden and Hudson (2003). The data would also contribute to understanding the applicability of the clumped isotope paleothermometer to fossil molluscan aragonite.

5.2: Methods:

5.2.1: Sampling and sample pre-preparation:

A total of 18 *P. strathairdensis* shells with the identifier '159-' (see Table 5.1) were collected from bed E of the Kildonnan member at Kildonnan Bay, Eigg (Fig. 5.3) (NM49608721). While the shells were not all complete specimens, all but two of shells measured (10a and 11b) looked to be several cm in shell length and had widths of at least 1 cm. These were likely adult specimens (John Hudson, Pers. Comm. 2021).

After careful removal of detrital material from host mudstones using a needle, shells were visually appraised for impurities. For some samples, the top surface of the shell was flaked away if there were areas of discoloration. There was no intentional differentiation between umbonal or dorsal/ventral areas when choosing samples.

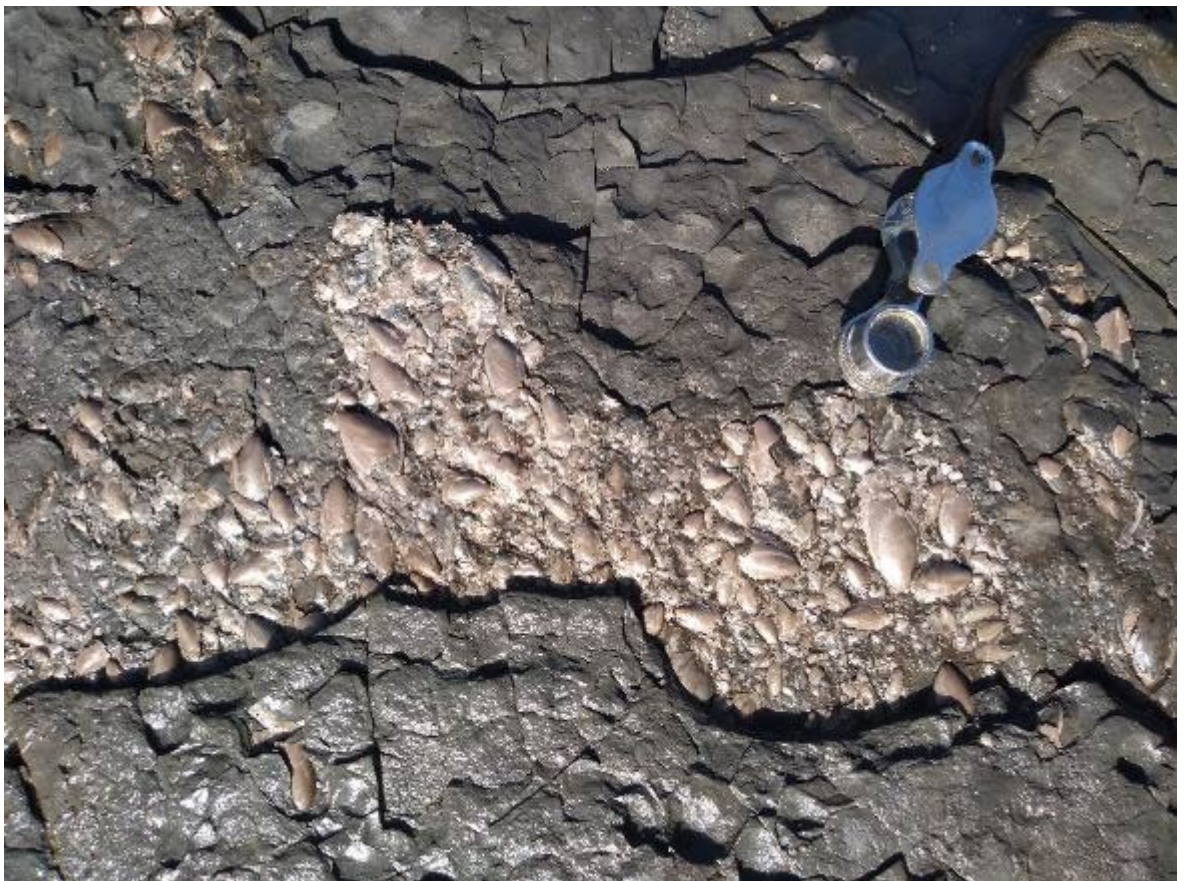


Figure 5.3: Shell plaster of *P. strathairdensis* in bed 5e of the Kildonnan member at the type section (Eigg). Note the distinctive pink colour of the skeletal aragonite. Hand lens is 6 cm long. Photo courtesy of Julian Andrews.

Sample	N	Aragonite %	$\delta^{13}\text{C}$ (‰, VPDB)	$\delta^{18}\text{O}_{\text{CARBONATE}}$ (‰, VPDB)	Δ_{47} (CDES-25)	T(Δ_{47}) (°C)	$\delta^{18}\text{O}_{\text{FLUID}}$ (‰, VSMOW)
159-7a	2	97	2.8 ± 0.0	-3.0 ± 0.0	0.568 ± 0.025	58 ± 12	5.0 ± 2.7
			2.9	-2.9	0.521	83	10.3
			2.8	-3.0	0.614	38	0.7
159-8a1	1	98	2.8 ± 0.0	-2.2 ± 0.1	0.623 ± 0.035	35 ± 14	0.9 ± 2.9
159-8a2	1	99	2.9 ± 0.0	-2.1 ± 0.1	0.595 ± 0.035	46 ± 15	3.4 ± 3.3
159-8b	2	99	2.7 ± 0.0	-2.6 ± 0.0	0.653 ± 0.025	25 ± 9	-1.8 ± 1.9
			2.7	-2.5	0.662	21	-2.4
			2.7	-2.6	0.644	28	-1.2
159-8c	1	98	2.7 ± 0.0	-2.4 ± 0.1	0.619 ± 0.035	37 ± 14	1.0 ± 3.0
159-9b	2	98	2.3 ± 0.0	-3.3 ± 0.0	0.577 ± 0.025	54 ± 12	3.7 ± 2.5
			2.3	-3.3	0.574	55	4.0
			2.3	-3.3	0.580	53	3.5
159-10a	1	100	2.8 ± 0.0	-1.7 ± 0.1	0.579 ± 0.035	53 ± 16	5.2 ± 3.5
159-11a	1	98	2.8 ± 0.0	-2.9 ± 0.1	0.607 ± 0.035	41 ± 15	1.5 ± 3.1
159-11b	1	100	2.9 ± 0.0	-2.2 ± 0.1	0.642 ± 0.035	28 ± 13	-0.7 ± 2.7
159-14a	2	99	3.1 ± 0.0	-1.8 ± 0.0	0.620 ± 0.025	36 ± 10	1.5 ± 2.2
			3.1	-1.8	0.594	47	3.7
			3.1	-1.9	0.645	27	-0.5
159-14c	5	99	2.9 ± 0.0	-1.5 ± 0.0	0.596 ± 0.016	46 ± 8	3.8 ± 1.6
			2.9	-1.5	0.575	55	5.8
			2.9	-1.4	0.615	38	2.3
			2.9	-1.6	0.576	54	5.6
			2.9	-1.5	0.595	46	3.9
			2.9	-1.5	0.620	36	1.8
159-14e	1	99	3.1 ± 0.0	-1.4 ± 0.1	0.580 ± 0.035	53 ± 16	5.4 ± 3.5
159-16a	7	99	3.2 ± 0.0	-1.8 ± 0.0	0.610 ± 0.013	40 ± 7	2.4 ± 1.4
			3.2	-1.8	0.642	28	-0.2
			3.2	-1.9	0.683	15	-3.1
			3.2	-1.9	0.587	50	4.2
			3.2	-1.8	0.614	39	2.0
			3.2	-1.8	0.591	48	4.0
			3.3	-1.6	0.579	53	5.3
			3.3	-1.8	0.571	57	5.9
159-20a	1	98	2.7 ± 0.0	-1.9 ± 0.1	0.603 ± 0.035	43 ± 15	2.8 ± 3.2
159-21a	2	99	2.9 ± 0.0	-2.1 ± 0.0	0.657 ± 0.025	23 ± 9	-1.6 ± 1.9
			2.9	-2.1	0.649	26	-1.0
			2.9	-2.1	0.666	20	-2.2
159-22a	7	100	2.6 ± 0.0	-2.1 ± 0.0	0.601 ± 0.013	44 ± 7	2.8 ± 1.4
			2.6	-2.1	0.569	58	5.8
			2.6	-2.1	0.660	22	-1.8
			2.6	-2.2	0.550	67	7.7
			2.5	-2.1	0.566	59	6.1
			2.6	-2.1	0.596	46	3.2
			2.6	-2.1	0.612	40	1.9
			2.6	-2.3	0.655	24	-1.6
159-23	2	100	1.6 ± 0.0	-4.5 ± 0.0	0.573 ± 0.025	56 ± 12	2.9 ± 2.6
			1.6	-4.5	0.577	54	2.7
			1.5	-4.6	0.570	57	3.2
159-18a	2	77	2.8 ± 0.0	-5.4 ± 0.0	0.621 ± 0.025	36 ± 10	-2.1 ± 2.2
			2.7	-5.4	0.657	23	-4.9
			2.8	-5.3	0.585	51	1.0
159-18e	2	75	2.3 ± 0.0	-5.6 ± 0.0	0.610 ± 0.025	40 ± 11	-1.5 ± 2.3
			2.3	-5.6	0.627	34	-2.9
			2.2	-5.6	0.592	48	0.1

Table 5.1: Clumped isotope results from *P. strathairdensis* shell collection '159-'. When N>1, average values are presented above data from individual measurement repeats. All ± values represent one standard error of the pooled standard deviation.

Sample	$\delta^{13}\text{C}$ (VPDB)	$\delta^{18}\text{O}_{\text{Carbonate}}$ (VPVB)	Sr (ppm)	$^{87}\text{Sr}/^{86}\text{Sr}$	Sr/Ca
94E7	2.54	-1.81	1955	0.710026	2.661
94E8-2	2.92	-1.8	1917	0.710042	2.284
E218	0.85	-4.78	4176	0.710122	5.696
E331	1.14	-4.45	5900*	0.710142	

Table 5.2: Results from Holmden and Hudson (2003) for the shells remeasured in this chapter.

*Sr concentration estimated using figures within Holmden and Hudson (2003).

Sample	N	$\delta^{13}\text{C}$ (‰, VPDB)	$\delta^{18}\text{O}_{\text{CARBONATE}}$ (‰, VPDB)	Δ_{47} (CDES-25)	T(Δ_{47}) (°C)	$\delta^{18}\text{O}_{\text{FLUID}}$ (‰, VSMOW)
94E7	3	3.0 ± 0.0	-1.7 ± 0.0	0.618 ± 0.020	37 ± 9	1.7 ± 1.9
		3.0	-1.7	0.641	29	-0.1
		3.0	-1.7	0.608	41	2.5
		3.0	-1.7	0.604	42	2.9
94E8-2	3	3.0 ± 0.0	-2.1 ± 0.0	0.643 ± 0.020	28 ± 8	-0.6 ± 1.7
		3.0	-2.1	0.644	28	-0.7
		3.0	-2.2	0.626	34	0.6
		3.1	-2.0	0.658	23	-1.6
E218	2	1.7 ± 0.0	-3.3 ± 0.0	0.632 ± 0.025	32 ± 10	-0.9 ± 2.1
		1.7	-3.2	0.644	28	-1.8
		1.7	-3.3	0.620	36	0.0
E331	3	1.5 ± 0.0	-5.1 ± 0.0	0.627 ± 0.020	34 ± 8	-2.3 ± 1.8
		1.5	-5.1	0.628	33	-2.4
		1.5	-5.1	0.632	32	-2.7
		1.5	-5.1	0.621	36	-1.8

Table 5.3: Clumped isotope results from *P. strathairdensis* shells that were also previously analysed by Holmden and Hudson (2003). For all shells average values are presented above data from individual measurement repeats. All ± values represent one standard error of the pooled standard deviation.

Four additional *P. strathairdensis* shells from the same locality were kindly provided by Chris Holmden; these have been previously investigated by Holmden and Hudson (2003). Samples were chosen to represent a range of high and low Sr compositions (Holmden and Hudson, 2003; see Tables 5.2 & 5.3).

Several other shells of varying ages and localities were also analysed in order to provide wider context to the clumped isotope technique. These are summarised in Table 5.4 and 5.5. These shells had been pre-prepared but were also inspected visually for impurities.

Mudstone hosted concretion body cements, two of which were kindly provided by Matt Wakefield (MWxxCB), were sampled from bed 5f and bed 6e (Hudson, 1966, Hudson et al., 1995; Fig. 5.2) of the Kildonnan Member at Kildonnan Bay, Eigg (Table 5.6).

5.2.2: XRD measurements:

Shell fragments were gently crushed into a fine powder using a pestle and mortar. XRD measurements of the '159-' *P. strathairdensis* shells were completed on resultant sample powders using a Rigaku Smartlab SE diffractometer (Cu K- α radiation; 25 to 44 deg; step: 0.02 deg; speed: 4 deg per min). Aragonite percentage was derived by comparing the peak area of the primary aragonite and calcite peaks ($aA_1/(aA_1 + aC_1)$) and comparing this with equivalent percentage aragonite (Milliman, 1974).

The results of this analysis were taken into account for the measurement of clumped isotopes: 16 of the shells measured were >97% aragonite, and the remaining two shells contained 75% and 77% aragonite, measured in order to provide a comparison to the more pristine samples.

5.2.3: Clumped isotopes:

5.2.3.1: Clumped isotope preparation and measurement:

Regardless of shell species, the method of preparing samples for clumped isotope analysis were the same. Shell fragments were gently crushed into a fine powder using a pestle and mortar. Care was taken when milling to ensure only gentle pressure was used, in order to avoid resetting.

For clumped isotope analysis, usually, 6 mg of sample was used for each replicate measurement (see Chapter 2.2). 1-6 replicates were measured for each shell. The clumped isotope preparation for these shells has been described in Chapter 2.3 and Table 2.1.

Sample CO₂ was measured as described in Chapter 2.4.

Sample	Grid Reference	Location	Formation	Age	Type
rpUnioKmgFmB3	NG 43678 75128	Kilmaluag Bay, Skye	Kilmaluag Formation (KF)	Middle Jurassic	<i>Unio andersoni</i>
16-5V1	NG 46826 71494	Staffin Bay, Skye	Staffin Shale Formation (SSF)	Late Jurassic	<i>Ammonite sp.</i>
16-5	NG 46826 71494	Staffin Bay, Skye	Staffin Shale Formation (SSF)	Late Jurassic	<i>Ammonite sp.</i>
jbel	NG 46824 71479	Staffin Bay, Skye	Staffin Shale Formation (SSF)	Late Jurassic	<i>Belemnite sp.</i>
JEA2805-1	TG 18700 43201	West Runton, Norfolk	'Monkey Gravel' Bed (MGB)	Pleistocene	Unionid
JEA11196-1	TG 18700 43201	West Runton, Norfolk	West Runton Freshwater Bed (WRFB)	Pleistocene	<i>Mya truncata</i>
JEA11196-2	TG 18700 43201	West Runton, Norfolk	West Runton Freshwater Bed (WRFB)	Pleistocene	<i>Mya truncata</i>
JEA11196-4	TG 18700 43201	West Runton, Norfolk	West Runton Freshwater Bed (WRFB)	Pleistocene	<i>Mya truncata</i>
JEA-SK-Mya	TF 96472 44186	Stiffkey Salt Marsh, Norfolk	Modern	Modern	<i>Mya truncata</i>

Table 5.4: Location, age and species information for other biogenic samples measured with clumped isotopes.

Sample	Species	Formation/Period	N	$\delta^{13}\text{C}$ (‰, VPDB)	$\delta^{18}\text{O}_{\text{CARBONATE}}$ (‰, VPDB)	Δ_{47} (CDES-25)	T(Δ_{47}) (°C)	$\delta^{18}\text{O}_{\text{FLUID}}$ (‰, VSMOW)
rpUnioKmgFmB3	<i>Unio andersoni</i>	KF, Jurassic	1	3.42 ± 0.03	-1.59 ± 0.065	0.563 ± 0.035	61 ± 17	6.9 ± 3.7
16-5V1	<i>Ammonite sp.</i>	SSF, Jurassic	3	-0.02 ± 0.03	-4.19 ± 0.031	0.686 ± 0.014	14 ± 5	-5.6 ± 1.1
				0.0	-4.1	0.674	18	-4.8
				0.0	-4.2	0.698	10	-6.4
				0.0	-4.2	0.685	14	-5.6
16-5	<i>Ammonite sp.</i>	SSF, Jurassic	6	-0.11 ± 0.01	-4.21 ± 0.015	0.692 ± 0.011	12 ± 5	-6.1 ± 1.0
				-0.1	-4.2	0.653	25	-3.4
				0.0	-4.2	0.730	1	-8.3
				-0.1	-4.2	0.704	9	-6.8
				-0.1	-4.3	0.690	13	-6.0
				-0.1	-4.3	0.704	9	-6.9
				-0.2	-4.2	0.673	18	-4.8
jbel	<i>Belemnite sp.</i>	SSF, Jurassic	4	1.89 ± 0.02	-0.56 ± 0.033	0.633 ± 0.018	31 ± 7	3.1 ± 1.4
				1.9	-0.6	0.641	29	1.1
				1.9	-0.5	0.633	32	1.8
				1.9	-0.5	0.625	35	2.4
				1.9	-0.6	0.634	31	1.6
JEA2805-1	Unionid	MGB, Pleistocene	2	-9.73 ± 0.06	-5.62 ± 0.631	0.766 ± 0.035	-8 ± 9	-11.7 ± 1.9
				-9.8	-5.6	0.801	-16	-13.4
				-9.7	-5.6	0.731	1	-9.8
JEA11196-1	<i>Mya truncata</i>	WRFB, Pleistocene	2	0.62 ± 0.02	1.36 ± 0.046	0.690 ± 0.025	13 ± 8	-0.4 ± 1.7
				0.6	1.3	0.688	13	-0.3
				0.7	1.4	0.692	12	-0.5
JEA11196-2	<i>Mya truncata</i>	WRFB, Pleistocene	1	-0.19 ± 0.03	1.47 ± 0.065	0.682 ± 0.035	15 ± 11	0.2 ± 2.4
JEA11196-4	<i>Mya truncata</i>	WRFB, Pleistocene	1	1.66 ± 0.03	2.35 ± 0.065	0.637 ± 0.035	30 ± 13	4.3 ± 2.6
JEA-SK-Mya	<i>Mya truncata</i>	Modern	3	-2.99 ± 0.02	1.46 ± 0.038	0.685 ± 0.020	14 ± 7	0.0 ± 1.5
				-3.0	1.5	0.700	10	-0.9
				-3.0	1.4	0.662	22	1.6
				-3.0	1.5	0.695	11	-0.6

Table 5.5: Clumped isotope results from all other biogenic material. When N>1, average values are presented above data from individual measurement repeats.

All ± values represent one standard error of the pooled standard deviation. Formation abbreviations refer to Table 5.4.

Sample	N	$\delta^{13}\text{C}$ (‰, VPDB)	$\delta^{18}\text{O}_{\text{CARBONATE}}$ (‰, VPDB)	Δ_{47} (CDES-25)	T(Δ_{47}) (°C)	$\delta^{18}\text{O}_{\text{FLUID}}$ (‰, VSMOW)
rp-159-24cbc	3	-9.0 ± 0.0	-1.5 ± 0.0	0.684 ± 0.017	15 ± 6	-1.3 ± 1.4
		-8.9	-1.4	0.682	15	-1.2
		-8.9	-1.4	0.709	7	-2.9
		-9.0	-1.6	0.660	22	0.2
MW-5FCB	4	-9.1 ± 0.0	-1.4 ± 0.0	0.691 ± 0.015	12 ± 6	-1.7 ± 1.2
		-9.1	-1.5	0.718	5	-3.6
		-9.1	-1.4	0.705	8	-2.6
		-9.1	-1.4	0.657	23	0.6
		-9.0	-1.4	0.683	15	-1.2
MW-5FCB	4	-9.7 ± 0.0	-2.8 ± 0.0	0.662 ± 0.015	21 ± 6	-1.2 ± 1.3
		-9.8	-2.9	0.697	11	-3.6
		-9.7	-2.8	0.678	16	-2.3
		-9.7	-2.8	0.659	22	-1.0
		-9.6	-2.8	0.615	38	2.1

Table 5.6: Clumped isotope results from *mudstone hosted concretions*. For all concretions, average values are presented above data from individual measurement repeats. All ± values represent one standard error of the pooled standard deviation.

5.2.3.2: Data handling:

One key difference in preparation from the majority of other data is that more than half of the measurements were analysed during periods where corrections were required to be applied to the Δ_{47} data, due to: a) experiments resulting in progressive reference gas contamination (Chapter 2.5.7.1); and b) gradual reference gas reequilibration (Chapter 2.5.7.2). Timeframes for this issue are indicated in Table 2.1 and have been made clear in Appendix 3 Part I & III.

Chapter 2 describes the data handling. Of note, for aragonite samples an acid fractionation correction was applied when calculating $\delta^{18}\text{O}(\text{aragonite})$ from $\delta^{18}\text{O}(\text{CO}_2)$ (VSMOW).

For the aragonite samples, the mollusc-specific aragonite-water isotope fractionation factor calibration of Grossman and Ku (1986) is used to derive $\delta^{18}\text{O}_{\text{FLUID}}$, as the majority of samples are in the phylum '*Mollusca*' (Equation 2.9).

For calcite, the calcite-water isotope fractionation factor calibration of Kim and O'Neil (1997) was used (Equation 2.7).

5.2.3.3: Uncertainty:

The standard error of the pooled standard deviation of the following collections of samples were calculated to represent $\delta^{13}\text{C}$, $\delta^{18}\text{O}_{\text{CARBONATE}}$ and Δ_{47} uncertainties:

- *P. strathairdensis* shell samples;

- *Ammonite* septa (although from the same ammonite, two septa were measured);
- Kildonnan Member mudstone-hosted concretion body samples.

Ordinarily, if a sample had been measured only once, no individual sample standard deviation or error would be achievable. However, although such a sample was not contributing to the pooled standard deviation of a group, a representative standard error could be calculated from the pooled standard deviation results of the other members of the same group. This uncertainty is considered appropriate as it is based on the principle that the uncertainty calculated from the population can be applied to a single member of the population, although it is acknowledged that the given values may not be a true representation of the uncertainty for a given individual sample. As standard error takes into account the number of measurement repeats, these samples report the highest uncertainty of all samples in a population.

For all other measurements where species specific pooled standard deviations were not available, two other methods were used to derive approximate uncertainties:

1. Using the sample standard deviation
2. Using pooled SD of the *P. strathairdensis* population

Method 2 was chosen for samples with $n=1$, and for samples with >2 repetitions, unless method 1 gave higher uncertainty for all three parameters ($\delta^{13}\text{C}$, $\delta^{18}\text{O}_{\text{CARBONATE}}$, Δ_{47}).

The pooled standard deviation of ETH3, a biogenic calcite standard, was considered for application to these samples; however, the uncertainty produced was lower than when calculated using the pooled standard deviation of *P. strathairdensis* and thus the latter was considered preferable, if only to demonstrate more clearly that these uncertainties are approximate.

Temperature and $\delta^{18}\text{O}_{\text{FLUID}}$ uncertainties were calculated using the standard error of Δ_{47} and $\delta^{18}\text{O}_{\text{CARBONATE}}$ values, with full propagation of the measurement and calibration uncertainties.

5.2.4: SEM

Four shells were investigated using scanning electron microscopy (SEM). Broken edges of shells were gold sputter coated with a Polaron SC7640 and viewed using a Zeiss Gemini 300 Field Emission SEM using secondary electron imaging mode.

5.2.5: CHN:

In order to measure water content of selected aragonite shell samples, hydrogen (H) was measured using an Exeter Analytical CE440 combustion CHN analyser. Samples were ground to a fine powder in an agate pestle and mortar and combusted and oxidised at 975°C before being reduced to elemental H at 620°C. Gas was then cleaned using scrubbers and passed through a thermal conductivity detector. Acetanilide was used as the analytical standard. Replicate analysis of LRM (internal standard) and SRM (certified sediment reference standard), corrected for acidification, gave a 2σ precision of ± 0.12 and ± 0.13 wt% H respectively.

5.3: Results

5.3.1: XRD:

Of the 18 *Praemytilus strathairdensis* shells screened by XRD, 16 had aragonite percentages of >97%, with only two (from the same hand specimen) showing evidence for higher calcite presence (23 and 25% calcite) (Table 5.7).

A unionid sample from the Pleistocene West Runton 'Freshwater Bed' (JEA2805-1) was composed of 100% aragonite.

5.3.2: Clumped isotopes: *Praemytilus strathairdensis* - '159-' collection:

A summary of the results of clumped isotope analysis of the suite of *P. strathairdensis* shells analysed are shown in Table 5.1; the number of sample measurements are also recorded – six shells measured only once and 9 measured twice.

Shells show variable $\delta^{13}\text{C}$ and $\delta^{18}\text{O}_{\text{CARBONATE}}$ results; however, as seen on Figure 5.4, the majority of shells fall in a 2‰ range in $\delta^{18}\text{O}$ and 1‰ range in $\delta^{13}\text{C}$. Values for $\delta^{13}\text{C}$ range from +1.6‰ to +3.2‰ VPDB, averaging +2.7‰. For the shells with >97% aragonite,

$\delta^{18}\text{O}_{\text{CARBONATE}}$ values range from $-1.4 \pm 0.1\text{‰}$ to -4.5‰ VPDB (Table 5.1). The two shells found by XRD to have only 75-77% aragonite preserved give more negative $\delta^{18}\text{O}_{\text{CARBONATE}}$ values of -5.4‰ and -5.6‰ VPDB.

Δ_{47} derived temperatures are highly variable, ranging from $23 \pm 9 \text{ °C}$ to $58 \pm 12 \text{ °C}$. Only three shells gave temperatures below 35 °C . The back-calculated $\delta^{18}\text{O}_{\text{FLUID}}$ values give a range between $-1.8 \pm 1.9\text{‰}$ and $+5.4 \pm 3.5\text{‰}$ (Fig. 5.5). For the (near-) fully aragonite shells these are highly temperature dependent, with the lowest $\delta^{18}\text{O}_{\text{FLUID}}$ values corresponding to the lowest temperatures, rather than related to changes in $\delta^{18}\text{O}_{\text{CARBONATE}}$. The two shells with high calcite percentage provide negative $\delta^{18}\text{O}_{\text{WATER}}$ values and are distinct from the other measurements when comparing $\delta^{18}\text{O}_{\text{WATER}}$ with temperature.

Sample ID	aA1/(aA1+aC1)	Percentage aragonite (%)	Percentage calcite (%)
159-7a	0.916306	97	3
159-8a1	0.948123	98	2
159-8a2	0.976159	99	1
159-8b	0.977681	99	1
159-8c	0.969556	98	2
159-9b	0.96863	98	2
159-10a	N/A	100	0
159-11a	0.972555	98	2
159-11b	N/A	100	0
159-14a	0.989613	99	1
159-14c	0.993624	99	1
159-14e	0.976503	99	1
159-16a	0.978207	99	1
159-18a	0.585392	77	23
159-18e	0.553681	75	25
159-20a	0.969323	98	2
159-21a	0.976453	99	1
159-22a	N/A	100	0
159-23	N/A	100	0
JEA2805-1	N/A	100	0

Table 5.7: Results of XRD analysis of *P. strathairdensis* and *unionids*.

5.3.3: Clumped isotopes: *Praemytilus strathairdensis* Holmden and Hudson (2003) samples:

Four samples of *P. strathairdensis*, provided by Chris Holmden and originally analysed by Holmden and Hudson (2003), were investigated using clumped isotope

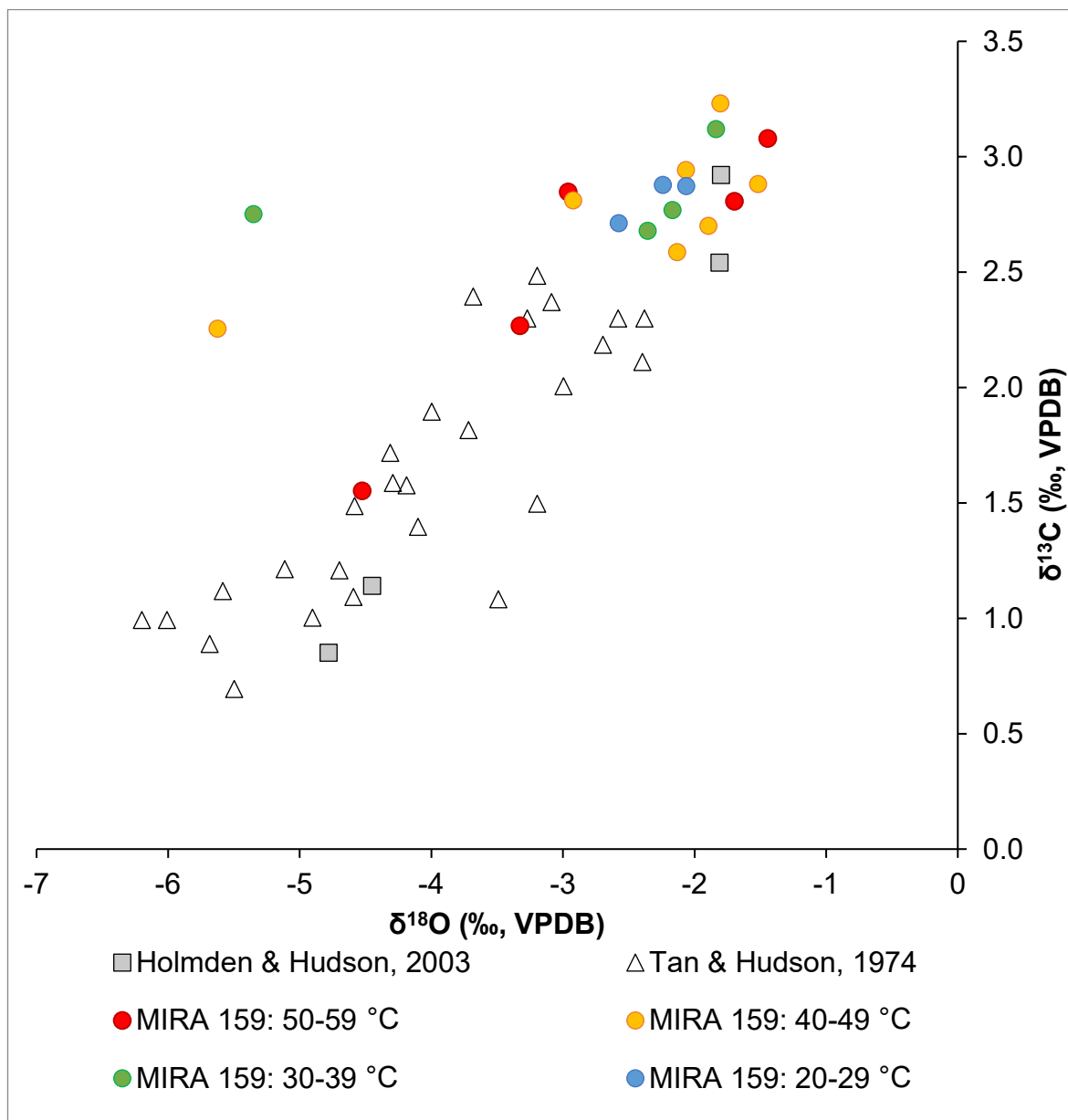


Figure 5.4: Measured $\delta^{13}\text{C}$ and $\delta^{18}\text{O}_{\text{CARBONATE}}$ values of suite '159-' *P. strathairdensis* shells, in comparison with shells previously measured by Tan and Hudson (1974) and Holmden and Hudson (2003). 10 °C groupings of Δ_{47} derived temperatures are indicated by colour (MIRA 159: xx-xx °C).

analysis. The previously reported data from Holmden and Hudson (2003) is displayed in Table 5.2. Results from MIRA are shown in Table 5.3.

The $\delta^{18}\text{O}_{\text{CARBONATE}}$ and $\delta^{13}\text{C}$ results from the two studies can be directly compared (Fig. 5.5). Two measurements are within 0.5‰ of one another; sample 'E 218' was 0.8‰ different in $\delta^{13}\text{C}$ and 1.5‰ different in $\delta^{18}\text{O}$, while sample 'E 331' had a 0.6‰ difference in $\delta^{18}\text{O}$. It should be noted that re-measurement on MIRA was done on different fragments of shell than those previously analysed, and due to the limitations of the clumped isotope method a much larger mass of sample was required for measurement. The temperatures derived through clumped isotope analysis for these shells ranged from

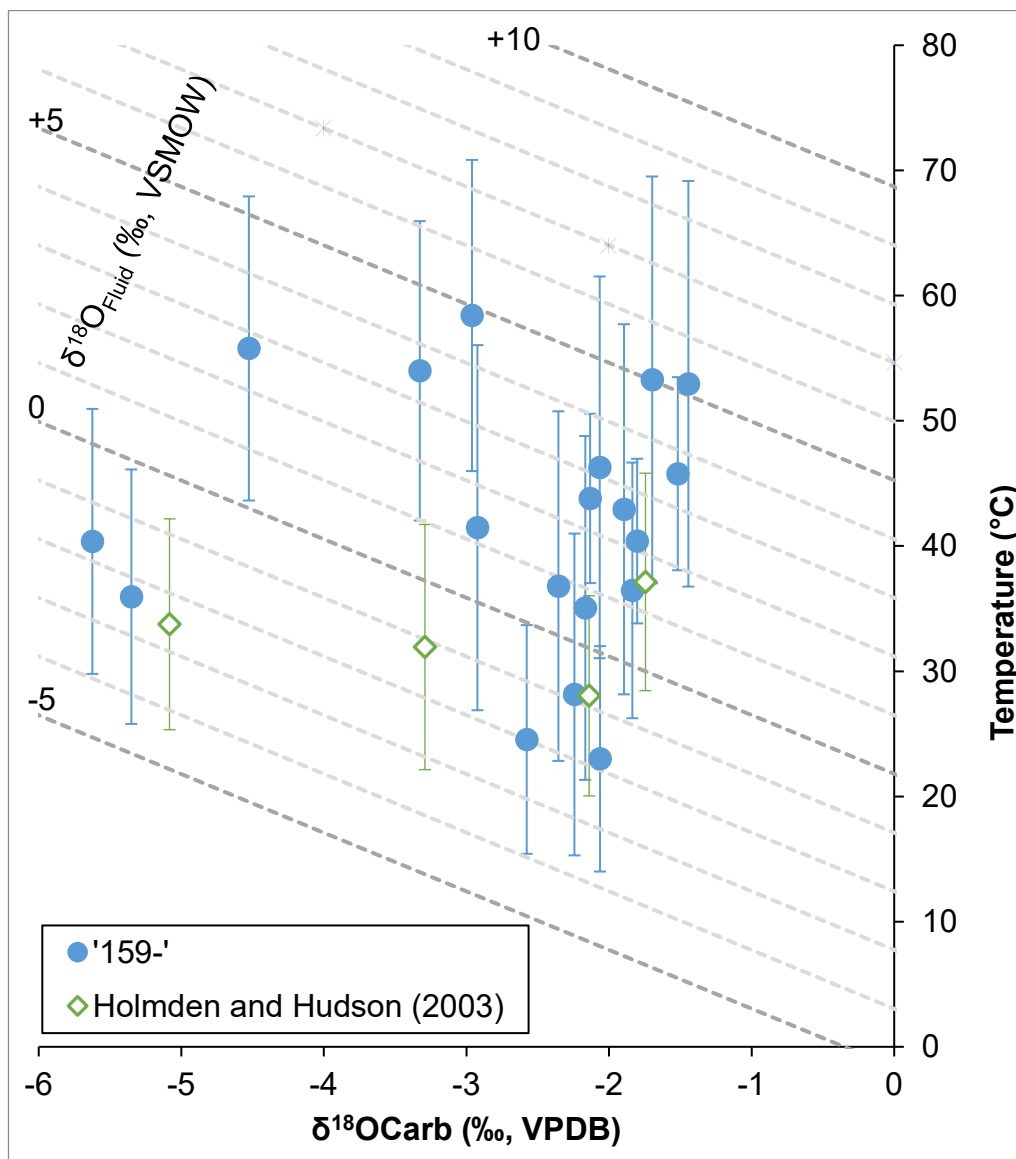


Figure 5.5: Clumped isotope results for *P. strathairdensis*, distinguishing between the '159-' collection and the shells provided by Holmden and Hudson (2003). Contours show $\delta^{18}\text{O}_{\text{FLUID}}$ values (‰, VSMOW).

28 ± 8 °C to 37 ± 9 °C. Back calculated $\delta^{18}\text{O}_{\text{FLUID}}$ results are between $+1.7 \pm 1.9$ ‰ and -2.3 ± 0.8 ‰ VSMOW.

5.3.4: Clumped isotopes: Other shells:

Seven other aragonite shells and one calcite belemnite guard, with a variety of sources and species (Table 5.4), were measured to further investigate clumped isotope analysis of biogenic carbonates and to contextualise the results of the main dataset, particularly, to compare with the high temperatures measured for *P. strathairdensis*. The results can be found in Table 5.5.

One single measurement of a *Unio andersoni*. collected at Kilmaluag Bay from the Bathonian Kilmaluag Formation of the GEG was the only other bivalve shell to give a hot

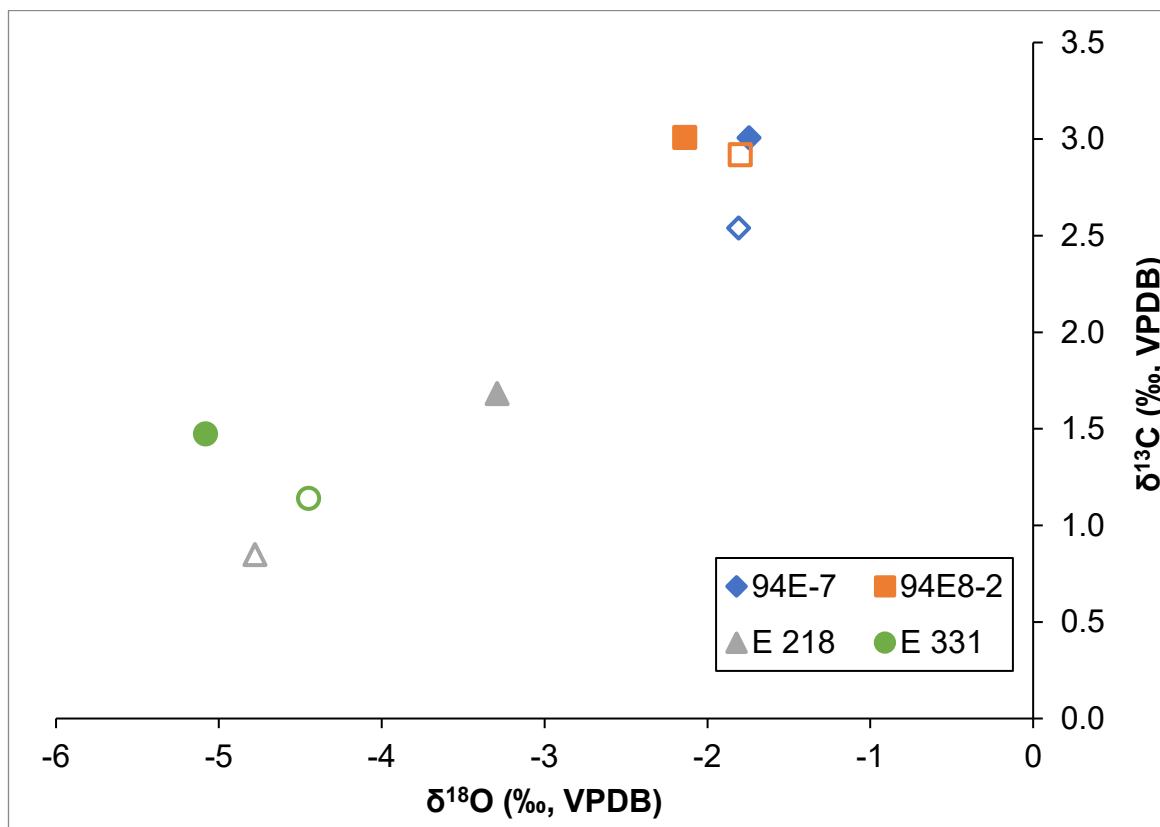


Figure 5.6: Comparison of $\delta^{18}\text{O}$ and $\delta^{13}\text{C}$ of shells measured by Holmden and Hudson (2003) (open markers) and remeasured here (filled markers).

temperature ($61 \pm 17 \text{ }^\circ\text{C}$) and this corresponded with a very positive $\delta^{18}\text{O}_{\text{FLUID}}$ estimate of $+6.9 \pm 3.7\text{‰}$ VSMOW. An ammonite from the Kimmeridgian Staffin Shale Formation (samples from Staffin Bay, Skye) gave much cooler values for two individual septa (12 ± 5 and $14 \pm 5 \text{ }^\circ\text{C}$) but fluid values that are unusual for marine organisms ($-5.6 \pm 1.1 \text{‰}$ and $-6.1 \pm 1.0 \text{‰}$). A calcite guard from a belemnite from the same formation and locality gave warmer temperatures, $31 \pm 7 \text{ }^\circ\text{C}$, and positive $\delta^{18}\text{O}_{\text{FLUID}}$ values of $+3.1 \pm 1.4\text{‰}$ VSMOW.

Samples of *Mya truncata* from the Pleistocene aged (West Runton Formation) ‘Monkey Gravel’ at West Runton, North Norfolk (UK) and a modern shell of the same species from a saline pan at Stiffkey Salt Marsh, North Norfolk (UK), largely gave temperatures close or equal to $14 \text{ }^\circ\text{C}$, although with uncertainty estimates between ± 7 and $11 \text{ }^\circ\text{C}$, with one exception ($30 \pm 13 \text{ }^\circ\text{C}$) from one of the Pleistocene samples. $\delta^{18}\text{O}_{\text{FLUID}}$ estimates for the cooler measurements were between $-0.4 \pm 1.7\text{‰}$ and $0.2 \pm 1.5 \text{‰}$ VSMOW; with the ‘hottest shell’ producing a $\delta^{18}\text{O}_{\text{FLUID}}$ value of $4.3 \pm 2.6\text{‰}$ VSMOW.

The unionid measurement from the Pleistocene West Runton Freshwater Bed, Norfolk (UK) gave a negative temperature (-5 °C) and a corresponding negative $\delta^{18}\text{O}_{\text{FLUID}}$ value of -11.0‰ (VSMOW).

5.3.5: SEM:

Three shells inspected by SEM were also analysed using clumped isotopes, while one other shell (18b) was not measured by XRD or clumped isotope analysis but was used as an example of a shell with visual discolouration.

SEM imaging of shells did not show evidence for aragonite alteration to calcite in 3 of 4 shells investigated (Fig. 5.7 and 8). Shell sample 18b, which showed chalky discoloration and was from the same hand sample as 18a and 18e (both of which had >20% calcite composition, Table 5.7) had possible evidence for nacre morphology change (see Fig. 5.8) which appeared to be limited to the shell upper and (particularly) lower surfaces. The only shell investigated by all three techniques (18a), was indicated by XRD to be composed of 23% calcite (see Table 5.7) but no aragonite alteration was visible in the broken section imaged, indicating that samples from this hand specimen were more likely contaminated by a thin calcite vein which the SEM 'transect' of the broken surface did not intersect.

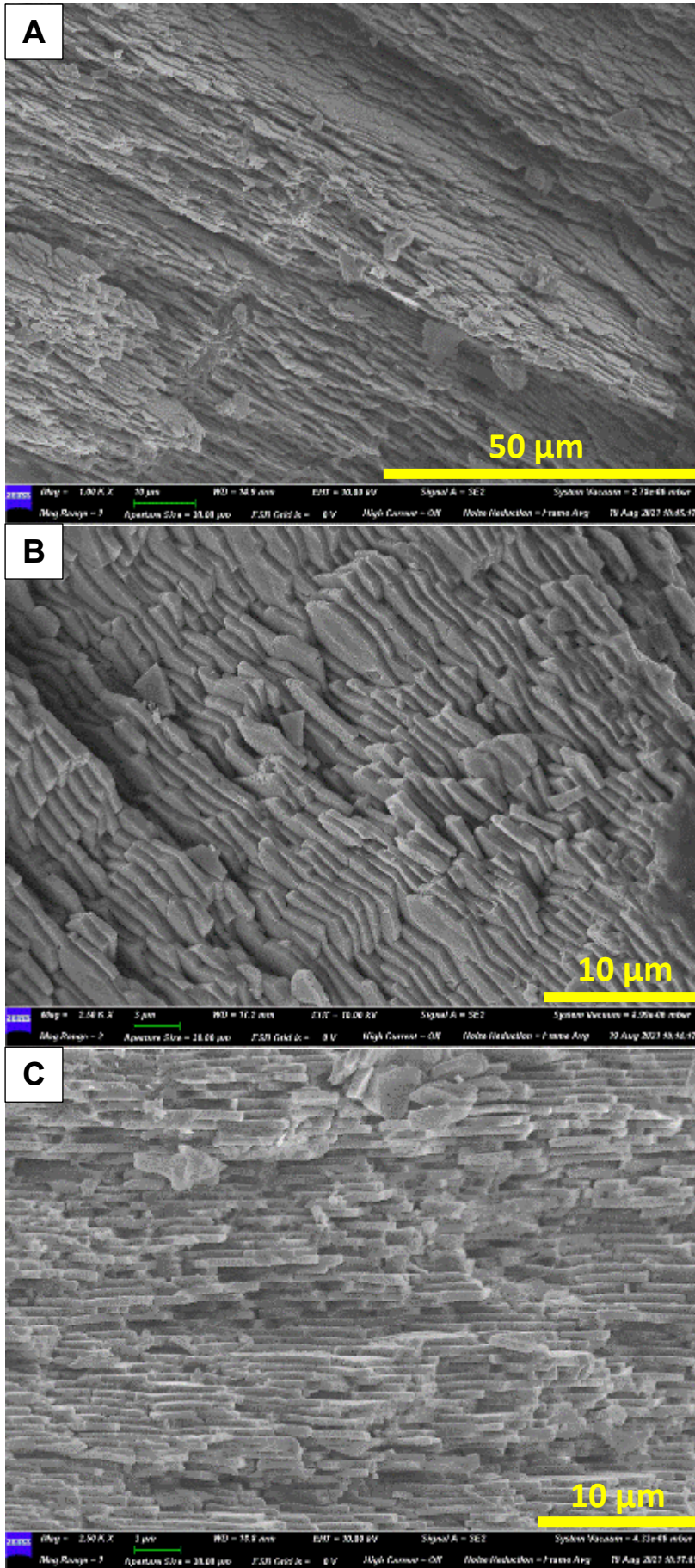


Figure 5.7: SEM images of aragonite nacre of shells A) 14a; B) 14c; C) 18a.

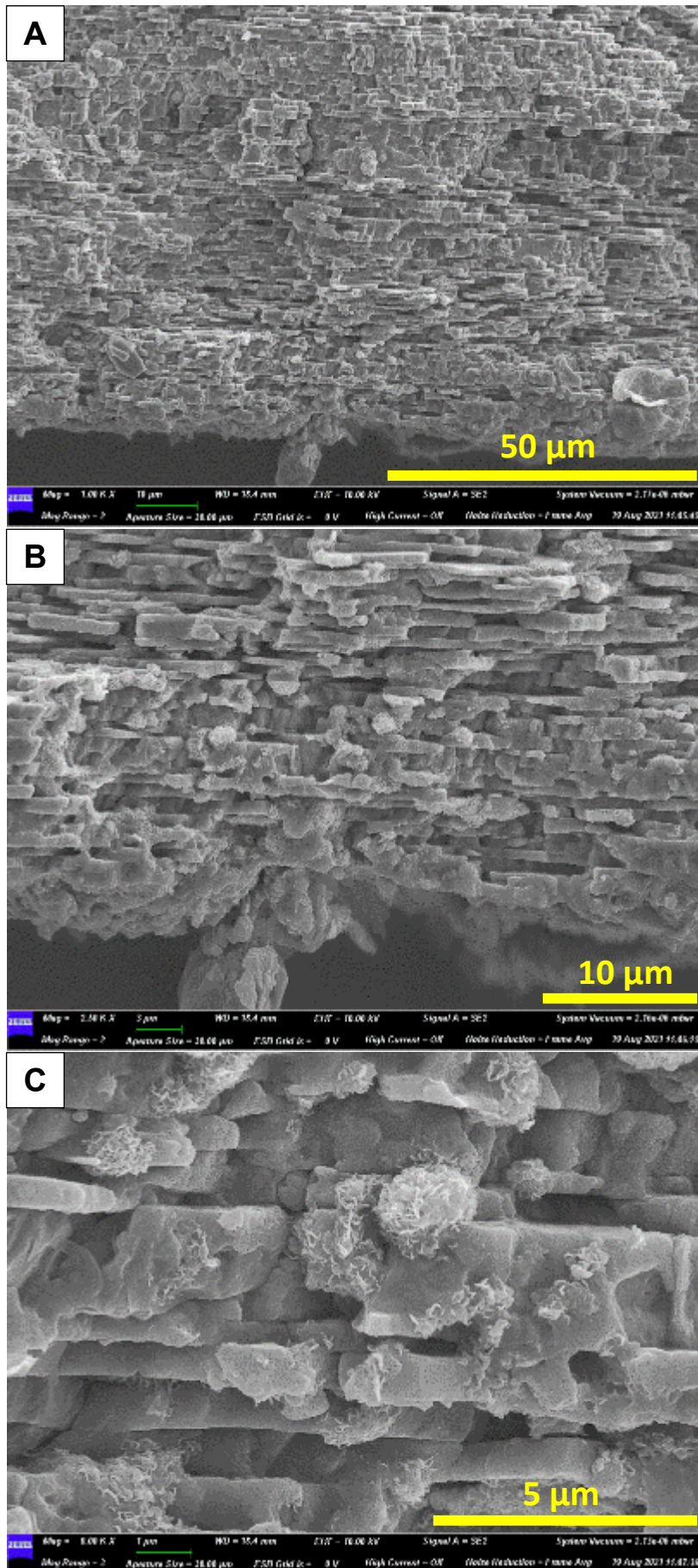


Figure 5.8: SEM images at increasing magnification of the bottom surface of shell 18b (not otherwise analysed). Possible neomorphism can be seen in the lowermost nacreous layers.

5.4: Discussion:

5.4.1: *Praemytilus strathairdensis*: High temperatures

The majority of the Δ_{47} derived temperatures for the Kildonnan Member *P. strathairdensis* from Eigg are higher than expected; only 3 shells gave temperatures that fell below 35 °C, and results range up to 58 ± 12 °C (see Fig. 5.5).

In order to interpret the results, it is important to consider whether these results can represent plausible living temperatures. Although *P. strathairdensis* is an extinct species, it is ancestral to modern shells of the genus *Mytilus* (Hudson, 1968) and was also potentially ecologically equivalent/cospecific with *Modiolus yunnanensis* Chen of China (Hudson et al., 1995; Holmden and Hudson, 2003).

A range of published thermal tolerances for modern *Mytilus* species are shown in Table 5.8. Although several metrics for tolerance are used, the majority of results show decreases in metabolism and increasing critical population mortality at 30 °C. A species which had much higher tolerance, *Mytilus californianus*, still attained 100% mortality at 41 °C (Denny et al., 2011), as did *Mytilus edulis* after a single 6-hour aerial exposure at the same temperature (Seuront et al., 2019). A survey of the upper lethal thermal limit of many bivalve species by Compton et al. (2007) gave a range of values representing 50% population mortality, between 23.7 °C and 41.8 °C.

Organisms acclimatised to higher temperatures can show higher upper thermal tolerances (e.g. Braby and Somero, 2006); however, it has been noted that for *Mytilus edulis*, increasing summer high temperatures within the last 50 years have been linked to a polewards shift in habitat range (Jones et al., 2010) implying limits to thermal tolerance by acclimation. The effects of prolonged acclimation temperature of *Modiolus barbatus* was studied by Anestis et al., (2008), finding that, after an initial acclimation of 18 °C and subsequent temperature elevation to 30 °C, 20% population mortality occurred after 30 days.

Considering the evidence from modern bivalves, it seems implausible that *P. strathairdensis* was able to grow and survive in temperatures greater than 35-40 °C, not least because the shells are abundant, suggesting that they were thriving in the Kildonnan member lagoons.

Species:	Metric:	Acclimation temperature (°C):	Temperature tolerance (°C):	Notes:	Author:
<i>Mytilus trossulus</i>	H_{crit}^*	14 21	23.50±0.93 - 24.20±1.36 26.90±1.53 - 26.00±0.59	Salinity acclimatation range 22-34 psu	Braby and Somero (2006)
<i>Mytilus galloprovincialis</i>	H_{crit}^*	14 21	25.70±0.41 - 28.30±1.08 29.90±0.60 - 30.90±0.41	Salinity acclimatation range 22-34 psu	Braby and Somero (2006)
<i>Mytilus edulis</i>	H_{crit}^*	14 21	25.50±0.99 - 24.20±0.89 29.00±0.47 - 28.50±0.51	Salinity acclimatation range 22-34 psu	Braby and Somero (2006)
<i>Mytilus edulis</i>	50% mortality of population	4 and 14	27.87		Compton et al. (2007)
<i>Mytilus edulis</i>	50% mortality of population		30.5	Shells from White Bay, Great Cumbrae, Scotland. 55°N	Davenport and Davenport (2005)
<i>Mytilus californianus</i>	Onset of mortality	14?†	36	†Population held at 14 °C after experiment	Denny et al. (2011)
	Total mortality		41		
<i>Mytilus edulis</i>	50% mortality of population following 5 successive 6 hr aerial exposures	18 & 13.5	30		Jones et al. (2009)
<i>Mytilus edulis</i>	50% mortality of population following 5 successive 6 hr aerial exposures	16	29	Metric chosen specifically here, but more parameters were investigated	Seuront et al. (2019)
<i>Mytilus edulis</i>	50% mortality of population following 6 hr aerial exposure	17	35.2 37.9	Two sample sites	Sorte et al. (2019)
<i>Mytilus edulis</i>	Similar to H_{crit}^*	15	30		Widdows (1973)

* H_{crit} = temperature at which heart rate rapidly falls)

Table 5.8: A survey of published thermal tolerances for modern *Mytilus* species. Note – often these experiments included a sharp transition in temperature, rather than a continuous high temperature.

In addition, such high temperatures are inconsistent with prior estimates for the depositional environment of the Kildonnan Member; although with the caveat that the majority of these estimates were made under the since-challenged assumption that the lagoonal system had a considerable marine component throughout the period of deposition. Temperatures were first estimated by Tan and Hudson (1974) for the *P. strathairdensis* shell $\delta^{18}\text{O}$ data, giving 22 °C as an average, a value lowered by Hudson (1980) to 18 °C by using a $\delta^{18}\text{O}_{\text{WATER}}$ estimate of -1‰ for the shells assumed to be displaying a Jurassic marine influence. Subsequently, Hudson et al. (1995) used an assumed temperature of 25 °C, based on estimates by Hudson and Andrews (1987) for the GEG lagoons as a whole, rather than one based on $\delta^{18}\text{O}_{\text{WATER}}$ composition assumptions.

As an independent measurement, Patterson (1999) calculated an average temperature of 23 °C by measuring fish otoliths from bed 3g of the Kildonnan Member at Eigg, specifically from the samples assumed to be migratory from the lagoon to marine waters – again using a -1‰ VSMOW $\delta^{18}\text{O}_{\text{FLUID}}$ (seawater) estimate. The fish otolith data from Patterson (1999) was considered by Holmden and Hudson (2003) to provide evidence that there was an occasional marine connection to the lagoon at times, despite their conclusion from Sr isotope data that marine fluids were significantly less important than had previously been assumed.

An additional source of evidence for temperatures within the Kildonnan member lagoon are provided by the measurement of concretion bodies from beds 5f and 6e (Hudson, 1966; Hudson et al., 1995) of the Kildonnan Member at Eigg. As concluded by Paxton et al. (2021) (see also Chapter 3), the microsparitic concretion body cements of mudstone hosted concretions can be used to estimate approximate bottom water temperatures for the sediments they precipitate in, due to their synsedimentary growth. Three concretion bodies were measured from beds 5f and 6e providing temperatures between 12 ± 6 °C and 21 ± 6 °C and pore fluid values between -1.7 ± 1.2 ‰ and -1.2 ± 1.3 ‰ VSMOW. These are slightly cooler than previous temperature estimates, but provide further evidence for lagoonal temperatures substantially lower than 30 °C. Perhaps significantly, the lowest temperatures measured for the *P. strathairdensis* shells gave similar temperatures (23 ± 9 °C and 25 ± 9 °C) to those previously published.

It can be assumed, therefore, that the range in temperatures derived through clumped isotope analysis of *P. strathairdensis* shells (Table 5.1) largely do not represent

environmental temperatures, despite most samples being formed of >97% aragonite. Several reasons for this are discussed below.

5.4.1.1: *Mixing:*

Briefly examined in Chapter 3.4 and Chapter 4.4.2, one possibility investigated to explain the elevated temperature trends is that of mixing. When two end-members with different $\delta^{18}\text{O}$ and $\delta^{13}\text{C}$ values are mixed, as is possible in clumped isotope analysis due to the large volume of sample powder required for analysis, while $\delta^{18}\text{O}$ and $\delta^{13}\text{C}$ values mix linearly, Δ_{47} can produce a non-linear effect, either artificially enhancing or decreasing reported temperature (Defliese and Lohmann, 2015). The *P. strathairdensis* shells have been reported to show seasonal variation within an individual shell, with variations in both $\delta^{18}\text{O}_{\text{CARBONATE}}$ and $\delta^{13}\text{C}$ (Hudson, 1968; Patterson, unpublished data).

William Patterson kindly provided unpublished, high resolution, stable isotope data from individual *P. strathairdensis* shells (including one from bed 5e) which were micro-milled to investigate seasonal growth variations of $\delta^{18}\text{O}$ and $\delta^{13}\text{C}$ preserved within growth laminae. The shell in bed 5e gave isotopic values that ranged between +3.2‰ to +3.6‰ in $\delta^{13}\text{C}$ and -2.2‰ to -2.9‰ in $\delta^{18}\text{O}$.

It was shown by Defliese and Lohmann (2015) that variation between end members of <2‰ would give variations far lower than the precision achieved by typical mass spectrometers. Indeed, using the extremes of $\delta^{13}\text{C}$ and $\delta^{18}\text{O}$ above as end members, it was found that the effects of non-linear mixing were not high enough to produce any temperature offset; the deviation from linearity was less than 0.00002‰ Δ_{47} . Therefore, seasonal variation within individual shell samples could not explain the high temperatures recorded by clumped isotope analysis.

5.4.1.2: *Vital effects and stress*

Earlier stable isotope data from *P. strathairdensis* aragonite (Tan and Hudson, 1974; Hudson, 1980; Hudson et al., 1995; Holmden and Hudson, 2003) has recorded what appear to be sensible palaeoenvironmental water compositions and temperatures, such that isotopic equilibrium between lagoon water and the precipitating shell aragonite has

been assumed, in line with what is known about most bivalves (see Immenhauser et al., 2015).

However, the new Δ_{47} data mean that disequilibrium (vital effects) precipitation should be reconsidered, especially as vital effects may be caused by other biological or external stressors (Immenhauser et al., 2015; Zhou et al., 2020). Of note the bivalve *Eurhomalea exalbida* experienced an increasing vital offset with shell age (Yan et al., 2012); and periods of environmental stress (heat wave and 'shock' after transplantation to a different site) can also cause $\delta^{18}\text{O}$ disequilibrium (Hahn et al., 2012).

The presumption that the $\delta^{13}\text{C}$ values recorded in mollusc shells represent ambient water $\delta^{13}\text{C}$ is complicated due to the varied sources of the precipitating shell's carbon pool, which is sourced from seawater/lagoon water DIC, metabolic and respired carbon, although the latter is less important in aqueous molluscs (e.g. McConnaughey, 1997; McConnaughey and Gillikin, 2008). The influence of the various pools on shell $\delta^{13}\text{C}$ can also change over a shell's lifetime; for example, Lartaud et al. (2010) showed, by introducing a ^{13}C -light food supply, changes in the $\delta^{13}\text{C}$ of *Crassostrea gigas* shells were evident when metabolic activity was enhanced.

The question of vital effects in clumped isotope data from bivalves were raised by both Eagle et al. (2013) and Henkes et al. (2013), where 'true' growth temperatures from modern shells were compared to Δ_{47} derived values in order to construct temperature calibrations. A range of Δ_{47} values were measured for shell samples from a known growth temperature by Henkes et al. (2013), although they could not definitively attribute this to inter-species vital effects, citing sample heterogeneity and inaccuracy in growth temperature estimates as complicating factors. Some bivalve species analysed by Eagle et al., (2013) gave values that were outside the 95% confidence limits of the constructed temperature calibration, suggesting that species specific vital effects may have been recorded but acknowledging the need for more specific study.

More recently, in a study of modern calcitic marine bivalves, disequilibrium vital effects were detected in juvenile shells of *Magallana gigas*, resulting in more negative Δ_{47} values than expected and thus more positive apparent temperatures, while adult shells showed no such disequilibrium (Huyghe et al., 2022). Slightly elevated temperatures were also measured in a high-resolution study of a modern sample of *Megapitaria aurantiaca* when compared to other species from localities only 70 km apart (Caldarescu et al., 2021). This seemingly systematic relationship led the authors to suggest species-specific vital effects as a cause.

Molluscs precipitate shell carbonate through the extrapallial fluid located between the mantle and growth surface of shells (see Marin et al., 2012 and references therein) rather than directly from seawater; thus this process could be a source of vital effects. Some brachiopods (which precipitate shell carbonate similarly) show vital effects due to kinetic isotope effects from the incomplete hydration and hydroxylation of DIC (Bajnai et al., 2018). The biomineralization of brachiopod shells does not involve the enzyme 'carbonic anhydrase', which is present in molluscs and acts as a catalyst between DIC species (e.g., McConnaughey and Gillikin, 2008). Bajnai et al. (2018) suggested that carbonic anhydrase might thus reduce kinetic isotope effects, although this enzyme is also present in corals (e.g., Chen et al. 2018, and references therein) and echinoderms (e.g. Chow and Benson, 1979) which still display vital effects in both $\delta^{18}\text{O}$ and Δ_{47} (Saenger et al., 2012; Spooner et al., 2016; Davies and John, 2019). McConnaughey and Gillikin (2008) suggest that milder alkinization in molluscs prevents the strong vital effects seen in corals.

Disequilibrium in the DIC-H₂O-CO₂ system caused by absorption and desorption were modelled by Guo (2020) to be a greater potential source of Δ_{47} vital effects than hydration and hydroxylation; results from corals fit well with the modelled predicted disequilibrium related to absorption, and explain the positive Δ_{47} values observed in comparison to the expected values. Molluscs have potential to experience disequilibrium due to CO₂ absorption or DIC speciation effects, and Huyghe et al., (2022) explained their disequilibrium results using the Guo (2020) model. It is important to note that the Guo (2020) models allow for both positive and negative Δ_{47} offset, which would cause lower and higher temperatures, respectively.

Regardless of cause, it seems from the studies of modern and fossil bivalves where Δ_{47} vital effects have been described, that these effects are species specific (Eagle et al., 2013; Henkes et al., 2013; Caldarescue et al., 2021; Huyghe et al., 2022), whereas there is a large range of variation between the individual *P. strathairdensis* shells measured here, implying that this is not a simple species-specific offset. Moreover, all shells sampled here, aside from samples 10a and 11b, were interpreted to be of adult size (cf. Hudson 1968), negating any issue caused by sampling juveniles (Huyghe et al., 2022). We also see a similar high temperature effect with the single measurement of a *U. andersoni* from the Kilmaluag Formation of the GEG, suggesting that this is a regionally significant issue.

In summary, there is no compelling evidence that the Δ_{47} values in *P. strathairdensis* have been caused by disequilibrium vital effects.

5.4.1.3: Measurement variability

The measurement precision for the *P. strathairdensis* shells analysed is low. For one shell with 7 repeat measurements, there is up to 45 °C difference between maximum and minimum measurement repeats. Another 7-measurement shell has an internal range of 42 °C, and one shell of 2 measurements has a 44 °C temperature difference. As these shells were ground to a fine homogeneous powder in a pestle and mortar, is not likely that such variability is due to real variations in the shell chemistry.

Most *P. strathairdensis* shell measurements were made during the time a reference gas experiment was occurring, which resulted in progressive incremental contamination of reference gas. A blanket correction for the whole time period (5 reference gas changes, ~1.5 months) was applied for all affected measurements (Chapter 2.5.7.1), created using an average of the gradients for the standards ETH1, ETH3 and UEACMST produced when all data of each standard was plotted against the time past reference gas change (in days). This created an added uncertainty, as addressed in Chapter 2.5.7.1. Individual gradients for each reference gas had some variation, most prominently those with fewer days of reference gas use. The precision of 7-measurement repeats slightly improves if data, ran during the periods where individual reference gas gradients are most different from the mean, are excluded. Some repeats were also measured during an unexplained reference gas drift in 2022 (Chapter 2.5.7.2) which had a similar correction applied, also potentially adding unquantifiable uncertainty.

Despite this internal inconsistency, as the shells are the same material (biogenic aragonite) and the environment at the time of deposition is unlikely to have experienced extremes in temperature, the mean of all measurements including repeats (n=54) can be used as a representative value for the population – doing so gives a mean of 41 °C with a standard deviation of 13.7 °C, 5th percentile of 22.8 °C and 95th percentile of 58.4 °C (not taking into account uncertainty relating to the temperature equation). The mean is at the warmest extreme of the survival temperatures of modern *Mytilus* (Table 5.8) and as discussed above, is not thought to represent environmental temperatures in these Jurassic lagoons.

Four shells, those previously used for Sr isotope analysis (provided by Chris Holmden) were, by chance, measured (repeated 2-3 times) during a period where there

were no additional corrections required in the data processing. Means for these repeats gave temperatures between 28 ± 8 °C and 37 ± 9 °C, with a mean of 33 °C for all 11 measurements. The standard deviation for all 11 measurements of the four shells is 6 °C, the 5th percentile is 25 °C and 95th percentile is 42 °C (not taking into account uncertainty relating to the temperature equation). These statistics are clearly lower than those for the main batch of data described above, excepting the 5th percentile value which is similar in both cases.

The standard deviation of the Δ_{47} results for all shell data is 0.034‰; in comparison, the pooled standard deviation of the biogenic standard used throughout the measurement period (Table 2.4) is 0.030‰. This is the highest standard deviation of ETH3 recorded throughout the work discussed in this thesis, probably due also to the correction issues outlined above. The 7-measurement shells (159-16a and 159-22a, with 5 repeats requiring correction each) had standard deviations of 0.040‰ and 0.051‰ (Appendix 3: Part II). Comparing these to other samples that were measured repeatedly but required no reference gas corrections, these values are high; the ammonite rp-16-5 measured 6 times had a standard deviation of 0.027; the sandstone concretion subsample M8605 (Chapter 4), repeated 10 times over the course of two weeks, has a standard deviation of 0.022‰. It is therefore possible that measurement issues have exaggerated the extreme temperatures, particularly as some shells were not measured more than once.

5.4.1.4: Organic contaminants

If gases released through acid digestion of organic material in shells have not been removed in the gas preparation cleaning process, this may cause isobaric interference, resulting in ‘contamination’ of the Δ_{47} values measured.

A negative shift in Δ_{47} (and thus increase in temperature) has been observed by Bergmann et al. (2017) for modern linguliform brachiopods with high organic content, attributed to hydrolysable carboxylic groups, which also caused depletions in $\delta^{13}\text{C}$ and $\delta^{18}\text{O}$ and a rise in Δ_{48} . However, using MIRA we have found that Δ_{47} more typically increases as a result of such contamination, causing cooler reported temperatures, although this will depend on the masses of the interfering molecules and both positive and negative distortions have been observed (Snell et al., 2019).

The organic preservation in *P. strathairdensis* is thought to be low (10-20% remaining of the original content; Hudson 1967). Despite this, it is worth interrogating our own data for potential influence of shell specific contamination. Due to the 'systematic contamination' issue in the period of time when the reference gas experiment was taking place, for our shells it is difficult to relate Δ_{47} to Δ_{48} with confidence, although we can apply a correction to these Δ_{48} values using the same method as applied to Δ_{47} (Chapter 2.5.7). The values of Δ_{48} measured for our samples are not unusual in comparison to other measurements. Comparing corrected Δ_{48} results to Δ_{47} derived temperature shows a correlation with $R^2 = 0.1$, and there is also no trend between $\delta^{13}\text{C}$ or $\delta^{18}\text{O}$ and temperature.

Additionally, after the main period of data gathering was complete, one *P. strathairdensis* shell was prepared for clumped isotope analysis as described in Chapter 2.3.2.7, but at the position of the sample bellows on MIRA, a quadrupole mass spectrometer was used to investigate the composition of the prepared gas. No unusual traces indicating the presence of a contaminant gas were found. We thus conclude that organic derived contamination has not affected our measurements.

5.4.1.5: Aragonite to calcite neomorphism

Aragonite is metastable at earth surface temperatures (Jamieson, 1953) and thus preservation over geological timescales is unusual (e.g., Hall and Kennedy, 1967; Cherns and Wright, 2009), limited to impermeable mudstone matrices where interaction with basinal fluids is minimised. Aragonite – calcite neomorphism has been shown to cause changes particularly in $\delta^{18}\text{O}$ and Δ_{47} , enhanced by both external (e.g., Ritter et al., 2017) and internal (Pederson et al., 2019; 2020) fluid involvement.

XRD analysis showed that some shells measured have trace amounts of calcite (Table 5.7), and two shells from the same hand specimen had ~25% calcite. No XRD analysis was performed at UEA for the shells provided by Chris Holmden as they were previously reported as being pristine (Holmden and Hudson, 2003).

For the shells with the highest calcite contents, both from hand sample '18', $\delta^{18}\text{O}$ values are the lowest recorded, below -5‰, and are >3 SD from the population mean. The $\delta^{13}\text{C}$ values are not unusual in comparison with the other shells measured, ranging from 0.2 to 1.2 standard deviations from the population mean.

Previous workers have reported $\delta^{18}\text{O}_{\text{CARBONATE}}$ values for *P. strathairdensis* shells from Kildonnan ranging from $<-6\text{‰}$ to -2‰ VPDB (see Tan and Hudson, 1974): values $<-5\text{‰}$ VPDB are not unusual. As many of the shells analysed in this study have $\delta^{18}\text{O}_{\text{CARBONATE}}$ values $>-2.5\text{‰}$ VPDB (Fig. 5.9) it is possible there may have been an unintentional bias during field sampling, in so far as the extent of exposure changes with time due to covering by mobile beach sediment. However, in these previous studies, $\delta^{13}\text{C}$ covaries with $\delta^{18}\text{O}$. The shells from hand specimen 18 are clear outliers when compared to the

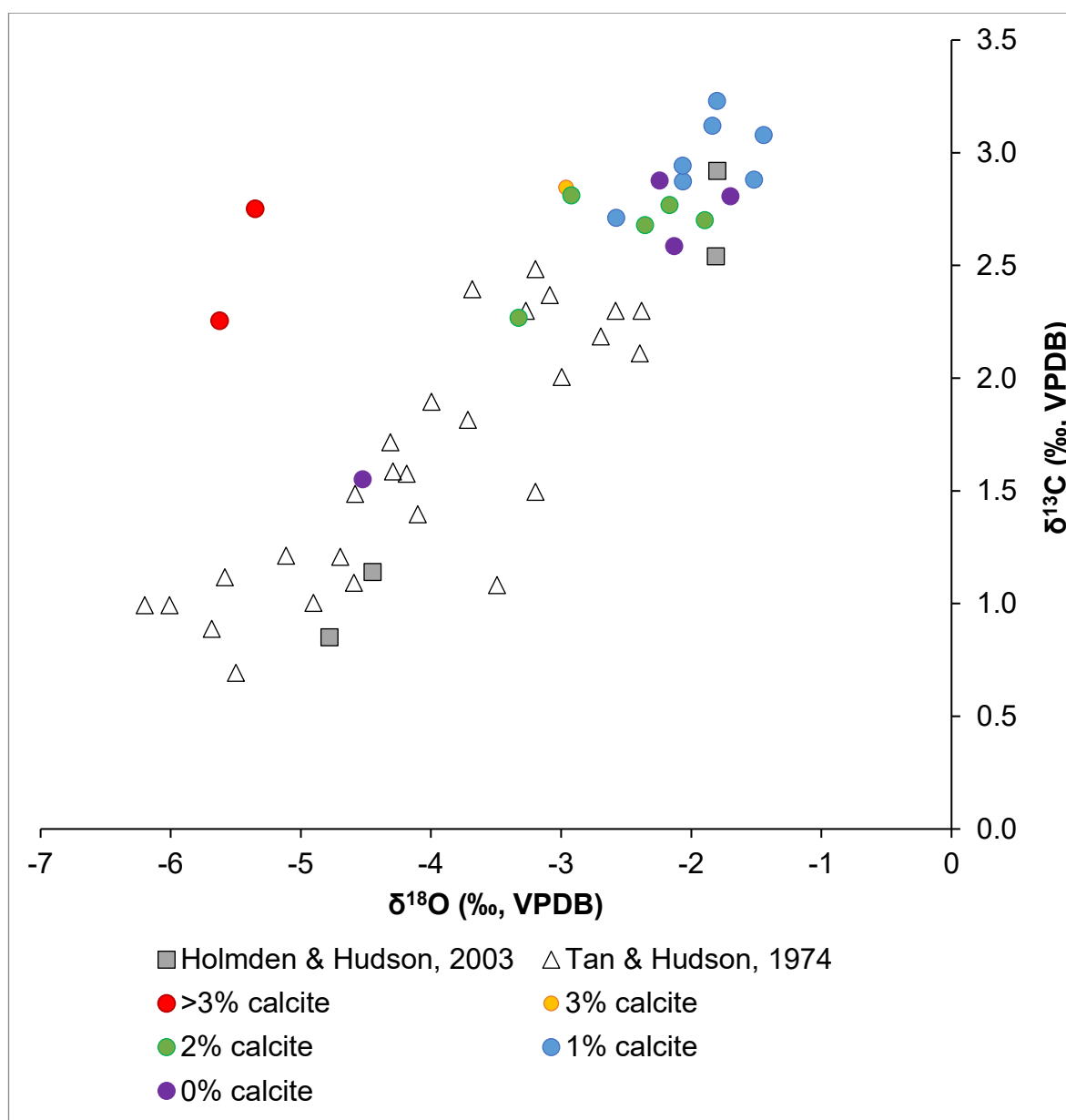


Figure 5.9: Covariant trend in $\delta^{13}\text{C}$ and $\delta^{18}\text{O}_{\text{CARBONATE}}$ seen in *P. strathairdensis* shells, including data previously measured by Tan and Hudson (1974) and Holmden and Hudson (2003). Coloured circles represent data measured by MIRA, with colours corresponding to the percentage of calcite indicated by XRD. The two shells with calcite percentage between 23-25% are clear outliers of this trend.

other measurements made here and with previously published data (Fig. 5.9). Only one other shell (E331 from Holmden and Hudson, 2003, thought to be pristine) measured by MIRA gave a $\delta^{18}\text{O}_{\text{CARBONATE}}$ value of $<-4\text{‰}$, but this shell clearly follows the covarying trend.

In previous studies, the presence of minor calcite has been related to measurable differences in Δ_{47} ; Wang et al. (2021) reported that aragonite shells with between 0.4 and 1.2% calcite gave lower $\delta^{18}\text{O}$ and $\delta^{13}\text{C}$ values, and Δ_{47} derived temperatures were $\sim 10\text{ °C}$ lower in comparison to ‘pristine’ shells (with $<0.4\%$ calcite).

For our shells, where XRD indicated between 0-3 % calcite (all bar 2, above), $\delta^{13}\text{C}$ and $\delta^{18}\text{O}$ data when plotted against one another do not show lower $\delta^{18}\text{O}$ for higher calcite content (gradient: 0.13, $R^2 = 0.1$). Excluding the two shells with $\delta^{18}\text{O} < -3\text{‰}$ and $\delta^{13}\text{C} < +0.5\text{‰}$ (in order to focus on shells plotting at $\sim -2\text{‰}$), there is only a weak trend towards $\delta^{18}\text{O}$ becoming more negative with calcite % (gradient -0.3 ; $R^2 = 0.25$). There is, in addition, no trend in temperature with increasing calcite %, even after exclusion of shells with $\delta^{18}\text{O} < -3\text{‰}$ and $\delta^{13}\text{C} < +0.5\text{‰}$ (gradient = 1.8; $R^2 = 0.02$).

SEM imaging of 3 shells showed no textural evidence for aragonite – calcite transition (Fig. 5.7), while a shell from the ‘18’ hand specimen showed fabric along its lowermost edge where aragonite may have reacted with micro-vein fed fluid (Fig. 5.8). It is thus unlikely that aragonite-calcite neomorphism has taken place, and there is little to no isotopic evidence for such reaction. It is possible that calcite spar-filled micro fractures were missed when choosing shells, particularly those from this hand specimen ‘18’, which would explain the higher calcite percentage recorded by XRD. There is no evidence that calcite percent has any relationship with Δ_{47} derived temperatures.

5.4.1.6: Carbonate-Fluid interaction:

CHN analysis of modern and fossil shells, including *P. strathairdensis*, led Hudson (1967) to observe that some shells had hydrogen concentrations that were higher than expected to be combined with organic carbon, concluding that ‘free water’ is trapped within the shell structure (finding as much as 2 wt.% water in both modern and some fossil shells). Such inclusions were observed to be more common in aragonite versus calcite, and more abundant still in aragonite with a nacreous structure (Hudson, 1967), an observation echoed by Towe and Thompson (1972) who investigated inclusions using

TEM. Subsequent work by Lécuyer and O'Neil (1994) indicated that the percentage of internal water in modern biogenic carbonates varies strongly between members of different species but is reproducible within species.

Aqueous fluids liberated from organics have been suggested by Pederson et al. (2019; 2020) to be important in the early alteration of biogenic carbonates, particularly with reference to aragonite/calcite neomorphism which also causes stable and clumped isotopic exchange.

There is also evidence that internal fluids may facilitate isotopic resetting without any phase transition; Nooitgedacht et al. (2021) observed for biogenic aragonite that with heating (175 °C for 90 minutes) there was strong evidence for oxygen isotopic exchange between internal fluids (both inclusions and organic associated water) and the carbonate, with fluid inclusion $\delta^{18}\text{O}$ increasing and carbonate $\delta^{18}\text{O}$ decreasing. Additionally, Δ_{47} decreased, leading to a temperature increase from the initial measurement of 31.9 ± 15.4 °C to 70.0 ± 19.2 °C (95% confidence). No mineralogical change was recorded, indicating that the principles normally thought to indicate 'pristine' preservation may not be enough to be confident that no change in Δ_{47} has occurred; they accept, however, that mineralogical change may have been below the instrumental detection limit.

The Kildonnan Member *P. strathairdensis* fossils are wholly aragonite, which is largely of nacreous structure (Hudson, 1968). They were observed by Hudson (1967) to also have excess hydrogen, calculated as 0.19% excess H (1.7 wt.% water), in comparison to modern nacreous shells with 0.22% excess H, equivalent to 2 wt.% water, thus isotopic exchange with both structurally trapped and organic associated aqueous fluids is plausible. For example, in some corals, liberation of fluid from organic matter is observed at temperatures as low as 60 °C (Dauphin et al., 2006), although most remains bound to higher temperatures (Cuif et al., 2004; Dauphin et al., 2006). This noted, most of the organic matter in the *P. strathairdensis* fossils is both degraded and in low concentration (compared to modern shells of similar type; Hudson, 1967). It is unknown whether fluid was liberated during any such post-depositional reactions.

The experiment on biogenic aragonite by Nooitgedacht et al. (2021) was necessarily (due to rate constraints) performed at much higher temperatures (175 °C) than the *P. strathairdensis* fossils are thought to have been exposed to. The Eigg Valtos Sandstone concretion cements provide an upper limit of 98 ± 9 °C (although this is fluid was heated by reaction with lavas). The warmest calcite cement value measured from

Kildonnan outcrop is 48 ± 9 °C (Fig. 4.24 and Table 4.4) which is a better estimate of burial temperature. Moreover, the experiment (Nooitgedacht et al. 2021) was held at temperature for only 90 minutes, rather than the millions of years of maximum burial as constrained by the Eigg lava chronologies (Chambers et al., 2005; Emeleus and Bell, 2005). Lower temperatures would implicate slower rates of exchange, on timescales that are not feasible to mimic experimentally. It is, therefore, difficult to constrain the feasibility for measurable changes in Δ_{47} and $\delta^{18}\text{O}$ caused by slower, cooler reactions over hundreds-of-thousands to millions-of-years. Indeed, Nooitgedacht et al. (2021) suggest that the fraction of carbonate available for isotopic exchange might increase with reaction time.

The $\delta^{18}\text{O}$ change reported by Nooitgedacht et al. (2021) was small – a $\sim 0.12\text{‰}$ decrease for their aragonite bivalve sample, although the Δ_{47} change raised the calculated temperatures by ~ 30 °C. We do not see a conclusive relationship between $\delta^{18}\text{O}$ and temperature when all our data are plotted; comparing the averages of shells with $\delta^{18}\text{O}_{\text{CARBONATE}}$ values $> -3\text{‰}$ VPDB against their Δ_{47} derived temperatures, there is a very weak positive trend with a gradient of 12 but an R^2 of 0.25. This is the opposite trend to that expected if higher temperatures were caused by isotopic exchange with internal fluids. Internal fluid values are likely to be more negative in $\delta^{18}\text{O}$ composition than *P. strathairdensis* $\delta^{18}\text{O}_{\text{CARBONATE}}$ – initial $\delta^{18}\text{O}$ for the internal fluid of an aragonite bivalve measured by Nooitgedacht et al. (2021) were $+1.7 \pm 2.2\text{‰}$ VSMOW, and Lécuyer and O’Neil (1994) measured fluid inclusion $\delta^{18}\text{O}$ between $+6\text{‰}$ and $+18\text{‰}$ SMOW for a range of marine and freshwater skeletal carbonates. However, the $\delta^{18}\text{O}_{\text{CARBONATE}}$ of *P. strathairdensis* shells are between $+25\text{‰}$ and $+29\text{‰}$ (converted to the VSMOW scale); exchange with internal fluids should result in more negative $\delta^{18}\text{O}_{\text{CARBONATE}}$.

Preliminary water content data for three *P. strathairdensis* shells and one unionid. shell measured for Δ_{47} were measured using a CHN analyser (Table 5.9). No relationship between water content and higher/lower temperature is evident. Moreover, shell E 218 (Holmden and Hudson, 2003) – was previously investigated for water content by Hudson (1967). One measurement of this shell had the second highest H% measured for *P. strathairdensis* (0.23% H) but gives a relatively cool Δ_{47} derived temperature of 32 ± 10 °C, supporting the notion that there is no relationship between high internal water content and high temperatures (Table 5.9).

It is concluded that it is unlikely that the high Δ_{47} derived temperatures for *P. strathairdensis* can be explained by isotopic exchange with internal fluids at geologically constrained temperatures between 50 °C and 100 °C, even allowing for the millions of years reaction time. There is no evidence for increasing temperature with decreasing $\delta^{18}\text{O}_{\text{CARBONATE}}$ and there is no evidence for high temperatures correlating with shell water content, although this is an aspect that could be investigated further.

It is also unclear whether shell water content would be related to a range of temperatures or a more uniform shift – the H% values measured by Hudson (1967) for *P. strathairdensis* ranging from 0.14 to 0.24%. In fact, this variation may itself be a product of diagenesis - Lécuyer and O’Neil (1994) found that % fluid data was highly reproducible within a species- a conclusion that appears consistent with modern shell data in Hudson (1967). It is unknown at what point, before or after maximum burial, fluid content may have decreased in some shells; however, if the sampling locality experienced fairly uniform burial heating, as is probable, a more systematic change in temperature might have been expected than is observed, using a species with fairly uniform fluid contents.

Sample ID	Species	$\delta^{18}\text{O}$ (‰, VPDB)	T (Δ_{47}) (°C)	H (%)	Water (wt. %)
E 218*	<i>P. strathairdensis</i>	-3.291 ± 0.046	32 ± 10	0.23 0.20	2.07 1.80
rp-159-16a	<i>P. strathairdensis</i>	-1.803 ± 0.025	40 ± 7	0.22	1.98
rp-159-21a	<i>P. strathairdensis</i>	-2.064 ± 0.046	23 ± 9	0.13	1.17
rp-159-22a	<i>P. strathairdensis</i>	-2.132 ± 0.025	44 ± 7	0.11	0.99
JEA2805-1	<i>Unio sp.</i>	-5.621 ± 0.046	-8 ± 7	0.26	2.34

Table 5.9: All ± values represent one standard error of the pooled standard deviation. Water content are an approximation that does not take into account alternate sources of hydrogen. *sample E 218 results are from Hudson (1967).

5.4.1.7: Solid-State Resetting

Another potential cause of Δ_{47} change in natural systems is ‘solid-state bond reordering’, or ‘resetting’. When exposed to high temperatures, the energy to break the bonds between ^{13}C – ^{18}O may be overcome, allowing diffusion to take place, and with this the Δ_{47} values of the material will begin to approach a new thermal equilibrium.

Early experiments investigating solid-state reordering focused on calcite spar crystals. Samples were heated to a high temperature and Δ_{47} was measured in time

increments, which showed that reordering takes place in two phases: initially a fast, non-first order reaction dominates, where a rapid decrease in measured Δ_{47} values is observed; after a period of time a slower, first order reaction then becomes dominant, where Δ_{47} decrease continues less rapidly (Passey and Henkes, 2012). These experiments were repeated by Henkes et al. (2014) for brachiopod shell calcite, with a similar pattern of results.

Both Passey and Henkes (2012) and Henkes et al. (2014) concluded that the initial, fast, non-first order reaction was due to the presence of crystal defects (for this purpose, 'vacancies' of atoms in the crystal lattice which are a preferred route for a molecule to diffuse to), the abundance of which allow rapid initial reordering. However, many of these defects rapidly anneal, meaning that the high rate of diffusion is not maintained. Annealing of defects has been observed in diffusion studies of carbonates as a process that reduces diffusive rates (e.g. Kronenberg et al., 1984; Farver 1994).

Henkes et al. (2014) developed a hypothesis to suggest that both rapid and slow processes were due to defects within the crystal structure, but the apparent two stages of reordering were due to annealable and non-annealable defects – some defects, such as structural defects (caused, for example, by dislocations, macro scale inclusions) are able to be annealed and become less abundant with time, and thus are the cause of the non-first order observation; whereas others, such as intrinsic defects (whose occurrence are thermodynamically controlled and which reequilibrate with temperature change), are un-annealable and thus diffusion takes place as a first order reaction. After the abundance of annealable defects has been reduced the diffusion through the presence of non-annealable defects is the main method of solid-state reordering.

A second 'reaction-diffusion' model was developed by Stolper and Eiler (2015) where the fast, non-first order reaction is explained as a rapid Δ_{47} decrease due to breakage of many $^{13}\text{C}-^{18}\text{O}$ bonds followed by isotopic exchange to an adjacent carbonate ion, forming 'singly-substituted isotopologue pairs' - a $^{13}\text{C}^{16}\text{O}_3$ is now immediately adjacent to a $^{12}\text{C}^{18}\text{O}^{16}\text{O}_2$, when initially a $^{12}\text{C}^{16}\text{O}_3$ was adjacent to a $^{13}\text{C}^{18}\text{O}^{16}\text{O}_2$. After this, slow first order diffusion is the cause of the subsequent lower rate process.

Similar experiments to those described above were performed on inorganic aragonite by Chen et al. (2019) who observed comparable results except near the aragonite-calcite transition where, after the previously observed rapid Δ_{47} decrease, Δ_{47} increased and then once again decreased to proceed towards thermodynamic equilibrium. Chen et al. used the 'reaction-diffusion' model of Stolper and Eiler (2015) to

explain this - a temporary reformation of clumps from pairs - and could not see how the defect-annealing model could explain this change.

Hemmingway and Henkes (2021) later proposed that a disordered kinetic model based on random walk diffusion could explain the experimental observations and model results of all prior work, suggesting that; a) defects may influence the ability to overcome activation energy that allows diffusion to take place, but that their presence is not vital for diffusion to take place, as in Henkes et al. (2014); and b) the clump-pair transition of Stolper and Eiler (2015) does not need to be modelled as a process separate to diffusion.

While able to re-create the experimental results of Chen et al. (2019), Hemmingway and Henkes (2021) did not apply their model to aragonite over geological time scales. For calcite, estimates of change over geological timescales were attempted by some modellers; Stolper and Eiler (2015) suggested that there would have been a <1 °C change for calcite held at 75 °C for 100 million years, and a 10 °C change at 100 °C for the same length of time, while Henkes et al. (2014) projected that there would be no change for a calcite held at 100 °C for 60 Ma, but a 26 °C change at 130 °C. However, Hemmingway and Henkes (2021) suggested that previous models overestimate the temperatures that are required to initiate solid-state reordering in calcite when compared to their model. Application of the Hemmingway and Henkes (2021) model by Barney and Grossman (2022) to Ordovician calcite brachiopod shells with a proposed burial history that reached maximum temperatures of 85 °C caused a Δ_{47} derived temperature change of only ~1 °C.

Regardless of model, the experiments, based on calcite, were done at higher temperatures than those that could have affected the Kildonnan member shell aragonites considered here. However, as observed by Staudigel and Swart (2016) in experimental heating of biogenic aragonite, changes were seen in Δ_{47} values at temperatures as low as 125 °C, with no evidence of mineralogical change, suggesting that the temperature threshold for the initiation of reordering in biogenic aragonite is lower than that observed in calcite. Experiments on the aragonite shell of the bivalve *Arctica islandica* supported this observation, showing a Δ_{47} decrease resulting in a ~26 °C temperature increase after being held at 100 °C for 20 weeks (Ritter et al., 2017).

First order Arrhenius equations produced by Staudigel and Swart (2016) based on their experiments (at temperatures between 125 °C and 425 °C; $E_a = 1.1 \times 10^5$ J/mol and $\ln(k_0) = 21.7$), when calculated for 100 °C, give a suggested time span for aragonite

equilibrium resetting of 0.3 years, and for 75 °C, 3.2 years. Wang et al. (2021) used the same equations to show that at 1 °C, total reequilibration could take place in ~100,000 years. At face value, this suggests that the Kildonnán member fossils would be fully annealed. However, depositional Δ_{47} temperatures from Jurassic belemnite phragmacone aragonite (Christian Malford Lagerstätte, southern England; Vickers et al., 2021) imply that their phragmacone aragonite is unaltered under maximum burial temperatures between 40-50 °C (Hudson and Martill, 1994; Green et al., 2001). Thus, near-pristine preservation must be possible over geological timescales, under shallow burial conditions.

While the experimental and modelling approaches are likely to be simplified - based on limited kinetic data (Wang et al., 2021), and while some of the equations only model the second, 'slow process' of reordering, the outcomes do overall suggest that reordering at temperatures <100 °C are not implausible on geological timescales. In the specific case of the *P. strathairdensis* shells from the Kildonnán Member, exposure to a burial temperature above or at 50 °C but below 100 °C may have meant that resetting had initiated, but that complete reequilibration had not been attained. The Christian Malford data suggests that the energy required for overcoming the activation energy for bond breaking and diffusion is unlikely to have started until burial temperatures were above 50 °C, which in the case of the Kildonnán member, cannot have happened until earliest Paleocene times (see Fig. 4.10, though note that lava thickness displayed is based on estimations from Skye), >100 million years after deposition of the shells: at this time the burial temperatures were then presumably above or at ~50 °C but below 100 °C for potentially <1 Ma (a length of time based on the apparent high erosion rates reported for the unroofing of Rum; Hamilton et al., 1998; Chambers et al., 2005) during extrusion and subsequent erosion of the Eigg lavas. Thus, although previous work on solid state reordering shows that the earliest stage of Δ_{47} resetting is a rapid process, a detectable amount of bond reordering must have been able to take place many millions of years after shell deposition. This seems to be the most plausible explanation for the higher-than-environmental temperatures measured for our *P. strathairdensis* shell population.

5.4.1.8: Summary of *Praemytilus strathairdensis*: High temperatures

There are several processes that have been discussed that could plausibly cause the unrealistically high temperatures derived within our sample population:

1. Measurement variability

- The measurement precision of shells ran multiple times is lower than average for our data, and indeed the population standard deviation is lower than for the regularly analysed biogenic standard. Additional corrections have also necessarily been applied to much of the *P. strathairdensis* Δ_{47} data, with varying effectiveness; these cannot be improved upon.
 - Results from samples measured only once or twice should be regarded as suspect and may have caused the significance of shells with extreme temperatures to be exaggerated.
 - Despite this, the population mean Δ_{47} temperature is still higher than expected, and shells measured when no correction has been required also give higher temperatures than would be probable for the envisioned environment of growth.
2. Organic contamination
- Gases released by acid digestion of organic material from within the shell structure, if not removed by the gas preparation/cleaning process, can cause isobaric interference resulting in ‘contamination’ of the Δ_{47} values measured, which can be both positive and negative.
 - We do not have evidence for contamination in our shells.
3. Vital effects
- Both species specific (Caldarescue et al., 2021; Eagle et al., 2013; Henkes et al., 2013) and juvenile (Huyghe et al., 2022) specific bivalve disequilibrium vital effects have been identified in reference to Δ_{47} .
 - It is unlikely that the temperature variability we see is due to vital effects, as all but one shell was thought to be adult size and vital effects tend to show systematic effects within species. They are also typically associated with vital effects in $\delta^{13}\text{C}$ and $\delta^{18}\text{O}$, and previous environmental interpretations of stable isotopes are not compatible with strong disequilibrium effects.
4. Mixing
- Although *P. strathairdensis* are known to record seasonal variations (Hudson, 1968; Patterson, unpublished data), the ranges in $\delta^{18}\text{O}$ and $\delta^{13}\text{C}$ are not large enough to cause non-linear Δ_{47} mixing effects as a result of sample inhomogeneity (calculated using the methods of Defliese and Lohmann, 2015).
5. Aragonite to calcite contamination/neomorphism

- Aragonite is metastable at Earth surface temperatures and readily transforms by neomorphism to calcite, which is known to cause $\delta^{18}\text{O}$ and Δ_{47} shifts (e.g., Hemmingway and Henkes, 2021; Ritter et al., 2017, Pederson et al., 2019; 2020; Wang et al., 2021). There is no SEM evidence for shell neomorphism.
 - Two shells measured here were shown by XRD to have ~25% calcite and 13 shells had traces of calcite ($\leq 3\%$). Shells with $>3\%$ had clearly identifiable decreases in Δ_{47} , the shell at 3% calcite may have also shown evidence for a $\delta^{18}\text{O}$ shift but other shells had no apparent $\delta^{18}\text{O}$ shift and Δ_{47} temperature showed no relationship even with ~25% calcite.
6. Fluid-carbonate isotopic exchange
- Isotopic exchange with internal fluids and hydrated organics has been thought to enhance changes in Δ_{47} when the material is exposed to higher temperatures, although an associated change in $\delta^{18}\text{O}$ is also observed (e.g., Staudigel and Swart, 2016; Nooitgedacht et al., 2021).
 - We cannot know if we observe any $\delta^{18}\text{O}$ shift as we do not have a definite original reference point for *P. strathairdensis*; however, Δ_{47} derived temperatures do not show a trend with decreasing $\delta^{18}\text{O}_{\text{CARBONATE}}$, even when excluding 'environmental trend' related outliers. We therefore do not have evidence of isotopic exchange that has reordered Δ_{47} values, and suggest it is not the cause of higher-than-expected temperatures.
7. Solid-state resetting
- If the activation energy of $^{13}\text{C}-^{18}\text{O}$ bond breakage is overcome, diffusion may take place, changing the abundance of 'clumped isotopes', leading to changes in Δ_{47} – higher temperatures are most often involved (for example due to burial) and Δ_{47} will tend towards a new equilibrium at a higher temperature. The beginning of this process appears to occur rapidly (Passey and Henkes, 2012; Henkes et al., 2014; Stolper and Eiler, 2015; Staudigel and Swart, 2016; Chen et al., 2019).
 - The energy required for solid-state bond reordering appears to be lower in aragonite than in calcite (Staudigel and Swart, 2016; Ritter et al., 2017, Chen et al., 2019). Experiments have shown Δ_{47} reordering at 100 °C when held for 20 weeks (Ritter et al., 2017), yet Jurassic aragonitic material, thought to have been exposed to burial temperatures < 50 °C, has been described as pristine (Vickers et al., 2021). It is possible that the Kildonnán Member *P.*

strathairdensis shells were buried to an intermediate temperature where the activation energy allowing the initiation of reordering, which may explain the high Δ_{47} derived temperatures. No $\delta^{18}\text{O}$ or $\delta^{13}\text{C}$ reordering is required in this scenario.

In summary, it is thought that the high temperatures derived using clumped isotope measurements of *P. strathairdensis* may be accentuated due to a period of low measurement precision, but this alone does not explain high temperatures measured after this period, or the overall trend of results. Partial solid-state resetting, despite burial at temperatures likely to have been well below 100 °C, is concluded to be the most likely cause.

5.4.2: Environmental conclusions from *P. strathairdensis* data

Despite the majority of the Δ_{47} data from *P. strathairdensis* equating to unusually hot values, several shells gave results that may give insights into the original environmental conditions of the Kildonnan Member lagoons.

The shell with the lowest average value gives a Δ_{47} derived temperature of 23 ± 9 °C and $\delta^{18}\text{O}_{\text{FLUID}}$ values of $-1.6 \pm 1.9\text{‰}$ VSMOW. Three other shells give measurements below 30 °C: one at 25 ± 9 °C ($\delta^{18}\text{O}_{\text{FLUID}} = -1.8 \pm 1.9\text{‰}$), and two at 28 ± 8 °C and 28 ± 13 °C ($\delta^{18}\text{O}_{\text{FLUID}} = -0.6 \pm 1.7\text{‰}$ and $-0.7 \pm 2.7\text{‰}$ VSMOW, respectively). These four shells have $\delta^{18}\text{O}_{\text{CARBONATE}}$ values between -2.1‰ and -2.6‰ and fall in the 'more positive' region of the $\delta^{13}\text{C}/\delta^{18}\text{O}$ covariant trend; there is no low temperature measurement that falls in the more negative region of the $\delta^{13}\text{C}/\delta^{18}\text{O}$ covariance.

We cannot be certain these results represent real depositional environment conditions or are simply part of the wide-ranging measurement variability. However, when plotting the temperature, $\delta^{18}\text{O}_{\text{FLUID}}$ and $\delta^{18}\text{O}_{\text{CARBONATE}}$ of all repeat measurements of shells (excluding values from shells with calcite % >22), a clear trend emerges, suggesting that $\sim 20\text{--}30$ °C may be close to original growth and calcification temperature, and therefore that original $\delta^{18}\text{O}_{\text{FLUID}}$ values were approximately 0‰ to -2‰ VSMOW (Fig 5.10): recalling that $\delta^{18}\text{O}_{\text{CARBONATE}}$ values are historically not thought to have been altered (Tan and Hudson, 1974; Hudson 1980; Hudson et al., 1995; Holmden and Hudson, 2003).

This conclusion relies on the assumption that the equation used to calculate $\delta^{18}\text{O}_{\text{FLUID}}$ from measured $\delta^{18}\text{O}_{\text{CARBONATE}}$ and Δ_{47} derived temperature, in this case the

mollusc specific calibration of Grossman and Ku (1986; equation 3), is representative of the true relationship between the three variables. This is one of several equations that exist for aragonite material and is in fact one of 3 published in Grossman and Ku (1986). At the temperatures we are interested in (20–30 °C) there is little difference between calibrations – for example, there is only a 0.2–0.3‰ difference between $\delta^{18}\text{O}_{\text{FLUID}}$ results calculated using the mollusk specific and ‘general’ aragonite calibrations of Grossman and Ku (1986), well below our uncertainty limits. This suggests that the Grossman and Ku (1986) equation 3 is appropriate, with the caveat that it is based on modern, not fossil, taxa.

Our Δ_{47} -derived temperatures, particularly the lowest temperatures, are consistent with previous estimates of *P. strathairdensis* palaeotemperatures (e.g., 18 °C, Hudson, 1980; 25 °C, Hudson et al., 1995; 23 °C, Patterson, 1999) and for the $\delta^{18}\text{O}_{\text{FLUID}}$ estimates from comparable samples wrt. the $\delta^{13}\text{C}/\delta^{18}\text{O}$ covarying trend (-1‰ VSMOW, Hudson et al., 1995; ~-0.5‰ VSMOW, Holmden and Hudson, 2003). They also fall within error of results from the calcitic bodies of mudstone hosted concretions from bed 5f and 6e (Hudson, 1966, Hudson et al., 1995), which give temperatures between 12 ± 6 °C and 21 ± 6 °C and $\delta^{18}\text{O}_{\text{FLUID}}$ values between -1.2 ± 1.3 ‰ and -1.7 ± 1.2 ‰ VSMOW; such concretions are argued, in Chapter 3 and Paxton et al. (2021), to provide bottom water temperature and fluid estimates due to their syngedimentary formation. With reference to the latest interpretations of the Kildonnan Member at Eigg by Holmden and Hudson (2003), $\delta^{18}\text{O}_{\text{FLUID}}$ values reported here for the low temperature shells (between -0.7 ± 2.7 ‰ and -1.8 ± 1.9 ‰ VSMOW) would represent evaporated ‘freshwater’ lagoon water. Due to the low number of ‘apparent’ true temperature and fluid compositions, in addition to the fact that most shells measured were, by chance, from the ‘evaporated water’ region of the covariant trend, it is difficult to draw any further conclusions that provide more clarity to this particular palaeoenvironmental reconstruction.

5.4.3: Wider context:

A small number of other Scottish Jurassic biogenic samples were also measured by clumped isotope analysis (Table 5.5). It is interesting that, although based on only one sample measurement, the temperature of aragonite from a Bathonian *U. andersoni* shell from the Kilmaluag Formation (GEG; Kilmaluag Bay, N. Skye) also gave an unreasonably high temperature (61 ± 17 °C), while measurement of septal aragonite from an ammonite in the younger (lower Kimmeridgian) Staffin Shale Formation (Staffin, N. Skye) gave

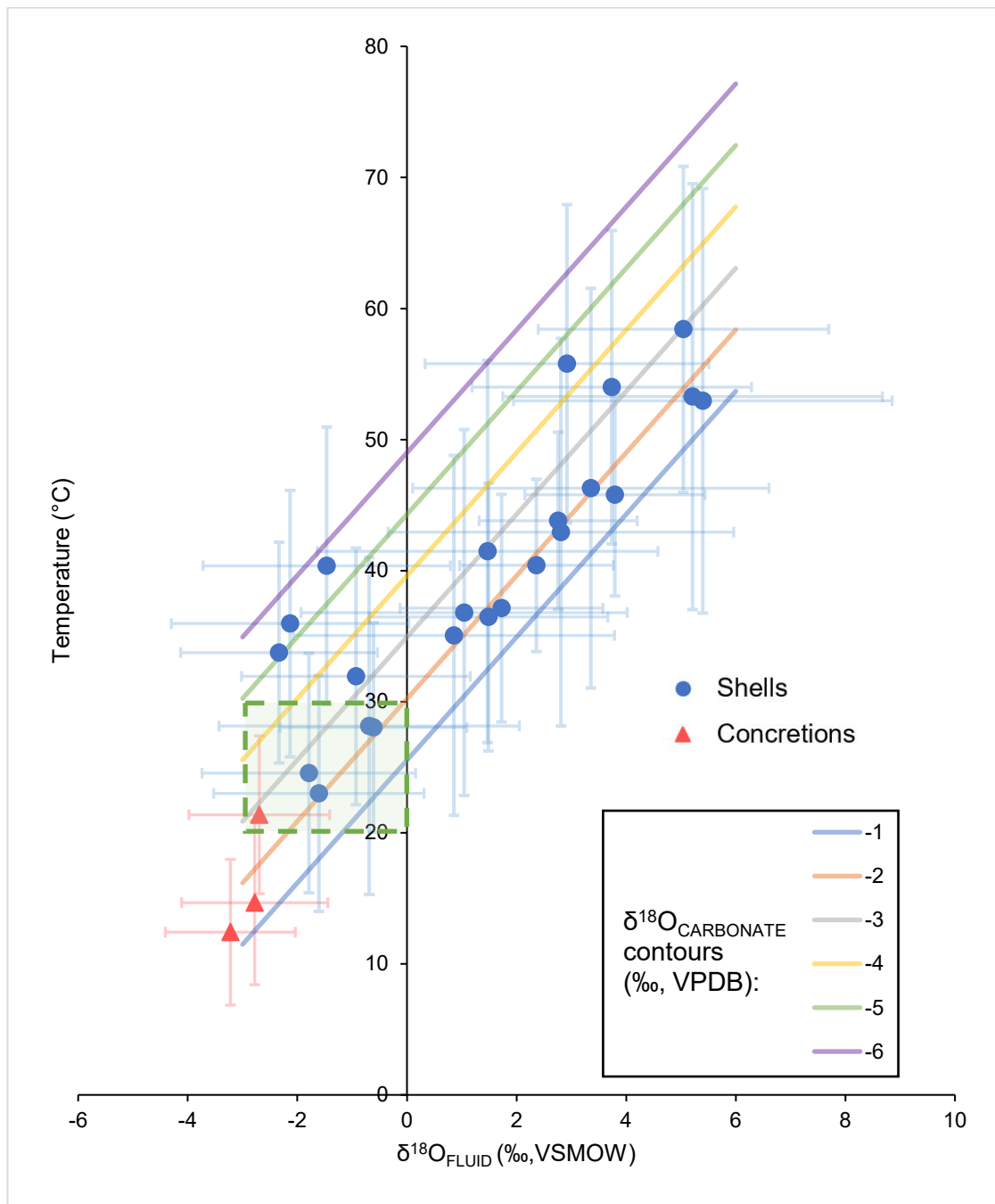


Figure 5.10: Δ_{47} derived temperatures and back calculated $\delta^{18}\text{O}_{\text{FLUID}}$ results of *P. strathairdensis* and mudstone hosted concretion bodies*, with contours indicating measured $\delta^{18}\text{O}_{\text{CARBOONATE}}$. Green box highlights the likely region of original temperature of growth and ambient $\delta^{18}\text{O}_{\text{FLUID}}$ of shells with $\delta^{18}\text{O}_{\text{CARBOONATE}}$ close to -2‰ (VPDB).

* Concretion $\delta^{18}\text{O}_{\text{FLUID}}$ values have been recalculated using Grossman & Ku (1986) for ease of comparison with $\delta^{18}\text{O}_{\text{CARBOONATE}}$ contours, thus are representative.

temperatures of 12 ± 5 and 14 ± 5 °C, much cooler than those from Belemnite rostrum calcite from the same formation (Vickers et al., 2021), but within error of two of the three calcite concretion bodies that record bottom water temperatures (Chapter 3; Paxton et al., 2021). The ammonite aragonite gives $\delta^{18}\text{O}_{\text{FLUID}}$ values of $-6.1 \pm 1.0\text{‰}$ and $-5.6 \pm 1.1\text{‰}$, very negative for Jurassic marine organisms, for which seawater values might be expected to have been closer to -1.2‰ VSMOW (Shackleton and Kennett, 1975).

These N. Skye, localities are ~5 km apart, and the Kilmaluag Formation, being older was definitely buried deeper than the Kimmeridgian sediments, perhaps by up to 200 m (inferred from Hudson and Andrews 1987; Fig. 5.4). This raises the possibility that the lower Δ_{47} values for the Bathonian *U. andersoni* reached a threshold burial temperature for Δ_{47} resetting, while the Kimmeridgian ammonites did not - a difference of 200 m would amount to 12 °C difference using the maximum proposed thermal gradient of Chapter 4 (60 °C km^{-1}). Alternatively, there may be ultrastructural differences between bivalve and ammonite shell nacre that make bivalve nacre more susceptible to thermal reordering. Clearly, more data from these, and other nearby localities are required to better understand these differences and resolve these intriguing questions.

5.5: Conclusions:

Fossil aragonite shell material from the GEG appears to have undergone variable but incomplete solid-state resetting towards warmer temperatures. This is presumed to have occurred when the sediments were buried by Paleocene lava, the maximum thickness of which is unknown (but at least 430 m, based on Emeleus and Bell, 2005). The sediments were held at maximum burial temperatures of not less than 50 °C (based on Δ_{47} temperatures for vein fed calcite cements from within the sedimentary sequence) for <1 ma (based on rapid erosion rates seen in Rum unroofing; Hamilton et al., 1998; Chambers et al., 2005), although there have been suggestions that resetting could occur at lower temperatures under geological timescales (Wang et al., 2021). Maximum burial temperature may have been >50 °C but cannot have been more than 100 C which is the highest Eigg Δ_{47} temperature recorded in the overlying Valtos Sandstone Formation.

Results for *P. strathairdensis* range between 23 ± 9 °C and 58 ± 12 °C (Fig. 5.5), the upper values far higher than plausible for bivalve life, let alone shell calcification. Interestingly, such a spread of results is similar to a study of calcite brachiopods from the Late Ordovician, which give Δ_{47} derived temperatures of 25 to 55 °C (Barney and

Grossman, 2022); this study used the model of Hemmingway and Henkes (2021) to project that solid state re-ordering had caused a maximum of 1 °C alteration in Δ_{47} derived temperatures, leaving the highest temperatures largely unexplained. Despite the differences in mineralogy between the two fossil groups -- with aragonite thought to require lower thermal influence to reset (Staudigel and Swart, 2016; Ritter et al., 2017, Chen et al., 2019) – there are strong similarities. The range of temperatures recorded by Δ_{47} in both studies cannot all be original depositional values; Δ_{47} values are spread widely despite the small range in $\delta^{13}\text{C}$ and $\delta^{18}\text{O}_{\text{CARBONATE}}$. We continue to favour partial solid-state resetting as the best explanation of this trend in our data.

For our results, high (>50 °C) Δ_{47} derived temperatures are present even in shells composed of 100% aragonite (Table 5.1); no covariance with $\delta^{18}\text{O}_{\text{CARBONATE}}$ or $\delta^{13}\text{C}$ was observed and no physical evidence for neomorphism was seen under SEM. It is therefore important to reiterate that traditional methods of assessing preservation are not enough to allow the assumption that Δ_{47} values are unaltered, a conclusion supported by experimental studies (e.g., Chen et al., 2019) and the results of other recent studies of clumped isotopes in aragonite shells (Nooitgedacht et al., 2021).

Interestingly, pilot results from one modern and two Pleistocene aged (West Runton Formation, >450 000 year old) aragonite shells (Table 5.5) collected from Norfolk (UK) give reasonable ‘temperate’ Δ_{47} derived temperatures (from 13 ± 8 °C and 15 ± 11 °C), while one singly measured Pleistocene shell gave a temperature of 30 ± 13 °C (noting that errors are estimated based on *P. strathairdensis* population pooled standard deviation, due to few or single measurements). While more work will be required to allow a more rigid comparison, these data support the notion that preservation of Δ_{47} in biogenic aragonite is entirely plausible over 100, 000 year timescales under shallow burial conditions.

The coolest results from the *P. strathairdensis* shells give the best estimate of the environmental temperatures (~20-30 °C) that the shells lived in; the lagoon waters had $\delta^{18}\text{O}_{\text{FLUID}}$ compositions (~ 0‰ to -2‰ VSMOW). Mudstone hosted concretions in Kildonnan Member beds slightly younger than the shells have Δ_{47} derived temperatures within error of the lowest shell values and corroborate the environmental reconstructions based on more traditional geochemical proxies (e.g., Hudson, 1980; Hudson et al., 1995; Patterson, 1999; Holmden and Hudson, 2003).

Despite their pristine appearance, it is clear that these *P. strathairdensis* shells have experienced a complex Δ_{47} history. By chance these shells seem to have experienced burial temperatures/durations just cool enough to allow preservation of some environmental information, but also warm (or long) enough that solid state resetting has commenced. The Kildonnan member biogenic aragonites may thus be a unique geological data set with which to complement experimental studies to understand how, when and why resetting of biogenic aragonite Δ_{47} occurs.

Chapter 6: Conclusion

The aims of this thesis, as outlined in Chapter 1, were to apply the clumped isotope paleothermometer to a range of geological case studies taken from the Middle to Upper Jurassic succession of the Inner Hebrides. The Δ_{47} derived temperatures have successfully allowed interpretation of temperature and pore fluid conditions of depositional, early and later (burial) diagenetic carbonates. The application of clumped isotope paleothermometry to skeletal aragonite has uncovered a complex picture involving lattice-scale reordering, with implications for other work on fossil aragonite, but has still allowed some paleoenvironmental interpretations to be made.

Chapter 3:

Diagenetic mudstone hosted carbonate concretions from the Upper Jurassic of Skye and the south of England are confirmed to have formed under shallow burial conditions, confirming previous interpretations (Hudson, 1978; Hudson et al., 2001; Hendry et al., 2006). The similarities in the early diagenetic data in particular, from this wide range of localities, indicates that the results are robust; Δ_{47} derived temperatures show that concretion bodies formed at between 9 ± 5 °C and 18 ± 5 °C, and back calculated $\delta^{18}\text{O}_{\text{FLUID}}$ values confirm this occurred in marine pore water. The difference between these results and earlier high temperature clumped isotope data from similar concretions from the south of England (Loyd et al., 2014) is thought to be mainly due to methodological differences.

The clumped isotope data from early diagenetic phases in concretions have the potential to be used to help reconstruct bottom water temperatures in ancient seas. These data from inorganic cements should be free from any complications caused by vital effects, as might occur for example in bottom living fossils. Robust reconstructions of bottom water temperature have the potential to be combined with clumped isotope data from free-swimming or floating organisms (e.g., ammonites, belemnites, foraminifers) to reconstruct temperature profiles in ancient seas of the post-Palaeozoic world.

Chapter 4:

The enigmatic metre-scale sandstone hosted carbonate concretions of the Valtos Sandstone Formation from the Middle Jurassic Great Estuarine Group are shown to have formed much later than previously assumed, from Paleocene meteoric pore fluids.

Cementation temperatures were elevated, due to an increased thermal gradient (between 40-60 °C km⁻¹) associated with the beginning of regional-scale volcanism, but more significantly through interaction of meteoric water with hot, earliest Paleocene lavas, which also caused the pore fluids to become ¹⁸O enriched. A combination of the new temperature information and field observations on differential compaction around the grown concretion, demonstrate that concretion growth was likely completed within <1 Ma, much more rapidly than previously suggested. This, in turn, has implications for both fluid flow rates and inferences based on concretion morphology – highly spherical concretions previously having been assumed to form in slowly moving or stagnant pore fluids (e.g., Wilkinson and Dampier, 1990).

The elevated temperatures and positive $\delta^{18}\text{O}_{\text{FLUID}}$ compositions are a feature of concretions in the north (Trotternish, Skye) and south (Isle of Eigg) of the study area, demonstrating that meteoric-water interaction with lavas was a basin wide phenomenon. The Valtos Sandstone Formation concretionary cements gave the warmest clumped isotope derived temperatures so far recorded in the Middle Jurassic of Scotland; they suggest that the porous aquifer sandstone was acting as a conduit for hot water during the early Paleocene. Some data from fracture-fed cements in the underlying Lealt Shale Formation suggest limited leakage of this hot fluid into the underlying aquitard. However, most other basinal cementation attributed to the Paleocene, gave lower temperatures (average 33 °C) and pore fluid values highly depleted in ¹⁸O (average: -12.7‰ VSMOW).

The $\delta^{18}\text{O}_{\text{FLUID}}$ values of Hebridean, Paleocene, meteoric-derived pore fluids are highly depleted in ¹⁸O, as originally proposed by Taylor and Forester (1971) and later supported by Fallick et al. (1985). The work of Taylor and Forester (1971) suggested that these meteoric fluids had values around -12‰ SMOW, and the new $\delta^{18}\text{O}_{\text{FLUID}}$ values derived from the cements studied here averaged -12.7‰ VSMOW. The most ¹⁸O depleted value for Paleocene meteoric water in this study was $-16.5 \pm 1.6\%$ VSMOW. A value of -12‰ VSMOW or lower has always been considered unexpectedly negative for the latitude at the time of formation. It suggests a local altitude effect, perhaps relating to the topography of the igneous centres and/or the lava pile, or an amount effect – paleofloral evidence suggests that the Hebridean Paleocene experienced high amounts of rainfall (Poulter, 2011).

The new clumped isotope data reported here means that the hydrogeological setting was quite different to that proposed by Wilkinson (1993). The new data requires

direct ingress of hot water from the growing lava pile at land surface locations where lava rested more or less directly on the eroded top of the sandstone. Such sites are present both in the north and south of the study area. Earlier suggestions that the concretions grew during the Middle or Upper Jurassic in a groundwater lens (Wilkinson, 1993) can no longer be supported.

In a wider context, these new results suggest that models for the timing and setting of concretionary cements in sandstones, particularly those published in the 1980s-2000s, should be reassessed. In particular, the study shows that $\delta^{18}\text{O}_{\text{carbonate}}$ values in sandstone cements are potentially ambiguous and in many case studies require the support of clumped isotope data to eliminate previously unavoidable assumptions. Moreover, the implication that the sandstone contained hot meteoric-sourced fluid, while other, more mudrock-dominated units in the sequence, were otherwise thermally insulated is significant. It suggests that basing basinal temperature estimates and basinal thermal histories on sandstone cements may lead to serious errors in interpretation, unless other supporting contextual information is available: if the Valtos Sandstone concretionary cements had been analysed in isolation, an overestimation of the overall basinal burial temperatures by $\sim 30\text{-}50^\circ\text{C}$ would have been possible.

Chapter 5

Clumped isotope analysis of skeletal aragonite of the Bathonian mussel *P. strathairdensis* gave $T(\Delta_{47})$ between $23 \pm 9^\circ\text{C}$ and $58 \pm 12^\circ\text{C}$, with many values above the likely threshold ($\sim 35^\circ\text{C}$) for survival of the organisms. This outcome was unexpected; the apparently pristine aragonite of *P. strathairdensis* had previously been interpreted to contain geochemical proxies that gave 'sensible' palaeoenvironmental outcomes (e.g., Hudson, 1980; Hudson et al., 1995; Holmden and Hudson, 2003).

Although the molluscan aragonite meets the criteria typically expected for excellent preservation (several shells being wholly aragonite, well-preserved nacreous ultrastructure and pearlescent macro-physical appearance), the Δ_{47} data are most satisfactorily explained by partial solid-state resetting of Δ_{47} , but with no relationship between apparent (reset) temperatures and preserved $\delta^{18}\text{O}_{\text{CARBONATE}}$ values. The implication, supporting other recent clumped isotope studies, is that the methods for assessing preservation quality of skeletal fossil aragonite are not sufficient to determine Δ_{47} signal preservation.

The solid-state partial resetting of shell aragonite has not resulted in a uniform offset; however, the trend of the large dataset, allows identification of a 'best estimate' for paleoenvironmental conditions. In this case, allowing for the statistical uncertainty in the data set, it is likely that environmental water temperatures were between 20-30 °C and pore fluid values were ~0‰ to -2‰ VSMOW, corroborating interpretations of earlier studies (e.g., Hudson, 1980; Hudson et al., 1995; Patterson, 1999; Holmden and Hudson, 2003).

Solid-state resetting of Δ_{47} must have proceeded under maximum burial conditions when the overlying strata were >430 m thick (early Paleocene Lavas; Emeleus and Bell, 2005) and temperatures were >50°C but <100°C, as constrained by T(Δ_{47}) results from other calcite cements in the same sedimentary sequence. The duration of maximum burial was <1 Ma, suggesting that partial resetting of aragonite Δ_{47} can take place under reasonably shallow burial conditions and in timescales of hundreds of thousands of years. These shells came from a single stratigraphic horizon with well-constrained environmental context and probably a rather unique burial history; our identification of partial resetting is highly fortuitous (a 'lucky strike') that highlights the need for vigilance when skeletal aragonite is used for deep time palaeoenvironmental studies. Δ_{47} signal preservation in Mesozoic and Cainozoic skeletal aragonite may not be straightforward.

6.1: Future work:

Recommendations follow for a continuation of the work reported in this thesis, both to further investigation into the sedimentary history of carbonates in the GEG and, more importantly, to improve our understanding of the clumped isotope paleothermometer, particularly with reference to biogenic material.

- To support the analysis of early diagenetic mudstone hosted concretions, particularly with respect to their utility as bottom water temperature indicators, cross-comparisons with other bottom dwelling organisms (such as *Gryphea* in the Jurassic) would be very useful.
- Earlier palaeohydrological models for the Valtos Sandstone Formation have been challenged in this work. Consequently, concretions in the Bearreraig Sandstone Formation deserve reconsideration. These concretions are thought to have very

early diagenetic marine core cementation, with growth continuing through later burial cementation from meteoric porewaters (Wilkinson, 1991). Analysis of these concretions should help further constrain basin history and should provide a contrast to the heated meteoric fluids identified in Valtos Sandstone cementation.

- In this study, an unavoidable sampling bias was caused by the sample size requirements; large, pure samples were used, limited mostly by the drill size. Consequently, the majority of cement sample procured were from fractures or larger vugs. All of these samples had strongly negative $\delta^{18}\text{O}_{\text{FLUID}}$ compositions ($< -12\text{‰}$ VSMOW) that indicated a Paleocene age. A targeted investigation of cements that could have formed during the Jurassic (for example, *Neomiodon*-rich shell beds within the Lealt Shale Formation, and other early diagenetic concretions such as those from the Lonfearn Member of the Lealt Shale) could greatly improve the characterisation of the diagenetic history of the succession and may confirm assumptions about Jurassic meteoric $\delta^{18}\text{O}_{\text{FLUID}}$ compositions.
- A number of avenues for future work stem from Chapter 5. Analyses of *P. strathairdensis* shells (100% aragonite) during a time period where there are no systematic measurement (MIRA) issues is a high priority, as would investigating shells with more negative $\delta^{18}\text{O}_{\text{CARBONATE}}$ and $\delta^{13}\text{C}$ compositions (from the covariant C-O trend; fig 5.4). Analysis of other GEG bivalve aragonites with cross-lamellar aragonite structure (e.g., *Neomiodon* sp., *Corbula* sp.) would allow investigation into whether shell structure had any influence on Δ_{47} preservation; pre-treatment of shells to oxidise any organic components should be trialled, although previous work at UEA suggests this will not alter the data quality.
- Measurement of dual Δ_{47} and Δ_{48} was not available from MIRA for most of the shell analysis period. However, this would be an ideal next step, as this technique can help distinguish kinetic disequilibrium (Bajnai et al., 2020; Fiebig et al., 2021) and would likely improve the understanding of the Δ_{47} results.
- A critical review of published clumped isotope data in biogenic carbonates is timely. We need to better understand: the criteria used to identify 'pristine preservation', how measurement variations are treated statistically, criteria for

rejecting values, and how errors are reported. Such a study would allow the community to move further towards a methodological consensus, with the goal of producing reliable and transparently reported paleoenvironmental data.

Chapter 7: References

- Affek, H. P. (2012). Clumped isotope paleothermometry: principles, applications, and challenges. *The Paleontological Society Papers*, 18, 101-114.
- Affek, H. P., Bar-Matthews, M., Ayalon, A., Matthews, A., & Eiler, J. M. (2008). Glacial/interglacial temperature variations in Soreq cave speleothems as recorded by 'clumped isotope' thermometry. *Geochimica et Cosmochimica Acta*, 72(22), 5351-5360.
- Anderson, F., & Cox, L. R. (1948). *The "Loch Staffin Beds" of Skye; with Notes on the Molluscan Fauna of the Great Estuarine Series*: Oliver & Boyd.
- Anderson, F. W., & Dunham, K. C. (1966). *The geology of northern Skye*: HM Stationery Office.
- Anderson, N., Kelson, J. R., Kele, S., Daëron, M., Bonifacie, M., Horita, J., Mackey, T. J., John, C. M., Kluge, T. & Petschnig, P. (2021). A unified clumped isotope thermometer calibration (0.5–1,100 C) using carbonate-based standardization. *Geophysical Research Letters*, 48(7), e2020GL092069.
- Anderson, T. F. and M. A. Arthur (1983). Stable isotopes of oxygen and carbon and their application to sedimentologic and paleoenvironmental problems. In: Arthur, M.A. Anderson, T.F. Kaplan, I.R. Veizer, J., Land, L.S., (Eds.), *Stable Isotopes in Sedimentary Geochemistry: Society of Economic Palaeontologists and Mineralogists Short course*, Vol. 10, p. 1.1–1–151.
- Andrews, J. E. (1984). *Aspects of sedimentary facies and diagenesis in limestone-shale formations of the (Middle Jurassic) Great Estuarine Group, Inner Hebrides*. Ph.D thesis, University of Leicester.
- Andrews, J. E. (1985). The sedimentary facies of a late Bathonian regressive episode: the Kilmaluag and Skudiburgh Formations of the Great Estuarine Group, Inner Hebrides, Scotland. *Journal of the Geological Society*, 142(6), 1119-1137.
- Andrews, J. E. (1986). Microfacies and geochemistry of Middle Jurassic algal limestones from Scotland. *Sedimentology*, 33(4), 499-520.
- Andrews, J.E., Hamilton, P., & Fallick, A. (1987). The geochemistry of early diagenetic dolostones from a low-salinity Jurassic lagoon. *Journal of the Geological Society*, 144(5), 687-698.
- Andrews, J. E., & Walton, W. (1990). Depositional environments within Middle Jurassic oyster-dominated lagoons: an integrated litho-, bio-and palynofacies study of the

- Duntulm Formation (Great Estuarine Group, Inner Hebrides). *Earth and Environmental Science Transactions of The Royal Society of Edinburgh*, 81(1), 1-22.
- Anestis, A., Pörtner, H. O., Lazou, A., & Michaelidis, B. (2008). Metabolic and molecular stress responses of sublittoral bearded horse mussel *Modiolus barbatus* to warming sea water: implications for vertical zonation. *Journal of Experimental Biology*, 211(17), 2889-2898.
- Bajnai, D., Fiebig, J., Tomašových, A., Milner Garcia, S., Rollion-Bard, C., Raddatz, J., Löffler, N., Primo-Ramos, C. & Brand, U. (2018). Assessing kinetic fractionation in brachiopod calcite using clumped isotopes. *Scientific reports*, 8(1), 1-12.
- Bajnai, D., Guo, W., Spötl, C., Coplen, T. B., Methner, K., Löffler, N., Krsnik, E., Gischler, E., Hansen, M. & Henkel, D. (2020). Dual clumped isotope thermometry resolves kinetic biases in carbonate formation temperatures. *Nature communications*, 11(1), 1-9.
- Balsamo, F., Storti, F., & Gröcke, D. R. (2012). Fault-related fluid flow history in shallow marine sediments from carbonate concretions, Crotone basin, south Italy. *Journal of the Geological Society*, 169(5), 613-626. doi:10.1144/0016-76492011-109
- Barney, B. B., & Grossman, E. L. (2022). Reassessment of ocean paleotemperatures during the Late Ordovician. *Geology*, 50(5), 572-576.
- Bergman, S. C., Huntington, K. W., & Crider, J. G. (2013). Tracing paleofluid sources using clumped isotope thermometry of diagenetic cements along the Moab Fault, Utah. *American Journal of Science*, 313(5), 490-515.
- Bergmann, K. D., Finnegan, S., Creel, R., Eiler, J. M., Hughes, N. C., Popov, L. E., & Fischer, W. W. (2018). A paired apatite and calcite clumped isotope thermometry approach to estimating Cambro-Ordovician seawater temperatures and isotopic composition. *Geochimica et Cosmochimica Acta*, 224, 18-41.
- Bernasconi, S. M., Müller, I. A., Bergmann, K. D., Breitenbach, S. F., Fernandez, A., Hodell, D. A., Jaggi, M., Meckler, A. N., Millan, I. & Ziegler, M. (2018). Reducing uncertainties in carbonate clumped isotope analysis through consistent carbonate-based standardization. *Geochemistry, Geophysics, Geosystems*, 19(9), 2895-2914.
- Bishop, A., & Abbott, G. (1995). Vitrinite reflectance and molecular geochemistry of Jurassic sediments: the influence of heating by Tertiary dykes (northwest Scotland). *Organic Geochemistry*, 22(1), 165-177.
- Bjørkum, P. A., & Walderhaug, O. (1990). Geometrical arrangement of calcite cementation within shallow marine sandstones. *Earth-Science Reviews*, 29(1-4),

145-161.

- Braby, C. E., & Somero, G. N. (2006). Following the heart: temperature and salinity effects on heart rate in native and invasive species of blue mussels (genus *Mytilus*). *Journal of Experimental Biology*, 209(13), 2554-2566.
- Breitenbach, S. F., Mleneck-Vautravers, M. J., Grauel, A.-L., Lo, L., Bernasconi, S. M., Müller, I. A., Rolfe, J., Gázquez, F., Greaves, M. & Hodell, D. A. (2018). Coupled Mg/Ca and clumped isotope analyses of foraminifera provide consistent water temperatures. *Geochimica et Cosmochimica Acta*, 236, 283-296.
- Brigaud, B., Bonifacie, M., Pagel, M., Blaise, T., Calmels, D., Haurine, F. and Landrein, P. (2020). Past hot fluid flows in limestones detected by Δ_{47} -(U-Pb) and not recorded by other geothermometers. *Geology*, 48(9), 851-856.
- Bristow, T. F., Bonifacie, M., Derkowski, A., Eiler, J. M., & Grotzinger, J. P. (2011). A hydrothermal origin for isotopically anomalous cap dolostone cements from south China. *Nature*, 474(7349), 68-71.
- Budd, D. A., Frost, E. L., Huntington, K. W., & Allwardt, P. F. (2013). Syndepositional Deformation Features In High-Relief Carbonate Platforms: Long-Lived Conduits for Diagenetic Fluids. *Journal of Sedimentary Research*, 83(1), 12-36.
- Burgener, L., Hyland, E., Huntington, K. W., Kelson, J. R., & Sewall, J. O. (2019). Revisiting the equable climate problem during the Late Cretaceous greenhouse using paleosol carbonate clumped isotope temperatures from the Campanian of the Western Interior Basin, USA. *Palaeogeography, Palaeoclimatology, Palaeoecology*, 516, 244-267.
- Caldarescu, D. E., Sadatzki, H., Andersson, C., Schäfer, P., Fortunato, H., & Meckler, A. N. (2021). Clumped isotope thermometry in bivalve shells: A tool for reconstructing seasonal upwelling. *Geochimica et Cosmochimica Acta*, 294, 174-191.
- Chambers, L., Pringle, M., & Parrish, R. R. (2005). Rapid formation of the Small Isles Tertiary centre constrained by precise $^{40}\text{Ar}/^{39}\text{Ar}$ and U-Pb ages. *Lithos*, 79(3-4), 367-384.
- Chen, S., Gagnon, A. C., & Adkins, J. F. (2018). Carbonic anhydrase, coral calcification and a new model of stable isotope vital effects. *Geochimica et Cosmochimica Acta*, 236, 179-197.
- Chen, S., Ryb, U., Piasecki, A. M., Lloyd, M. K., Baker, M. B., & Eiler, J. M. (2019). Mechanism of solid-state clumped isotope reordering in carbonate minerals from

- aragonite heating experiments. *Geochimica et Cosmochimica Acta*, 258, 156-173.
- Cherns, L., & Wright, V. P. (2009). Quantifying the impacts of early diagenetic aragonite dissolution on the fossil record. *Palaios*, 24(11), 756-771.
- Chow, G., & Benson, S. C. (1979). Carbonic anhydrase activity in developing sea urchin embryos. *Experimental cell research*, 124(2), 451-453.
- Compton, T. J., Rijkenberg, M. J., Drent, J., & Piersma, T. (2007). Thermal tolerance ranges and climate variability: a comparison between bivalves from differing climates. *Journal of Experimental Marine Biology and Ecology*, 352(1), 200-211.
- Cox, B., Gallois, R., & Sumbler, M. (1994). The stratigraphy of the BGS Hartwell borehole, near Aylesbury, Buckinghamshire. *Proceedings of the Geologists' Association*, 105(3), 209-224.
- Craig, H. (1963). The Isotopic geochemistry of water and carbon in geothermal areas, nuclear geology on geothermal areas. *Spoletto 1963*, 17-53.
- Cui, J., Li, S., & Mao, Z. (2019). Oil-bearing heterogeneity and threshold of tight sandstone reservoirs: A case study on Triassic Chang7 member, Ordos Basin. *Marine and Petroleum Geology*, 104, 180-189.
- Cui, J., & Liu, Y. (2021). Determination of Formation Time of Calcareous Cements in Marine Sandstone and Their Influence on Hydrocarbon Accumulation: A Case Study of the Carboniferous Donghe Sandstone in the Hadexun Oilfield, Tarim Basin. *Geofluids*, 2021.
- Cuif, J. P., Dauphin, Y., Berthet, P., & Jegoudez, J. (2004). Associated water and organic compounds in coral skeletons: quantitative thermogravimetry coupled to infrared absorption spectrometry. *Geochemistry, Geophysics, Geosystems*, 5(11).
- Daëron, M., Blamart, D., Peral, M., & Affek, H. P. (2016). Absolute isotopic abundance ratios and the accuracy of Δ_{47} measurements. *Chemical Geology*, 442, 83-96.
- Daëron, M., Drysdale, R. N., Peral, M., Huyghe, D., Blamart, D., Coplen, T. B., Lartaud, F. & Zanchetta, G. (2019). Most Earth-surface calcites precipitate out of isotopic equilibrium. *Nature communications*, 10(1), 429.
- Dale, A., John, C. M., Mozley, P. S., Smalley, P., & Muggeridge, A. H. (2014). Time-capsule concretions: unlocking burial diagenetic processes in the Mancos Shale using carbonate clumped isotopes. *Earth and Planetary Science Letters*, 394, 30-37.
- Dansgaard, W. (1964). Stable isotopes in precipitation. *Tellus*, 16(4), 436-468.
- Dauphin, Y., Cuif, J.-P., & Massard, P. (2006). Persistent organic components in heated coral aragonitic skeletons—implications for palaeoenvironmental reconstructions.

Chemical Geology, 231(1-2), 26-37.

- Davenport, J., & Davenport, J. L. (2005). Effects of shore height, wave exposure and geographical distance on thermal niche width of intertidal fauna. *Marine Ecology Progress Series*, 292, 41-50.
- Davies, A. J., Davis, S., & John, C. M. (2021). Evidence of taxonomic non-equilibrium effects in the clumped isotope composition of modern cephalopod carbonate. *Chemical Geology*, 578, 120317.
- Davies, A. J., & John, C. M. (2017). Reducing contamination parameters for clumped isotope analysis: The effect of lowering Porapak™ Q trap temperature to below–50° C. *Rapid Communications in Mass Spectrometry*, 31(16), 1313-1323.
- Davies, A. J., & John, C. M. (2019). The clumped (¹³C¹⁸O) isotope composition of echinoid calcite: Further evidence for “vital effects” in the clumped isotope proxy. *Geochimica et Cosmochimica Acta*, 245, 172-189.
- De Craen, M., Swennen, R., Keppens, E., Macaulay, C., & Kiriakoulakis, K. (1999). Bacterially mediated formation of carbonate concretions in the Oligocene Boom Clay of northern Belgium. *Journal of Sedimentary Research*, 69(5), 1098-1106.
- De Winter, N. J., Müller, I. A., Kocken, I. J., Thibault, N., Ullmann, C. V., Farnsworth, A., Lunt, D. J., Claeys, P. & Ziegler, M. (2021). Absolute seasonal temperature estimates from clumped isotopes in bivalve shells suggest warm and variable greenhouse climate. *Communications Earth & Environment*, 2(1), 1-8.
- Defliese, W. F., & Lohmann, K. C. (2015). Non-linear mixing effects on mass-47 CO₂ clumped isotope thermometry: Patterns and implications. *Rapid Communications in Mass Spectrometry*, 29(9), 901-909.
- Defliese, W. F., & Lohmann, K. C. (2016). Evaluation of meteoric calcite cements as a proxy material for mass-47 clumped isotope thermometry. *Geochimica et Cosmochimica Acta*, 173, 126-141.
- Del Sole, L., & Antonellini, M. (2019). Microstructural, petrophysical, and mechanical properties of compactive shear bands associated to calcite cement concretions in arkose sandstone. *Journal of Structural Geology*, 126, 51-68.
- Dennis, K., Cochran, J., Landman, N., & Schrag, D. (2013). The climate of the Late Cretaceous: New insights from the application of the carbonate clumped isotope thermometer to Western Interior Seaway macrofossil. *Earth and Planetary Science Letters*, 362, 51-65.
- Dennis, K. J., Affek, H. P., Passey, B. H., Schrag, D. P., & Eiler, J. M. (2011). Defining an

- absolute reference frame for 'clumped' isotope studies of CO₂. *Geochimica et Cosmochimica Acta*, 75(22), 7117-7131.
- Dennis, P. F. (2014): On the cause of mass spectrometer non-linearity during clumped isotope measurements. figshare: <https://doi.org/10.6084/m9.figshare.1254807.v1>
- Dennis, P. F., Vinen, S., Marca-Bell, A., & Rowe, P., (2014): MIRA: a new isotope ratio mass spectrometer for clumped isotope studies of CO₂. figshare: <https://doi.org/10.6084/m9.figshare.899817.v1>
- Dennis, P. F., Myhill, D. J., Marca, A., & Kirk, R. (2019). Clumped isotope evidence for episodic, rapid flow of fluids in a mineralized fault system in the Peak District, UK. *Journal of the Geological Society*, 176(3), 447-461.
- Denny, M. W., Dowd, W. W., Bilir, L., & Mach, K. J. (2011). Spreading the risk: small-scale body temperature variation among intertidal organisms and its implications for species persistence. *Journal of Experimental Marine Biology and Ecology*, 400(1-2), 175-190.
- Devereux, I. (1967). Temperature measurements from oxygen isotope ratios of fish otoliths. *Science*, 155(3770), 1684-1685.
- Dickson, J. A. D. (1991). Disequilibrium carbon and oxygen isotope variations in natural calcite. *Nature*, 353(6347), 842-844. doi:10.1038/353842a0
- Donnadieu, Y., Dromart, G., Godd eris, Y., Puc eat, E., Brigaud, B., Dera, G., Dumas, C. & Olivier, N. (2011). A mechanism for brief glacial episodes in the Mesozoic greenhouse. *Paleoceanography*, 26(3).
- Duff, D. (1975). Paleoeology of a bituminous shale—the Lower Oxford Clay of central England: *Paleontology*, v. 18.
- Duplessy, J. C., Lalou, C., & Vinot, A. C. (1970). Differential isotopic fractionation in benthic foraminifera and paleotemperatures reassessed. *Science*, 168(3928), 250-251.
- Eagle, R., Eiler, J. M., Tripathi, A., Ries, J., Freitas, P., Hiebenthal, C., Wanamaker Jr, A., Taviani, M., Elliot, M. & Marenssi, S. (2013). The influence of temperature and seawater carbonate saturation state on 13 C–18 O bond ordering in bivalve mollusks. *Biogeosciences*, 10(7), 4591-4606.
- Eiler, J. M. (2007). "Clumped-isotope" geochemistry—The study of naturally-occurring, multiply-substituted isotopologues. *Earth and Planetary Science Letters*, 262(3-4), 309-327.
- Eiler, J. M. (2011). Paleoclimate reconstruction using carbonate clumped isotope thermometry. *Quaternary Science Reviews*, 30(25-26), 3575-3588.

- Eiler, J. M., & Schauble, E. (2004). $^{18}O/^{16}O$ in Earth's atmosphere. *Geochimica et Cosmochimica Acta*, 68(23), 4767-4777.
- Emeleus, C. H., Bell, B. R. (2005). *The Palaeogene volcanic districts of Scotland* (Vol. 3): British Geological Survey Nottingham.
- Emery, D., Hudson, J. D., Marshall, J. D., & Dickson, J. A. D. (1988). The origin of late spar cements in the Lincolnshire Limestone, Jurassic of central England. *Journal of the Geological Society*, 145(4), 621-633.
- Emiliani, C. (1978). The cause of the ice ages. *Earth and Planetary Science Letters*, 37(3), 349-354.
- England, R. W. (1994). The structure of the Skye lava field. *Scottish Journal of Geology*, 30(1), 33-37.
- Erez, J. (1978). Vital effect on stable-isotope composition seen in foraminifera and coral skeletons. *Nature*, 273(5659), 199-202.
- Evans, D., Sahoo, N., Renema, W., Cotton, L. J., Müller, W., Todd, J. A., Saraswati, P. K., Stassen, P., Ziegler, M. & Pearson, P. N. (2018). Eocene greenhouse climate revealed by coupled clumped isotope-Mg/Ca thermometry. *Proceedings of the National Academy of Sciences*, 115(6), 1174-1179.
- Fallick, A., Jocelyn, J., Donnelly, T., Guy, M., & Behan, C. (1985). Origin of agates in volcanic rocks from Scotland. *Nature*, 313(6004), 672-674.
- Fan, M., Hough, B.G. and Passey, B.H. (2014). Middle to late Cenozoic cooling and high topography in the central Rocky Mountains: Constraints from clumped isotope geochemistry. *Earth and Planetary Science Letters*, 408, 35-47.
- Farver, J. R. (1994). Oxygen self-diffusion in calcite: Dependence on temperature and water fugacity. *Earth and Planetary Science Letters*, 121(3-4), 575-587.
- Fernandez, A., Müller, I. A., Rodríguez-Sanz, L., van Dijk, J., Looser, N., & Bernasconi, S. M. (2017). A reassessment of the precision of carbonate clumped isotope measurements: Implications for calibrations and paleoclimate reconstructions. *Geochemistry, Geophysics, Geosystems*, 18(12), 4375-4386.
- Fiebig, J., Daëron, M., Bernecker, M., Guo, W., Schneider, G., Boch, R., Bernasconi, S. M., Jautzy, J. & Dietzel, M. (2021). Calibration of the dual clumped isotope thermometer for carbonates. *Geochimica et Cosmochimica Acta*, 312, 235-256.
- Finnegan, S., Bergmann, K., Eiler, J. M., Jones, D. S., Fike, D. A., Eisenman, I., Hughes, N. C., Tripathi, A. K. & Fischer, W. W. (2011). The magnitude and duration of Late Ordovician–Early Silurian glaciation. *Science*, 331(6019), 903-906.

- Forester, R. W., & Taylor, H. P. (1977). 18 O/16 O, D/H, and 13 C/12 C studies of the Tertiary igneous complex of Skye, Scotland. *American Journal of Science*, 277(2), 136-177.
- Fowler, S. J., Bohron, W. A., & Spera, F. J. (2004). Magmatic evolution of the Skye igneous centre, western Scotland: modelling of assimilation, recharge and fractional crystallization. *Journal of Petrology*, 45(12), 2481-2505.
- Fyfe, L.-J. C., Schofield, N., Holford, S., Hartley, A., Heafford, A., Muirhead, D., & Howell, J. (2021). Geology and petroleum prospectivity of the Sea of Hebrides Basin and Minch Basin, offshore NW Scotland. *Petroleum Geoscience*, 27(4), petgeo2021-2003.
- Garrels, R., & Christ, C. L. (1965). Solutions, Minerals and Equilibria, Harpers' Geoscience Series, Haper & Row. *New York*.
- Gholamrezaie, E., Scheck-Wenderoth, M., Sippel, J., & Strecker, M. R. (2018). Variability of the geothermal gradient across two differently aged magma-rich continental rifted margins of the Atlantic Ocean: the Southwest African and the Norwegian margins. *Solid Earth*, 9(1), 139-158.
- Ghosh, P., Adkins, J., Affek, H., Balta, B., Guo, W., Schauble, E. A., Schrag, D. & Eiler, J. M. (2006). 13C–18O bonds in carbonate minerals: a new kind of paleothermometer. *Geochimica et Cosmochimica Acta*, 70(6), 1439-1456.
- Gibson, S. A. (1990). The geochemistry of the Trotternish sills, Isle of Skye: crustal contamination in the British Tertiary Volcanic Province. *Journal of the Geological Society*, 147(6), 1071-1081.
- Gibson, S. A., & Jones, A. P. (1991). Igneous stratigraphy and internal structure of the Little Minch sill complex, Trotternish Peninsula, northern Skye, Scotland. *Geological Magazine*, 128(1), 51-66.
- Given, R. K., & Lohmann, K. C. (1986). Isotopic evidence for the early meteoric diagenesis of the reef facies, Permian Reef Complex of West Texas and New Mexico. *Journal of Sedimentary Research*, 56(2), 183-193.
- Gorzalak, P., Stolarski, J., Małkowski, K., & Meibom, A. (2012). Stable carbon and oxygen isotope compositions of extant crinoidal echinoderm skeletons. *Chemical Geology*, 291, 132-140.
- Green, P. F., Thomson, K., & Hudson, J. D. (2001). Recognition of tectonic events in undeformed regions: contrasting results from the Midland Platform and East Midlands Shelf, Central England. *Journal of the Geological Society*, 158(1), 59-73.

- Grossman, E. L., & Ku, T.-L. (1986). Oxygen and carbon isotope fractionation in biogenic aragonite: temperature effects. *Chemical Geology: Isotope Geoscience section*, 59, 59-74.
- Guo, W. (2020). Kinetic clumped isotope fractionation in the DIC-H₂O-CO₂ system: patterns, controls, and implications. *Geochimica et Cosmochimica Acta*, 268, 230-257.
- Guo, W., Mosenfelder, J. L., Goddard III, W. A., & Eiler, J. M. (2009). Isotopic fractionations associated with phosphoric acid digestion of carbonate minerals: insights from first-principles theoretical modeling and clumped isotope measurements. *Geochimica et Cosmochimica Acta*, 73(24), 7203-7225.
- Guo, Y., Deng, W., Liu, X., Kong, K., Yan, W., & Wei, G. (2021). Clumped isotope geochemistry of island carbonates in the South China Sea: Implications for early diagenesis and dolomitization. *Marine geology*, 437, 106513.
- Hahn, S., Rodolfo-Metalpa, R., Griesshaber, E., Schmahl, W. W., Buhl, D., Hall-Spencer, J., Baggini, C., Fehr, K. & Immenhauser, A. (2012). Marine bivalve shell geochemistry and ultrastructure from modern low pH environments: environmental effect versus experimental bias. *Biogeosciences*, 9(5), 1897-1914.
- Hall, A., Kennedy, W., & Taylor, J. H. (1967). Aragonite in fossils. *Proceedings of the Royal Society of London. Series B. Biological Sciences*, 168(1013), 377-412.
- Hallam, A. (1993). Jurassic climates as inferred from the sedimentary and fossil record. *Philosophical Transactions of the Royal Society of London. Series B: Biological Sciences*, 341(1297), 287-296.
- Hamilton, M. A., Pearson, D. G., Thompson, R. N., Kelley, S.P., & Emeleus, C. H. (1998). Rapid eruption of Skye lavas inferred from precise U–Pb and Ar–Ar dating of the Rum and Cuillin plutonic complexes. *Nature*, 394(6690), 260-263.
- Hamilton, P. J., Fallick, A. E., Andrews, J. E., & Whitford, D. J. (1992). Middle Jurassic clay-minerals from the Minch Basin: isotopic tracing of provenance and post-depositional alteration. *Geological Society, London, Special Publications*, 62(1), 155-158.
- Harker, S.D. (2002). Chapter 12: Cretaceous. In: Trewin, .H., ed., *The Geology of Scotland* (4th edition): London, The Geological Society, p. 351–360.
- Harris, J. P. (1989). The sedimentology of a Middle Jurassic lagoonal delta system: Elgol Formation (Great Estuarine Group), NW Scotland. *Geological Society, London, Special Publications*, 41(1), 147-166.

- Harris, J. P. (1992). Mid-Jurassic lagoonal delta systems in the Hebridean basins: thickness and facies distribution patterns of potential reservoir sandbodies. *Geological Society, London, Special Publications*, 62(1), 111-144.
- Harris, J. P., & Hudson, J. D. (1980). Lithostratigraphy of the Great Estuarine Group (Middle Jurassic), Inner Hebrides. *Scottish Journal of Geology*, 16(2-3), 231-250.
- Hays, P. D., & Grossman, E. L. (1991). Oxygen isotopes in meteoric calcite cements as indicators of continental paleoclimate. *Geology*, 19(5), 441-444.
- Heimhofer, U., Meister, P., Bernasconi, S. M., Ariztegui, D., Martill, D. M., Rios-Netto, A. M., & Schwark, L. (2017). Isotope and elemental geochemistry of black shale-hosted fossiliferous concretions from the Cretaceous Santana Formation fossil Lagerstätte (Brazil). *Sedimentology*, 64(1), 150-167.
- Hemingway, J. D., & Henkes, G. A. (2021). A disordered kinetic model for clumped isotope bond reordering in carbonates. *Earth and Planetary Science Letters*, 566, 116962.
- Hendry, J. P. (1993). Geological Controls on Regional Subsurface Carbonate Cementation: An Isotopic-Paleohydrologic Investigation of Middle Jurassic Limestones in Central England: In: Diagenesis and Basin Development, A. D. Horbury, A. G. Robinson
- Hendry, J. P., Pearson, M. J., Trewin, N. H., & Fallick, A. E. (2006). Jurassic septarian concretions from NW Scotland record interdependent bacterial, physical and chemical processes of marine mudrock diagenesis. *Sedimentology*, 53(3), 537-565.
- Henkes, G. A., Passey, B. H., Grossman, E. L., Shenton, B. J., Pérez-Huerta, A., & Yancey, T. E. (2014). Temperature limits for preservation of primary calcite clumped isotope paleotemperatures. *Geochimica et Cosmochimica Acta*, 139, 362-382.
- Henkes, G. A., Passey, B. H., Grossman, E. L., Shenton, B. J., Yancey, T. E., & Pérez-Huerta, A. (2018). Temperature evolution and the oxygen isotope composition of Phanerozoic oceans from carbonate clumped isotope thermometry. *Earth and Planetary Science Letters*, 490, 40-50.
- Henkes, G. A., Passey, B. H., Wanamaker Jr, A. D., Grossman, E. L., Ambrose Jr, W. G., & Carroll, M. L. (2013). Carbonate clumped isotope compositions of modern marine mollusk and brachiopod shells. *Geochimica et Cosmochimica Acta*, 106, 307-325.
- Hesselbo, S. P., & Coe, A. L. (2000). *Jurassic sequences of the Hebrides Basin, Isle of Skye, Scotland*.
- Hill, I., Worden, R., & Meighan, I. (2000). Geochemical evolution of a palaeolaterite: the Interbasaltic Formation, Northern Ireland. *Chemical Geology*, 166(1-2), 65-84.
- Hoareau, G., Crognier, N., Lacroix, B., Aubourg, C., Roberts, N.M., Niemi, N., Branellec, M.,

- Beaudoin, N. and Ruiz, I.S. (2021). Combination of Δ_{47} and U-Pb dating in tectonic calcite veins unravel the last pulses related to the Pyrenean Shortening (Spain). *Earth and Planetary Science Letters*, 553, 116636.
- Holford, S. P., Green, P. F., Hillis, R. R., Underhill, J. R., Stoker, M. S., & Duddy, I. R. (2010). Multiple post-Caledonian exhumation episodes across NW Scotland revealed by apatite fission-track analysis. *Journal of the Geological Society*, 167(4), 675-694.
- Holmden, C., & Hudson, J. D. (2003). $^{87}\text{Sr}/^{86}\text{Sr}$ and Sr/Ca Investigation of Jurassic mollusks from Scotland: Implications for paleosalinities and the Sr/Ca ratio of seawater. *Geological Society of America Bulletin*, 115(10), 1249-1264.
- Huck, S., & Heimhofer, U. (2021). Early Cretaceous sea surface temperature evolution in subtropical shallow seas. *Scientific reports*, 11(1), 1-9.
- Hudson, J. D. (1962). The stratigraphy of the Great Estuarine Series (Middle Jurassic of the Inner Hebrides). *Transactions of the Edinburgh Geological Society*, 19(2), 139-165.
- Hudson, J. D. (1963). The ecology and stratigraphical distribution of the invertebrate fauna of the Great Estuarine Series. *Palaeontology*, 6, 327-348.
- Hudson, J. D. (1966). Hugh Miller's Reptile Bed and the Mytilus Shales, Middle Jurassic, Isle of Eigg, Scotland. *Scottish Journal of Geology*, 2(3), 265-281.
- Hudson, J. D. (1967). The elemental composition of the organic fraction, and the water content, of some recent and fossil mollusc shells. *Geochimica et Cosmochimica Acta*, 31(12), 2361-2378.
- Hudson, J. D. (1968). The microstructure and mineralogy of the shell of a Jurassic mytilid (Bivalvia). *Palaeontology*, 11(2), 163-182.
- Hudson, J. D. (1970). Algal limestones with pseudomorphs after gypsum from the Middle Jurassic of Scotland. *Lethaia*, 3(1), 11-40.
- Hudson, J. D. (1978). Concretions, isotopes, and the diagenetic history of the Oxford Clay (Jurassic) of central England. *Sedimentology*, 25(3), 339-370.
- Hudson, J. D. (1980). Aspects of brackish-water facies and faunas from the Jurassic of north-west Scotland. *Proceedings of the Geologists' Association*, 91(1-2), 99-105.
- Hudson, J. D. (1983). Mesozoic sedimentation and sedimentary rocks in the Inner Hebrides. *Proceedings of the Royal Society of Edinburgh, Section B: Biological Sciences*, 83, 47-63.
- Hudson, J. D., & Anderson, T. F. (1989). Ocean temperatures and isotopic compositions through time. *Earth and Environmental Science Transactions of The Royal Society of Edinburgh*, 80(3-4), 183-192.

- Hudson, J. D., & Andrews, J. E. (1987). The diagenesis of the Great Estuarine Group, Middle Jurassic, Inner Hebrides, Scotland. *Geological Society, London, Special Publications*, 36(1), 259-276.
- Hudson, J. D., Clements, R. G., Riding, J. B., Wakefield, M. I., & Walton, W. (1995). Jurassic paleosalinities and brackish-water communities: a case study. *Palaios*, 392-407.
- Hudson, J. D., Coleman, M. L., Barreiro, B. A., & Hollingworth, N. T. J. (2001). Septarian concretions from the Oxford Clay (Jurassic, England, UK): involvement of original marine and multiple external pore fluids. *Sedimentology*, 48(3), 507-531.
- Hudson, J. D., & Harris, J. P. (1979). Sedimentology of the Great Estuarine Group (Middle Jurassic) of north-west Scotland. Symp. Sédimentation Jurassique W. Européen, Paris, 1977. *Assoc. Sédimentol. Fr. Publication Speciale* 1, 1-13.
- Hudson, J. D., & Martill, D. M. (1994). The Peterborough Member (Callovian, Middle Jurassic) of the Oxford Clay Formation at Peterborough, UK. *Journal of the Geological Society*, 151(1), 113-124.
- Hudson, J.D., and Trewin, N.H., (2002). Chapter 11: Jurassic. In: Trewin, .H., ed., *The Geology of Scotland* (4th edition): London, The Geological Society, p. 323–350.
- Hudson, J. D., & Wakefield, M. I. (2018). The Lonfearn Member, Lealt Shale Formation, (Middle Jurassic) of the Inner Hebrides, Scotland. *Scottish Journal of Geology*, 54(2), 87-97.
- Huntington, K. W., Eiler, J. M., Affek, H. P., Guo, W., Bonifacie, M., Yeung, L. Y., Thiagarajan, N., Passey, B., Tripathi, A., Daëron,, M. & Came, R. (2009). Methods and limitations of ‘clumped’CO₂ isotope (Δ_{47}) analysis by gas-source isotope ratio mass spectrometry. *Journal of Mass Spectrometry*, 44(9), 1318-1329.
- Huntington, K. W., Budd, D. A., Wernicke, B. P., & Eiler, J. M. (2011). Use of clumped-isotope thermometry to constrain the crystallization temperature of diagenetic calcite. *Journal of Sedimentary Research*, 81(9), 656-669.
- Huntington, K. W., & Lechler, A. R. (2015). Carbonate clumped isotope thermometry in continental tectonics. *Tectonophysics*, 647, 1-20.
- Huyghe, D., Daëron, M., de Rafelis, M., Blamart, D., Sébilo, M., Paulet, Y.-M., & Lartaud, F. (2022). Clumped isotopes in modern marine bivalves. *Geochimica et Cosmochimica Acta*, 316, 41-58.
- Immenhauser, A., Schoene, B. R., Hoffmann, R., & Niedermayr, A. (2016). Mollusc and brachiopod skeletal hard parts: Intricate archives of their marine environment. *Sedimentology*, 63(1), 1-59.

- Irwin, H., Curtis, C., & Coleman, M. (1977). Isotopic evidence for source of diagenetic carbonates formed during burial of organic-rich sediments. *Nature*, 269(5625), 209.
- Jamieson, J. C. (1953). Phase equilibrium in the system calcite-aragonite. *The Journal of chemical physics*, 21(8), 1385-1390.
- Jimenez-Rodriguez, S., Quade, J., Dettinger, M., Huntington, K. W., & Kelson, J. R. (2022). Comparing isotopic estimates of paleoelevation from carbonates and volcanic glass from the Miocene-age Chucal Formation in northern Chile. *Chemical Geology*, 596, 120798.
- Johnson, M. (1989). Paleogeographic significance of oriented calcareous concretions in the Triassic Katberg Formation, South Africa. *Journal of Sedimentary Research*, 59(6), 1008-1010.
- Jones, S. J., Mieszkowska, N., & Wethey, D. S. (2009). Linking thermal tolerances and biogeography: *Mytilus edulis* (L.) at its southern limit on the east coast of the United States. *The Biological Bulletin*, 217(1), 73-85.
- Kaempf, N., & Schwertmann, U. (1982). The 5-M-NaOH concentration treatment for iron oxides in soils. *Clays and clay Minerals*, 30(6), 401-408.
- Kenig, F., Hayes, J., Popp, B., & Summons, R. (1994). Isotopic biogeochemistry of the Oxford Clay Formation (Jurassic), UK. *Journal of the Geological Society*, 151(1), 139-152.
- Kim, S.-T., & O'Neil, J. R. (1997). Equilibrium and nonequilibrium oxygen isotope effects in synthetic carbonates. *Geochimica et Cosmochimica Acta*, 61(16), 3461-3475.
- King, P. M. (1976). *The secondary minerals of the tertiary lavas of northern and central skye-zeolite zonation patterns their origin and formation*: University of Aberdeen (United Kingdom).
- Kirk, R. (2017). *Development of clumped isotope techniques and their application to palaeoclimate studies*. Ph.D thesis, University of East Anglia.
- Kluge, T., Affek, H., Marx, T., Aeschbach-Hertig, W., Riechelmann, D., Scholz, D., Riechelmann, S., Immenhauser, A., Richter, D. & Fohlmeister, J. (2013). Reconstruction of drip-water $\delta^{18}\text{O}$ based on calcite oxygen and clumped isotopes of speleothems from Bunker Cave (Germany). *Climate of the Past*, 9(1), 377-391.
- Knox, R. O. B. (1977). Upper Jurassic pyroclastic rocks in Skye, west Scotland. *Nature*, 265(5592), 323-324.
- Kronenberg, A. K., Yund, R. A., & Giletti, B. J. (1984). Carbon and oxygen diffusion in

- calcite: effects of Mn content and P H₂O. *Physics and chemistry of minerals*, 11(3), 101-112.
- Lachniet, M. S. (2015). Are aragonite stalagmites reliable paleoclimate proxies? Tests for oxygen isotope time-series replication and equilibrium. *Bulletin*, 127(11-12), 1521-1533.
- Lartaud, F., Emmanuel, L., De Rafélis, M., Pouvreau, S., & Renard, M. (2010). Influence of food supply on the $\delta^{13}\text{C}$ signature of mollusc shells: implications for palaeoenvironmental reconstitutions. *Geo-Marine Letters*, 30(1), 23-34.
- Lécuyer, C., & O'Neil, J. R. (1994). Stable isotope compositions of fluid inclusions in biogenic carbonates. *Geochimica et Cosmochimica Acta*, 58(1), 353-363.
- Lefort, A., Hautevelles, Y., Lathuilière, B., & Huault, V. (2012). Molecular organic geochemistry of a proposed stratotype for the Oxfordian/Kimmeridgian boundary (Isle of Skye, Scotland). *Geological Magazine*, 149(5), 857-874.
- Leng, M. J., & Marshall, J. D. (2004). Palaeoclimate interpretation of stable isotope data from lake sediment archives. *Quaternary Science Reviews*, 23(7-8), 811-831.
- Letulle, T., Suan, G., Daëron, M., Rogov, M., Lécuyer, C., Vinçon-Laugier, A., Reynard, B., Montagnac, G., Lutikov, O. & Schlögl, J. (2022). Clumped isotope evidence for Early Jurassic extreme polar warmth and high climate sensitivity. *Climate of the Past*, 18(3), 435-448.
- Loyd, S. J., Corsetti, F. A., Eiler, J. M., & Tripathi, A. K. (2012). Determining the Diagenetic Conditions of Concretion Formation: Assessing Temperatures and Pore Waters Using Clumped Isotopes. *Journal of Sedimentary Research*, 82(12), 1006-1016.
- Loyd, S. J., Dickson, J., Boles, J. R., & Tripathi, A. K. (2014). Clumped-isotope constraints on cement paragenesis in septarian concretions. *Journal of Sedimentary Research*, 84(12), 1170-1184.
- Macgregor, D. S. (2020). Regional variations in geothermal gradient and heat flow across the African plate. *Journal of African Earth Sciences*, 171, 103950.
- Mangenot, X., Gasparrini, M., Gerdes, A., Bonifacie, M. and Rouchon, V. (2018). An emerging thermochronometer for carbonate-bearing rocks: $\Delta_{47}/(\text{U-Pb})$. *Geology*, 46(12), 1067-1070.
- Mangenot, X., Deçoninck, J. F., Bonifacie, M., Rouchon, V., Collin, P. Y., Quesne, D., Gasparrini, M. & Sizun, J. P. (2019). Thermal and exhumation histories of the northern subalpine chains (Bauges and Bornes—France): Evidence from forward

- thermal modeling coupling clay mineral diagenesis, organic maturity and carbonate clumped isotope (Δ_{47}) data. *Basin Research*, 31(2), 361-379.
- Marin, F., Luquet, G., Marie, B., & Medakovic, D. (2007). Molluscan shell proteins: primary structure, origin, and evolution. *Current topics in developmental biology*, 80, 209-276.
- Matthews, A., Affek, H., Ayalon, A., Vonhof, H., & Bar-Matthews, M. (2021). Eastern Mediterranean climate change deduced from the Soreq Cave fluid inclusion stable isotopes and carbonate clumped isotopes record of the last 160 ka. *Quaternary Science Reviews*, 272, 107223.
- McBride, E. F. (1988). Contrasting diagenetic histories of concretions and host rock, Lion Mountain Sandstone (Cambrian), Texas. *Geological Society of America Bulletin*, 100(11), 1803-1810.
- McBride, E. F., Picard, M. D., & Milliken, K. L. (2003). Calcite-cemented concretions in Cretaceous sandstone, Wyoming and Utah, USA. *Journal of Sedimentary Research*, 73(3), 462-483.
- McConnaughey, T. A., Burdett, J., Whelan, J. F., & Paull, C. K. (1997). Carbon isotopes in biological carbonates: respiration and photosynthesis. *Geochimica et Cosmochimica Acta*, 61(3), 611-622.
- McConnaughey, T. A., & Gillikin, D. P. (2008). Carbon isotopes in mollusk shell carbonates. *Geo-Marine Letters*, 28(5), 287-299.
- Methner, K., Mulch, A., Fiebig, J., Wacker, U., Gerdes, A., Graham, S.A. and Chamberlain, C.P. (2016). Rapid middle Eocene temperature change in western North America. *Earth and Planetary Science Letters*, 450, 132-139.
- Mettam, C., Johnson, A. L., Nunn, E. V., & Schöne, B. R. (2014). Stable isotope ($\delta^{18}\text{O}$ and $\delta^{13}\text{C}$) sclerochronology of Callovian (Middle Jurassic) bivalves (*Gryphaea* (*Bilobissa*) *dilobotes*) and belemnites (*Cylindroteuthis puzosiana*) from the Peterborough Member of the Oxford Clay Formation (Cambridgeshire, England): evidence of palaeoclimate, water depth and belemnite behaviour. *Palaeogeography, Palaeoclimatology, Palaeoecology*, 399, 187-201.
- Milliman, J. D. (1974). *Marine Carbonates*. New York: Springer-Verlag.
- Morad, S., Al-Ramadan, K., Ketzer, J. M., & De Ros, L. (2010). The impact of diagenesis on the heterogeneity of sandstone reservoirs: A review of the role of depositional facies and sequence stratigraphy. *AAPG bulletin*, 94(8), 1267-1309.
- Morton, N. (1987). Jurassic subsidence history in the Hebrides, NW Scotland. *Marine and*

Petroleum Geology, 4(3), 226-242.

- Morton, N., & Hudson, J. D., (1995). Field guide to the Jurassic of the isles of Raasay and Skye, Inner Hebrides, NW Scotland. In: Taylor, P. D., ed., *Field geology of the British Jurassic*: London, The Geological Society, p. 209-280.
- Mozley, P. S., & Burns, S. J. (1993). Oxygen and carbon isotopic composition of marine carbonate concretions; an overview. *Journal of Sedimentary Research*, 63(1), 73-83.
- Mucciarone, D. A., & Williams, D. F. (1990). Stable isotope analyses of carbonate complicated by nitrogen oxide contamination: a Delaware Basin example. *Journal of Sedimentary Research*, 60(4).
- Noh, J. H., & Lee, I. (1999). Diagenetic pore fluid evolution in the Pohang Miocene sediments: oxygen isotopic evidence of septarian carbonate concretions and authigenic mineral phases. *Geosciences Journal*, 3(3), 141-149.
- Nooitgedacht, C., van der Lubbe, H., Ziegler, M., & Staudigel, P. (2021). Internal water facilitates thermal resetting of clumped isotopes in biogenic aragonite. *Geochemistry, Geophysics, Geosystems*, 22(5), e2021GC009730.
- Nunn, E. V., Price, G. D., Hart, M. B., Page, K. N., & Leng, M. J. (2009). Isotopic signals from Callovian–Kimmeridgian (Middle–Upper Jurassic) belemnites and bulk organic carbon, Staffin Bay, Isle of Skye, Scotland. *Journal of the Geological Society*, 166(4), 633-641.
- Nyman, S. L., Gani, M. R., Bhattacharya, J. P., & Lee, K. (2014). Origin and distribution of calcite concretions in Cretaceous Wall Creek Member, Wyoming: Reservoir-quality implication for shallow-marine deltaic strata. *Cretaceous Research*, 48, 139-152.
- Pálmason, G., & Sæmundsson, K. (1979). Summary of conductive heat flow in Iceland *Terrestrial heat flow in Europe* (pp. 218-220): Springer.
- Passey, B. H., & Henkes, G. A. (2012). Carbonate clumped isotope bond reordering and geospeedometry. *Earth and Planetary Science Letters*, 351, 223-236.
- Passey, B. H., Levin, N. E., Cerling, T. E., Brown, F. H., & Eiler, J. M. (2010). High-temperature environments of human evolution in East Africa based on bond ordering in paleosol carbonates. *Proceedings of the National Academy of Sciences*, 107(25), 11245-11249.
- Patterson, W. P. (1999). Oldest isotopically characterized fish otoliths provide insight to Jurassic continental climate of Europe. *Geology*, 27(3), 199-202.
- Paxton, R. B., Dennis, P. F., Marca, A. D., Hendry, J. P., Hudson, J. D., & Andrews, J. E.

- (2021). Taking the heat out of British Jurassic septarian concretions. *The Depositional Record*, 7(2), 333-343. Supplemental information: <https://doi.org/10.6084/m9.figshare.13567667.v2>
- Pearson, M., Hendry, J., Taylor, C., & Russell, M. (2005). Fatty acids in sparry calcite fracture fills and microsparite cement of septarian diagenetic concretions. *Geochimica et Cosmochimica Acta*, 69(7), 1773-1786.
- Pederson, C., Mavromatis, V., Dietzel, M., Rollion-Bard, C., Breitenbach, S., Yu, D., Nehrke, G. & Immenhauser, A. (2020). Variation in the diagenetic response of aragonite archives to hydrothermal alteration. *Sedimentary Geology*, 406, 105716.
- Pederson, C., Mavromatis, V., Dietzel, M., Rollion-Bard, C., Nehrke, G., Jöns, N., Jochum, K. & Immenhauser, A. (2019). Diagenesis of mollusc aragonite and the role of fluid reservoirs. *Earth and Planetary Science Letters*, 514, 130-142.
- Petersen, S. V., Dutton, A., & Lohmann, K. C. (2016). End-Cretaceous extinction in Antarctica linked to both Deccan volcanism and meteorite impact via climate change. *Nature communications*, 7(1), 1-9.
- Poulsen, C. J., Pollard, D., & White, T. S. (2007). General circulation model simulation of the $\delta^{18}\text{O}$ content of continental precipitation in the middle Cretaceous: A model-proxy comparison. *Geology*, 35(3), 199-202.
- Poulter, J. J. (2011). *Mid Paleocene fossil floras and climate from western Scotland*. Ph.D. thesis, University of Leeds.
- Price, G. D., Bajnai, D., & Fiebig, J. (2020). Carbonate clumped isotope evidence for latitudinal seawater temperature gradients and the oxygen isotope composition of Early Cretaceous seas. *Palaeogeography, Palaeoclimatology, Palaeoecology*, 552, 109777.
- Price, G. D., & Passey, B. H. (2013). Dynamic polar climates in a greenhouse world: Evidence from clumped isotope thermometry of Early Cretaceous belemnites. *Geology*, 41(8), 923-926.
- Prokoph, A., Shields, G., & Veizer, J. (2008). Compilation and time-series analysis of a marine carbonate $\delta^{18}\text{O}$, $\delta^{13}\text{C}$, $^{87}\text{Sr}/^{86}\text{Sr}$ and $\delta^{34}\text{S}$ database through Earth history. *Earth-Science Reviews*, 87(3-4), 113-133.
- Purvis, K., Dennis, P., Holt, L., & Marca, A. (2020). The origin of carbonate cements in the hildasay reservoir, Cambo Field, Faroe-Shetland Basin; clumped isotopic analysis and implications for reservoir performance. *Marine and Petroleum Geology*, 104641.

- Quade, T. (1993). Stable carbon and oxygen isotopes in soil carbonates. *Climate change in continental isotopic records. Geophysical Monograph*, 78, 217-231.
- Raiswell, R. (1976). The microbiological formation of carbonate concretions in the Upper Lias of NE England. *Chemical Geology*, 18(3), 227-244.
- Raiswell, R., & Fisher, Q. (2000). Mudrock-hosted carbonate concretions: a review of growth mechanisms and their influence on chemical and isotopic composition. *Journal of the Geological Society*, 157(1), 239-251.
- Riding, J. B., & Thomas, J. E. (1997). Marine palynomorphs from the Staffin Bay and Staffin Shale formations (Middle-Upper Jurassic) of the Trotternish Peninsula, NW Skye. *Scottish Journal of Geology*, 33(1), 59-74.
- Ritter, A. C., Mavromatis, V., Dietzel, M., Kwiecien, O., Wiethoff, F., Griesshaber, E., Casella, L. A., Schmahl, W. W., Koelen, J. & Neuser, R. D. (2017). Exploring the impact of diagenesis on (isotope) geochemical and microstructural alteration features in biogenic aragonite. *Sedimentology*, 64(5), 1354-1380.
- Robinson, S. A., Scotchman, J. I., White, T. S., & Atkinson, T. C. (2010). Constraints on palaeoenvironments in the Lower Cretaceous Wealden of southern England, from the geochemistry of sphaerosiderites. *Journal of the Geological Society*, 167(2), 303-311.
- Ruebsam, W., Reolid, M., & Schwark, L. (2020). $\delta^{13}\text{C}$ of terrestrial vegetation records Toarcian CO₂ and climate gradients. *Scientific reports*, 10(1), 1-8.
- Saenger, C., Affek, H. P., Felis, T., Thiagarajan, N., Lough, J. M., & Holcomb, M. (2012). Carbonate clumped isotope variability in shallow water corals: Temperature dependence and growth-related vital effects. *Geochimica et Cosmochimica Acta*, 99, 224-242.
- Saha, Narotam (2013): Application of clumped isotope thermometry on Sea Mere lake sediment carbonate to recover palaeoclimate signal throughout the last 700 years. Master's thesis, University of East Anglia.
- Saigal, G., & Bjørlykke, K. (1987). Carbonate cements in clastic reservoir rocks from offshore Norway—relationships between isotopic composition, textural development and burial depth. *Geological Society, London, Special Publications*, 36(1), 313-324.
- Sample, J. C., Torres, M. E., Fisher, A., Hong, W.-L., Destrigneville, C., Defliese, W. F., & Tripathi, A. E. (2017). Geochemical constraints on the temperature and timing of carbonate formation and lithification in the Nankai Trough, NanTroSEIZE transect.

- Geochimica et Cosmochimica Acta*, 198, 92-114.
- Scarrow, J. H. (1992). *Petrogenesis of the Tertiary lavas of the Isle of Skye, NW Scotland*. Ph.D. thesis, University of Oxford.
- Schauble, E. A., Ghosh, P., & Eiler, J. M. (2006). Preferential formation of ^{13}C – ^{18}O bonds in carbonate minerals, estimated using first-principles lattice dynamics. *Geochimica et Cosmochimica Acta*, 70(10), 2510-2529.
- Schauer, A. J., Kelson, J., Saenger, C., & Huntington, K. W. (2016). Choice of ^{17}O correction affects clumped isotope (Δ_{47}) values of CO_2 measured with mass spectrometry. *Rapid Communications in Mass Spectrometry*, 30(24), 2607-2616.
- Schofield, N., Jerram, D. A., Holford, S., Archer, S., Mark, N., Hartley, A., Howell, J., Muirhead, D., Green, P. & Hutton, D. (2016). Sills in sedimentary basins and petroleum systems *Physical geology of shallow magmatic systems* (pp. 273-294): Springer.
- Searl, A. (1992). Sedimentology and early diagenesis of the Broadford Beds (Lower Jurassic), Skye, north-west Scotland. *Geological Journal*, 27(3), 243-270.
- Selles-Martinez, J. (1996). Concretion morphology, classification and genesis. *Earth-Science Reviews*, 41(3-4), 177-210.
- Sellwood, B. W., & Valdes, P. J. (2008). Jurassic climates. *Proceedings of the Geologists' Association*, 119(1), 5-17.
- Seuront, L., Nicastro, K. R., Zardi, G. I., & Goberville, E. (2019). Decreased thermal tolerance under recurrent heat stress conditions explains summer mass mortality of the blue mussel *Mytilus edulis*. *Scientific reports*, 9(1), 1-14.
- Seyfried Jr, W., Ding, K., & Berndt, M. (1991). Phase equilibria constraints on the chemistry of hot spring fluids at mid-ocean ridges. *Geochimica et Cosmochimica Acta*, 55(12), 3559-3580.
- Shackleton, N., & Kennett, J. (1975). Paleotemperature history of the Cenozoic and the initial of Antarctic glaciation: oxygen and carbon isotope analyses in Deep Sea Drilling Project Sites 277, 279, and 181. *DSDP*, 29, 599-612.
- Sheppard, S. M. F. (1986). Characterization and isotopic variations in natural waters. *Reviews in Mineralogy and Geochemistry*, 16(1), 165-183.
- Smith, A. G., Smith, D. G., & Funnell, B. M. (2004). *Atlas of Mesozoic and Cenozoic coastlines*: Cambridge University Press.
- Snell, K. E., Koch, P. L., Druschke, P., Foreman, B. Z., & Eiler, J. M. (2014). High elevation of the 'Nevadaplano' during the Late Cretaceous. *Earth and Planetary Science Letters*,

386, 52-63.

- Snell, K.E., Passey, B.H., Bergmann, K.D. & Davidheiser-Kroll, B. (2019) How contaminants affect accurate measurement of clumped isotopes in CO₂. *7th International Clumped Isotope Workshop*, Long Beach CA, Oral Presentation.
- Sorte, C. J., Bernatchez, G., Mislán, K., Pandori, L. L., Silbiger, N. J., & Wallingford, P. D. (2019). Thermal tolerance limits as indicators of current and future intertidal zonation patterns in a diverse mussel guild. *Marine Biology*, *166*(1), 1-13.
- Spooner, P. T., Guo, W., Robinson, L. F., Thiagarajan, N., Hendry, K. R., Rosenheim, B. E., & Leng, M. J. (2016). Clumped isotope composition of cold-water corals: A role for vital effects? *Geochimica et Cosmochimica Acta*, *179*, 123-141.
- Staudigel, P. T., & Swart, P. K. (2016). Isotopic behavior during the aragonite-calcite transition: Implications for sample preparation and proxy interpretation. *Chemical Geology*, *442*, 130-138.
- Stolper, D. A., & Eiler, J. M. (2015). The kinetics of solid-state isotope-exchange reactions for clumped isotopes: A study of inorganic calcites and apatites from natural and experimental samples. *American Journal of Science*, *315*(5), 363-411.
- Stolper, D. A., Eiler, J. M., & Higgins, J. A. (2018). Modeling the effects of diagenesis on carbonate clumped-isotope values in deep-and shallow-water settings. *Geochimica et Cosmochimica Acta*, *227*, 264-291.
- Suarez, M. B., González, L. A., & Ludvigson, G. A. (2011). Quantification of a greenhouse hydrologic cycle from equatorial to polar latitudes: the mid-Cretaceous water bearer revisited. *Palaeogeography, Palaeoclimatology, Palaeoecology*, *307*(1-4), 301-312.
- Suarez, M. B., & Passey, B. H. (2014). Assessment of the clumped isotope composition of fossil bone carbonate as a recorder of subsurface temperatures. *Geochimica et Cosmochimica Acta*, *140*, 142-159.
- Swanson, E. M., Wernicke, B. P., Eiler, J. M., & Losh, S. (2012). Temperatures and fluids on faults based on carbonate clumped–isotope thermometry. *American Journal of Science*, *312*(1), 1-21.
- Swart, P. K. (2015). The geochemistry of carbonate diagenesis: The past, present and future. *Sedimentology*, *62*(5), 1233-1304.
- Swart, P. K., Burns, S., & Leder, J. (1991). Fractionation of the stable isotopes of oxygen and carbon in carbon dioxide during the reaction of calcite with phosphoric acid as a function of temperature and technique. *Chemical Geology: Isotope Geoscience*

section, 86(2), 89-96.

- Tan, F. C., & Hudson, J. D. (1974). Isotopic studies on the palaeoecology and diagenesis of the Great Estuarine Series (Jurassic) of Scotland. *Scottish Journal of Geology*, 10(2), 91-128.
- Taylor JR, H. P., & Forester, R. W. (1971). Low-O₁₈ igneous rocks from the intrusive complexes of Skye, Mull, and Ardnamurchan, Western Scotland. *Journal of Petrology*, 12(3), 465-497.
- Thompson, G. E. K. (1977). Temperature gradients within and adjacent to the North Island volcanic belt. *New Zealand Journal of Geology and Geophysics*, 20(1), 85-97.
- Thrasher, J. (1992). Thermal effect of the Tertiary Cuillins Intrusive Complex in the Jurassic of the Hebrides: an organic geochemical study. *Geological Society, London, Special Publications*, 62(1), 35-49.
- Tobin, T. S., Wilson, G. P., Eiler, J. M., & Hartman, J. H. (2014). Environmental change across a terrestrial Cretaceous-Paleogene boundary section in eastern Montana, USA, constrained by carbonate clumped isotope paleothermometry. *Geology*, 42(4), 351-354.
- Towe, K. M., & Thompson, G. R. (1972). The structure of some bivalve shell carbonates prepared by ion-beam thinning. *Calcified tissue research*, 10(1), 38-48.
- Umbo, S. (2020). *Clumped isotopes in planktonic foraminifera: application in a multiproxy North Atlantic study*. Ph.D. thesis, University of East Anglia.
- Urey, H. C. (1947). The thermodynamic properties of isotopic substances. *Journal of the Chemical Society (Resumed)*, 562-581.
- Urey, H. C., Lowenstam, H. A., Epstein, S., & McKinney, C. R. (1951). Measurement of paleotemperatures and temperatures of the Upper Cretaceous of England, Denmark, and the southeastern United States. *Geological Society of America Bulletin*, 62(4), 399-416.
- Veizer, J., Ala, D., Azmy, K., Bruckschen, P., Buhl, D., Bruhn, F., Carden, G. A., Diener, A., Ebner, S. & Godderis, Y. (1999). ⁸⁷Sr/⁸⁶Sr, δ¹³C and δ¹⁸O evolution of Phanerozoic seawater. *Chemical Geology*, 161(1-3), 59-88.
- Veizer, J., Bruckschen, P., Pawellek, F., Diener, A., Podlaha, O. G., Carden, G. A., Jasper, T., Korte, C., Strauss, H. & Azmy, K. (1997). Oxygen isotope evolution of Phanerozoic seawater. *Palaeogeography, Palaeoclimatology, Palaeoecology*, 132(1-4), 159-172.
- Vickers, M. L., Bernasconi, S. M., Ullmann, C. V., Lode, S., Looser, N., Morales, L. G., Price,

- G. D., Wilby, P. R., Hougård, I. W. & Hesselbo, S. P. (2021). Marine temperatures underestimated for past greenhouse climate. *Scientific reports*, 11(1), 1-9.
- Vickers, M. L., Fernandez, A., Hesselbo, S. P., Price, G. D., Bernasconi, S. M., Lode, S., Ullmann, C. V., Thibault, N., Hougard, I. W. & Korte, C. (2020). Unravelling Middle to Late Jurassic palaeoceanographic and palaeoclimatic signals in the Hebrides Basin using belemnite clumped isotope thermometry. *Earth and Planetary Science Letters*, 546, 116401.
- Wakefield, M. I. (1995). Ostracoda and palaeosalinity fluctuations in the Middle Jurassic Lealt shale formation, Inner Hebrides, Scotland. *Palaeontology*, 38(3), 583-618.
- Wang, Y., Passey, B., Roy, R., Deng, T., Jiang, S., Hannold, C., Wang, X., Lochner, E. & Tripathi, A. (2021). Clumped isotope thermometry of modern and fossil snail shells from the Himalayan-Tibetan Plateau: Implications for paleoclimate and paleoelevation reconstructions. *GSA Bulletin*, 133(7-8), 1370-1380.
- Weber, J. N., & Raup, D. M. (1966). Fractionation of the stable isotopes of carbon and oxygen in marine calcareous organisms—the Echinoidea. Part I. Variation of C13 and O18 content within individuals. *Geochimica et Cosmochimica Acta*, 30(7), 681-703.
- Weber, J. N., & Woodhead, P. M. (1970). Carbon and oxygen isotope fractionation in the skeletal carbonate of reef-building corals. *Chemical Geology*, 6, 93-117.
- Wierzbowski, A., Coe, A. L., Hounslow, M. W., Matyja, B. A., Ogg, J. G., Page, K. N., Wierzbowski, H. & Wright, J. K. (2006). A potential stratotype for the Oxfordian/Kimmeridgian boundary: Staffin Bay, Isle of Skye, UK. *Volumina Jurassica*, 4(4), 17-33.
- Wilkinson, M. (1989). *Sandstone-hosted concretionary cements of the Hebrides, Scotland*: University of Leicester (United Kingdom).
- Wilkinson, M. (1991). The concretions of the Bearreraig Sandstone Formation: geometry and geochemistry. *Sedimentology*, 38(5), 899-912.
- Wilkinson, M. (1992). Concretionary cements in Jurassic sandstones, Isle of Eigg, Inner Hebrides. *Geological Society, London, Special Publications*, 62(1), 145-154.
- Wilkinson, M. (1993). Concretions of the Valtos Sandstone Formation of Skye: geochemical indicators of palaeo-hydrology. *Journal of the Geological Society*, 150(1), 57-66.
- Wilkinson, M., & Dampier, M. D. (1990). The rate of growth of sandstone-hosted calcite concretions. *Geochimica et Cosmochimica Acta*, 54(12), 3391-3399.

- Yan, L., Schöne, B. R., & Arkhipkin, A. (2012). *Eurhomalea exalbida* (Bivalvia): A reliable recorder of climate in southern South America? *Palaeogeography, Palaeoclimatology, Palaeoecology*, *350*, 91-100.
- Yapp, C. J. (1991). Oxygen isotopes in an oolitic ironstone and the determination of goethite $\delta^{18}\text{O}$ values by selective dissolution of impurities: the 5M NaOH method. *Geochimica et Cosmochimica Acta*, *55*(9), 2627-2634.
- Zachos, J., Pagani, M., Sloan, L., Thomas, E., & Billups, K. (2001). Trends, rhythms, and aberrations in global climate 65 Ma to present. *Science*, *292*(5517), 686-693.
- Zhao, L., Shirai, K., Tanaka, K., Milano, S., Higuchi, T., Murakami-Sugihara, N., Walliser, E. O., Yang, F., Deng, Y. & Schöne, B. R. (2020). A review of transgenerational effects of ocean acidification on marine bivalves and their implications for sclerochronology. *Estuarine, Coastal and Shelf Science*, *235*, 106620.
- Zhou, J., Poulsen, C., Pollard, D., & White, T. (2008). Simulation of modern and middle Cretaceous marine $\delta^{18}\text{O}$ with an ocean-atmosphere general circulation model. *Paleoceanography*, *23*(3).
- Ziveri, P., Stoll, H., Probert, I., Klaas, C., Geisen, M., Ganssen, G., & Young, J. (2003). Stable isotope 'vital effects' in coccolith calcite. *Earth and Planetary Science Letters*, *210*(1-2), 137-149.